Measuring Smoke Evolution at Full-Scale with Video Recordings

by

Jennifer Ellingham

A thesis
presented to the University of Waterloo
in fulfillment of the
thesis requirement for the degree of
Masters of Applied Science
in
Mechanical and Mechatronics Engineering

Waterloo, Ontario, Canada, 2021

Examining Committee Membership

The following served on the Examining Committee for this thesis. The decision of the Examining Committee is by majority vote.

Supervisor:	Elizabeth Weckman Professor, Dept. of Mechanical and Mechatronics Engineering University of Waterloo
Internal-External Member:	Zhongchao Tan Professor, Dept. of Mechanical and Mechatronics Engineering University of Waterloo
Internal-External Member:	Andrew Milne Lecturer, Dept. Mechanical and Mechatronics Engineering University of Waterloo

Author's Declaration

I hereby declare that I am the sole author of this thesis. This is a true copy of the thesis, including any required final revisions, as accepted by my examiners.

I understand that my thesis may be made electronically available to the public.

Abstract

Many knowledge gaps exist in our current understanding of fire and smoke dynamics — caused in large part by a lack of data on smoke evolution in fires. Advances in computer technology, however, now make it possible for high volumes of data to be processed at low cost. Video processing on an image-by-image basis is presently economically feasible and, consequently, visible aspects of fire and smoke evolution can be observed and measured in detail to help gain a better understanding of fire dynamics. Better tools for assessment of the evolution of smoke layer height are of interest to fire analysts because the predominant method of measurement in intermediate- and full-scale fire experiments is a subjective method wherein observers visually estimate the time the smoke layer takes to reach objects of known height in video recordings. Alternative methods for estimating smoke layer height require expensive sensors and utilize varying levels of subjectivity. Thus, development of a low-cost, frame-by-frame, fine mesh video analysis method forms the subject of the present research project. The method will facilitate measurement of the evolution of smoke layer height with time with more precision than previously possible and with limited subjectivity. The method also allows smoke density to be measured at many locations, a significant benefit given that previously smoke density could only be measured in limited locations, if at all, due to the cost of the necessary equipment and the challenges associated with installation of the equipment in intermediate- and full-scale fire experiments.

The new method, called the radiance method, is an adaptation of a recently adopted measurement technique in the air pollution field. It compares recorded radiance in light and dark pixel analysis areas in a camera view to the original values on a continuous basis. In this work, the radiance method is derived theoretically before an iterative method development process is used to develop a ten-step radiance approach for analysis of video records from fire experiments.

Existing video, thermocouple and heat release rate data from 11 well-instrumented, full-scale house fire experiments, fueled by five (Type A-E) sofa materials, are used in conjunction with results from 29 small-scale tests to characterize smoke evolution in the full-scale experiments. The video data from the 11 full-scale fire experiments are then used to develop and refine the radiance method through four method iterations. In all cases examined, the radiance method smoke layer descent times fall within the observer characterized times. Conversely, the other smoke layer height estimation methods can be off by more than 155 seconds relative to the observer determined values. Relative ranking of the values of maximum smoke density as determined by the radiance method match the characterized smoke density rank where comparison is possible. Two additional full-scale house fire experiments, fueled by Type F sofa materials, include revised instrumentation aimed toward improving radiance method results and determining possible applications of the method.

Collectively, the results indicate that the radiance method can estimate smoke layer descent time from video recordings with visible light areas to within 91 seconds of observer-based estimates. It may be possible to minimize these differences further via a sensitivity analysis on the choice of smoke layer threshold value. If a backlit light area and adjacent dark area are visible in the video recording, then maximum smoke density results can be obtained using the radiance method. In all cases, the maximum smoke density values for each fuel type (across experiments) fall within ±1% of the average value. The maximum smoke density values are distinct between fuel types and agree with characterization rankings (where available). Moreover, the method can be applied to existing and future colour and IR (black and white) video recordings. The radiance method can be applied to video recordings on a frame-by-frame basis but, for this application, an averaging scheme is employed to smooth the data for clearer results. Inclusion of checkerboards and cameras, with carefully selected camera models and placement, can significantly increase the amount and precision of the smoke evolution data that can be obtained. A caveat is that the red, green, and blue colour streams of colour images are influenced (to different extents) in different lighting conditions. The availability of camera calibration data, which converts recorded pixel values to radiance values, can impact the smoke layer descent times by up to 11 seconds and maximum smoke density by up to 2%.

In this work, the radiance method is used to measure smoke layer descent time and smoke density at up to 69 different vertical locations within a compartment, from a single camera angle, on a second-by-second basis. The maximum smoke density was measured at up to 14 different locations down the window in the compartment from a single camera angle. The novel radiance method developed in this thesis shows incredible promise for smoke analysis in full-scale fire experiments. Results can be useful both in aggregate and for comparison against detailed computational fire models where data on a fine mesh is needed to validate smoke progression and associated impacts in fire and evacuation models. Use of this method to analyze smoke evolution in more fire experiments, with different set-ups, scales, and instrumentation, is recommended and would further validate the radiance method as presented in this thesis.

Acknowledgements

I would like to thank many people for their help in making this thesis possible. Thanks to my incredible friends and colleagues at the lab for always going above and beyond. I would like to thank Bronwyn for her help and support over the hours counting pixels when this thesis was born and every day since. A big thank you to Vusal for stepping up to help with last minute requests and for running tests when I could not be there. Thanks to Hannah, Jay and Ginelle for your time and effort in watching videos over and over, sometimes frame-by-frame. I would also like to thank Andy for all the little and big things that were instrumental in making the experiments possible.

I would like to my virtual writing support group buddies, you know who you are, you kept me company (and accountable) on the long lonely writing road. And Jane, thank you for helping me discover that writing can be fun.

I would like to thank my family (including my fur family) for their love and support, particularly over the last year. When everything was crazy you kept me sane.

Last, but certainly not least, I would like to thank my amazing supervisor Beth. Without your help none of this would have been possible. Your knowledge and insight have helped me learn so much as a researcher, writer, student, teacher and person. I look forward to continuing to work with you on the next steps on the journey I am on.

Dedication

To Taylor. Your love and support made all of this possible.

Table of Contents

List of Figures

List of Tables

List of Abbreviations

2SW	second floor south-west room
A#	Type A material experiment repetition # of 3
a posteriori	reasoning deduced from observations or experiences
a priori	reasoning deduced from theory
ASTM	American Society for Testing and Materials
B#	Type B material experiment repetition # of 3
BNC	Bayonet-Neil-Concelman
BS	British Standards Institution
BTU/s	British thermal unit per second (unit of energy)
B&W	black and white
C#	Type C material experiment repetition # of 3
CAD	Canadian dollars
Cam#	Video camera # (Type A-E experiments)
CB#	checkerboard #
CFD	Computational Fluid Dynamics
D	door
D1	Type D material experiment repetition 1 of 1
DAQ	data acquisition
DOCS	Digital Opacity Compliance System
DOM	Digital Optical Method
DVR	digital video recorder
E1	Type E material experiment repetition 1 of 1
e.g.	*exempli gratia* (for example)
et al.	*et alia* (and others)
etc.	*et cetera* (and so forth)

F#	Type F material experiment repetition # of 2
FDS	Fire Dynamics Simulator
fps	frames per second (unit of recording speed)
FR	fire-retardant
ft	foot (unit of length)
FTIR	Fourier Transform Infrared Spectroscopy
g	gram (unit of mass)
horiz.	horizontal
HRR	heat release rate
i.e.	*id est* (that is)
IP	ingress protection
ISO	International Organization for Standardization
K	kelvin (unit of temperature)
kg/m^3	kilogram per metre cubed (unit of density)
kW	kilowatt (unit of energy)
kW/m^2	kilowatts per metre squared (unit of energy)
LED	light-emitting diode
LFR	lightly fire-retardant
LR	living room
m	metre (unit of length)
max.	maximum
min.	minimum
mm	millimetre (unit of length)
mL	milliliter (unit of volume)
MOD	mass optical density
orient.	orientation
px	pixel (unit of length, unit of area in digital images)
NBS	National Bureau of Standards (now NIST)

NFPA	National Fire Protection Association
NFR	non fire-retardant
NI	National Instruments
NIST	National Institute of Standards and Technology
NW	north-west
ref.	reference
RGB	red, green, blue
s	Second (unit of time)
SFPE	Society of Fire Protection Engineers
SE	south-east
SI	International System of Units
std.	standard
SW	south-west
T#	thermocouple rake #
T&Y	Tanaka & Yamana
USD	United States dollars
UW	University of Waterloo
V#	Video camera # (Type F experiments)
vert.	vertical
vol.	volume
vs.	versus
W	window

List of Symbols

°C	degrees Celsius (unit of temperature)
$	dollar (unit of money)
#	number
%	percent
a	beginning of integration region, linear equation slope
A	area
α	power law heat release rate curve constant
b	end of integration region, linear equation intercept
C_1	constant
C_2	constant
C_n	interpolation constant
D_m	maximum specific optical density
D_S	specific optical density
$D_{S,max}$	maximum specific optical density
f	fraction/ percentage
h	ceiling height above fire base
H	floor ceiling height
h_b	height of fire base
h_r	ratio calculation height
i	counter
I	transmitted light intensity
$\bar{I}_b$	average background intensity
I_{crit}	intensity at t_{crit}
I_i	pixel intensity of each column
I_0	Incident light intensity
$\bar{I}_s$	average exit sign intensity

I'	relative visibility
j	contrast pair counter
k	constant
ℓ	length
m	mass
m_0	initial mass
Δm	change in mass
n	counter total
N	Percentage, radiance scattered into transmission path
N_1*	radiance scattered into transmission path segment 1
N_2*	radiance scattered into transmission path segment 2
N_3*	radiance scattered into transmission path segment 3
N_{B0}	radiance emitted by black background area
N_B	incident radiance at camera apparently from black background area
N_S*	radiance scattered into the transmission path by smoke
N_{W0}	radiance emitted by white background area
N_W	incident radiance at camera apparently from white background area
O	opacity
p	parameter
p_{av1}	direct parameter average
p_{av2}	reciprocal parameter average
r	uniformity ratio
r_ℓ	lower layer uniformity ratio
r_u	lower layer uniformity ratio
ρ_s	smoke density
s	physical scaling factor
σ	extinction coefficient
t	time

t_0	incubation time
t_{crit}	critical time for exit sign visibility
t_g	growth time
T	temperature, transmission
T_1*	radiance transmission losses in path segment 1
T_2*	radiance transmission losses in path segment 2
T_3*	radiance transmission losses in path segment 3
T_S*	radiance transmission losses due to smoke
ΔT	change in temperature
V	volume, visibility
x	location in x direction
X_1	path segment 1 between camera and background area
X_2	path segment 2 between camera and background area
X_3	path segment 3 between camera and background area
y	location in y direction
z	height, location in z direction
Z	smoke layer height
z_{top}	height of highest sensor
$Z_{100°C}$	100 °C isotherm smoke layer height
Z_{im}	smoke layer height from images
Z_{int}	integral ratio smoke layer height
$Z_{N\%}$	N-percent smoke layer height
Z_{NFPA}	NFPA smoke layer height
$Z_{T\&Y}$	Tanaka & Yamana smoke layer height

Chapter 1

Introduction

The primary goals of fire safety engineering are to safeguard the public and protect property and business against damages and loss due to fire. In order for engineers to achieve their goals, the science – fire safety science – must be well understood and translated into practical engineering approaches. To accomplish this, research is required into the fundamental behaviour of fires and this must be coupled with new tools and methods to predict that behaviour under a wide range of possible circumstances. One key aspect of fire behaviour that must be understood is smoke -- its evolution and movement from compartment to compartment during fires. The dynamics of smoke development is important for evacuation (occupant egress) and general scientific understanding of new fire environments, which are both critical to advancing the field of fire safety science.

Smoke can be produced by a fire in small or large quantities, ranging in temperature from warm to extremely hot, appear optically “thin” or “thick,” and contain low or high concentrations of toxic gases. All these properties evolve over time in a fire scenario because smoke evolution is intrinsically tied to the development of the fire that created it and the environment in which the fire occurs. Further, the specific properties of smoke impact a person’s ability to escape a fire, thus playing a large role in fire safety and evacuation because smoke almost always spreads further than the fire itself. Outdoors, smoke rises up and can travel away from the fire source depending on ambient conditions, while in a compartment smoke rises and often spreads outward along a ceiling, thereafter migrating from room to room or area to area within a larger indoor structure.

Numerous aspects of a fire environment impact the ability of a person attempting to escape. Direct contact with the fire can result in skin burns. Alternatively, as the temperatures in the vicinity adjacent to a fire rise, it becomes more uncomfortable for a person trying to escape and, beyond a certain point, exposure to the heated smoke may burn their throat and lungs. At the same time, occupant visibility is reduced by smoke, and this, coupled with exposure to toxic gases, can possibly lead to disorientation and often slows down their escape. While burns frequently cause injuries and deaths, exposure and disorientation due to smoke cause

many more. This is why smoke has been called the 'silent killer': it causes about 70% of fire-related deaths in Canada [1]. Given the potential for injury and death due to smoke, the study of smoke evolution, movement, and consequent impact on evacuation is a key element of fire safety.

Well-designed fire experiments can provide information on specific details of fire and smoke progression. However, fire experiments can be very costly so limited numbers are conducted, and results can usually be applied only to scenario(s) similar to those studied. Post-fire investigations also provide limited information but, some critical specifics of the scenario and potential compounding factors are inevitably unknown. Together with physics, results of fire experiments and post-fire investigative evidence form the basis of much of our current understanding of how real fires develop over time. Fire models (from manual calculations to computational simulations) are based on simplifications of the complex underlying physics of fire dynamics, coupled with our current situational understanding, and are cross-compared and modified based on available information. Every model, simple or complex, requires use of physical assumptions that limit the fire situations for which they can be used. Similarly, every model requires input data, which are typically critical to the outcome of the model, although the amount and type of input required often varies by complexity of model. In many realistic fire cases, the necessary data simply do not exist [2]. "It might be said that modern computer technology has allowed fire modelling to develop too rapidly, outstripping our understanding of fire dynamics and our ability to use the models in a safe and constructive manner. This is chiefly due to the fact that insufficient experimental data are available to enable verification of the models." [3: p.177].

Data relating to smoke evolution during fires are particularly scarce. This dearth of data is driven by a lack of viable methods and opportunities for collection of information about smoke evolution, toxicity and movement in harsh fire environments. The lack of opportunities and methods are both driven by the challenges of finding instrumentation that is robust enough to withstand the hostile fire environment or that is economical enough that it can be replaced after each experiment. In practice this means that experimentalists must carefully select and position instruments to maximize the amount and quality of data gathered, while simultaneously protecting the instruments from the fire environment and visa versa. Despite this difficulty, it is possible to measure some components of smoke evolution in large fire experiments. For example, an accepted but very subjective method for determining smoke presence is to watch the smoke develop and make notes of smoke location at various times. The location of the smoke can also be inferred, with varying degrees of accuracy and subjectivity, from temperature and gas sensor measurements. For the most part, however, non-subjective, direct measurement methods for tracking smoke location during large fires do not exist. Likewise, a small number of instruments can indirectly estimate smoke optical "thickness" with different levels of accuracy and subjectivity; however, it is seldom economically feasible to install many, or often even one, of these

instruments in a fire experiment where they may be damaged. Thus, there is a dire need for less subjective, direct measurement methods that can provide much needed data on smoke development in fires.

A lack of well-instrumented, large fire experiments also limits the opportunities to collect data on smoke evolution in fires. Historically, the cost-benefit of undertaking full fire experiments has resulted in either a small number of large, well-instrumented fire experiments or a large number of smaller fire experiments with instrumentation chosen to be most robust and therefore focused around a subset of factors and physical variables of interest. These often include temperature and video recording of the fire, though it is only in rare instances that the data have been used to undertake detailed analyses of smoke progression during the experiments. To derive the most benefit from a new method for measurement of smoke evolution in fires not only should it be designed to withstand the harsh experimental fire environment, but it should also be able to extract data from existing experimental data on fires. Development of such a method is the essence of the present research.

Video recordings are ideal data sources by which to study smoke evolution in fires. There are three main reasons for this. First, smoke (or more precisely the particulate matter within smoke) is visible and, therefore, smoke location as a function of time can be directly measured from video recordings. Second, a large pool of video data exists since video is often recorded at numerous locations during fire experiments to qualitatively inform understanding of fire and smoke evolution. Instead thermocouples, and thus temperatures, have been used more widely to infer smoke location in larger-scale fire experiments, leaving the corresponding video recording untapped for this purpose. Further, in today's security conscious world, additional sources of video recordings from fires or fire investigations may exist which, if analyzed, could further expand the existing data pool. Finally, video analysis is now a financially viable option due to technological advancements and ever-decreasing costs for higher video resolution systems and processing power. What is needed to capitalize on this wealth of information, therefore, is development of consistent analysis protocols to deconvolute the key characteristics of smoke development from existing, and future, video records of fires. While currently feasible, a suite of well-designed smoke analysis methods has a promising future since, as video technology continues to advance, the methods and information obtained will necessarily become more precise.

Accordingly, the main objective of this research is to develop an optical measurement method for investigating time-varying smoke evolution, smoke layer height and smoke density, from video recordings of fires. The method is designed to minimize subjectivity by the analyst and should be appropriate for application to video recordings from a wide variety of past, present, and future fire scenarios.

The present research is motivated by a desire to improve public safety. In this regard, a method that meets the above objectives could potentially generate large quantities of sorely needed data on smoke evolution during a range of different fire scenarios. Results will lead to improved insight into fire and smoke evolution, and consequently result in modification and advancement of existing models for these complex processes. In combination, the deeper understanding and better tools might, in turn, drive improvements to building design for fire safety, fire safety protocols, and public awareness of the dangers of fire and smoke.

To accomplish the objective, this thesis is divided into five chapters. Background information and the literature review are in Chapter 2 which begins with detailing the complex interactions between fire and smoke as a context for the remainder of this work. Existing smoke layer height and smoke density estimation methods are evaluated to determine gaps and weakness that provide basis for the proposed new smoke evolution method. Chapter 3 outlines the methods used in this work. Extant smoke layer height and density methods were initially used to characterize these properties using data collected in full-scale house fire experiments. The proposed radiance method is then derived from theory. The five iterations required to refine the radiance method conclude the chapter. The results from these methods are presented and discussed in Chapter 4. Finally, conclusions and recommendations regarding the proposed radiance method comprise Chapter 5.

Chapter 2

Background

Smoke evolution is the focus of this work. Smoke is inexorably tied to fire, often in a complex manner. For this reason, a review of the basics of fire and fire dynamics is presented first. Once the basic interactions between fire and smoke evolution are well understood, focus shifts to discussing how smoke layer height and density have been measured in the past, including the advantages and disadvantages of the various measurement methods. The genesis of the method proposed in this thesis completes this chapter.

2.1 Fire and Smoke Dynamics

According to the National Fire Protection Association, fire is "a rapid oxidation process, which is a chemical reaction resulting in the evolution of light and heat in varying intensities." [4,5]. Three components are required for the chemical reactions that are fire (or combustion) to take place: fuel, oxidizer and heat [4]. The three components share a complex relationship. Changing any one component can influence the other two and is likely to influence the behaviour of the fire and, consequently, smoke from that fire.

The comparatively simple example of a fireplace or campfire (*e.g.*, Figure 2.1) can demonstrate all of these interactions. In this example, wood is the typical fuel and the oxidizer is oxygen (about 21% [4]) in air. The final component required for the chemical reactions to take place is heat that is often provided in the form of a lighter, match or something similar. Since the fuel (wood) is a solid, it must first be heated to the point of vapourization to produce the vapour which is the component that ignites when mixed with air and sufficiently heated. A fire ignites if the chemical reactions are initiated and continue to burn if the chemical reactions can be sustained [4]. Thus, establishing a fire depends on the heat source to provide heat long enough that the chemical reactions are initiated (ignition) and the fuel vapourizes and mixes with oxidizer fast enough to reach a burning rate that in turn produces enough heat to sustain its own chemical reactions. In the case of a wood burning fire, a match or lighter is not usually large enough to directly start the chemical reactions. A different fuel (or fuels), with a lower heat requirement, is used to initiate ignition of the wood logs [3]. For example, paper can be ignited by a small heat source such that the burning paper in turn ignites kindling (small, dry twigs and branches) that, if they burn long enough and hot enough, can then ignite the logs. The paper is typically crumpled partially for

ventilation (oxygen supply) purposes, though many may not realize it. A stack of paper would not be used because it is less likely to ignite, and continue to burn as readily, in part because insufficient air can ingress to sustain the chemical reactions. The crumpled paper, on the other hand, allows air to readily reach the burning area. Of course, this is once again simplified because the crumpled paper also focuses the heat source thereby heating a localized area consistently (and potentially igniting kindling in that area) rather than spreading out the heat as a flat piece of paper would.

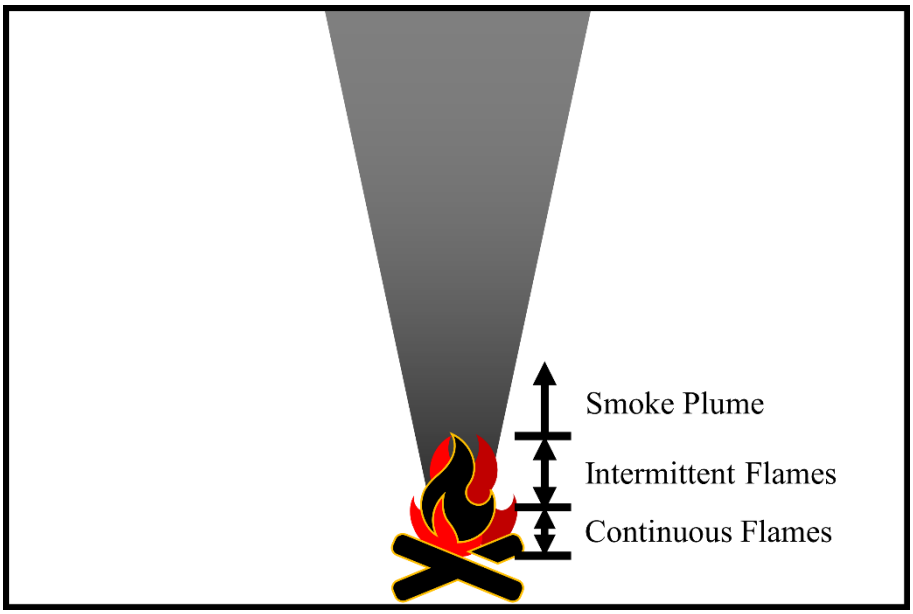

Figure 2.1: A “simple” campfire

To dig further into the example, the wood (fuel) will also have an impact on the fire because soft or hard, dry or wet wood in small or large logs will ignite more or less readily and burn for shorter or longer durations, respectively [3]. A “tee-pee” or “log cabin” or “fall where it will” log configuration will change the air flow patterns, and thus the burning rate, of the fire. (Wood cribs, similar to the “log cabin” configuration, are often used in fire experiments and are well studied [3].) Throw some wet leaves or needles (potential fuel) on the fire before the logs ignite and the fire may be smothered since the leaves cover the area, cutting off the necessary oxygen supply, and the water in the leaves or needles acts as a heat sink. Alternatively, throw some dry leaves or needles on the fire after the logs are burning and they might ignite instantly and create large particulate matter that floats in the air.

Although few likely consider it, many aspects that are inherent in a campfire are generally well known because the scenario has been so common that the knowledge has grown and been passed down between generations. However, as previously stated, this “simple” campfire turns into a complex example of fire dynamics (the study of fire behaviour incorporating the engineering disciplines of heat transfer and fluid dynamics and the science

disciplines of chemistry and physics [3]). This simple scenario is already so complex that it would be very difficult to model the interactions between fuel, oxidizer, and heat because every factor plays a role (*e.g.*, it would be almost impossible to create a detailed model of the campfire in Figure 2.1).

If there is no wind, once a fire ignites on a horizontal surface it can be divided into three sections from the base of the fire: continuous flame, intermittent flame, and smoke plume [4]. As the names imply, the continuous and intermittent flames are the part of the fire where the flames are continuously or intermittently present, respectively [4]. These sections are denoted in Figure 2.1 for the "simple" example of a campfire.

Smoke begins to be visible in the intermittent flames (grey in Figure 2.1) and rises forming a smoke plume [3]. Smoke from a campfire or fireplace is visually identifiable because of its dark colour. The smoke can be a "thin" light grey, a "thick" or "dense" dark grey or black, and it sometimes appears lighter at night when it reflects the fire light. Technically, smoke is defined as "the airborne solid and liquid particulates and gases evolved when a material undergoes pyrolysis or combustion, together with the quantity of air that is entrained or otherwise mixed into the mass." [3–5]. The airborne particulates are the visual part of the smoke; the larger particulates such as floating burnt or glowing ash and the suspended smaller particulates give air the appearance of being grey. Certain fuels (*e.g.*, leaves and needles) are more prone to producing large particulates when they burn. Smoke is intrinsically tied to the fire that created it and, therefore, changes that affect the fire also affect the smoke. For example, if a fire is under ventilated then the fuel vapour may not be completely oxidized and it may contribute to the generation of small particulate matter that is visible in smoke. That is, less ventilation often results in more particulate matter and soot. This incomplete combustion results in the formation of gases such as carbon monoxide, which are invisible and typically toxic to humans. The particulate matter and hot fire gases cause burning sensation in the eyes and can make it difficult to breathe often leading to people sitting up-wind of the smoke and moving if the wind direction shifts.

Many materials, including wood, undergo incomplete combustion producing carbon monoxide (gas) and carbon (solid *i.e.*, particulate matter and soot) as by-products of the chemical reactions in addition to the complete combustion products of water vapour (gas), carbon dioxide (gas), light (energy) and heat (energy). In high enough concentrations, these by-products can be dangerous and even deadly to humans. Thus, fuel, ventilation, and heat all play a crucial role in a fire, the smoke it produces, and ultimately the safety of humans.

In a fire, the smoke is initially hotter than the surrounding air so buoyancy forces the smoke to rise [3]. As shown in Figure 2.1, the smoke plume is typically conical in shape because it gets wider as more air is entrained while it rises [3]. In this case, external air flows such as wind or building ventilation are neglected but could add yet another complexity to smoke movement in fires [3]. The air that is entrained is cooler than the initial smoke, thereby

cooling the smoke and reducing the buoyancy force [4]. The buoyancy force is also reduced due to convection to the adjacent cooler air or conduction to adjacent solids [4]. Solids, liquids, and gases adjacent to the smoke plume also create drag that counteracts the upward buoyant force; either viscous drag (gases or liquids, *e.g.*, air) or friction (solids, *e.g.*, walls) [4]. Eventually the upward force reaches zero and the smoke stagnates (rising no higher) [3,4].

Modeling of fire and smoke dynamics becomes even more complex if the smoke's upward movement is obstructed by a ceiling or other object. If the fire is indoors and there is sufficient buoyant force, the smoke will collect at the ceiling. In this instance, the smoke plume, following the path of least resistance, is forced to travel outwards horizontally at the ceiling (called a ceiling jet) [3,4]. The friction between the smoke plume and ceiling, viscous drag with the air beneath, and heat loss to the ceiling and ambient air through conduction and convection will all continue slowing the smoke plume velocity until it stops unless it hits an obstacle (such as a wall). If the ceiling constrained smoke plume is surrounded by walls, as it would be in an enclosure like a house, the smoke cannot escape and begins to collect at the ceiling and/or flow down the walls. The collection of smoke at the ceiling is called the smoke layer (or sometimes hot gas layer).

To come full circle, the smoke layer in a fire compartment influences the fire. When flames extend into the smoke layer, the temperature of the smoke layer increases. Lower oxygen levels in the smoke layer limit combustion and increase the amount of unburnt fuel being added to the smoke layer, further increasing temperature and limiting available oxygen [3]. As the temperature increases, the large surface area of the smoke layer can lead to significant thermal radiation [3,4]. Smoke layer height is critical because radiation is driven by temperature (to the fourth power) and distance squared, which are both directly related to smoke layer height. The smoke layer radiation affects everything below it, including the fuel. As such, heat transfer to the fuel from a descending smoke layer may escalate the burning rate and fire size. As a fire continues to burn and the smoke layer builds, the fire may transition into a "fully-developed" fire [3,4]. A rapid transition from a localized fire plume to a fully developed fire is 'flashover' an event when every combustible material surface in the compartment (heated by radiation) reaches ignition temperature, igniting within seconds such that the room appears to become engulfed in flames almost instantaneously [3,4]. In a "fully-developed" fire (entire room on fire) temperatures exceed 900-1100 °C and humans can no longer survive [3].

The crucial interactions between fire, smoke and environment are complex and, consequently, difficult to model. One common fire model simplification is to divide a room (compartment) into two stacked zones (two-zone models): the smoke layer (upper layer) and the cooler, clear air below (lower layer). However, this simplification does not capture the mixing or "transition zone" between the smoke layer and the air below, caused by numerous

complex physical phenomena that include buoyancy, entrainment mixing, viscous drag, and convection [3,4]. The mixing zone can be very thin or quite thick (up to several feet thick [6]) depending on the fire, smoke, and compartment. In the case of a thin mixing zone (see Figure 2.2), it is relatively easy to distinguish the interface between the upper and lower layers. The interface is much more difficult to distinguish when the mixing zone is larger (see Figure 2.3), giving rise to numerous definitions for distinguishing the interface. Fire dynamics models used to determine how long people have to exit sometimes select a conservative definition such as the "lower edge of the transition zone" [7] and "first indication of smoke" [6]. Overly simplified definitions pose a problem in two-zone fire models because properties within each zone are assumed to be constant [8–13]. Incorrectly assigning the upper- and lower-layer interface further impacts the accuracy of two-zone models because the associated zone properties do not accurately represent the average zone properties in the fire compartment and the estimated size of each zone is incorrect. Thus, vague terms like the "bulk" of the smoke layer (closer to 80-90% of the transition [6]) are used to distinguish where the smoke layer is present.

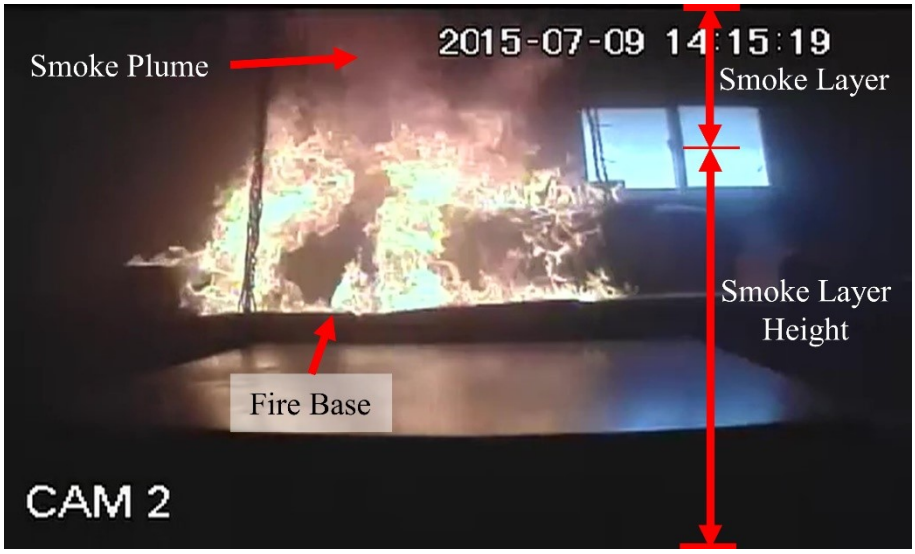

Figure 2.2: Photo with smoke layer parameters

Several terms are used to describe different parameters related to the smoke layer. The smoke-fill rate captures how quickly the smoke layer drops down from the ceiling in a confined space. For example, fires that produce equal volumes of smoke will tend to fill a small space at a faster smoke-fill rate than a larger space. The smoke layer depth refers to the physical depth of the smoke layer from the ceiling (shown in Figure 2.3) and is related to the smoke-fill rate. The smoke layer descent time is the time required for the smoke layer to reach a specific height. Finally, the smoke layer height represents the height of the smoke layer from the floor (shown in Figure 2.2 and Figure 2.3). Thus, in a room with a flat ceiling the smoke layer height is the ceiling height less the smoke layer depth. However, many

models calculate the smoke layer height with reference to the base of the fire rather than the floor of the fire compartment [6,8,10], so it is important to convert the results to the height above the floor if the fire base is at a different elevation (*e.g.*, a fire that starts on a sofa as in Figure 2.2). The smoke layer height is often the desired value when studying fire and smoke dynamics because it indicates the height where a human attempting to escape would encounter smoke. In assessing smoke layer height, it is important to distinguish between the smoke layer height and the height of the neutral plane in a fire compartment. The neutral plane is the plane at which the pressure difference across an opening (*e.g.*, doorway) in a fire compartment is zero and it marks the interface between the flow of smoke exiting and flow of cold air entering the fire compartment. Thus, while it is sometimes considered that the height of this plane is coincident with the height of the visible edge of the smoke layer, in reality due to mixing across the smoke-air interface, the heights are often different [11,12,14,15].

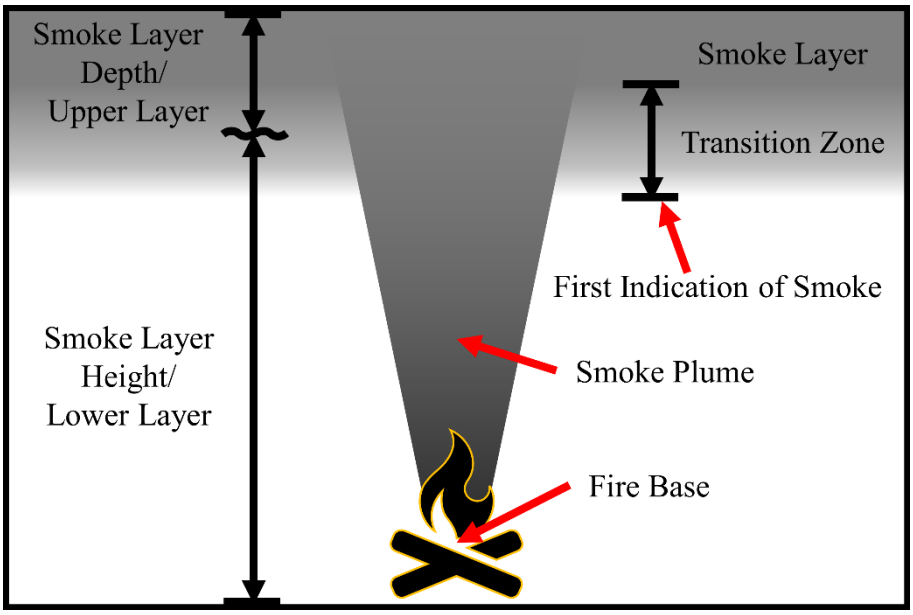

Figure 2.3: Diagram of smoke layer parameters

The smoke layer has many properties relevant to fire models including thermal properties, gas concentrations, unburnt fuel (pyrolyzate [4]) concentration, and varying levels of particulate matter and aerosols. Though cooler than the combusting fuel vapours that can easily exceed 1200 °C [4], a smoke layer can still reach temperatures over 600 °C. This is why it is often referred to as the hot gas layer. In many engineering scenarios, properties (*e.g.*, density) are assumed to be constant as temperature changes to simplify calculations. However, given the large temperature ranges in fire and smoke analysis, changes in properties with temperature must be carefully considered. Gas concentrations (dependent on density) are relevant to determining how long occupants have to escape before the toxic

gases cause incapacitation (and possible death). High enough concentrations of unburnt fuel in the smoke layer can result in ignition and flames in that layer if there is also sufficient heat and oxygen present (the three components of fire). Unburnt solid fuel, particulate matter, and aerosols form the visible component of the smoke layer. The perceived "thickness" of the visible component is often called smoke "density," although definitions vary depending on how the component is measured and the application [3,16].

If the smoke layer depth in the fire compartment descends to the top of an opening, such as an open doorway or stairwell, then the smoke will follow the path of least resistance and flow into the adjacent space and subsequently build a smoke layer in that space [17]. If the fire continues to burn and generate smoke, then this sequence may repeat as room after room has smoke collect at the ceiling until the smoke layer depth is sufficient to enter the next adjacent space. In this way, a fire that produces a lot of smoke can fill every room in a house with smoke. The farther the smoke travels from the fire compartment, the more it mixes with cooler air. The entrained air causes the smoke to be visibly less "thick" and reduces the concentration of toxic gases. However, the effects on the smoke layer height depend on how much the added air causes the smoke layer volume to increase compared to the volume decrease caused by the temperature, and therefore density, decrease. If there is no working fire alarm (as is reported to occur in 31% of Canadian [18] and 33% of US [19] residential fires), it is possible for occupants to be incapacitated (rendered unconscious) or even killed by the toxic gases without being aware of the fire. If occupants are aware of the fire, the impact of the spreading smoke on visibility and toxic gas concentrations may make exiting more difficult or even impossible.

Fire dynamics are complex. Even apparently simpler examples like a campfire can quickly become so complex that detailed modelling of the fuel, oxidizer, heat, smoke and environment interactions are challenging. This is even more true for scenarios such as a living room furniture fire in a house, which forms the subject of this thesis. Global parameters like smoke layer spread and height must be measured and understood before it is possible to focus on local parameters such as smoke and toxic gas distributions within the smoke layer. Therefore, this work focuses on measurements of the global parameters of smoke layer presence and bulk smoke density. The first step of this process is to understand existing estimation methods for both parameters. Smoke layer height estimation methods can be broadly grouped into visual, sensor-based, and analytical methods, which are addressed next in turn (Sections 2.2, 2.3 and 2.4, respectively) followed by smoke density estimation methods (Section 2.5). Existing methods capable of estimating both smoke layer height and smoke density at the same time are discussed in Section 2.6. The chapter concludes with the origins of the proposed novel smoke layer height and density measurement method are detailed in Section 2.7.

2.2 Visual Smoke Layer Estimation Methods

The existing smoke layer height estimates can be broadly classified as visual, sensor-based, and analytical methods. The visual methods are discussed in this section followed by the sensor-based and analytical methods in Sections 2.3 and 2.4, respectively.

As established, smoke layer height is specific to a particular fire scenario. Consequently, while scaled models (*i.e.*, intermediate-scale experiments) have been used in the past [14,20,21], the smoke layer height is almost always estimated at full-scale. Continuously measuring the smoke layer height from floor to ceiling in a compartment is not economically or physically feasible in intermediate- or full-scale fire experiments. However, video cameras that record a broad view of a space record at numerous frames per second can be used by observers to estimate the smoke layer height. Similarly, thermocouples, sensors which record temperatures for a single point, can be installed in a thermocouple "rake" with several stacked thermocouples at different heights. The thermocouple data, collected at regular, small time intervals, can be interpreted to discern the descent of the hot gas-cold air interface, thereby estimating smoke layer height (see sensor-based smoke layer estimation methods in Section 2.3). Accordingly, although other experimental data have also been used, the relatively low cost and small size of thermocouples and video cameras compared to some alternatives have led to an abundance of smoke layer height estimation methods that rely on these inputs. In this work, visual methods are divided into two classifications: i) observer-based and ii) image analysis-based smoke layer height estimation methods, and they are addressed in Sections 2.2.1 and 2.2.2, respectively.

2.2.1 Observer-based Smoke Layer Height Estimation

Observer-based methods are by far the most common approach to estimating smoke layer height in fire experiments. Observers typically determine smoke layer height on a macro-scale by interpreting smoke patterns as the experiment progresses and the smoke layer descends. The smoke pattern interpretation by the observers makes this method quite subjective (*i.e.*, biased). While the specifics of the observer-based methods are rarely the same between experimental series, smoke layer height estimation is almost always conducted using known height markers. In a few cases, objects of known height are used to estimate the location of the smoke layer [14,22–25]. However, using explicit and evenly spaced height markers is more common, including lines marking heights [21,26–28], scales [20,29,30], and indicator lights positioned at regular intervals [9,20,31]. There is some controversy [22] but, in almost all cases [13,21,27,31,32], observer-based smoke layer height is assumed to be the same as the actual smoke layer height.

In early smoke studies, observers directly recorded values of smoke layer height during an experiment [26,29]. In a set of experiments in 1970, 20 observers were outfit in breathing apparatus and supplied with a flashlight, clipboard and stopwatch [26]. They stood at various locations throughout a space and observed when the smoke front reached their locations, the

subsequent smoke layer depth, and whether the smoke appeared “dense” or “thin” [26]. The disadvantages of this method, including safety concerns and observer consistency, were noted in the report [26]. As the hot smoke mixed with clear air below, it became more difficult for observers to distinguish the smoke layer. Observations were more consistent for dense smoke rather than thin smoke [26]. With the safety concerns [26] and the present availability of video cameras that allow post-experiment analysis, this practice is now rare.

Video recordings are a series of images (frames) captured numerous times per second that are stored as data in such a way that they can be played back at the same, faster, or slower speed as desired. Thus, video recordings have become the standard method for visually estimating smoke layer height in full-scale fire experiments. In addition to circumventing the safety concerns associated with direct human observation, other benefits of video recordings include

- removal of time pressure because video can be paused or re-played
- consistent view and ability to focus on various areas of interest in camera view
- time-synchronization with other experimental data if video recordings include time stamps
- recording at speeds faster than a human can differentiate in real-time allowing frame-by-frame review if desired
- comparison between videos and experiments to ensure consistency because the videos can be reviewed by the same observer and without the typical time delay between experiments
- post-experiment analysis reduces human resource demand during an experiment

These video recording benefits are more generally applicable to all smoke layer height estimation methods that use video recordings, including image analysis-based estimation (the second classification of visual method) that is discussed next.

2.2.2 Image Analysis-based Smoke Layer Height Estimation

As computer power and digital recording tools have increased, video traces of smoke could be analyzed in more detail and more rapidly. Video recordings are separated into their basic images and the image data from specific areas relevant to smoke patterns can be analyzed. Image analysis has taken observer-based smoke layer estimation one step further by automating part(s) of the analysis and potentially reducing subjectivity by the observers. Image analysis is typically used to look at a small area or areas within the image (observer or program selected) and extracts recorded value(s) within those locations which are then interpreted.

Videos are made up of a series of images that are, in turn, made up of pixels (storing data values). Each pixel stores values that indicate the conditions at the time each image is captured. For example, a 640-pixel by 480-pixel (*i.e.*, length by length) resolution video

camera records 307,200 pixels (*i.e.*, area) of data in each image. Generally speaking, newer video cameras record more pixels in each image and at a higher rate of image capture than older models. These increases allow resolution of smaller and smaller areas within each image and measurement at faster and faster rates that can result in higher precision smoke development results. However, even with automated image analysis, the extracted pixel values must still be interpreted which leads to subjectivity because, whether directly or indirectly through programming, a researcher is still responsible for interpreting the extracted values. When the method has been applied in enough varied scenarios, it is possible that the programming could be modified to interpret the extracted values with minimal subjectivity. Two image analysis methods have been developed but both require further application to achieve minimal subjectivity.

The first image analysis method was developed for the purposes of having data that could be used to validate the results of a computational fluid dynamics (CFD) model [28]. Five experiments with four different fuel sources, two liquid (heptane and toluene) and two solid (wood crib [x2] and PMMA crib), were conducted in a 500 m^3 compartment that included a single 2 m by 2 m vent. Two CCD-cameras, one inside and one outside the compartment, and two thermocouple rakes (nine thermocouples each) were used to estimate the smoke layer height. Based on the experimental results from the image analysis method, images were selected approximately every 30 seconds for analysis. This method analyzed a series of n vertical one-pixel-wide columns, i, to determine the maximum (grey scale) pixel intensity of each column, I_i, and the average maximum intensity across all columns analyzed in the image. The smoke layer height, Z_{im}, was estimated to be located at a fraction, f, or percentage of that average highest value when scaled by a physical size indicator, s, as shown in Equation 2.1.

$$Z_{im} = f \cdot \frac{\sum_i^n [max(I_i)]}{n} \cdot s \qquad 2.1$$

This method only worked for the two liquid fuels. For the other two (solid) fuels, the smoke was too white for the image analysis method to separate smoke from the white background. Thus, the smoke layer height was estimated by observers (see Section 2.2.1). For the two fuels for which the image analysis method could interpret the smoke layer characteristics, the fraction, f, used in the smoke layer height calculation changed (no reason was given) based on the fuel: one was f=0.55 (toluene) and the other (heptane) was not provided [28]. Further, the authors state that "the image analysis could not be used after 3 minutes for toluene and after 6 minutes for heptane and the following values [were] based on visual observation." (no reason was given) [28]. As a potential indicator of the accuracy of this image analysis method, the smoke layer height results show that the image analysis method results appear to vaguely follow the unstable results obtained from thermocouple measurements using a variation on one (or more) of He's methods (see Section 2.3.4).

Second, Verstockt and a team from Ghent University [33–35] developed a video-based fire forecasting model that included estimation of smoke layer height. Their system was developed using several different experimental layouts with various room configurations and a variety of furniture fuel sources (including sofas) and layouts [33–35]. The image analysis video recordings were captured with Lynksys/Cisco WVC2300 cameras recording in 640 x 480 pixel resolution at 30 frames per second (fps) [35,36].

One of their later works [34] clearly and concisely details the algorithm and process. However, a high-level summary of the process used to estimate smoke layer height by the Ghent team is included here. Their image analysis process first takes images from a video recording and decomposes the images using a discrete wavelet transform. This decomposition allows determination of pixel 'energy' by measuring pixel distinction relative to the surroundings. The algorithm selects 'high-energy' vertical lines from early images without smoke and then measures the energy within the lines by vertical location as the video (*i.e.*, time) progresses. The presence of smoke makes the pixels less distinct relative to the surroundings and, consequently, degrades the pixel energy. The smoke layer height in each image is determined to be when the energy versus height profile(s) is greater than or equal to a specific slope. In these early works, a slope value of 20% of the maximum energy was selected subjectively as a starting point.

As verification for this smoke layer height estimation algorithm, a small number of subjective visual evaluations were also made. The algorithm appeared to correctly identify the smoke layer height [33,34] and "thermocouple-based smoke layer height detection" from the door openings indicated similar smoke layer height patterns [35] as well. The latter verification method is quite unclear because a) there are many possible ways to use thermocouples to estimate smoke layer height (discussed in detail in the next section) and b) thermocouples in a doorway would indicate the smoke layer height of the doorway but not necessarily of the compartment [11,12,14,15]. In a later work, compartment smoke layer height estimates from the algorithm were compared with doorway smoke interface heights calculated using thermocouples and the least-squares method (see Section 2.3.4) with mixed results [36].

As mentioned and inferred in the image analysis verification detailed in this section, thermocouple data are often used to estimate the smoke layer height. There are numerous such sensor-based smoke layer estimation methods and several more common methods are detailed in the next section.

2.3 Sensor-based Smoke Layer Estimation Methods

Given the subjective nature of methods for estimating smoke layer height by observers, it is not surprising that numerous alternative methods have been devised over the years. With image and video processing only becoming economically feasible in approximately the last decade, most alternative methods used other sensors (temperature, concentration,

transmission, *etc.*) to indirectly infer smoke layer height. In all cases, the measured data were used to locate the interface such that a bi-value function, such as the one shown in Figure 2.4, can be determined. Smoke properties are then averaged above and below the assigned smoke layer height

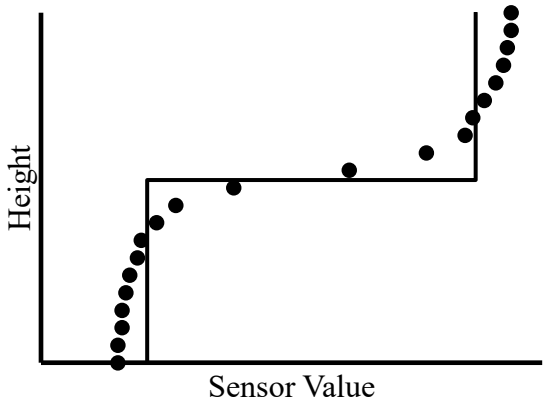

Figure 2.4: Bi-value function (line) from hypothetical fine-mesh sensor data (points)

Sensor-based smoke layer height estimation methods using variations of this method include:

- First change method [29]
- Specific value method [22]
- N-percent rule [9,37]
- Integral ratio method [13]
- Least-squares method [13]
- Deviation from average sensor value [15]
- Sensor value profile discontinuities [38]
- Sensor value profile inflection points [11]

These sensor-based methods are typically based on temperature data [9,11,13,15,20,22,29,37–39] but occasionally transmission [9,29,40] or gas concentration [27,40] data are used. Of the sensor-based methods listed, the first five are most common and are discussed in more detail in the coming sections.

2.3.1 First Change Method

The first change method was common historically but no literature using this method was found beyond 1991 [6,29,40]. This method does not have an official name; in text it has been referred to as “the time that each sensor started to respond” [29], “first temperature rise” [6], “first indication of rise in [sensor value]” [40] and “first indication of smoke by [sensor type]” [40]. Collectively, the smoke layer height determined using the first change method is chosen to be at the sensor height when a sensor first changes value. By definition, this

method represents the first indication of smoke. As with most sensor-based smoke layer height estimation methods, thermocouples (measuring temperatures) are used most often [6,29,40]. Transmission sensors [29,40] and gas concentrations [40] are also occasionally used.

2.3.2 Specific Value Method

The specific value method is similarly straightforward and is the method used in the well-known, heavily-instrumented 2006 Dalmarnock fire tests [22,41,42] wherein experimental results were compared to *a priori* (*i.e.*, without knowing the results of the experiment) and *a posteriori* (*i.e.*, using experimental results) results from computer models of the tests [39,43]. "The Dalmarnock Fire Tests provided measurements at sufficient spatial resolution to be compared with field models, not on an averaged level, but on a scale comparable to the grid size" [43]. For example, over 450 thermocouples were used in each experiment [41]. Within this work, the specific temperature value used to indicate smoke layer height is taken to be different values by different researchers: 100 °C [22,42], 150 °C [43] or expected to fall in the range of 90 °C to 250 °C [43].

2.3.3 N-percent Rule

The N-percent rule, developed by Cooper *et al.* in 1982 [9], is the most commonly used sensor-based smoke layer height estimation method. This is the recommended method for determining smoke layer height from experimental data in the National Fire Protection Association's NFPA 92 standard [6,37]. The method requires stacked sensor values of a parameter, most commonly temperature, such that a vertical data profile can be measured. For example, if temperature is used, a vertical thermal profile from at least two temperature sensors (thermocouples) is required; though more sensors are better for spatial resolution. The N-percent rule effectively calculates the range of measured sensor values and the smoke layer height is deemed to be present at N-percent (N/100) of that range [9]. Thus, the N term must have a value in the range of 0 to 100. This is similar to the method used by Mulholland *et al.* in 1981 [44]. The smoke layer marker for a measurement parameter, p, that varies as a function of time and height from the floor is originally calculated using Equation 2.2 [9].

$$p(z,t) = \frac{N}{100}\left\{\max\left[p\left(z_{top},t\right)\right] - p\left(z_{top},t=0\right)\right\} + p(z,t=0) \qquad 2.2$$

There are now some variations including the NFPA 92 [6] version that combines N/100 into an interpolation constant, C_n, that acts as a more traditional percent value (*i.e.*, if N=20 then C_n = 0.2). The parameter value measured by the sensor, $p(z,t)$, is a function of both sensor height, z, and time, t. Thus, the highest sensor is located at z_{top} and the smoke layer height, $Z_{N\%}$, is the lowest sensor height that matches or exceeds the valve obtained using Equation 2.2. If the sensors are measuring temperature (T), as in Figure 2.5, then the smoke layer height can only be determined if $T(z,t) - T(z,t=0) > 0.5$ [K/°C] [9].

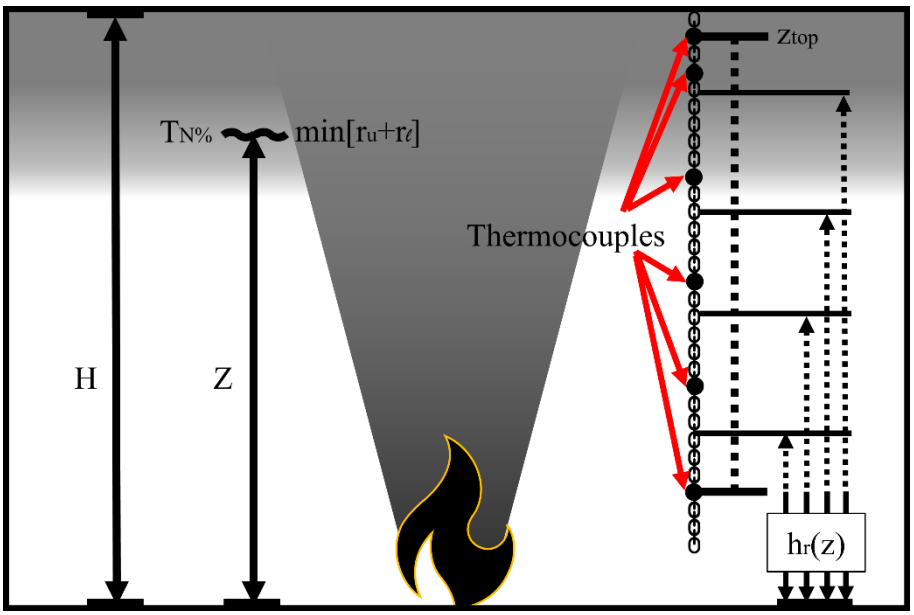

Figure 2.5: Smoke layer height estimation diagram for the N-percent rule and integral ratio method

As shown in Table 2.1, many different N-percent values are used in the literature to estimate the smoke layer height from measured data in a wide variety of fire experiments [6,9,46,47,13,20,21,27,31,32,44,45]. The selected *N* value can have very little or a significant impact on the estimated smoke layer height if the transition zone is small or large, respectively [13]. Cooper *et al.*'s [9] original work used *N* = 10-20 because N-percent results from thermocouple and photometer sensor values largely agreed with visual results in 19 methane burner fires with an artificial white smoke source [9]. The NFPA 92 standard defines this *N*=10-20 range as the "first indication of smoke" and a range from *N*=80-90 as the "smoke layer interface" [6]. Most use these high or low values but some use in between values to estimate the smoke layer height as shown in Table 2.1. It has been said that "when using the N-percentage rule to process experimentally measured temperature data, one is often baffled with the selection of the *N* value." [13]. For example, the use of *N*=60 in one work [46] is based on a reference chain that only leads to values of *N*=50 or less. The article states: "For determining the interface height using predictions of CFD models, a value of C_n between 0.5 and 0.6 is recommended." [46]. The reference for that statement [48] does not mention the N-percent rule or any specific smoke layer height estimation method though it indirectly refers to two articles: [47] and [13]. In the first work, *N*=50 is selected to represent the smoke layer height without any reference [47]. Whereas the second reference [13] develops the method detailed in the next section and has *N*=10, 15, 20 and 50 in one plot to demonstrate the sensitivity and subjectivity of selection of differing values of *N* to use in the N-percent method.

Table 2.1: N-percent values in the literature

N	References
10	[6,9,13,20,21]
15	[6,9,13,20]
20	[6,9,13,20,21,27,44,45]
30	[21,32]
50	[13,47]
60	[46]
80	[6,45]
85	[6,31]
90	[6]

2.3.4 Integral Ratio and Least-Squares Methods

In 1998, He *et al.* [13] published an article with two mathematically derived interface height estimation methods: the integral ratio and least-squares methods. Both methods were designed as parameter averaging schemes that intended to eliminate the subjectivity in the processing of parameter data. Experimental data were collected from a nine-thermocouple rake installed in the hallway outside a burn room, between the burn room doorway (open) and a stairwell, where two flashover sofa fires with different building ventilation conditions were started. The measured temperature data were used to estimate the smoke layer height using the integral ratio, least-squares and N-percent (with *N*=15,20) methods. All four estimated smoke layer height traces had different values though the patterns were generally similar. However, the authors note that, without verification by visual observation (see Section 2.2) or use of the method(s) with smoke density (rather than temperature) as the parameter (see Section 2.5.2), it cannot be confirmed whether the proposed methods can satisfactorily identify smoke layer height [13]. None of the literature used the method with either visual or smoke density as the examined parameter so the inference of smoke layer height via these techniques is still unproven. Within the subsequent literature, the integral ratio method was used more frequently [20,21,49] than the least-squares method [36]. This may be a result of the authors' conclusion that the least-squares method was "more sensitive to spatial fluctuations of the temperature profile" when the method was applied to experimental data with temperature as the parameter examined [13]. Accordingly, the integral ratio method is examined in further detail in this thesis.

The integral ratio method gets its name from the ratio of direct and reciprocal averages, represented by integrals. The method derivation begins by showing that, in the vertical direction (*i.e.*, z direction) the ratio, r, of the direct average of a parameter, $p_{av1} = \{b-a\}^{-1}\int_a^b p(z)dz$, and reciprocal average, $p_{av2} = \{b-a\}/\int_a^b p(z)^{-1}dz$, is $r = p_{av1}/p_{av2} \geq 1$ but achieves a value of 1 when the parameter, p, is uniform over the region a

to b. If a compartment is divided into an upper (u) and lower (ℓ) layer, two ratios are needed: $r_u = p_{av1,u}/p_{av2,u}$ and $r_l = p_{av1,l}/p_{av2,l}$, respectively. In both cases (r_u and r_ℓ), lower ratio value means higher uniformity. Thus, the ideal interface height is located where the collective upper- and lower-layer uniformity is maximized (*i.e.*, $\min(r_u + r_\ell)$). Then, if the ceiling height is H and each possible smoke layer height is h_r, a series of ratios for a given parameter can be calculated by solving Equation 2.3

$$r_u + r_l = \frac{1}{(H-h_r)^2}\int_{h_r}^{H} p(z)dz \int_{h_r}^{H} \frac{1}{p(z)}dz + \frac{1}{{h_r}^2}\int_{0}^{h_r} p(z)dz \int_{0}^{h_r} \frac{1}{p(z)}dz \qquad 2.3$$

at any point in time as long as the value of that parameter is positive or negative for locations throughout the entire region (*i.e.*, Kelvin is used for temperature). The interface height, Z_{int}, is then the value of h_r that results in the lowest value of $r_u + r_\ell$ at a particular point in time. In Figure 2.5 the parameter of interest is temperature as measured by thermocouples.

Two existing types of visual and four types of sensor-based smoke layer height estimation methods have now been examined. The final type of smoke layer estimation method considered in this work is analytical methods based on correlation of experimental data and is discussed in the next section. Smoke density estimation methods, and methods that can estimate both smoke layer height and density are discussed in Sections 2.5 and 2.6, respectively. Finally, the origins of the proposed smoke layer height and density estimation method are detailed in Section 2.7.

2.4 Existing Smoke Layer Height Analytical Methods

Given the importance of smoke layer height in designing for evacuation in a fire scenario, it is not surprising that simple hand-calculations have been developed for estimating the smoke layer height in a fire compartment. Three dominant hand-calculations have emerged calculating smoke layer heights during fires in spaces without mechanical smoke ventilation systems [4,6,7,17]. The Zukoski [8], Tanaka & Yamana [10], and the National Fire Protection Association's (NFPA's) standard NFPA 92 [6] analytical methods (from 1978, 1985 and 1990, respectively) is detailed in this section.

Zukoski [8] created a "simple analytical model… to determine the time required for a room to fill with products of combustion from a small fire." This model was theoretically derived from mass and energy conservation equations for a closed fire compartment with small exterior leaks. The original calculation involved numerically solving a differential equation or, now more simply, using the chart provided with the appropriate inputs and outputs for a specific situation to determine the necessary values to proceed with the smoke layer height calculation [8,17]. The derivation process in the work required many assumptions, so the results were at best order of magnitude estimates [8,17]. This was Zukoski's intent because the calculation was used to estimate the relative importance of fire size, room geometry, leak location, fire elevation and fire geometry in a smoke filling scenario [8]. However, the fire

was modeled assuming that it had a constant energy release rate with time. This assumption limits the applicability of the method because few real-world fires can be reasonably approximated as having a constant energy (heat) release rate with time over anything but a very short time period. This may be the reason for the more prevalent use of the theoretically derived Tanaka & Yamana [10] analytical method that can be applied for fires with t^n heat release rate (HRR) curves where $n \geq 0$, which include the common t^2 heat release rate design fire growth curves.

Tanaka & Yamana [10] theoretically derived smoke layer height estimates for several scenarios, including non-steady fires with no mechanical venting [4,10,17,50]. In a separate paper, they conducted two 1.3 MW methanol pan fire tests in a 26.3 m tall space where thermocouple and photometer data were captured [29]. The smoke layer height was estimated using the derived calculation [10] that showed better agreement when compared with first change method (see Section 2.3.1) results from the thermocouple and photometer data, and observer-based results (see Section 2.2.1) [29]. The calculation first makes the common assumption of a two-zone fire model with constant smoke density (ρ_s) in the upper layer as shown in Figure 2.6. The smoke layer height, $Z_{T\&Y}$, is

$$Z_{T\&Y} = \left(k \cdot \frac{\alpha^{1/3}}{A_s} \cdot \frac{2}{n+3} t^{\left\{1+\frac{n}{3}\right\}} + \frac{1}{H^{2/3}} \right)^{-3/2} \qquad 2.4$$

where A_s is the constant cross-sectional area of the fire compartment, H is the height of the compartment, and heat release rate is modeled as the form αt^n. The constant, k, can be assumed to be approximately 0.0764 for ambient standard temperature and pressure in the lower layer in the compartment based on a long derivation and iteration process [17].

In 1991, the NFPA published NFPA 92B 'Guide for smoke management systems in malls, atria and large areas' [6] which also incorporates estimation methods for smoke layer height. NFPA 92B and its counterpart NFPA 92A, 'Recommended practice for smoke-control systems', had many of the same requirements and were eventually consolidated into NFPA 92 'Standard for smoke control systems' in 2011 [6]. In these are two empirically derived smoke layer height equations; one for steady fires and another for unsteady t^2 fires [6,37,40]. Both equations are also included as the standard empirical smoke layer height analytical calculations in the Society of Fire Protection Engineers (SFPE) Handbook [7]. The steady-state fire smoke layer height equation was derived based on correlation of experimental results from four gas and liquid fuel test series conducted prior to 1987 [40]. In total, the steady-state fire smoke layer height correlation appears to have been created using 17 smoke layer height data points that were estimated using the first change method (Section 2.3.1) or N-percent method (Section 2.3.3) [6,9,40,51]. The smoke layer height equation for unsteady t^2 fire growth was derived from one propylene burner test in a 6 m tall compartment with what appears to be nine smoke layer height data points estimated using the first change

method (Section 2.3.1) [40,51]. Neither equation has changed since they were initially introduced for committee approval in 1990 [52] but additional data sources (latest collected in 1991) were added to associated plots in the standards (regardless of data fit) [6,7,40].

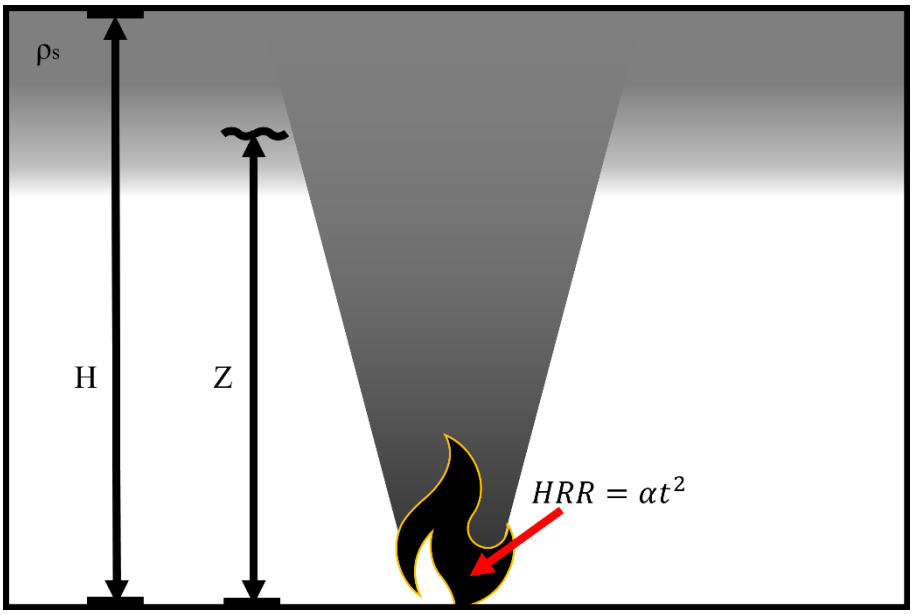

Figure 2.6: Smoke layer height calculation diagram

Given the small data sets from markedly different fire scenarios, there is some uncertainty about the validity of applying the smoke layer height analytical methods for t^2 fires to a living room sofa fire. However, they are most likely significantly better than the smoke layer height analytical calculations for steady fires due to the comparatively rapid growth of the fire scenario in question.

Thus, existing visual, sensor-based and analytical methods have been investigated for smoke layer height estimation. Some of these methods are used to characterize the smoke layer height in living room sofa fires as a baseline comparison for the radiance method developed in this thesis. The selected methods are detailed in Section 3.2 with the results presented in Section 4.1. Since the radiance method includes estimations of smoke density as well as smoke layer height, a similar understanding of existing methods for estimating smoke density is required. Accordingly, existing smoke density estimation methods are investigated next.

2.5 Existing Smoke Density Estimation Methods

The focus of this work is to undertake visual analysis to extract data from recordings of fire events. Although individual particulates are not visible, ‘smoke’ can be seen, and thus measured, at macro-scale. Accordingly, it is feasible to derive optical intensity estimations of smoke density.

Since fire and the smoke it creates are directly related to the fuel, oxygen, heat and fire environment (*i.e.*, outdoors, compartment, wind, adjacent flammable materials), smoke would ideally be measured in the same or similar environment as the scenario to be modelled. This is not practicable, hence many small- and intermediate-scale tests have been used to estimate quantity or characteristics of smoke from materials and assemblies. However, these test results may or may not be truly representative of specific fire scenarios. Thus, to select representative smoke values, it is crucial to understand how smoke measurements are or have been obtained. Rasbash and Phillips [53], Flisi [54], and Whiteley [16] summarized various measures that have been used to describe 'smoke'. In context of measured parameters, following is a list of some of the extant measures: smoke mass, smoke concentration, smoke density, smoke extinction area, smoke extinction area per unit mass, smoke extinction area per unit mass of volatile fuel burned (specific extinction area), smoke extinction area per unit surface area, transmission of incident light (or light attenuation), light attenuation per unit length, volume of smoke required to reach a specific value of light attenuation, visibility, opacity, optical density, optical density per unit length, standard optical density, specific optical density, mass optical density, obscuration, obscuration potential, smoke generating coefficient, smoke production factor, smoke production rating, rate of smoke production, smoke produced per unit mass, total smoke produced, and, in one instance, "level of smokiness" [16,53,54]. As Flisi stated, "each one of the various test methods gives different results, and for this reason the method should be mentioned whenever smoke density data are given or reported" [54].

Despite variable nomenclature and formulae, most of the above smoke measures are related to the transmission of light and the Beer-Lambert law[1] [16,53–55]. In most cases, the instrumentation emits light (often from a diode or a laser for monochromatic light), the light travels through the air/smoke mixture of interest wherein some of the light is lost in transmission, and a portion of the emitted light is measured by a receiver. A diagram of the general set-up for transmission measurement is shown in Figure 2.7. Application of the Beer-Lambert law requires an assumption of uniform particle distribution along the path of the light and monochromatic light [16,53–55] although white light is sometimes used for illumination as well [53,55]. The smoke measurement calculations then originate from two common equations that are based on the Beer-Lambert law: $\rho_{S1} = \ln(I_0/I) = C_1 l$ and $\rho_{S2} = \log_{10}(I_0/I) = C_2 l$, where ρ_s is smoke density, I_0 is incident light, I is transmitted light, ℓ is the distance that the light travels between source and detector, and C_1 and C_2 are constants comprised of differing values and coefficients that depend on the smoke measure in question [16,53,55].

[1] Also referred to as Beer's law, Lambert's law, Bouguer's law, and Lambert-Beer's law.

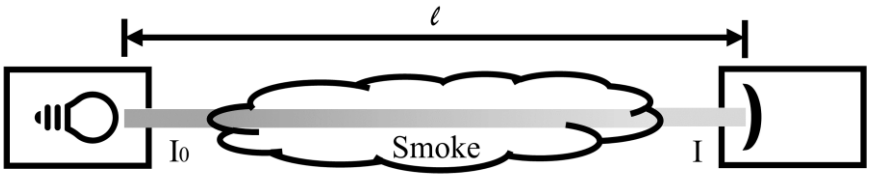

Figure 2.7: General set-up for transmission measurement

Over time, a few of the smoke measurement tests began to dominate as they were adopted into standard test systems with specific criteria that materials had to pass before use in a particular environment [54]. Now, the National Bureau of Standards (NBS) Smoke Density Chamber is accepted globally and is likely the most widely used test apparatus for measuring smoke density [3,54,55]. A main reason for this popularity is that it has one of the lowest levels of variation between tests although in reality with a variability of about ±25% (depending on material) it is still relatively high [3,56,57].

2.5.1 Smoke Density Chamber

The NBS Smoke Density Chamber (or smoke density chamber) is a small-scale smoke measurement test apparatus that has formed the basis for many test standards globally. Today's systems are similar but not identical to the NBS one. Two test standards dominate:

- ASTM International (originally American Society for Testing and Materials [58]) standard ASTM E662 "Standard Test Method for Specific Optical Density of Smoke Generated by Solid Materials" [57]
- International Organization for Standardization (ISO) standard ISO 5659-2 "Plastics — Smoke generation — Part 2: Determination of optical density by a single-chamber test" [56]

These two standards are the basis for all others that use a measure from the smoke density chamber. British Standards Institution standard BS 6401 is based on ASTM E662 [59]. National Fire Protection Association (NFPA) standard NFPA 258 has been withdrawn and simply refers to ASTM E662 for the material [60]. NFPA 270 replaces NFPA 258 and presents largely the same material as can be found in ISO 5659-2 [56,61].

The smoke density chamber is used to measure the specific optical density of smoke produced by a 75 mm by 75 mm sample up to 25 mm in thickness [62]. Representative samples are cut from materials (the fuel), conditioned to constant temperature (23 °C ± 2 °C) and relative humidity (50% ± 10%) for 24 hours, wrapped in a single layer of aluminum foil, and placed in the sample holder (that only exposes 65 mm by 65 mm of material) [56,57,62] as shown in Figure 2.8 for an ISO 5659-2 test. The sample material can oriented either horizontally (ISO 5659-2 [56] and related standards) or vertically (ASTM E662 [57] and related standards) during the test. In the horizontal orientation, a load cell measures the mass

of the sample on a continuous basis so mass loss can be calculated [56]. A photo of a smoke density chamber in the ISO 5659-2 configuration, the one used in this work, without the sample holder installed is provided in Figure 2.9.

Figure 2.8: Smoke density chamber ISO 5659-2 sample holder with a sample of material 3 (flexible polyurethane foam) for the third repetition in a particular heating mode

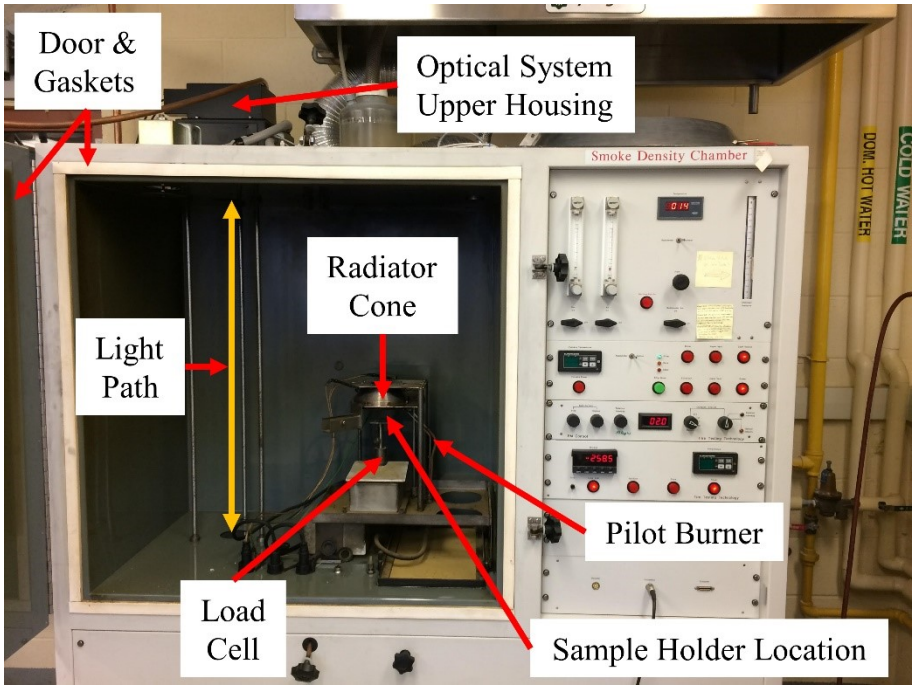

Figure 2.9: University of Waterloo smoke density chamber in ISO 5659-2 configuration with relevant components marked and without the sample holder installed (location indicated)

A radiant heat source positioned at a distance of 25 mm from the sample surface is used to heat the sample (see Figure 2.9). The heat source is set to either 25 kW/m^2 or 50 kW/m^2 (ISO 5659-2 [56] and related standards). With each radiant heat exposure, a pilot burner can be

used for flaming ignition or removed for non-flaming exposure conditions, respectively [56,57]. Thus, there are four heat exposure modes in ISO 5659-2 [56,57]. In all cases, testing of three repeat samples are required for each material and for each heat exposure mode under the standard test conditions [56,57].

Daily smoke density chamber pressure tests ensure an adequate seal for testing [56,57,62]. The chamber door remains sealed throughout the 10-minute test (see Figure 2.9). Therefore, all smoke produced is captured in the fixed volume of the chamber [56,57] and the available oxygen is also a fixed quantity that can lead to ventilation-limited burning of the sample [3]. The oxygen concentration is not measured in the standard test apparatus [56,57] (though expensive "add-ons" are capable [62]), adding uncertainty in terms of the test environment, and how it might change with time, during testing of a given sample. Light transmission is measured each second by a detector measuring the intensity of a light beam that shines between the top and bottom of the chamber (see Figure 2.9). The amount of smoke is calculated according to the change in transmission relative to the initial reference value [56,57]. Once the 10-minute test is complete, the smoke is evacuated from the chamber and a "clear beam" transmission is measured to estimate and can be used to correct for how much of the reduced light transmission was due to soot deposit on the optical windows (at the top and bottom of the chamber) during the experiment.

The smoke density chamber measures the specific optical density (D_S) from percent light transmittance (T = 100 x I/I_0 [3]) by calculating $D_S = (V/\{A \cdot l\}) \log_{10}(100/T) = 132 \log_{10}(100/T)$. Volume ($V$ = 0.51 m^3), exposed sample area (A = 0.0042 m^2) and light path length (ℓ = 0.915 m) for the test unit is reduced to a constant value of 132 [56,63]. The maximum smoke density ($D_{S,max}$ [56] or D_m [3,57]) is the maximum value that is recorded during the test and is the value usually listed in the literature. In horizontal orientation, the mass optical density (MOD) can also be calculated using $MOD = (D_S/L) \times (V/\Delta m)$ with the added mass loss ($\Delta m = m - m_0$) term [56].

Sample material and orientation have a significant impact on the repeatability (within lab) and reproducibility (between labs) of results obtained from the smoke density chamber [54,56,64]. Changing material shape and changing surface location relative to the radiant heat source (*e.g.*, a material that melts) can increase uncertainty in test results [64]. For example, flexible polyurethane foam (a large component of the fuel in the full-scale experiments discussed in this work) is known to melt when heated. The horizontal configuration is preferred to maximize the amount of sample material tested since less is likely to drip out of the holder (which is one of the reasons for wrapping the sample in aluminum foil). However, the horizontal configuration does not eliminate the changing radiant heat levels caused by increasing distance from the heater as the material melts (shrinking towards the bottom of the sample holder). This helps explain the more variable results for flexible polyurethane foam noted during interlaboratory round-robin testing (*e.g.*,

non-flaming, 50 kW/m^2 – ±36% repeatability, ±63% reproducibility) [56] in comparison to the typical variability ±25% [3].

Table 2.2: Published smoke density values for flexible polyurethane foam with the standard used (Std.), volume (Vol.) of the equipment, sample orientation (Orient.) and heat flux applied

Std.	Sample Orient.	Heat Flux [kW/m^2]	Material	Max. Smoke Density (D_m)	Ref.
Flaming					
ISO 5659-2	Horiz.	25	Flexible Polyurethane Foam (27 kg/m^3, 25.0 mm thick)	Mean 80	[56]
ASTM E662	Vert.	25	Flexible polyurethane foam (high resiliency, 12.7 mm)	Mean 80.1 (41.1-167.9)	[57, 65]
N/A*	Horiz. or Vert.	25 or 40	Flexible Polyurethane Foam (20 kg/m^3, 12.7 mm thick)	Mean 32.8 (26.5-39.3)	[53]
Non-Flaming					
ISO 5659-2	Horiz.	25	Flexible Polyurethane Foam (27 kg/m^3, 25.0 mm thick)	Mean 178	[56]
ISO 5659-2	Horiz.	50	Flexible Polyurethane Foam (27 kg/m^3, 25.0 mm thick)	Mean 127	[56]
ASTM E662	Vert.	25	Flexible polyurethane foam (high resiliency, 12.7 mm)	Mean 99 (75-126)	[57, 65]
ASTM E662	Vert.	25	Polyurethane flexible foam (non-fire retarded)	Mean 188 (187-188)	[63]
N/A	Horiz.	25	Polyurethane flexible foam (non-fire retarded)	Mean 193 (182-284)	[63]
N/A	“Dual” Vert.	25	Polyurethane flexible foam (non-fire retarded)	Mean 169 (155-183)	[63]
N/A*	Horiz. or Vert.	25 or 40	Flexible Polyurethane Foam (20 kg/m^3, 12.7 mm thick)	Mean 177 (160-193)	[53]

*Smoke potential was measured and converted to specific optical density.

Additional uncertainty exists if the material does not ignite at 25 kW/m^2 [56]. Smoke production from all materials should be interpreted only as a relative ranking because of the known comparatively high variability of this test method (relative to many in other science and engineering fields). Accordingly, measured numerical values of smoke density should not be used directly as model input. Even when comparing smoke production rankings, a round-robin study found that smoke density values for materials with less than 12% difference between the average values could be ranked differently at different labs [64]. A

series of published smoke density results for flexible polyurethane foam are summarized in Table 2.2. Available information on the testing standard (Std.), sample orientation (Sample Orient.), radiative heat flux [kW/m^2], sample material description, maximum smoke density (Max. Smoke Density (D_m)) value, and associated reference(s) (Ref.) are included in the table from left to right. In addition to the mean value, where available, the range of maximum smoke density values obtained during testing is included in brackets. These values are used as a basis for comparison when smoke density chamber test results are presented later in this thesis work.

In present day, there is a renewed interest in smoke production measurements, particularly if coupled with Fourier Transform Infrared Spectroscopy (FTIR) gas concentration measurements, because smoke visibility (and toxicity) information is needed for fire models. Even better are results from full-scale experiments discussed in the next section.

2.5.2 Full-Scale

The demand for visibility data for model validation has resulted in the development of various measurement methods that can be applied in full-scale experiments. Small-scale results have the advantage of lower cost and potentially better repeatability due to the control of important parameters. However, well-designed, well-documented and repeatable full-scale data well aligned to specific fire scenarios may be better suited to modelling than small-scale data. The suitability is directly related to the intricate relationships among fuel, oxygen, and heat in a fire scenario and consequent impact on the global parameters of smoke production and layering, and visible density of the smoke.

Most existing full-scale smoke measurement methods use the Beer-Lambert law and light transmission to measure the visible components of smoke. Similar to smoke layer height estimations, full-scale methods for measuring smoke visibility can broadly be grouped into two categories: visual and sensor based. However, unlike estimations of smoke layer height that can be made using data obtained from numerous sensor types, sensor-based visibility measurements in full-scale fires have been limited to transmission sensors.

Transmission sensors have several configurations and are referenced in the literature by a variety of names: photocell [26,29], photometer transmitter-receiver pairs [9], smoke turbidimeter [51], laser smoke obscuration sensor [41], and MIREX system (measures extinction coefficient) [28,66]. Typically only one or two transmission sensors are used in fire experiments, if they are used at all, and no more than 12 have been reported [9,26,28,29,41,51,66]. Transmission sensors are used sparsely in fire experiments because they typically either need

a) to be purchased from a company that designed the system and sensors to withstand the extreme environments in fire experiments and are, consequently, expensive[2] and bulky, possibly influencing the smoke dynamics being measured [66], and thus require time and patience to set up, align, and trouble-shoot

or

b) time, knowledge and skills to design, build and calibrate a system and time and patience to set up, align, and trouble-shoot the system and sensor(s).

A certain amount of redundancy is often incorporated into fire experiment design because fire experiments are notorious for instrumentation failure due to the extreme environment. However, with transmission measurements there are rarely redundancies; this can lead to data gaps if a transmission sensor fails or is deemed inaccurate (*e.g.*, [22,28,42]).

At least four visual methods have been used to estimate three smoke visibility components: visibility [m] [67,68], extinction coefficient [m^{-1}] [66–68], and relative visibility [%] [28]. The visibility and extinction coefficient were found to be inversely proportional to one another for light reflecting and light emitting (illuminated) exit signs [67,68] such that the visibility can be estimated using the extinction coefficient and visa versa.

In Jin's original work [68], the extinction coefficient (σ) was measured and visibility (V) was the target parameter estimated by observers (see note on observer subjectivity in Section 2.2.1) [67,68]. It was empirically found that $V_{reflective} = (2\sim4)/\sigma$ and $V_{illuminated} = (5\sim10)/\sigma$ for signs between 5.5 m to 15.5 m away from the observer with non-irritant smoke [67,68]. This relation has since been used in reverse to calculate the extinction coefficient $\sigma = 3/V_{reflective}$ when the visibility of reflective exit signs (4-10 m) [28] or light-reflecting objects (<5.9 m) [22] were known. This method works well for smoke development in large open spaces with exit signs but may not be as useful in fire experiments with few reflective surfaces.

Another method for visually estimating the extinction coefficient of smoke is in development [66]. The preliminary experiment used to test this method used a Canon 80D with a Canon 18 mm to 35 mm lens (high-resolution digital camera and lens system) that took a photo every second to track the change in extinction coefficient from a vertical string of light-emitting diode (LED) lights (lights spaced about 167 mm apart, 141 total) [66]. The smoke was generated by a 500 g (~735 mL) heptane pool fire that was burned over approximately 3 minutes in a 337 m^3 space and the camera was placed such that 1 pixel ≈ 0.88 mm in the analysis [66]. Preliminary results show LED results that identify similar trends and order of magnitude results relative to the MIREX sensor results at one height, though additional investigation work is needed for a more conclusive validation [66]. Although temperatures in

[2] As an approximation, transmissometers (same concept, different name) from the air pollution field cost >$10,000USD per sensor [71,72,74].

this experiment were not mentioned [66], the common consumer LED strip used [66] is unlikely to operate (or survive) in a high-temperature fire scenario. Additionally, significant resources would be required in order to utilize very high-resolution cameras in an extreme fire environment.

A relative visibility of exit signs was used as part of the smoke and toxic gas validation work for the popular CFD fire model Fire Dynamics Simulator (FDS) and Smokeview (results visualization tool) [28]. Video recordings of four fire experiments with four different fuels (two liquid, two solid) were converted into grey scale images from which intensity values of exit signs and the adjacent background were extracted [28]. A critical time for exit sign visibility (t_{crit}) was taken as the earliest time at which the exit sign was completely obscured. This critical time was determined by taking the time when the ratio of the average intensity (grey scale) value of the exit sign ($\bar{I}_s$) and background ($\bar{I}_b$) went to one (*i.e.*, $t_{crit} = t(\bar{I}_s/\bar{I}_b = I_{crit} \approx 1)$. Then, the relative visibility (I') was calculated as $I'(t) = [(\bar{I}_s/\bar{I}_b) - I_{crit}]/\left[\left(\bar{I}_{s,t=0}/\bar{I}_{b,t=0}\right) - I_{crit}\right]$. While the relative visibility results for an exit sign across the room in each experiment were presented, they were not used directly in the validation of the FDS model results. The relative visibility results were used to determine the critical time for exit sign visibility and, thus, the extinction coefficient at that time could be calculated. The MIREX system failed during the experiments so the extinction coefficient at the critical time could not be compared with measured MIREX results as planned [28]. However, measured values of critical time for exit sign visibility for each fuel were compared to model CFD results. The two liquid fuels had similar critical times in the experiment and Smokeview visualization without gray level parameter adjustment. Conversely, measured and predicted values of the critical times differed for the two solid fuels. In these cases, the experimental results were used to adjust the gray level parameters in the Smokeview visualization by a unique value for each of the two solid fuels. In addition to the subjective use of the results to change model parameters by unique values for each fuel to make the model output match experimental results, the lack of cross-verification due to MIREX the malfunction leaves some questions about applicability of this smoke visibility estimation method to other scenarios.

Smoke visibility measures are one of the less common measures obtained during full-scale fire experiments. However, of the options presented, transmission sensors appear to be used much more frequently than the other methods despite the associated cost and finicky nature of the sensors. This prevalence is likely because of their applicability to a wide variety of scenarios and reduced subjectivity of results. These transmission sensor measurements can also be interpreted to estimate smoke layer height as are addressed in the next section.

2.6 Combined Methods

A practicable method capable of measuring both smoke layer height and density would be very helpful in fire experiments because method implementation could either reduce the

amount of instrumentation, and therefore resources, required or increase the amount of redundant data collection thereby increasing confidence in both usable data and results. It is possible to measure both smoke layer height and smoke density at the same time. In practice, this requires using a full-scale measure of smoke density to determine the smoke layer height in an experiment. Hypothetically, all of the full-scale smoke density measures can be used to determine smoke layer height because they are capable of measuring smoke density at various heights. The smoke layer height can then be estimated from smoke density measurements using one of the sensor-based smoke layer height estimation methods. However, only transmission sensors have been used in this manner and even then only in rare instances [9,29,44].

Such a combined smoke density and smoke layer height estimation technique is rare because multiple transmission sensors must be stacked to determine the smoke layer height and, from a resource perspective, it seldom makes sense to gather the desired information in this manner. The method being developed with LED light strips may change this balance for less severe fire environments in the future, but due to the harsh, high temperature environment, challenges remain for use in severe fire environments. Thermocouples are less expensive, more reliable in a severe fire environment, and often already included to gather critical temperature data; so, are more commonly used to estimate the smoke layer height than transmission sensors. If smoke density information is necessary, then useful information can be gleaned from a small number of smoke density measurements from carefully selected locations. Thus, while it is possible to collect smoke layer height and density data from the same method, it is impractical at present. However, in this thesis, a novel method is developed that is capable of estimating both smoke layer height and smoke density. The origins of this method are detailed in the next section and the development to date comprises the remainder of this work.

2.7 Proposed Novel Smoke Layer Height and Density Estimation Method

The novel smoke layer height and density estimation method developed during the present research was first conceived during a guest lecture at the University of Waterloo in October 2018 [69]. Dr. Rood's lecture, titled 'Optical Remote Sensing of Particulate Matter to Quantify Plume Opacity and Mass Emission Factors,' outlined some results obtained using a Digital Optical Method (DOM) developed by Dr. Rood's team at the University of Illinois [69]. Although intended for measurement of emission plumes in the air pollution field [69], the basic concepts of the DOM appeared to relate closely enough to measurement of smoke layer development in fire scenarios to give merit to the possibility of developing a similar method for application to fire scenarios. This idea was particularly attractive since the theory and development of the DOM had been thoroughly investigated for air pollution applications [70–76] and parts had even been patented for these applications [77].

The DOM uses camera images and software to analyze and quantify the opacity (O = 100% - transmission [%]) of air emissions. It was conceived as an alternative to subjective values obtained using "smoke school" trained observers, which were re-certified every six months [70]. Certified observers are used to monitor visual opacity of emissions in accordance with environmental agency requirements [71]. The DOM was not the first image analysis system developed as an alternative to certified observers in the air pollution field; it was preceded by the Digital Opacity Compliance System (DOCS) [78–82]. The DOM was pursued for this research, however, because it was better suited to analysis of smoke development during experimental fires than the DOCS method. A summary of differences in the methods is detailed in Table 2.3 along with reasons for selection of DOM as the basis for this work. The first reason was a need to be able to adapt the method to smoke analysis via a first principals approach (*i.e.*, through derivation). This is not possible if the details and derivation of the original system equations are not well understood. The remaining four requirements for adaptation to fire experiments are discussed in more detail later in this section after a general description of the DOM itself. To proceed with the discussion, it is important to understand the general premise behind to two existing versions of the DOM and characteristics that justify pursuing an adaptation of the method for investigation of smoke evolution in fire scenarios per the outlined objectives.

In essence, the DOM quantifies background changes (*e.g.*, the sky or a roof) as a result of air pollution emitted or created by a source such as the industrial smokestack shown in Figure 2.10 [70–77]. Two versions of the DOM have been developed: the contrast [70–77] and transmission [70–73,75,77] versions. As the first step in assessment, every assumption in each of the two versions are reviewed from the point of view of application to fire experiments to determine its validity and potential application in this context. The transmission version of the DOM uses a uniform sky background to determine the opacity of air pollution emissions. During review of the method, however, it becomes clear that many assumptions in the derivation hinge on the background being the sky and, therefore, only works outside. Since the intent is to develop a method that can be used for fire experiments and compartment fires in particular (indoors by definition), the transmission version of the DOM is not pursued further.

The DOM contrast method, on the other hand, uses background areas visible in an image that have contrasting colours (black and white squares in Figure 2.8) and compares the contrast between the colours when air pollution is and is not present at the location of interest. These contrast areas can include but do not require the sky. Similar to smoke density discussed in Section 2.5, the DOM uses transmission to determine the opacity or density of the air pollution though it does not use the Beer-Lambert Law. The generic DOM contrast calculation is shown in Equation 2.5.

Table 2.3: Comparison of Digital Opacity Compliance System (DOCS) and Digital Optical Method (DOM) validations to fire experiment requirements

Digital Opacity Compliance System (DOCS)	**Digital Optical Method (DOM)**	**Fire Experiments**
DOCS internal software analysis details are sparse [78–82]	Detailed derivation provided for each DOM application [70–76]	Derivation is necessary for fire scenarios and the derivation must be clear for results to be accepted/ validated
DOCS validated for 0-40% opacity [78–82]	DOM validated for 0-100% opacity [70–76]	Fire smoke opacity (density) values from 0-100% are expected
DOCS never used at night [78–82]	DOM validated for night-time use [72]	A wide variety of lighting conditions are possible
Varied DOCS performance with different cameras [81]	Consistent DOM performance with different cameras [70–76]	Many different cameras are used
DOCS never used with video recorders [78–82]	DOM validated for camcorder use [76]	Video recordings are frequently used

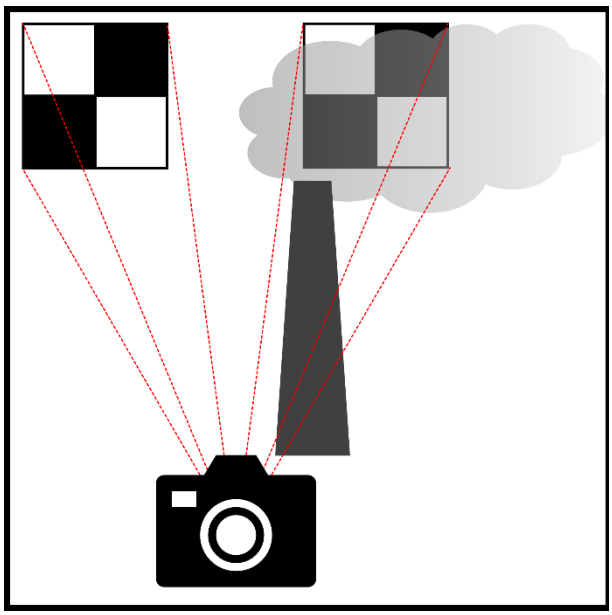

Figure 2.10: Diagram of the contrast Digital Optical Method (DOM) that compares contrasting backgrounds in an image without (left) and with (right) air pollution particulate from a smokestack.

$$Opacity\ [\%] = 100\% - Transmission\ [\%] = 100\% - \frac{Contrast\ with\ Pollution}{Contrast\ without\ Pollution} \quad 2.5$$

In this equation, the 'contrast without pollution' acts as a colour scaling factor for the image. Thus, small changes in the contrast will have high transmission and low opacity, while the opposite is true for large contrast changes. Like the DOM based on transmission, the DOM contrast method also requires use of various assumptions, including: path radiance and transmission losses being equal for both the black and white areas at a given point in time, the radiance emitted by the background remains constant as the fire experiment progresses, the transmission losses through the air remain constant as a fire experiment progresses, and constant particle density in the plume. The nature of these assumptions, however, makes it more feasible to determine and understand their impact on smoke measurement in fire scenarios [70–77]. Detailed explanations of how each assumption might impact measurement of smoke evolution in fires are provided in context in Section 3.4, wherein the theoretical derivation of the method applied in this research is completed. For now, what is important is that the assumptions are valid or will introduce only acceptable levels of uncertainty when applied to smoke measurement in fire scenarios.

Upon early review, it is deemed possible that a variation of the DOM can be used to estimate opacity of smoke in outdoor fire scenarios captured by camera (still or video), since the particulate matter in smoke is analogous to particulate matter in air pollution which is, in

fact, sometimes actually smoke (hence, smokestack). However, this application is not of interest in this work, since the key parameter of interest is smoke layer height within a compartment fire. Nonetheless, application to outdoor fires may be worth investigation in future if the adapted method developed in this thesis proves useful.

There are several obvious differences between measurements of smoke/plume density in air pollution applications and indoor fire scenarios of interest here. However, there is also ample evidence in the literature related to development of DOM that adaptation to fire scenarios would be feasible. Some of the related literature, briefly detailed in Table 2.3, is described further here. First, accuracy over the full opacity range (0-100%) is critical for fire scenarios which often produce smoke that is dense enough to result in more than 40% decrease in background intensity (limit of accurate range in the DOCS system [78–82]). The DOM can provide acceptable results over the full range (0-100%) of opacity values [70–76]. Similarly, a fire can produce smoke that appears white or black; thus, it is significant that the DOM was tested over the full range of opacity values for both black and white smoke [70–76].

Lighting indoors is different than outdoors where the DOM has been tested. While the DOM does not appear to have been used indoors, it has been used successfully in sunny [70,71,74,76], cloudy [70,71,76], misty [71], and nighttime (front and backlit) [72] conditions. This broad range of tested ambient lighting conditions, particularly the low light nighttime conditions, indicates that extension to indoor conditions encountered in a fire environment is likely possible.

Using similar logic, it should be possible to extend the DOM for use with cameras having characteristics different from those used in the published works. The wide range of cameras used in the development of the DOM contrast method (five different models of digital still cameras [70–75,77], two smartphone cameras [75], and one camcorder [76]) indicates that any constraints on the selection of recording device due to the harsh conditions and lighting levels encountered in fire experiments should not impact the applicability of the method. Further, the successful use of a camcorder [76] indicates that extension analysis of images captured using video cameras is possible. This consideration matters because videos of fire experiments are often recorded as a series of images that are later used for analysis.

Availability of appropriate background contrast areas for analysis is a necessary element of DOM. Maximum contrast can be obtained with well-defined regions of pure white and pure black in the background; however, as with fire scenarios, this is practicably impossible to obtain in air pollution applications which are typically industrial or environmental in nature. The necessary high contrast regions have been obtained by installing checkerboards with black and white squares in the background of an image [70,72–74,77] (*e.g.*, Figure 2.10) as well as by careful selection of contrast areas in an image based on the existing background [70–73,75–77]. Studies on application of the DOM method have shown that contrast has a significant impact on the uncertainty of analysis results [75,76]. Specifically, higher contrast

background areas reduce uncertainty, though usable results can be obtained with lower contrast in some situations as well [75,76]. The ability to use an existing background and varying contrast is important to the present work because the images, particularly those in existing fire recordings, do not usually have demarcated black and white areas in the background.

Air pollution emissions are often monitored for a fixed source like a smokestack. Fires, on the other hand, can spread, which changes the location of smoke production. Further, smoke immediately adjacent to a fire can be difficult to distinguish from the fire. Thus, adaptation of DOM for fire scenarios would be far more useful if the smoke could be measured away from the fire. Smokestacks are designed to rapidly disperse air pollution [83], making it important that opacity measurement be done close to the air pollution source. Although the DOM was largely tested with fixed smokestack air pollution sources [70–73,75–77], fugitive emissions, those made by sources that are not fixed, were studied on one occasion [74]. The team studied the dust "kicked up" by trucks driving on an unpaved road [74] as shown in Figure 2.11. In this case, the truck is the source of energy that creates the air pollution, yet measurement must occur away from the truck to avoid capturing the truck rather than dust in the background areas of interest in the image. This type of analysis, therefore, is much more applicable to indoor fire scenarios than that based on emissions from a fixed stack.

This study of fugitive emissions also introduced the concept of analysis using separate images [74] as shown in Figure 2.11. An image, Figure 2.11 left, was captured immediately before the truck arrived (*i.e.*, without dust emissions) and another, Figure 2.11 right, shortly after the truck departed (*i.e.*, with dust emissions). The ability to use separate images is crucial for a fire scenario because, as shown in Figure 2.12, once a smoke layer begins to form at the ceiling it is no longer possible to see the background without smoke. Unlike the fugitive emissions scenario, the fire scenario in Figure 2.12 is depicted with a video camera (previous DOM use in [76]) rather than a still camera to better align with the fire scenario investigations that are used in this work.

Collectively, early investigations indicate that a fire-specific adaptation of the Digital Optical Method shows promise for development as an optical measurement method for investigating time-varying smoke evolution from video recordings of fires with application to past, present, and future fire scenarios but minimal analyst subjectivity. The fire-specific method presented in this thesis is developed through an iterative process. The methods used are detailed in Chapter 3 with results and discussion in Chapter 4. The final chapter (Chapter 5) details the conclusions and recommendations that are made based on the information in the coming chapters.

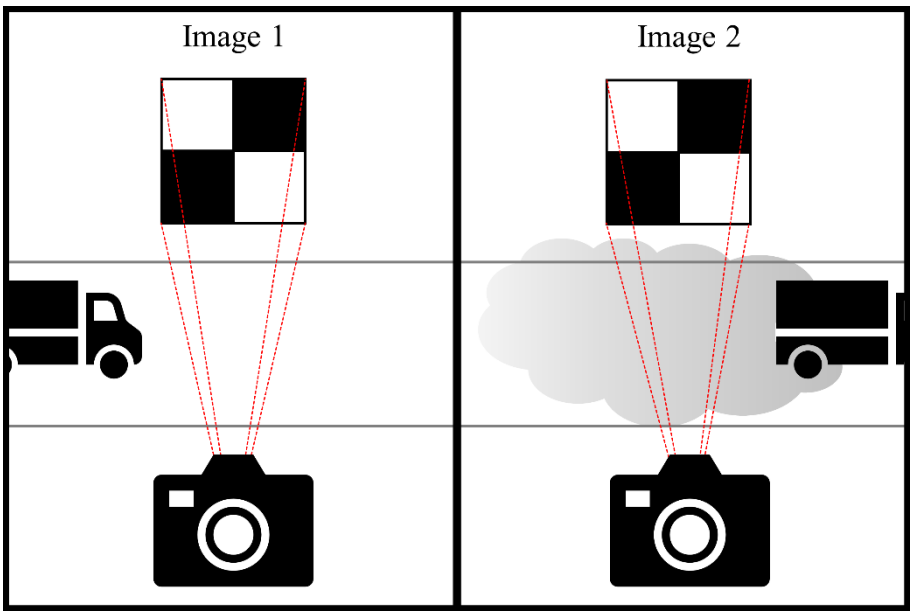

Figure 2.11: Diagram of the Digital Optical Method (DOM) applied to a fugitive emission scenario with an image taken before a truck passes (left) and after a truck passes creating dust emissions (right)

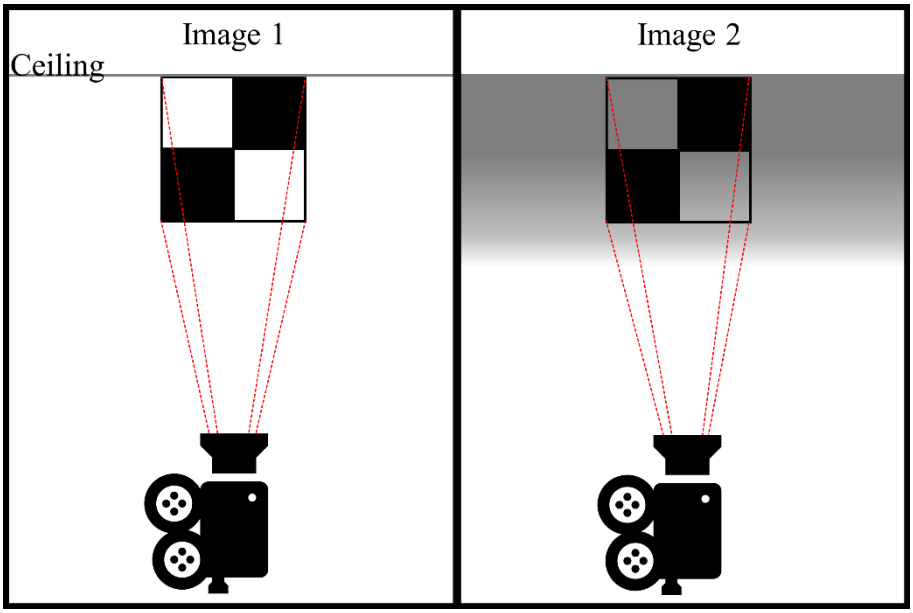

Figure 2.12: Diagram of Digital Optical Method (DOM) logic applied to an indoor fire scenario with an image taken before (left) and after (right) a smoke layer forms

Chapter 3

Methodology

This chapter outlines the approach undertaken to develop a new method for measuring smoke evolution, specifically smoke layer height and optical density, in full-scale fire experiments. Data from full-scale ‘burn house’ fire experiments were used to build the method, beginning with development of the theoretical basis through several method iterations as shown in Figure 3.1. This chapter begins with a description of the details of the apparatus, instrumentation and experimental procedure used to obtain the full-scale burn data. Thirteen experiments, detailed in Table 3.1, were conducted in the University of Waterloo’s ‘burn house’ experimental fire apparatus (burn house going forward).

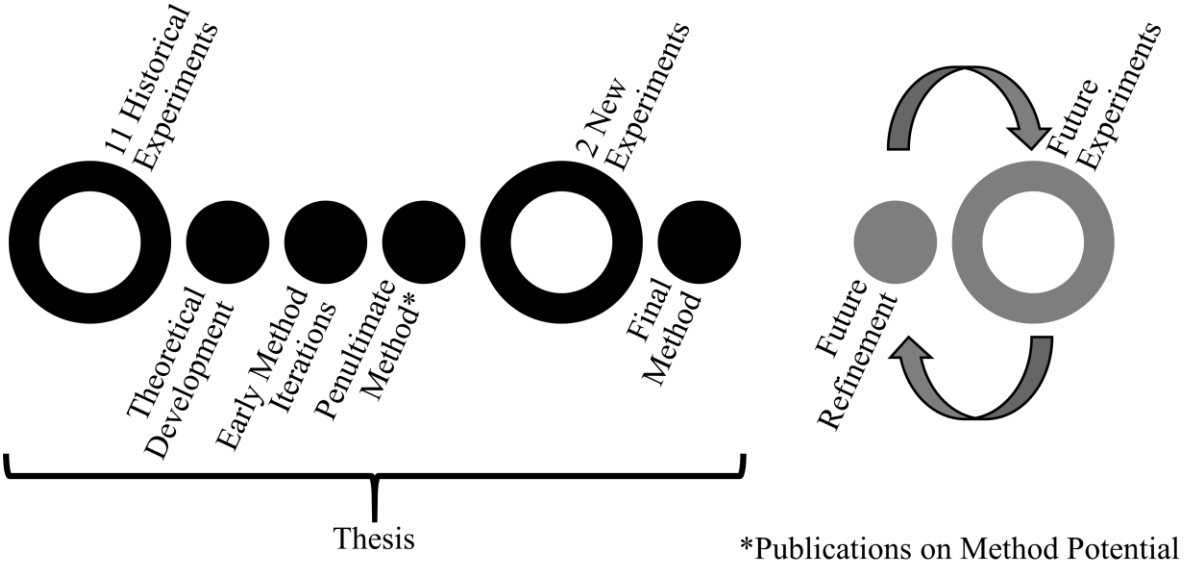

Figure 3.1: Thesis approach 'timeline' including experiments, theoretical development, method iterations and existing publications [23,24,84,85]

After a description of the experiments, Sections 3.2 and 3.3 detail extant methods that are used to characterize the smoke layer height and smoke density, respectively. These initial smoke characterizations are used to gain basic understanding of the smoke progression during the historical experiments and to develop a set of baseline data for the analysis. With

this in hand, Section 3.4 details the theoretical derivation of the radiance method that is developed. The method is refined through iteration in Section 3.5. To close the chapter, Section 3.6 presents the final method in this thesis and summarizes the entire refined method in a stand-alone manner.

Table 3.1: Thirteen burn house fire experiments with fire-retardant (FR), lightly fire-retardant (LFR) and non fire-retardant (NFR) sofa material combinations

Experiment	Material	FR Class	Repetition	Timeline	Ventilation
A1	Type A	NFR1	1 of 3	Historical	Limited
A2	Type A		2 of 3	Historical	Limited
A3	Type A		3 of 3	Historical	Limited
B1	Type B	FR	1 of 3	Historical	Limited
B2	Type B		2 of 3	Historical	Limited
B3	Type B		3 of 3	Historical	Limited
C1	Type C	LFR	1 of 3	Historical	Limited
C2	Type C		2 of 3	Historical	Limited
C3	Type C		3 of 3	Historical	Limited
D1	Type D	NFR2	1 of 1	Historical	Mixed 1
E1	Type E	NFR3	1 of 1	Historical	Mixed 2
F1	Type F	NFR4	1 of 2	New	Limited
F2	Type F		2 of 2	New	Limited

3.1 Burn House Experimental Apparatus and Procedure

The experimental apparatus and procedure are detailed first to provide context for the data used as the basis for development and refinement of the methods described in this research. The experiment reference names (*e.g.*, experiment A1) shown in Table 3.1 are used going forward except where the experiments are grouped by type when all repeats of that material type are included (*e.g.*, Type A experiments = experiments A1, A2 and A3). This naming convention was selected because it indicates the material type and, where relevant, repetition which is the information crucial to the analysis in this work.

The experimental set up used in these experiments has been outlined in detail elsewhere [86–90] but, for context, an overview is provided below. Eleven (11) of the 13 experiments (Types A-E) preceded this work so represent historical data and the remaining two experiments (F1 and F2, instrumentation detailed in Section 3.1.2) that were conducted using the modified instrumentation employed for this analysis. All experiments were conducted in the full-scale, two-storey, steel burn house located at University of Waterloo Live Fire Research Facility and shown in Figure 3.2.

The interior layout of the burn house is shown in Figure 3.3. The main floor consisted of the fire compartment (living room), main floor SW room and main floor corridor. The second floor had a smaller SW room and larger SE room connected by the second-floor corridor.

The two floors were connected by a set of stairs. There was also a sealed, central shaft that housed the primary in-house data acquisition equipment.

Figure 3.2: External view of the SE (left) and NW (right) corners of the UW burn house

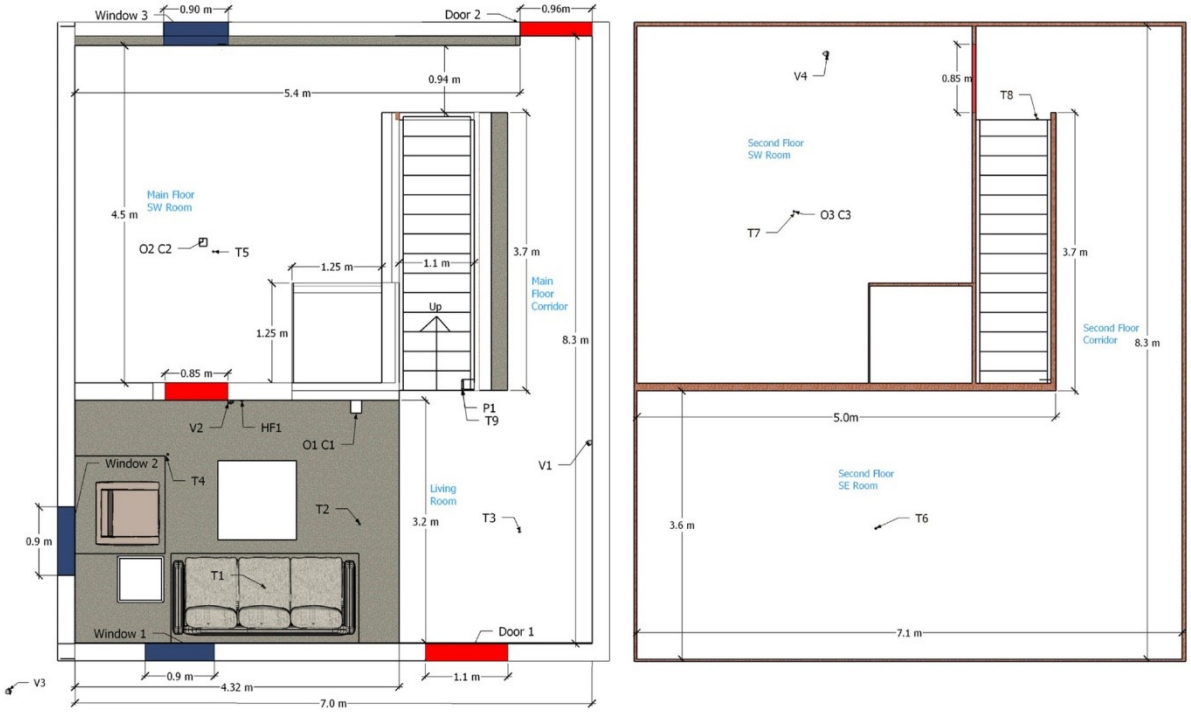

Figure 3.3: Original burn house experimental apparatus instrumentation layout, borrowed with permission from [89]

For the experiments, the living room was outfitted with a sofa, chair, coffee table, and end table (visible in Figure 3.4a)). Type A, B, C and F sofas were three cushions wide. The Type D and E sofas were two cushions wide (sometimes called a love seat). Each sofa was ignited using a British Standard 5852 crib #4 [91] (*i.e.*, consistent ignition heat source) and allowed to burn unimpeded.

The nine Type A-C experiments were used to established repeatability and the impact of fire retardants in the custom-built sofa materials on the fire growth and development. The burn house was sealed for these experiments to represent an oxygen-limited environment. Tests with each sofa type were repeated three times. Results indicated that the fires established on the Type A, B and C sofas resulted in different fire and smoke progression but tests for a given Type of sofa were repeatable relative to other full-scale fire experiments [86].

The D1 and E1 experiments were conducted with two non-fire retarded fuel combinations and different, mixed ventilation conditions. The burn house was not sealed for these experiments, and the East door near the sofa was closed at 221 seconds and 337 seconds into experiments D1 and E1, respectively. Therefore, the fire growth and development were at least partially fuel-limited, rather than being limited by the ventilation, and thus quantity of available air. As a result, the fire and smoke progression were anticipated to be different for each of these two experiments, as well as relative to that observed in the Type A-C experiments.

The two Type F experiments were trial burns (*i.e.*, instrumentation checks) for a series of experiments to be conducted. As in the Type A-C experiments, the burn house was sealed for experiments F1 and F2 to represent an oxygen-limited environment. The fire and smoke progression for these experiments were expected to be repeatable between F1 and F2 but different relative to the Type A-E experiments due differences in sofa construction and materials from any of those burns.

Thus, as listed in Table 3.1, the 13 full-scale living room furniture fire experiments captured results for six different furniture material combinations (material Types A-F) and four sets of repeatable experiments (Type A [x3], Type B [x3], Type C [x3] and Type F [x2]). Each sofa had flexible polyurethane foam cushions wrapped in fabric and together the different foam and fabric material combinations (Type A-F) were non fire-retardant (Type A, D, E & F), fire-retardant (Type B), or lightly fire-retardant (Type C). The ignition heat source (British Standard 5852 crib #4 [91]) was consistent for all experiments. Ventilation-limited conditions were present for the Type A, B, C, and F experiments. Therefore, fuel source (furniture material) was the primary difference between those experiments and each material was expected to have different smoke evolution properties. Conversely, repeat experiments were expected to exhibit similar smoke evolution. Ventilation conditions and fuel varied in Type D1 and E1 so each of those were distinct from all others. These expectations are the important take-aways for the upcoming analysis: under similar ventilation conditions the same materials should have similar smoke evolution and different materials should result in different smoke evolution.

3.1.1 Original Instrumentation

The instrumentation layout shown in Figure 3.3 is from the 11 historical fire experiments in the burn house. The instrumentation included load cells, thermocouples, a heat flux gauge, video cameras, smoke and heat detectors, velocity probes, and oxygen and carbon monoxide gas sensors. The thermocouples and video cameras are relevant to this work. Detailed information on the other instrumentation has been documented by Senez *et al.* [86]. Output signals from the load cells and thermocouples were fed into a National Instruments (NI) Compact FieldPoint data acquisition (DAQ) system which sampled data every 1.1 seconds [86] during the experiments. Temperatures were measured using 24-gauge, Type K thermocouples, with ceramic insulation and Inconel overbraid, installed in vertical "thermocouple rakes" throughout the structure. This permitted time-dependent measurement of temperature at each thermocouple location (x, y, z) and determination of vertical temperature gradients at each thermocouple tree position (x, y). Three stationary security cameras were located inside the structure with Camera 1 (Cam1) viewing the living room, Camera 2 (Cam2) viewing the sofa, and Camera 4 (Cam4) viewing the upstairs landing, while the final camera (Cam3) was mounted outside as shown in Figure 3.4.

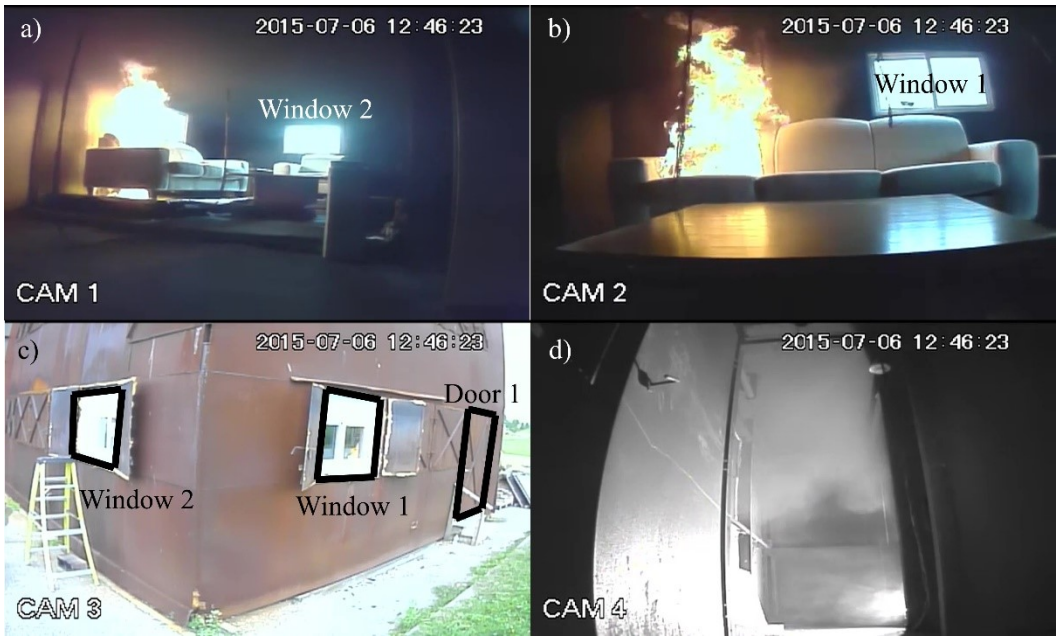

Figure 3.4: Time-synchronized images from experiment A1 of a) Cam1 (location: living room, view: broad), b) Cam2 (living room, sofa), c) Cam3 (external, SE corner), and d) Cam4 (second floor SW room, second-floor corridor).

The video cameras used in the Type A-C experiments were Lorex® MC7572 cameras with a Q-See® QC958 digital video recorder (DVR). The same model of DVR was used in experiments D1 and E1. The video camera models were not recorded at the time of the latter

experiments and the video recordings make it clear that a combination of cameras were installed. The cameras could have included Lorex® CVC7731-C (possible for Cam3), Q-See® QCA7207B (possible for Cam1-4) and/or Q-See® QTA8027B (possible for Cam1-4). Videos were recorded at 30 frames per second (fps) for all cameras in all experiments, except for Cam2 and 4 in experiments D1 and E1 which were set to record the video at 15 fps. The Type A-C experiment videos were recorded exclusively in 480p (720x480 pixels) while, in experiments D1 and E1, Cam1, 2, and 4 were recorded in 720p (1280x720 pixels) and Cam3 was recorded in 960H (960x480 pixels). As a result, the resolution of images does change from test to test as well. A summary of these camera details is provided in Table 3.2 for reference.

Table 3.2: Type A-E experiment camera equipment

		Camera	DVR	Recording	Resolution
Type A-C	All 4	Lorex® MC7572	Q-See® QC958	30 fps	480p
Type D & Type E	Cam1	2 Possibilities	Q-See® QC958	30 fps	720p
	Cam2	2 Possibilities	Q-See® QC958	15 fps	720p
	Cam3	3 Possibilities	Q-See® QC958	30 fps	960H
	Cam4	2 Possibilities	Q-See® QC958	15 fps	720p

Some of the temperature and video data from Type A-C experiments were used to characterize the smoke evolution using existing smoke layer height and density estimation methods (Sections 3.2 and 3.3, respectively). The radiance method was theoretically derived (Section 3.4) and then the characterization was used as a baseline for comparing the new method results as the method developed through iteration (Section 3.5.1). Video data from Type A-E experiments was used in the iterative method development process (Section 3.5.2). However, questions remained that could not be answered with the existing historical data so the instrumentation (and associated procedure) was altered in the new experiments with the intent of answering those questions. The relevant changes to the instrumentation and procedure are detailed in the next section. The method for the final iteration of the radiance method is detailed in Section 3.6.

3.1.2 New Experiment Instrumentation

For the new (Type F) experiments, the burn house configuration and general experimental procedure (detailed in Section 3.1) remained the same as in historical (Type A-E) experiments except as it pertains to the revised instrumentation used in the present research. Numerous analyses were conducted [87–89,92–94] in the years between the Types A-E and the Type F experiments which resulted in many “lessons learned” that were applied to experiments F1 and F2. As a result, the instrumentation was changed for the Type F experiments. In particular, a new system of controlled contrast ‘checkerboards’ and specific

video cameras were installed for the smoke evolution analysis as outlined after the general overview of the test instrumentation and set up in Figure 3.5 below.

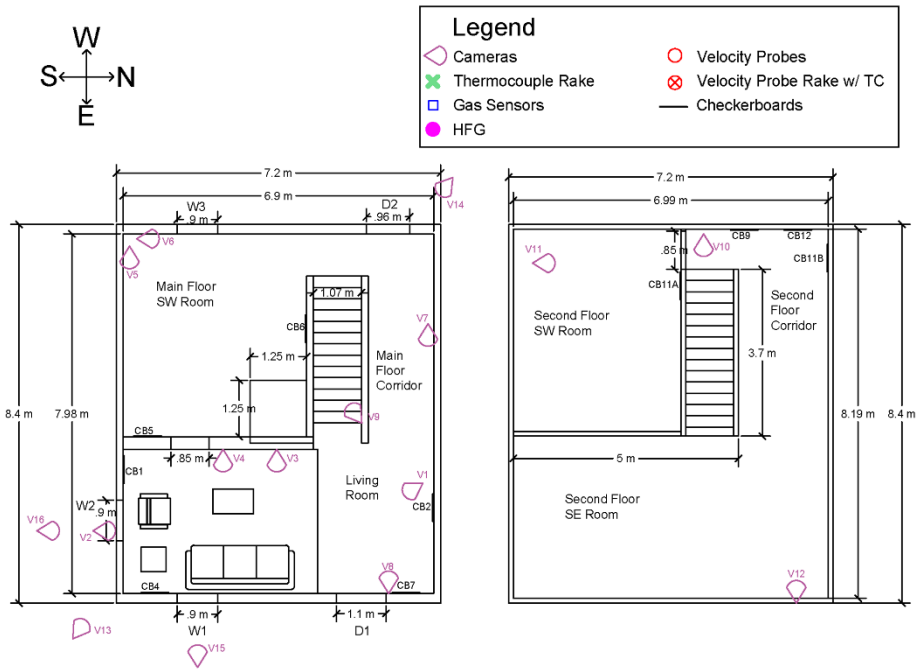

Figure 3.5: Burn house experimental apparatus video analysis instrumentation layout for Type F experiments

The revised layout for the Type F experiments is shown in Figure 3.5. This layout details the locations of the video cameras (V) and new video analysis checkerboards (CB). For clarity in upcoming analysis, the historical video cameras are denoted as Cam1-4 while the new video cameras are denoted as V1-16. The windows (W), doors (D) and sofa and chair locations are noted for reference. The instrumentation also included load cells, thermocouples, heat flux gauges, smoke detectors, velocity probes, and gas sensors for several gas species. Only the instrumentation related to the video cameras (V) and video analysis "checkerboards" (CB) are discussed in detail here because they were used to collect the additional data used in the final sections of the present research.

Checkerboards

Large black and white "checkerboards" were used in the new (Type F) experiments with intent to include specific dark and light areas within each camera image to ease later analysis of smoke progression with time. These were modelled after the background boards installed in the Digital Optical Method [70,72–74,77] to ensure that known areas of white and black would appear in each camera image used in that analysis. Unlike the near normal ambient temperatures related to applications using the Digital Optical Method, however, the checkerboards in the new burn house experiments had to survive harsh, high temperature fire

and smoky environments. Thus, the checkerboards were constructed using 12.7 mm thick light duty drywall with high temperature paint, as shown in Figure 3.6, to be able to handle the extreme conditions. Drywall was selected as the checkerboard "base" because it was readily available and was known to survive high temperature, fire conditions with the main failure mode being that the paper lining on the drywall burns or flakes off [95]. Since high temperature paint was applied to the surface of the drywall, it was believed that heavier duty drywall (including fire rated drywall) was unlikely to have sufficient added benefit to justify the increase in cost and weight of each board. To fit within the available space in the burn house, the 4 ft by 8 ft (1219 mm by 2438 mm) sheets of light weight drywall were cut in half to make standard checkerboard background boards of dimension 2 ft by 8 ft (610 mm by 2438 mm).

Figure 3.6: Camera V2 view of checkerboard CB2 a) before flip (experiment F1) and b) after flip (experiment F2)

Post fire analysis and analysis of the video traces from previous experiments indicated that soot was deposited on the compartment walls. Since no quantification of these deposits had been made during the tests, soot deposit could not be accounted for in the analysis of Type A-E experiments. This was taken into consideration in the design of checkerboards for the Type F experiments since the deposits could impact the measurement of smoke evolution. It was also anticipated that the stratified smoke layer might preferentially damage the top of the drywall over the course of an experiment, so the checkerboard paint was applied in a vertically symmetric pattern. In that way, the checkerboard could be flipped (top to bottom), as shown in Figure 3.6, between fire experiments when only the top half of the board had been impacted or damaged by smoke. Similarly, undamaged but soot covered checkerboards were designed such that they could be cleaned between experiments to minimize the number of replacement checkerboards required for a long experiment series.

Several considerations were taken into account with respect to applying the checkboard pattern to each of the drywall sheets. Drywall has paper on both sides, one side is light grey and the other is brown. To ensure that the white squares were as white as possible, it was decided to apply the paint to the light grey side of the drywall. In addition, to test whether the

light grey side of the drywall was light enough that it could be used as a light area of contrast two sets of boards were made. Some were painted with both black and white squares and the others were painted with black squares only and the final results compared.

Several high temperature paints, available at local hardware stores [96–99], were considered for application of the squares on the checkerboards. Given the potential for damage to the boards during an experiment, the paint chosen needed to be cost-effective, as well as resistant to smoke layer temperatures. Thus, options were compared based on temperature resistance, cost, and availability in both black and white as summarized in Table 3.3 [96–99]. Of the options listed, only two were available in both black and white [96–99]: Rust-oleum® Specialty High Heat Enamel and Tremclad® High Heat Enamel – Gloss. From these, Rust-oleum® Specialty High Heat Enamel was selected because it could withstand high temperatures, cost the least and was available in both black and white. The paint spray can label notes that the paint tends to off-gas the first time it is heated [100] which might have an impact on gas sensor measurements but quantifying the impact is beyond the scope of this work.

Table 3.3: High temperature paints considered for use on the checkerboards

Product	Temp. [°C]	Cost [CAD]	B&W	Ref.
Rust-oleum® Specialty High Heat Enamel	648	$11-13	Yes	[96,99]
Rust-oleum® Automotive High Heat Enamel	1093	$14-15	No	[96,97]
Tremclad® High Heat Enamel – Flat	650	$12-15	No	[97]
Tremclad® High Heat Enamel – Gloss	350	$13-15	Yes	[96,98,99]
Tremclad® High Heat Enamel – Flat (brush on)	650	$26	No	[97,98]

Black and white squares were made on the light grey side of each drywall board by overlaying areas where a specific paint colour was not desired with 300 mm by 300 mm ceramic tiles. A can of spray paint was put into a spray can holder and each colour applied as evenly as possible until the desired checkerboard pattern was complete. Each board was left to dry for about 1 hour (until touch dry) before being moved to pre-installation storage. The checkerboards were installed in the burn house at the necessary locations prior to experiment F1. All checkerboards remained in place until just prior to experiment F2 at which point checkerboard replacement, flipping and cleaning was completed. Each checkerboard was either fastened to the drywall/concrete board on the burn house walls with drywall screws (main floor) or leaned up against steel walls (second floor). The height of each checkerboard division (from the floor) was recorded to facilitate the post-experiment smoke evolution observations and calculations. Post-experiment, checkerboards were inspected for damage and any damage or destruction was noted in the experimental log for that test.

Video Cameras

Security cameras and the associated DVR systems are typically used at the UW Fire Research Lab for recording full-scale fire experiments in the burn house because of their relatively low cost, ability to be synchronized in time, and remote data storage capability. They were used in the experiments discussed in this research primarily because of their low cost and the option for remote data storage since the likelihood of damage or destruction of the cameras themselves was high in full scale fire experiments such as those being studied in this research. Although destruction of at least one camera in a given test was almost guaranteed, the video recordings obtained prior to damage to the camera were deemed to be worth the cost of the camera. Further, time synchronized images were required for the present tests in order to better follow, and thus obtain valuable insight into, the development of the dynamic fire environment. In the present case as well, they form the only method by which to visualize the progression of the smoke in the compartments. Finally, since security camera footage is commonly available in "real life" scenarios, use of them in these experiments might also allow extension of the methods for use in fire investigations.

In contrast to the cameras used to videotape the historical fire experiments, the security cameras chosen for the modified experimental methods developed during this research were specifically selected for the purposes of smoke evolution analysis. Four additional factors were considered. They were recording speed, durability (against temperature, soot and water), mounting flexibility, and image resolution. All except image resolution were quite straight forward to determine. Since smoke progression can be captured at relatively low recording speeds, the recording speed did not prove to be a major consideration here and was selected to be 30 frames per second (fps) for the purposes of other future analyses.

Conversely, the camera durability related to temperature, dust, and water resistance of the cameras was an important consideration. Although no low-cost security camera was rated for operation at the high temperature encountered during a fire (>400 °C for cameras facing the sofa), they can be rated for "extreme climates" with manufacturer stated operating temperatures of up to 60 °C [101]. Despite being wrapped in insulation, small amounts of exposed plastic on cameras close to the fire was still of concern so cameras with plastic housings were used at positions remote from the fire and less likely to be engulfed in high temperature fire gases while camera(s) closer to the fire were ideally outfitted with metal housings. The environmental rating, or Ingress Protection (IP) rating, for each camera was also relevant because it indicates how much dust (*i.e.*, soot) and liquid (*i.e.*, fire fighter spray) would ingress into an exposed camera. Both IP66 and IP67 cameras completely protect against dust ingress [101]. IP66 limits water ingress with low pressure water jets from all directions while IP67 cameras limit water ingress with strong water jets from all directions [101]. IP66 and IP67 cameras rated for "extreme climates" were, therefore, considered to be sufficiently durable for these fire experiments. Another important factor considered in choice

of camera for these experiments was the mounting flexibility because of the odd mounting positions required to properly position cameras to view the checkboards or other important features of the fire environment. While the above three factors probably apply to a broad range of fire experiments, the final consideration, image resolution, was more complex and experiment specific as discussed below.

The desired image resolution was determined based on consideration of the possible camera and checkerboard locations coupled with positions deemed as the best to facilitate the smoke progression analysis. For this, camera positions used in previous experiments were supplemented by installation of cameras at additional positions where interesting aspects of smoke progression could be captured in areas of the house not observed by video in the previous experiments. At the same time, the checkerboards had to be visible to the associated camera but could not interfere with the other planned instrumentation, which necessitated compromise on all sides. Finally, since the video recordings were used to gather more information than just smoke progression, the final camera positioning had to accommodate other data collection as well. In the end, 16 camera (11 indoors and 5 outdoors) and 10 checkerboard locations were agreed upon as detailed in Table 3.4.

Table 3.4: Video camera details (all experiments)

New Camera	Historical Camera	Checker-board	Floor/ Ext.	Location	View
V1	Cam1	CB1	Main	Living room	Living room broad
V2	-	CB2	Ext.	South window	Living room broad
V3	Cam2	-	Main	Living room	Sofa (left)
V4	-	CB4	Main	Living room	Sofa (centre)
V5	-	CB5	Main	SW room	SW room (East)
V6	-	CB6	Main	SW room	SW room (North)
V7	-	CB7	Main	Corridor	Corridor (East)
V8	-	-	Main	Living room	Corridor (West) & Stair landing (main)
V9	-	CB9	Main	Stair landing (main)	Stairs & landing (2^{nd})
V10	-	-	2^{nd}	Stair landing (2^{nd})	Stairwell
V11	Cam4	CB11A&B	2^{nd}	SW room	SW room (North) & Stair landing (2^{nd})
V12	-	CB12	2^{nd}	SE room	Corridor (West)
V13	Cam3	-	Ext.	SE corner	South & East sides
V14	-	-	Ext.	NW corner	North & West sides
V15	-	-	Ext.	East side	East window
V16	-	-	Ext.	South side	South window

Once the checkerboard and camera locations were determined, available cameras with resolutions of 960H (960x480 px), 720p (1280x720 px) and 1080p (1920x1080 px) were

tested to determine the ideal resolution for these experiments. A test board with black and white areas of known dimensions was placed approximately at each checkerboard location, and a short recording was captured by each camera that was similarly placed at the corresponding angles and positions. A representative image was selected from each recording; see, for example, the composite shown in Figure 3.7. From these images, the number of pixels contained in each black and white block of the test board was determined.

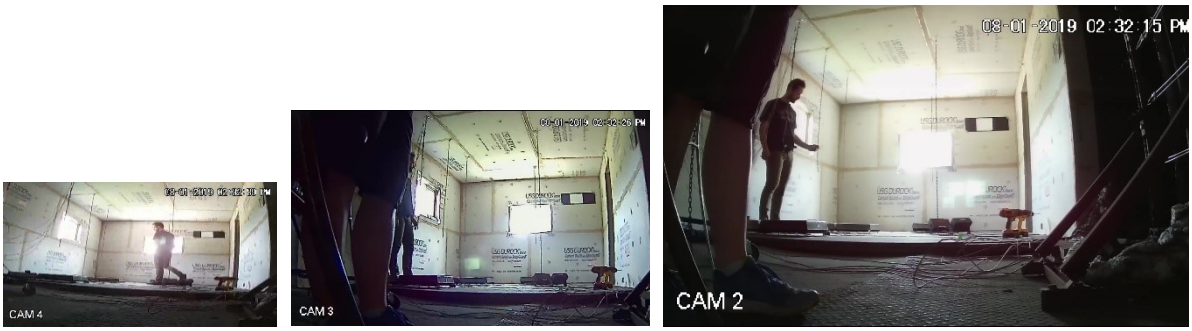

960H (960x480 px) 720p (1280x720 px) 1080p (1920x1080 px)

Figure 3.7: Representative images for the V1 and CB1 location at 960H (left), 720p (middle) and 1080p (right) resolutions displayed at 15% of their original size.

Ideally, it was desired to increase the number of smoke evolution measurement points within the vertically stratified smoke layer and areas of 10x10 pixels worked well for the DOM contrast method [76]. Thus, a value of 10x10 pixels per 100 mm^2 was sought because this would allow each 300 mm x 300 mm square in the checkerboard to be divided into at least three vertical segments. The procedure indicated cameras and checkerboards needed to be placed relatively close together to achieve a resolution of 10x10 pixels per 100 mm^2 with 960H (smallest resolution) cameras, while that resolution could be obtained for all but one camera and checkerboard pair with 1080p (largest resolution tested) cameras. As a result, it was decided to use cameras with 1080p resolution and 30 fps with IP66 or IP67 housings and flexible mounts in experiments F1 and F2.

Cameras from Lorex, Q-See and Swann were investigated. Each had plastic cameras that could satisfy the requirements, but metal cameras were much more difficult to locate and were also more expensive. Therefore, metal cameras were purchased only for locations at which the camera might be exposed to very high heat and plastic cameras were used for the remainder of locations. Since it was preferred to buy all cameras from a single manufacturer, Lorex® LBV2531U (plastic) [102] and LBV2711 (metal) [103] cameras were purchased in conjunction with a Lorex® DV900 DVR [104]. The DVR was selected because it was compatible with the cameras selected, was able to record up to 16 time-synchronized 1080p camera feeds at 30 fps, and offered storage capacity adequate to hold video recordings from at least one full living room furniture fire experiment. Time-synchronized images from the 12

camera views (V1-12) recording fire and smoke progression inside the burn house are shown in Figure 3.8.

Figure 3.8: Time-synchronized images from cameras with interior views (V1-12) 210 seconds after ignition in experiment F1

Two metal cameras were installed at the locations directly facing the sofa that was ignited and burned (V3 and V4). Plastic cameras were installed in the remaining 14 locations. A diagram of a typical camera installation is shown in Figure 3.9. Bayonet-Neil-Concelman (BNC) cables provided both power to the cameras and data connections from the cameras to the DVR. The male BNC cable ports on each individual camera were connected and the 60 ft (18.3 m) BNC cables run out of the house along a route that would experience the least possible exposure to high temperature gases to a junction location. Female-to-female connectors were used to join the BNC data ports while the BNC power ports were directly connected at the junction location. The second 60 ft (18.3 m) BNC cable was long enough to run to the remote instrumentation station. Here, the data ports connected to the DVR and the power ports were connected, through a series of four-camera power splitters, to the appropriate power supplies. After installation and camera alignment, the cameras and BNC

cables on the main floor were insulated to further protect them from heat exposure as much as possible.

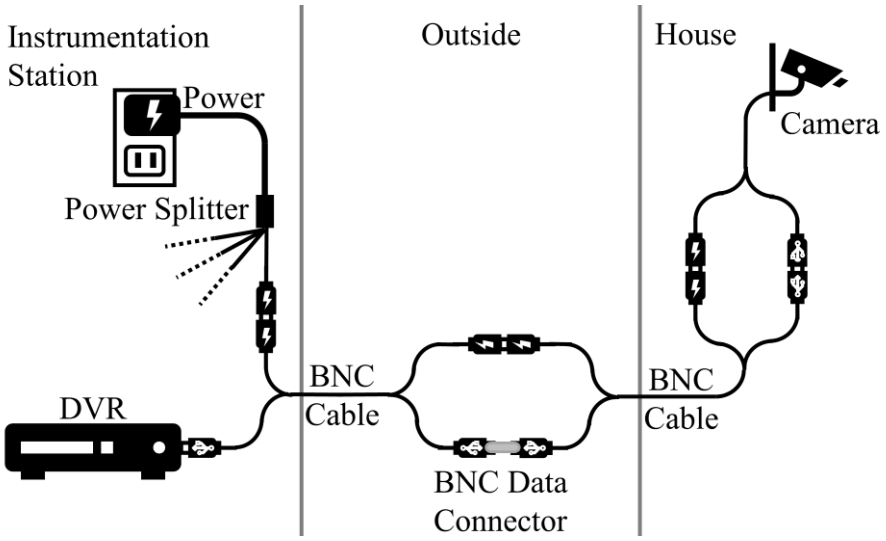

Figure 3.9: Video system connection diagram

Prior to each experiment, the lens on each camera was cleaned and the camera angles reviewed for alignment and repositioned as necessary. Once everything was positioned, and prior to each experiment, a X-Rite ColorChecker Video XL unit (camera calibration tool) was held in front of each camera and checkerboard and a short video was recorded. Finally, all cameras were set to record at least two minutes of video prior to ignition to increase the likelihood of capturing a good pre-ignition reference image. Video was then recorded for the entire experiment. Once it was deemed safe to re-enter the burn house after an experiment, a white piece of printer paper was held up in front of each camera and checkerboard and another short video clip recorded for use later in estimation of soot deposit on each camera and checkerboard. Cameras were also inspected for damage, and any damage or destruction noted in the experimental log for that test.

Having now covered the experimental method, it is possible to move on to the analysis methods used in this thesis.

3.2 Initial Smoke Layer Height Characterizations from Full-Scale Data

Five different methods were employed to estimate the smoke layer height in experiments A2, B2 and C2 which represented Type A, B, and C materials, respectively, as outlined in Section 3.1.1. Where possible, these methods were employed in the living room (fire compartment) and upstairs (far from fire compartment) in order to cover the full spectrum of possible scenarios observed in the experiments. First, an observer-based analysis method was used to estimate smoke development from video recordings using distinct height markers included in the images. Then, analytical methods were used to predict the smoke layer

height. Finally, three temperature-sensor based smoke layer height estimation methods that are the most common present-day methods, the specific value, N-percent rule and integral ratio methods, were used to estimate the smoke layer height in each of the experiments. Each of these methods is described in more detail in the subsequent sections.

3.2.1 Observer-Based Estimates

Observer-based analysis was conducted on images taken from video recordings captured by Cam1 (living room broad), Cam2 (living room sofa) and Cam4 (second floor SW room and stair landing) shown in Figure 3.4 a), b) and d), respectively. Following the path of smoke movement, the living room (fire compartment) was detailed first before the physically distant second floor. In all cases, the smoke layer height was estimated, by observers of the video recordings, to be equal to the height of smoke above the floor at a time when the bulk of the smoke layer visually reached objects of known height.

As noted in the earliest smoke layer height estimations, "differences between observers [are] inevitable in this kind of observation." [26] Thus, to minimize the subjectivity inherent in using a single visual observation, three independent observers estimated and recorded the time when the bulk of the smoke layer reached each marker to obtain a range of possible values. Unless otherwise noted, three observers were used for all observations in this work and the same three individuals always estimated times for smoke to reach specific marker from a given camera view. However, the three individuals were not the same across the analysis of all different markers and experiments. In total, six individuals made observations used in this work.

In the broad living room view of Cam1 video recordings, observers estimated when a distinct (but "thin") smoke layer was first visible at the ceiling (z=2.350 m) to indicate the earliest smoke layer presence in the experiment. Observers also estimated when the Cam1 view was fully obscured by smoke and this was taken to be the time that the smoke layer reached that camera height (z=0.410 m).

In the Cam2 view of the living room, the heights of the top and bottom of the window above and behind the sofa are known (z=1.885 m and 1.350 m, respectively) and were used as visual markers for analysis of all of the recordings. Observers estimated and recorded the time when the bulk of the smoke layer reached the top, and then the bottom of the window for each experiment. Observers also estimated when the Cam2 (z=0.600 m) view was fully obscured by smoke.

On the second floor, observers again estimated when a distinct (but "thin") smoke layer was first visible at the ceiling (z=2.600 m). The door soffit and handle (z=2.125 m and 1.120 m, respectively), and horizontal I-beam (z=1.050 m) were also used as known height markers from the Cam4 recordings. For these videos, observers estimated all of these times as well as the time that had elapsed until the camera view was fully obscured by smoke (z=0.300 m).

Finally, a more detailed smoke layer height analysis was conducted using Cam2 video recordings of experiments A2, B2 and C2. The smoke layer height was estimated by creating a 20 pixel by 20 pixel grid in Microsoft Paint [105] and overlaying that onto the Cam2 recordings of the three experiments using Filmora software [106]. An example image extracted from the recording with overlaid grid is shown in Figure 3.10. Two individuals watched each video recording together and agreed on the location of the smoke layer height at 10-second intervals through the recording. If the smoke layer was located between the top and bottom of the window, the number of pixels down from the top of the window was counted and recorded. The height of the smoke layer was later calculated using the known dimensions of the window.

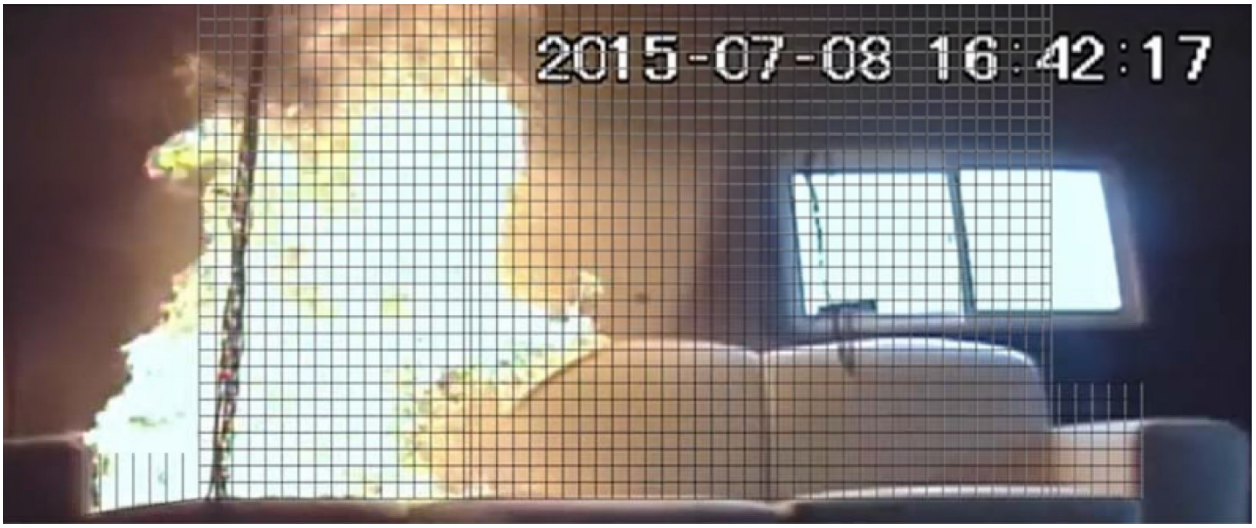

Figure 3.10: Cam2 image with grid overlay [94]

3.2.2 Analytical Methods

As a comparative measure to the observer-based analysis outlined above, two common smoke layer analytical methods (detailed in Section 2.4) were selected to estimate the smoke layer height in the fire compartment (living room) for experiments A2, B2 and C2. The empirically derived NFPA standard 92 [6] and theoretically derived Tanaka & Yamana [10] smoke layer height analyses were selected because variations exist for non-constant heat release rate fires. Forrest [90] showed that a simple t^2 heat release rate (HRR [kW]) fire growth curve could be used to represent the heat release rates of the A2, B2 and C2 experiments in the early stages of the fire (approximately the first 350, 400 and 700 s, respectively). t^2 HRR fire growth curves have the form shown in Equation 3.1 for SI units (1055 kW = 1000 BTU/s) when there was an incubation period. The fire growth curves based on the incubation time, t_0, and α as determined by Forrest for experiments A2, B2 and C2 [90] are shown in Figure 3.11. Also shown is the growth time, t_g, calculated using Equation 3.2 for when there was an incubation time. Wherever Type A, B and C results are plotted

together going forward they are represented by red, navy blue, and light grey (appearing medium, dark and light grey if in greyscale), respectively.

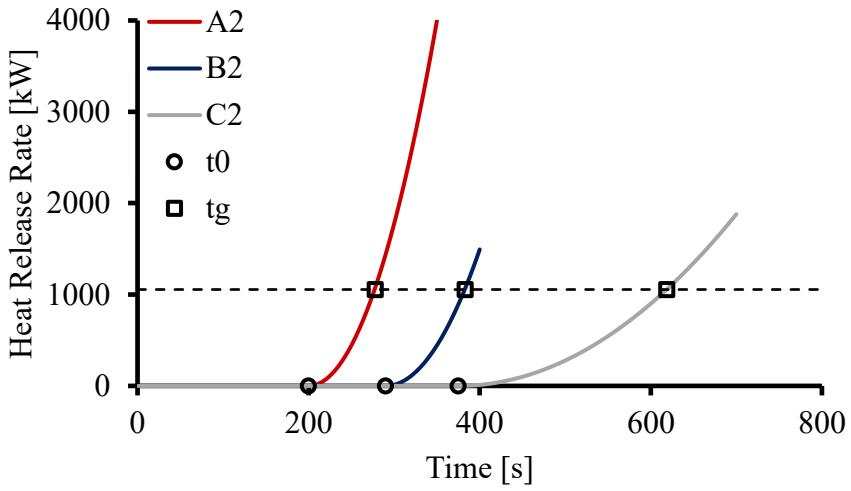

Figure 3.11: t^2 heat release rate curves for experiments A2, B2 and C2 with incubation time (t0) and time to 1055 [kW] (tg) indicated

$$HRR = \alpha(t - t_0)^2 = \frac{1055}{\left(t_g + t_0\right)^2}(t - t_0)^2 \quad 3.1$$

$$\alpha = \frac{1055}{\left(t_g + t_0\right)^2} \Rightarrow t_g = \sqrt{\frac{1055}{\alpha}} + t_0 \quad 3.2$$

The Tanaka & Yamana method for calculating smoke layer height, $Z_{T\&Y}$ [m], at time, t [s], of a t^2 fire is shown in Equation 2.4.

$$Z_{T\&Y} = \left(k \cdot \frac{\alpha^{1/3}}{A} \cdot \frac{2}{5}(t - t_0)^{5/3} + \frac{1}{h^{2/3}}\right)^{-3/2} + h_b \quad 3.3$$

This equation is slightly modified from the generic Equation 2.4. First, n=2 for a t^2 fire growth curve so that value has been substituted accordingly. An incubation time, t_0 [s], has been added to Equation 3.3 because the method application in Part 2 of the work makes it clear that an incubation time should be applied when applicable [29] (though it did not appear in the original Part 1 derivation [10]). Both α [kW/s^2] and t_0 [s] are taken to be the values determined by Forrest [90]. The calculation was intended to be used based on the height from the base of the fire to the ceiling so a correction, shown in Figure 3.12, was required when this was not the case. In these experiments, the fire base (*i.e.*, sofa cushion) was h_b = 0.543 m above the floor so this term was added after the prescribed smoke layer

height calculation with h being the distance between the base of the fire and the ceiling [10] (h = 1.807 m) in order to be comparable to other smoke layer height estimations. For simplicity, the constant, k, was selected assuming standard temperature and pressure in the ambient environment [17]. Given the dependence on the heat release rate curve, this calculation can only be applied to the fire compartment, hence the constant cross-sectional area, A = 13.8 m^2 [90], was that of the living room. Finally, this equation assumes no vents or openings (*i.e.*, doors or windows), therefore it was likely to give a conservative estimate of smoke layer height given that there were openings into the corridor and SW room on the main floor and the stairwell to the second floor in these experiments.

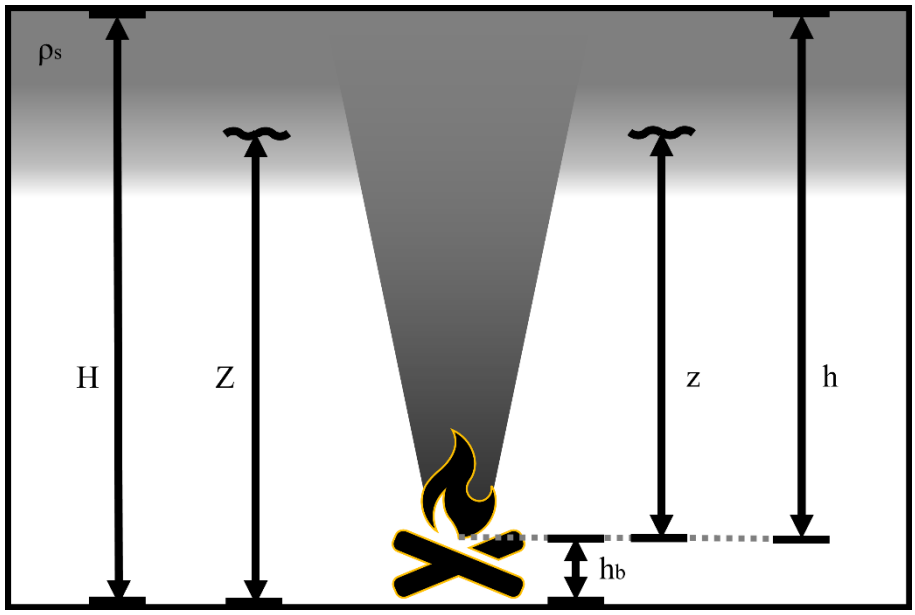

Figure 3.12: Smoke layer height calculation diagram with height of fire base (h_b) > 0 at time, t, whereby the smoke layer height, Z, from full ceiling height, H, was calculated after determining the smoke layer height above the fire base, z, using the ceiling height above the fire base, h

The NFPA 92 standard smoke layer height calculation, Z_{NFPA} [m], at time, t [s], for t^2 fires is shown in Equation 3.4.

$$Z_{NFPA} = 0.91h\left((t - t_0)(t_g - t_0)^{-2/5}h^{-4/5}(A/h^2)^{-3/5}\right)^{-1.45} + h_b \qquad 3.4$$

Modifications have again been made to the standard NFPA 92 calculation [6] to accommodate the height of the fire base (h_b) and incubation time (t_0), as described above. Similarly, the constant cross-sectional area, A, was of the living room as this calculation also only applies to the fire compartment. However, in this case the heat release rate curve was applied through the growth time, t_g, that was calculated using Equation 3.2 for each

experiment based on the t_0 and α determined by Forrest [90]. This empirical correlation was tested only on scenarios where $0.9 < A/h^2 < 14$ and $z > 0.2h$ [7]. The results of this calculation are also expected to be conservative because, not only does it assume no vents or openings as in the T&Y calculation, but it was originally developed based on "first indication of smoke" methods [6,40].

3.2.3 Specific Value Estimates

The smoke layer height as it varied with time was also estimated for comparison with observer-based analysis using the specific value direct method, detailed in Section 2.3.2, based on a specific threshold value of measured temperature. To align with smoke development estimated in the Dalmarnock full-scale sofa fire experiments [22], the progression of the smoke layer height with time was estimated to be located where the temperature reached 100 °C, though no explanation for that threshold value was provided in their research. This analysis was conducted using four thermocouple rakes, T2, T3, T4 and T7, with locations shown in Figure 3.3 and individual thermocouple heights listed in Table 3.5.

Table 3.5: Thermocouple heights on rakes T2, T3 and T4 (living room), and T7 (2nd floor SW room)

Living Room (Main Floor)			2nd Floor
Centre	Corridor Side	SW Corner	SW Room
T2	T3	T4	T7
2.28 m	2.28 m	2.28 m	2.30 m
2.06 m	2.06 m		2.02 m
1.87 m	1.87 m	1.75 m	1.83 m
1.65 m	1.65 m		1.65 m
1.43 m	1.43 m	1.24 m	
1.24 m	1.21 m		
1.03 m	0.99 m		
0.55 m	0.52 m		

As with the Dalmarnock experiments, the temperature data were linearly interpolated between measurement points so 100 °C could be located at any time when it fell between the top and bottom thermocouple [22]. If all thermocouples were below or above 100 °C, then the smoke layer was assumed to be out of range for the smoke layer height calculation. The Dalmarnock experiments used the 100 °C isotherm (horizonal plane) [22] so the living room smoke layer height, $Z_{100°C,LR}$ [m], was calculated by arithmetically averaging estimates of smoke layer height based the heights at which a 100 °C temperature was registered on thermocouples in each thermocouple rake within the room of interest. If all thermocouples on a given rake indicated temperatures that were out of range, that rake was not included. Thus,

if the T2, T3 and T4 thermocouple rakes all indicated measured temperature value that were in range, the living room smoke layer height, $Z_{100°C,LR}$, was calculated as shown in Equation 3.5 for a given point in time.

$$Z_{100°C,LR} = \frac{Z_{100°C,T2} + Z_{100°C,T3} + Z_{100°C,T4}}{3} \quad 3.5$$

To compare smoke layer height results with the observer-based method, the smoke layer height estimate for the second floor was based on temperatures in the SW room, where the only video camera on the second floor was located. The thermocouple rake in the second floor SW room was T7 so its value was used to determine the 100 °C isotherm for that room (*i.e.*, $Z_{100°C,2SW} = Z_{100°C,T7}$).

3.2.4 N-percent Rule Estimates

The N-percent rule [9], detailed in Section 2.3.3, was used to estimate the thermal interface height at thermocouple tree locations T2, T3 and T4 in the living room, and T7 in the second floor SW room (locations and heights shown in Figure 3.3 and Table 3.5, respectively). These values were then compared to the observer-based values (outlined in Section 3.2.1). Temperature was selected as the parameter of interest because it has been most common in practice, and the thermocouple rakes (*i.e.*, vertically stacked thermocouples that could measure a thermal profile) were well situated away from walls and doorways. The velocity probe rake at the stairway entrance in the living room (shown in Figure 3.3) was not used because it was located at an opening and measured velocity; both of those factors lend themselves to measuring the neutral plane across the opening rather than the smoke layer height of the room.

The method is described by Equation 3.6 as

$$T_{N\%}(z,t) = T(z_{top}, t=0) + \frac{N}{100}\{max[T(z_{top},t)] - T(z_{top}, t=0)\} \quad 3.6$$

over the course of each experiment, temperature data at time, t [s], and height, z [m] above the floor, were used to calculate a smoke layer height temperature, $T(z,t)$ [K]. This was the sum of the initial ambient temperature, $T(z_{top},t=0$ s), where z_{top} was the height of the top thermocouple in a rake at the position being analyzed, and N-percent of the difference between the maximum temperature value, max[$T(z_{top},t)$], measured up to the time of calculation, t, and the initial ambient temperature [9].

These values were then compared to the measured temperature, $T(z,t)$ [K], and the smoke layer height at that time was estimated to correspond with the lowest height from the floor, z, where this interface temperature, $T(z,t)$, occurred or was exceeded as shown in Figure 2.5. Linear interpolation between temperature measurements from different heights in the same thermocouple rake was used as suggested by the NFPA 92 standard [6]. The initial term in Equation 3.6, $T(z_{top},t=0$ s), deviates slightly from Equation 2.2 because, based on review of

the experimental results, it was determined that the ambient temperature at the top thermocouple was a reasonable representation of the ambient temperature at all heights in the compartment. The N-percent rule only applied when $\Delta T = N/100\left\{max\left[T\left(z_{top},t\right)\right] - T\left(z_{top},t=0\right)\right\} > 0.5$ K to account for instrument error [9].

The *N* values that have been used in N-percent analyses reported in the literature are detailed in Table 2.1. In the present research, various *N* values are tried to assess a range of approaches that have been used previously. Values of 10 and 20 were selected on the basis that this was the range used in the original work [9], this was the "first indication of smoke" as defined in NFPA 92 standard [6], and most research to date has used values in this range (see Table 2.1). At the other end of the spectrum, an *N* value of 90 corresponded to the top end of the NFPA 92 standard range of 80-90 for the "smoke layer interface" [6]. Finally, *N*=50 is included because it is the mid-point of the percentage range (0-100%) so provides insight between the two common extremes. Thus, *N* values of 10, 20, 50, and 90 are used in this portion of the analysis.

3.2.5 Integral Ratio Estimates

Smoke layer interface can also be estimated using the integral ratio method and the least-squares method detailed in Section 2.3.4 [13]. The more popular integral ratio method [20,21,49,86] was selected for use in this work for comparison with the observer-based analysis results. The integral ratio equations for the upper layer, r_u, and lower layer, r_l, are shown in Equations 3.7 and 3.8, respectively, which are solved using temperature (T) profiles for each possible height, h_r, and every time-step as shown in Figure 2.5. The smoke layer height, $Z_{int}(r_t)$, at a particular point in time, is the height that results in the lowest total ratio, r_t, as shown in Equation 3.9.

$$r_u = \frac{1}{(H-h_r)^2}\int_{h_r}^{H} T(z)dz \int_{h_r}^{H} \frac{1}{T(z)}dz \tag{3.7}$$

$$r_l = \frac{1}{{h_r}^2}\int_{0}^{h_r} T(z)dz \int_{0}^{h_r} \frac{1}{T(z)}dz \tag{3.8}$$

$$r_t(h_r) = min[r_u + r_l] \tag{3.9}$$

The integral ratios relate to the uniformity of the vertical temperature profile in a selected region or zone of a space, with a value closer to 1 representing more uniformity of that parameter in the zone of interest. To apply the method to analysis of smoke layer height, the compartment of interest was first divided into an upper and lower layer with the potential interface height, h_r [m], falling somewhere between the floor (z=0 [m]) and the ceiling (H=2.35 [m]). With these two zones, the sum of the integral ratios for the upper layer, r_u, and the lower layer, r_l, would reach a minimum (*i.e.*, closest to 2) when the upper and lower layer

could be divided into two regions, collectively with the most uniform distribution of the measurement parameter at a particular point in time. The height of the interface between these two regions was the smoke layer height (Z_{int}) for that time.

Temperature is selected as the parameter of interest in the integral ratio analysis for the same reasons as it is selected for the N-percent rule, as well as to present comparative analyses based on a consistent measured variable. Unlike with previous methods, which could use any units, absolute units of the chosen parameter are used for the integral ratio method and the value of that parameter did not change from positive to negative at any point [13]. Thus, when the parameter of interest is temperature, units of Kelvin [K] are used.

Following the approach of [13], values of measured temperature for a given thermocouple rake were linearly interpolated by assuming the thermal profiles of the form $T(z)=az+b$ to connect temperature measurement points. The function representing the continuous vertical profile of temperature is divided into linear segments such that there are ℓ intervals in the lower layer (h_r) and u intervals in the upper layer (H-h_r). If z_i and z_{i-1} are the height at the top and bottom of each segment in the upper layer (z_j and z_{j-1} in the lower layer), then Equations 3.7 and 3.8 can be expressed numerically as Equations 3.10 and 3.11 respectively. In this work, Equations 3.10 and 3.11 are solved at 20 mm vertical intervals within the compartment and their sums are used to determine the interface height per Equation 3.9.

$$r_u = \frac{1}{(H-h_r)^2}\sum_{i=1}^{i=u} T_{1,i}\sum_{i=1}^{i=u} T_{2,i} \; where \; T_{1,i} = \frac{a_i({z_i}^2 - {z_{i-1}}^2)}{2} + b_i(z_i - z_{i-1}) \qquad 3.10$$

$$and \; T_{2,i} = \begin{cases} \frac{1}{a_i}\ln\left\{\frac{|a_i z_i + b_i|}{|a_i z_{i-1} + b_i|}\right\} \; for \; a_i \neq 0 \\ \frac{z_i - z_{i-1}}{b_i} \; for \; a_i = 0 \end{cases}$$

$$r_l = \frac{1}{{h_r}^2}\sum_{j=1}^{j=l} T_{1,j}\sum_{j=1}^{j=l} T_{2,j} \; where \; T_{1,j} = \frac{a_j\left({z_j}^2 - {z_{j-1}}^2\right)}{2} + b_j\left(z_j - z_{j-1}\right) \qquad 3.11$$

$$and \; T_{2,j} = \begin{cases} \frac{1}{a_j}\ln\left\{\frac{|a_j z_j + b_j|}{|a_i z_{i-1} + b_i|}\right\} \; for \; a_j \neq 0 \\ \frac{z_j - z_{j-1}}{b_j} \; for \; a_j = 0 \end{cases}$$

3.3 Initial Smoke Density Characterizations

Relative smoke density was characterized using both small- and full-scale data. First, the smoke density chamber was used to estimate and rank smoke density for representative samples of the materials in Type A, B and C sofas. Then, the data from all nine Type A, B and C burn house experiments outlined in Section 3 were used to rank the smoke density for each experiment using a novel method detailed in Section 3.3.2. Smoke density determinations

based solely upon the objects of known height and at the same distance from the stationary cameras disappearing from the camera view implies that all sofas produced smoke with the same smoke density which is not true in these experiments. Thus, the extinction coefficient estimation method, detailed in Section 2.5.2, was not considered in this initial smoke density characterization.

3.3.1 Estimates from Small-Scale Data

Type A, B and C materials, both polyurethane foam and fabric, were saved from the associated experiments for the purposes of subsequent small-scale investigations of the smoke generation properties of the materials that fueled the fires. The smoke density chamber [62], located at the UW Live Fire Research Facility, was used to gain insight into the material behaviour under radiant heating conditions. As detailed in Section 2.5.1, the smoke density chamber is a popular small-scale test used for ranking the smoke production potential of different materials [3,54,55]. Smoke density tests were conducted on the different fuel materials using a Fire Testing Technology (FTT) Smoke Density Chamber with an enhanced photomultiplier control unit [62] and FTT SmokeBox version 3.7 software [107] to record the data and calculate the results.

The FTT unit can be operated in either the ISO 5659-2 standard mode [56,62] or the ASTM E662, NFPA 258 or BS 6401 standard modes [57,59,60,62]. The ISO 5659-2 method was used here because the sample is horizontally oriented which is necessary when testing materials like polyurethane foam which melt as they are heated [56,64]. Further, heat fluxes up to 50 kW/m^2 are specified as part of this standard [56]. This flexibility was important because prior cone calorimeter (another small-scale test) results showed that the foams did not ignite under exposure to heat flux levels of 25 kW/m^2 [90]. Piloted ignition was not used in the smoke density chamber because standard practice does not use pilot ignition for small-scale fire tests of upholstered furniture [108,109]. This is in line with observations of flame spread by radiation (*i.e.*, off-gassing and flames appearing in locations remote from the fire) during the experiments. Thus, 50 kW/m^2 incident radiant heat flux and no pilot ignitor was used for these tests.

A total of 29 tests were conducted in the smoke density chamber over three different series of tests as shown in Table 3.6. The first two series comprised of nine total tests each wherein three repeat tests on each of Type A, B and C materials were conducted. The first series of nine tests used polyurethane foam only and the second series of nine tests used the Type A, B and C polyurethane foam and fabric combinations from the associated full-scale experiments. The final test series with 11 polyurethane foam only tests was conducted because it was discovered that the range extension filter in the smoke density chamber was not functioning correctly during the first two series; so, additional tests were required to estimate the accuracy of the first 18 tests.

Table 3.6: Smoke density chamber tests conducted

Series	Material	Repeats		
		A	B	C
1	Foam	3	3	3
2	Foam/Fabric	3	3	3
3	Foam	4	4	3

The smoke density chamber measured transmission over a 10-minute (600 s) period which was converted into specific optical density, D_s, by the software [62,107]. The 'maximum specific optical density' was used to rank the smoke production propensity of each material combination [56]. Sample plots of these values are shown in Figure 3.13. The numerical maximum specific optical density results were compared to published values, shown in Table 2.2, and the rank was compared to the full-scale results obtained using the full-scale method described in the next section. Although the variability in results from the smoke density chamber is typically ±25% [3], the repeatability and reproducibility for flexible polyurethane foam has previously been reported as high as ±36% and ±70%, respectively, with the ISO 5659-2 standard [56]. Within this established range, the maximum repeatability by material type for the tests in Table 3.6 were ±9% (Type C), ±27% (Type C) and ±35% (Type B) in Series 1, 2 and 3, respectively.

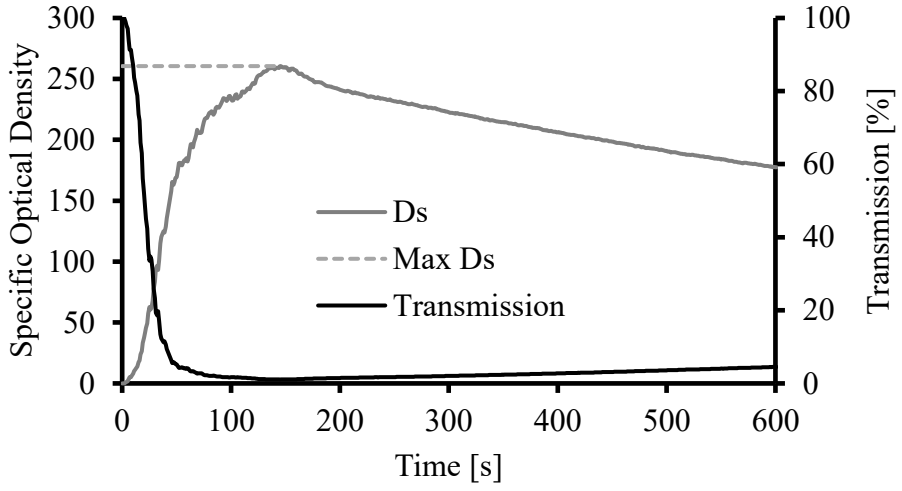

Figure 3.13: Sample transmission and maximum specific optical density from the smoke density chamber

3.3.2 Estimates from Full-Scale Data

Finally, a single, crude full-scale method of ranking smoke density was used to characterize the observed smoke density in the Type A, B, and C experiments with results compared to the small-scale characterization of smoke density detailed in the previous section. A

screenshot from Cam2 was taken from each of the nine Type A-C burn house experiments at a time when the smoke partially covered the window behind the sofa (*e.g.*, see Figure 3.14). Three observers then ranked the apparent visual density of the smoke from the fire in the screenshot for each of the nine Type A-C experiments using a scale of 1 (highest observed density) through 9 (lowest observed density). From three repeat fires for each material, this resulted in three observer ranks for each fire except Type A materials that were missing one observer rank for experiment A3 (*i.e.*, N=8 for Type A and N=9 for Types B & C). The arithmetic average was calculated from the individual rankings of smoke density for each material type which was in turn used to determine the average observed material smoke density rank (1-3) in each of the three fire types.

Figure 3.14: Sample Cam2 image with smoke mid-window from experiment A2

This smoke density estimation method with three observers and an average observed material smoke density rank was selected for several reasons. Three observers were used to minimize observer subjectivity (similar to Section 3.2.1). An average was used because the smoke density was expected to be approximately the same for the three fires fueled by each material type. Further use of an average value was consistent with reported repeatability in controlled small-scale experiments like the smoke density chamber (discussed in the previous section), because similar variability between experiments fueled by the same material combinations was expected.

Thus, a variety of analytical methods, and small-scale and full-scale estimates detailed in this section were used to characterize both the smoke layer height and smoke density of the Type A-C experiments. These characterizations were then used as baseline results for comparison with results obtained using the novel method developed in this research and described in more detail in the coming sections.

3.4 Theoretical Development of the Method for Fire Image Analysis

This section covers the theoretical development of the method used in this research for tracking and measuring the progression of smoke in a fire compartment. The theoretical

development of the present method largely follows the development of the contrast version of the Digital Optical Method (DOM) [70–77] but with specific application to interior fire experiments in mind. Section 2.7 outlines the basic premise of the contrast DOM and establishes the transferable aspects of the method, justifying pursuit of further development of this method for fire image analysis.

The general premise of the novel radiance method for smoke analysis developed in this thesis is depicted in Figure 3.15. The basic concept was quite simple: images captured in video recordings are used to measure the smoke density at various heights within the compartment, and the density profile was used to determine the smoke layer height as the experiment progresses.

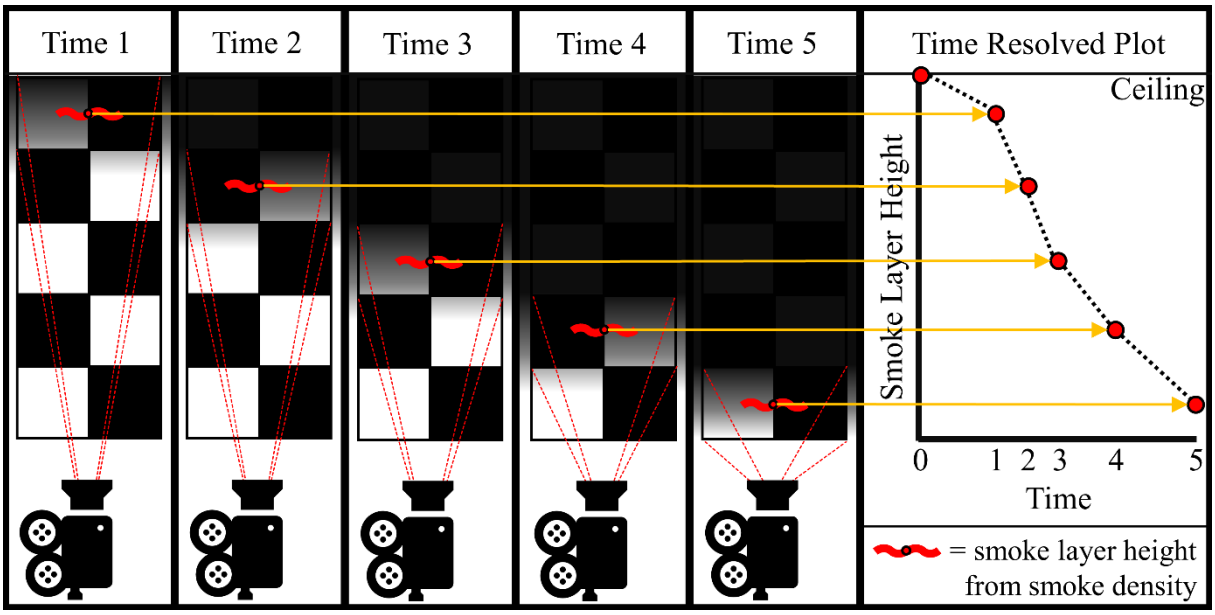

Figure 3.15: General premise of the novel radiance method for measuring smoke layer height from smoke density using video recordings

While the premise was simple, care was required in deriving the theory in such a way that meaningful results can be obtained from a compartment fire scenario. To begin, some high-level requisite knowledge of atmospheric radiation is provided so that the concepts presented later can be understood in context. The remainder of the section comprises details of the theoretical derivation of the analysis method used in this research. For this, the complex radiation interactions in a fire scenario are simplified, by making reasoned assumptions, to reach a tractable procedure by which to calculate optical smoke density from video images. The final optical smoke density calculations involve use of variables that are known and can be obtained (relatively) easily from measurements that can be made in a fire scenario. Pertinent assumptions embodied in each step of the derivation and how they relate to smoke analysis from fire video images are discussed in context below. Smoke layer height

determination is outlined in subsequent sections of this chapter once the optical smoke density calculations are theoretically derived.

The derivation relies on concepts from atmospheric radiation that are reiterated, briefly below, as a starting point for the analysis. Every object emits radiation, either within or outside the visible light spectrum, and all objects on earth reflect and absorb light to some extent depending on their temperature, electromagnetic wavelength (perceived as colour in the visible range) and texture [4,110]. Further, transparent and semi-transparent (translucent) objects can transmit light [111]. Regardless of the original source, radiance (the quantity of interest here) is the electromagnetic radiation measured as light in the visible spectrum that is perceived to originate from an object. As the radiation travels through the air, some portion is lost by absorption. Further, all forms of radiation - direct, diffuse, or reflected - are both lost and gained in varying, and not necessarily equal, amounts due to scattering. Thus, as shown in Figure 3.16, the incident radiance that reaches a surface (the lens of the camera in this case) at some distance from the original object (black checkerboard square in this case) is a combination of the radiance emitted by the original object and the radiance emitted by other sources (here, two windows and the fire) that scatters into the transmission path between the surface and original object.

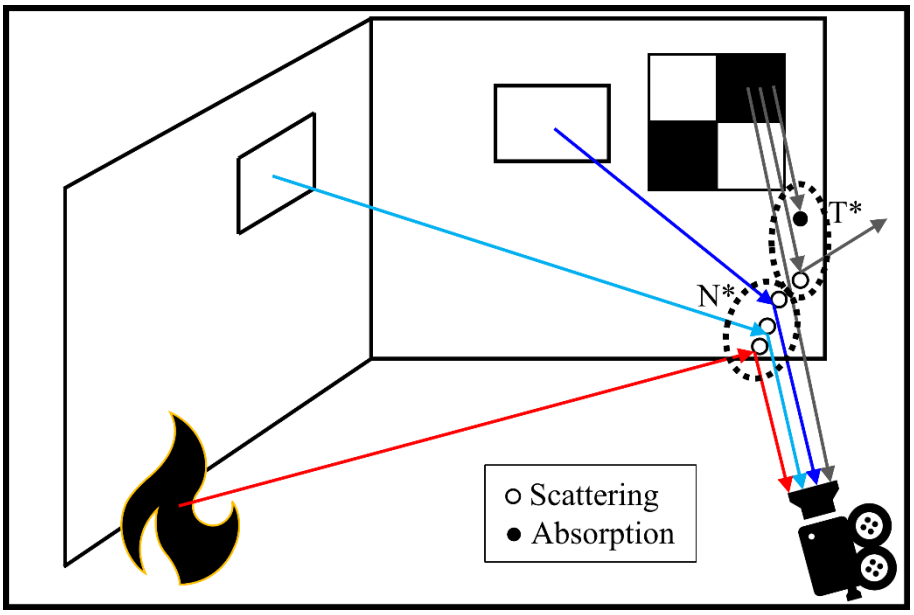

Figure 3.16: A simple example of the radiance incident on a video camera lens after transmission losses, T*, and path radiance, N*, along a path as result of scattering (○) and absorption (●)

Hence, for the proposed derivation, the radiance that reaches the video camera (the parameter measured in this method) is a combination of radiance from the background and radiance that scatters into the path of transmission as depicted in Figure 3.16. Some of this combined

radiance is lost to secondary processes, for instance, absorption or scattering during transmission between the background and camera. In this analysis, the radiance values are indirectly recorded in the form of image pixel values that can be converted using a unique algorithm for each camera [73,112] discussed in detail in Section 3.6.4. Since smoke-free images occur only before smoke is present in an experiment, and subsequently smoke continues to build up throughout the experiment, necessity requires extension of the DOM concept to allow determination of time-resolved optical smoke density results. A single common smoke-free image, the reference image, is used for the contrast reference. As the experiment progresses, contrast in subsequent images is compared back to the contrast in the reference image.

To define the variables used in the subsequent derivation, this process is schematically shown in Figure 3.17 (note radiation travels from right to left in the schematic) for a reference image that has no smoke present. Some of the radiance emitted by the contrasting (ideally black and white) background areas (to the right in the schematic), N_{B0} and N_{W0}, respectively, will travel the full path and reach the video camera (to the left in the schematic). Here, the full path of travel has been divided into three segments (X_1, X_2, and X_3) for future comparison when there is smoke present. As the light passes through each segment, there are transmission losses, denoted T_1*, T_2*, and T_3* for each respective path segment, due to absorption and scattering by the ambient air particles. There is also light scattered into each path segment, denoted N_1*, N_2*, and N_3*, respectively, each portion of which is also exposed to the same transmission losses as it travels along the path to the video camera. Collectively, the radiance that reaches the video camera is then the sum of the remaining radiance along the path from the contrasting black and white areas, designated as N_B and N_W, respectively in Figure 3.17. In order to measure the optical smoke density profile (and consequently determine smoke layer height) it is necessary to select contrast pairs, denoted with index j, at different vertical heights within the camera image. The calculations for the radiance reaching the video camera for the j^{th} pair of black and white areas, respectively, are shown in Equations 3.12 and 3.13.

When smoke is present, there are more transmission losses, T_S*, due to the presence of the smoke along the applicable path segment and possibly a change in the light scattered into the path, N_S*, as well. The schematic diagram, adapted to represent this condition, is shown in Figure 3.18. Further, since the analysis method is intended to analyze sequential images in which the smoke density is changing with time, an additional index, i, is required to represent each image used in the analysis. The calculations for the j^{th} pair of contrasting black and white areas in the i^{th} sequential image are shown in Equations 3.14 and 3.15, respectively.

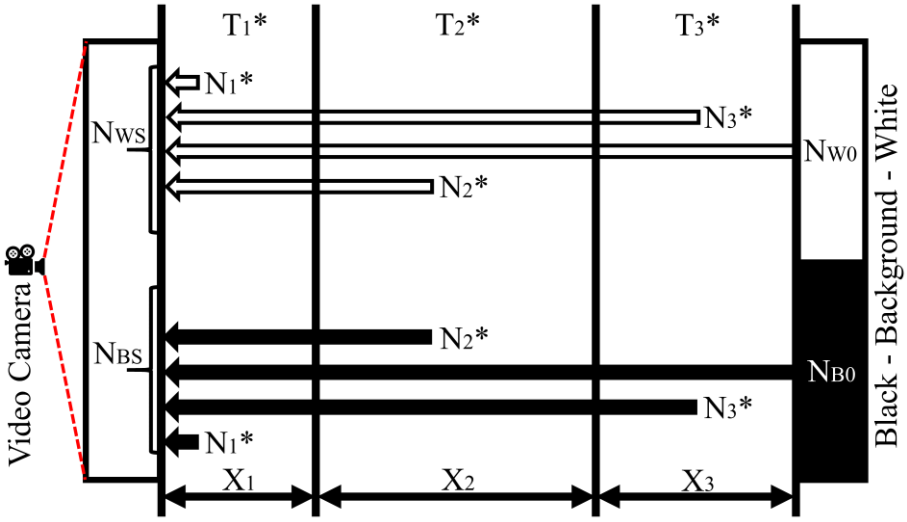

Figure 3.17: Schematic diagram without smoke present

$$N_{W,j} = \left[\left(N_{W0,j}T_3^* + N_3^*\right)T_2^* + N_2^*\right]T_1^* + N_1^* \quad 3.12$$

$$N_{B,j} = \left[\left(N_{B0,j}T_3^* + N_3^*\right)T_2^* + N_2^*\right]T_1^* + N_1^* \quad 3.13$$

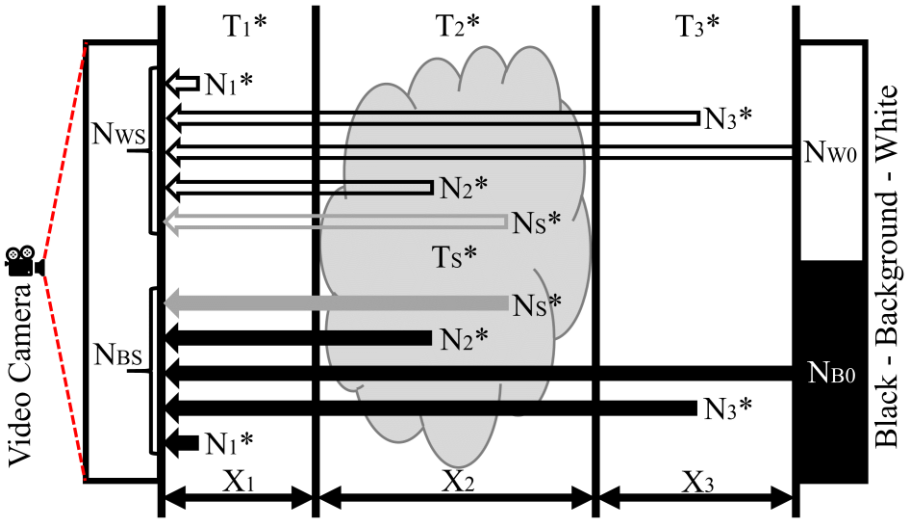

Figure 3.18: Schematic diagram with smoke present

$$N_{WS,ij} = \left[\left(N_{W0,j}T_3^* + N_3^*\right)T_{S,ij}^*T_2^* + N_S^* + N_2^*\right]T_1^* + N_1^* \quad 3.14$$

$$N_{BS,ij} = \left[\left(N_{B0,j}T_3^* + N_3^*\right)T_{S,ij}^*T_2^* + N_S^* + N_2^*\right]T_1^* + N_1^* \quad 3.15$$

Here, the transmission loss due to the presence of smoke (T_S*) is assumed to be constant in the second path segment (X_2). This is not strictly true because the smoke layer stratifies as discussed in the previous chapter. However, a significant portion of extant smoke layer height estimation methods explicitly assume that smoke density in the smoke layer is constant or implicitly assume the same by attempting to transform the measured profile into a bi-value function (see Section 2.3). Thus, in line with similar works in the fire safety field, the assumption of constant smoke density in the smoke layer is deemed acceptable for this method, at least during initial development, as well.

To apply Equations 3.14 and 3.15 directly would necessitate quantifying the amount of radiance scattering into the path (N*) over time during each fire scenario. This is both technically challenging and prohibitively expensive. On the other hand, comparison of the contrasting black and white radiance values allows a method to be developed that is independent of direct scattered radiance measurement. If the radiance values are normalized by means of dividing the radiance value by the full range of possible radiance values, the normalized radiance value for pure white becomes 1 and pure black 0. Then, subtracting the normalized radiance of the black area from the normalized radiance of the white area results in a positive value that falls in the range between 0 and 1. Subtracting these values to eliminate the radiance that has been scattered into the path during transmission inherently assumes that the path radiance and transmission losses are equal for both the black and white areas at a given point in time, which is not strictly true. However, if the black and white areas chosen from the video images and used in the analysis are located sufficiently close together, for full-scale fire scenarios at least, the differences may be considered negligible. Thus, the calculations for the differences in radiance reaching the video camera for the j^{th} pair of black and white areas are shown in Equations 3.16 and 3.17 for the reference and i^{th} subsequent image respectively.

$$N_{W,j} - N_{B,j} = \left(N_{W0,j} + N_{B0,j}\right)T_3^* T_2^* T_1^* \tag{3.16}$$

$$N_{WS,ij} - N_{BS,ij} = \left(N_{W0,j} + N_{B0,j}\right)T_3^* T_2^* T_1^* T_{S,ij}^* \tag{3.17}$$

If the reference image is carefully selected, the result from Equation 3.16 should provide the maximum radiance range possible for the j^{th} pair of black and white areas. This range roughly equates to the "clear beam" reading used in other smoke density estimation methods [56]. Thus, Equation 3.17 can be used to estimate the transmission as the fire experiment progresses, with Equation 3.16 acting as a scaling factor. These roles are evident if Equation 3.17 is re-arranged, equated with Equation 3.16, and then the combined equations are re-arranged to isolate the desired value of smoke transmission, T_S*, resulting in Equation 3.18.

$$N_{W,j} - N_{B,j} = \frac{\left(N_{WS,ij} - N_{BS,ij}\right)}{T_{S,ij}^*}$$

$$T^*_{S,ij} = \frac{\left(N_{WS,ij} - N_{BS,ij}\right)}{\left(N_{W,j} - N_{B,j}\right)} \quad 3.18$$

Two further assumptions have been made when equating Equations 3.16 and 3.17 to form Equation 3.18. First is the assumption that the radiance emitted by the background ($N_{W0,j}$ and $N_{B0,j}$) remains constant as the fire experiment progresses. This may not be true if soot deposits or burnt material impact the background as the experiment progresses, a consideration addressed later (in Section 3.6.6). The background radiance may also change as a result of longer-term effects due to variations in lighting as a compartment fills with smoke, an effect that is discussed here. For cameras placed in compartments away from the compartment of fire origin, the assumption of constant background radiance is unlikely to cause issue unless the amount of light reaching the background increases due to stray light sources in a structure or decreases due to transmission losses as the smoke builds. For cameras in the fire compartment, this assumption is valid if the fire remains approximately the same size for the duration of the analysis time period. On the other hand, this assumption is questionable if the fire size, and thus the corresponding light emitted from the fire itself, changes sufficiently over the course of the analysis time period. In these instances, increased uncertainty associated with such effects must be acknowledged, though the uncertainty can be reduced as much as possible by selecting reference areas farther from the fire and/or cross-correlating results from several different measurement locations.

Second, equating Equations 3.16 and 3.17 assumes that the transmission losses through the air remain constant as a fire experiment progresses. Once again, this assumption is not strictly true and the associated uncertainty will grow as the fire progresses due to temperature and concentration differences in the compartment gases and the potential that particulate matter may be drawn into regions below the descending smoke layer due to mixing and entrainment within the compartment. As the experiment progresses, the gas temperature in the smoke layer (and to a lesser extent the air below it) will increase, changing the transmission properties. Accounting for any of these changes might be possible in certain situations but would increase the method complexity. Since the primary goal of this thesis work is to determine if a radiance-based method can be utilized, simplifications such as this allow the method to be developed without added complexities. Thus, while worthy of assessment for each different case, the uncertainty from assuming constant transmission losses over time must be incurred during the method development presented in this thesis and quantified (if possible) as part of future work.

As the final step in the derivation of the general method developed for this phase of the research, values of radiance are converted into smoke density. Since the exact definition of smoke density varies throughout the fire safety field based on the method through which the value was obtained, smoke density here is considered to be “the percent of visible light attenuated by the smoke layer at a particular location” [84] at a given time. Using this

definition, smoke density can be represented by $1 - T_{S,ij}$*, or scaled and normalized radiance not including transmission losses through the smoke layer. Therefore, the equation used to calculate the smoke density in image i for contrast pair j, D_{ij}, is given in Equation 3.19.

$$D_{ij} = 1 - \frac{\left(N_{WS,ij} - N_{BS,ij}\right)}{\left(N_{W,j} - N_{B,j}\right)} \tag{3.19}$$

A vertical profile of smoke density can be created by applying Equation 3.19 to contrasting pairs of radiance values selected at different heights within a compartment. The smoke density profile can then be used to estimate the smoke layer height. When applied to a video recording or sequential images, both smoke density and smoke layer height can be calculated in a time resolved fashion as was depicted in Figure 3.15.

Once the general theoretical basis for the method had been developed, the method could be applied in practice. The initial iterations and refinements of the method application are detailed in Section 3.5. The final iteration of the applied radiance method is detailed in Section 3.6, followed by presentation of results in Chapter 4.

3.5 Method Development with Historical Data

Following the theoretical development in the previous section, the radiance method was applied to existing historical data from 11 experiments. The experimental apparatus and procedure were previously detailed in Section 3 and the instrumentation in Section 3.1.1. Several iterations of the method, detailed in this section, were developed using the historical data before the method was finally tuned for application to new experimental data in Section 3.6. The early iterations are detailed in the coming Section 3.5.1 and the penultimate application of the method is detailed in Section 3.5.2. The results of each iteration, presented in Chapter 4, guide the refinements made to the radiance method application process in subsequent iterations.

3.5.1 Early Method Iterations

In an initial attempt to apply the Digital Optical Method (DOM) method to analysis of existing video recordings to determine the time evolution of smoke density during fire experiments, the existing DOM software was requested. However, despite an initially positive response, proprietary limitations and patent considerations prevented sharing and modifying the existing software [77,113,114]. Therefore, a step-by-step method, similar to DOM, was developed and applied to existing video recordings from historical experiments C1, C2 and B1 which have been detailed in Table 3.1, and Sections 3 and 3.1.1.

Following the original DOM [70–77], seven important stages in the analysis were identified as outlined briefly in Table 3.7 and discussed further below.

Table 3.7: Seven important analysis stages used in early method iterations

Stage	Brief Description
A	Convert fire video into images.
B	Select a reference image from the beginning of the fire.
C	Select contrasting light and dark areas in the reference image.
D	Extract pixel values for each area on each image.
E	Convert pixel values to radiance values.
F	Calculate the smoke density for all pairs and images.
G	Plot smoke density values with time.

In the first stage, videos were converted into individual frames using the VLC Media Player to extract one image every second. The VLC Media Player is a user-friendly, free and open source media player that can play all common (and most uncommon) video file types and can run on all computer platforms [115].

In Stage B, a reference image was selected from the images created for each of the fire experiments. Two options were considered. First, the reference image could be selected prior to or at ignition, allowing the analysis to be completed for the entire experiment. This option was possible for Cam2 in Experiment C2 as shown in Figure 3.19.

Figure 3.19: Recorded Cam2 image at ignition (left) and just after door closes (right) in Experiment C2

However, the choice of reference image has to be carefully considered in some instances due to the assumptions made during the theoretical derivation of the method. The derivation dictated that the path and background radiance must be as consistent as possible for the duration of the analysis. In Cam1 in Experiment C2 shown in Figure 3.20, for example, examination of the video images indicates differing lighting conditions due to the presence of researchers and/or an open door at the beginning of the tests. This necessitated selecting a reference image from those taken after all personnel had left the burn structure and the door had been closed. When taken after ignition, the reference images for each experiment were necessarily selected before a smoke layer had begun to form at the ceiling so that the presence of smoke did not

skew the reference radiance values. For the same reason, all images that were recorded prior to the reference image were removed from the analysis.

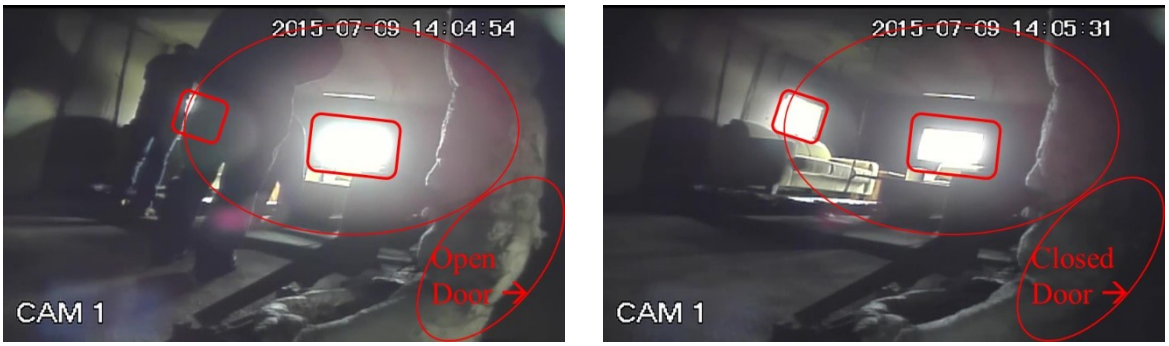

Figure 3.20: Recorded Cam1 image at ignition (left) and just after door closes (right) in Experiment C2

Contrasting light and dark areas were then chosen from the reference image in Stage C of the process. In cases with backlighting (*e.g.*, a window), an image from later in the experiment was also used to ensure that the selected light and dark areas remained light and dark and were not artificially altered by the presence of glare. To better assess the overall method at this preliminary stage, several light and dark areas of different sizes and locations were selected in the reference image. Results were compared to investigate the sensitivity of the final results across a choice of different contrast areas in a single reference image. Knowing that the smoke layer would stratify vertically in the compartment but that uniformity of obscuration was inherently assumed, the contrast areas for each reference pair were selected to be at approximately the same vertical height to obtain a more physically meaningful comparison. In addition, the areas selected had radiance levels that were as close to black and white as possible for maximum contrast while still keeping the areas as close together as possible in order to minimize path radiance uncertainty. Sets of selected areas are shown in Figure 3.21 with pairs of black and white contrast areas, same outline colour, matched in height and overlaid on the reference image (left), as well as on a subsequent image during analysis (right). Thus, the method was applied in the early stages by identifying, to some extent using a trial and error approach, areas in the images that had sufficient contrast for the analysis.

Different software was needed to proceed to Stage D and to extract pixel values from the selected light and dark areas in each image. For this, ImageJ (through FIJI [117]) was selected because it is a free and open source program that is relatively user friendly and can run on Windows, Mac OS X and Linux computers [117–119]. To facilitate assessment of the choice of pixel parameters on application of the analysis method to fire videos, the ImageJ batch measure feature was used to extract mean, median and mode pixel values as well as the standard deviation of pixel values from all of the selected light and dark areas in each image.

Figure 3.21: Preliminary method analysis area selection from the reference image (left) and during the experiment (right) [116]

Until this point, the data has been conveyed as pixel values that were generated by the recording camera for storage and transmission purposes. However, the actual colour, or "radiance", value was required for analysis necessitating conversion. Thus, in Stage E of application of the analysis method, the pixel values from the previous stage were converted into radiance values. This would typically be done by calibrating the video cameras prior to image analysis (pre-experiment in this application). However, analysis of the video recordings at a pixel-level had not been envisioned at the time these experiments were conducted. Hence, the video cameras were not calibrated, and no calibration curves were obtained from the manufacturer. Without actual calibration data available, an assumption was required to convert pixel values into the desired radiance (*i.e.*, actual colour) values. In the early iterations, as a starting point, the camera calibration curve was assumed to be a 1:1 ratio of radiance to pixel value (*i.e.*, $N = PV$). This was the approach used in the DOM fugitive plume scenario [74] which was deemed sufficiently similar to this fire analysis situation to merit use of a similar approach in the fire experiments.

Equation 3.19 was used to calculate the smoke density, D_{ij}, for each contrasting pair, j, of light (ideally white, W) and dark (ideally black, B) areas for all images, i, with and without smoke (S) in the field of view (Stage F). Results of this calculation were plotted over time (*i.e.*, for the sequential images) for each contrasting pair and fire test video analyzed (Stage G).

The iterative results from Experiments C1, C2 and finally B1, detailed in Section 4.3, were analyzed and used to refine the method. Following these three early iterations, the penultimate method was sufficiently well developed to provide confidence that results would be usable. The penultimate method was therefore applied to more than one indoor fire scenario to further test its applicability in different smoke measurement contexts.

3.5.2 Penultimate Method Iteration

This penultimate method is a modified and expanded version of the early method described above. It was developed based on the lessons learned during analysis of the results from the iterations undertaken during analysis of Experiments C1, C2 and B1 and was then applied to a wider range of fire tests to facilitate more in-depth analysis of smoke progression in various

situations. All 11 historical fire experiments detailed in Table 3.1 were analyzed using this method. The results and lessons learned from the application of this penultimate method to the historical fire experiments are incorporated into the final radiance method iteration, outlined in Section 3.6, that was applied to new fire experiments. There are nine main steps to application of the penultimate method as listed in Table 3.8.

Table 3.8: Nine main steps to the application of the penultimate method

Step	Brief Description
1	Parse the fire video into individual frames.
2	Select a frame of reference from the beginning of the fire.
3	Select contrasting light and dark areas in the reference image.
4	Extract mean pixel values for each area on each image, convert to radiance values, and plot with time.
5	Calculate the smoke density for all images and each contrast pair, and plot with time.
6	Determine when the smoke layer reaches the height of each contrast pair.
7	If density converges, determine maximum smoke density.
8	If available, compare results to other cameras in the same area.
9	Assess uncertainty.

As in the early iterations, VLC Media Player [115] or other similar software was used to convert the fire video into individual frames. Most video systems record images at 15 fps or 30 fps, which for a test that takes 10 or 15 minutes to complete, would result in a large number of images for the analysis if every frame was used. Although images may be individually small, the space required to store such large numbers of images can be very large. In the Type A, B and C experiments for example, with image resolution of only 480p, parsing every frame in a ten-minute video segment (from one camera in one experiment) created a gigabyte of images for analysis. Therefore, a main consideration in parsing the fire videos for analysis was the frequency at which frames should be output. Here the frame output frequency was chosen to be specific to the fire scenario and the resources available. A frequency analysis, considering image extraction rate and possible averaging schemes, was completed with intent to determine the ideal rate at which images should be parsed from the videos (and later averaged if necessary).

Preliminary examination of the output (raw) image data in the frequency analysis indicated that selection area radiances in the images fluctuated because of the flickering and growing nature of the fire; hence, various image averaging schemes were assessed using images from the indoor cameras (Cam1, Cam2, and Cam4) in experiments A1, B1 and C1. This set of videos was thought to represent an appropriate cross-section of images from all historical fire experiments since they were from very similar fire scenarios, save differences in fuel type and thus smoke production. In addition, all of the videos were recorded at the same speed,

three of five sofa materials were represented, and the three indoor camera angles were represented. For experiments A1, B1 and C1, a 300-second video segment was selected from a critical period in the fire experiment, in particular when the smoke layer was growing rapidly just before low lighting forces the camera to change to IR recording mode. The image extraction rate (frequency) and averaging scheme options shown in Table 3.9 were applied to four selected areas in each image: the full image, a large area encompassing the part of the image that was expected to contain the final contrast areas, a small light area, and a small dark area. The results from each of these areas and options, presented in Section 4.4, were compared to determine that the ideal image extraction rate and averaging scheme for these experiments was one frame every second with a 10 second rolling average (option f in Table 3.9). Thus, one image was extracted each second from each video for every experiment. The selected averaging scheme was noted and applied to the extracted data later (in Step 4).

Table 3.9: Averaging scheme options considered

Option	Image Freq. [Hz]	Averaging Scheme	Resulting Data [Hz]
A	30	None	30
B	1	None	1
C	10	None	0.1
D	30	1 second average	1
E	1	10 second average	0.1
F	1	10 second rolling average, centred	1

In Step 2 of the method, a reference image was selected from the beginning of the fire. Due to considerations identified during application of the early method iterations, the reference image was chosen based on the following criteria:

- The image must be from the time before the smoke layer forms at the ceiling so that the presence of smoke does not skew the reference radiance values, and optimally at, or prior to, ignition of the fire allowing analysis to be completed for the entire experiment.
- Lighting conditions in the relevant area(s) of the reference image must be the same as the remainder of the experiment (excluding the growing fire) so that the path and background radiance are as consistent as possible.

Once the reference image was determined, the light and dark areas that form the contrasting pairs were selected in Step 3 of the method. Again, based on the early iteration results, the following expanded guidelines were followed:

- Each contrasting pair was selected at the same height to be more physically meaningful in the stratified smoke environment.
- Each contrasting pair was selected with the same dimensions.

- Contrasting pairs were selected at known heights (or heights that could be deduced).
- Areas in each contrasting pair were as close, in colour, to black and white as possible to maximize contrast.
- Contrasting pairs were selected at positions as far away from the fire as possible to minimize the impact of radiance from the growing fire on the path radiance of interest.
- Light and dark areas in each contrasting pair were physically close together to minimize the impact of path radiance differences.
- Light areas were selected to include natural radiance from light coloured materials (not materials brightened by glare) to minimize the change in path radiance that was discovered to be important in the early method iterations.
- Dark areas were selected to include natural radiance from dark materials (not materials darkened by shadows) to minimize the change in path radiance that was discovered to be important in the early method iterations.
- Areas of the image with shadows or glare were avoided when possible to minimize the change in path radiance that was discovered to be important in the early method iterations.

In each video under analysis, several contrasting areas were selected in Cam1 images at known heights as shown in Figure 3.22. Light areas (outlined in black) were selected from the window, and dark areas (outlined in white) were selected at the same heights as the light areas but extended to the ceiling to determine whether useful information could be gleaned from the dark areas alone. The DOM analysis areas of ≥100 pixels [76] were used as a guideline in this penultimate method. This guideline was then examined in further detail in the final radiance method (see Section 3.6.3). Thus, for the Type A to C experiments, the window in Cam1 was split into three vertical areas of 10 pixels by 10 pixels (*i.e.*, 100 pixels) such that three heights (1.55 m, 1.40 m and 1.25 m) were selected for analysis. A single height aligned with the middle of the selected contrast areas was selected to represent the height at which to assign values from the range (10 pixels) of each contrast pair. The horizontal positions were selected on the right side of the window because it was further from the fire. The specific horizontal positions of these light and dark areas were selected because they were close together, as well as to maximize contrast while reducing the impact of glare and shadows.

Dividing the window into three vertical segments worked well for Type A-C experiments (see Section 4.4). Thus, in analysis of Type D and E experiments, the same Cam1 areas were selected but were expanded to a size of 25 pixels by 25 pixels (*i.e.*, 625 pixels total) because of the higher resolution of the recordings in Type D and E experiments.

Figure 3.22: Cam1 light (black outline) and dark (white outline) areas at a) 35 seconds (reference image) b) 240 seconds and c) 320 seconds [85]

With contrast areas selected, Step 4 of the method involved extracting mean weighted RGB colour values for each pixel in each selected light and dark area using the ImageJ software [117–119]. This was done for every image in the sequence from the reference image through to the last image in the desired range of analysis. The end of analysis was again set depending on the evolution of smoke in a particular test series. For these tests, the endpoint corresponded to the time at which the camera flipped to black and white recording due to low lighting conditions, but it could equally be taken when the image was completely obscured by smoke, when the experiment ended, or at any other time as appropriate to a particular situation. Once coded with the desired areas for data extraction, ImageJ [118] was able to rapidly extract the desired data for all selected areas and images for a given experiment within a few minutes (less than a minute in most cases).

The extracted mean pixel values were converted into normalized radiance values to be used in determination of the smoke optical density. First, each pixel value was divided by 255 to normalize it based on the scale of pure white having a pixel value of 255 and pure black a value of 0. Next, the camera calibration curve that converts pixel value (PV) to radiance value (N) was applied. Further investigation was conducted after the early iterations and a gamma = 2.2 decoding scheme was selected because conversion curves close to this are necessary for the NTSC video format [120] that these cameras use [121] such that the conversion from mean pixel value to radiance value was given by Equation 3.20.

$$N = \left(\frac{PV}{255}\right)^{2.2} \tag{3.20}$$

Once converted, the averaging scheme was applied to the values. As determined in Step 1, a 10 second rolling average centred on the fifth second was applied to the radiance values. Once the light area and dark area radiance values were determined for a particular video sequence, they were plotted with time to gain a better understanding of input values into the smoke density calculation (see Section 4.4.4).

In Step 5 of the penultimate method, the smoke density, D_{ij}, was calculated for all contrasting pairs in all images using Equation 3.19 in Section 3.4, recalling that $N_{W,j}$ and $N_{B,j}$ are light and dark area radiance values for pair j taken from the reference image, respectively.

Similarly, $N_{WS,ij}$ and $N_{BS,ij}$ were the light and dark area radiance values, respectively, for pair *j* from image *i* which were being analyzed to determine whether or not a smoke layer was present. The resulting smoke density values are plotted against time to see how the smoke progresses at each height from image to image based on a given video sequence from each fire test.

Step 6 involved analysis of the collected data in order to determine the smoke layer height. The smoke layer height determination was attempted using two methods. The first method determined the smoke layer height via the smoke density values per the original intent of the method. The second method was subsequently added as a possibility based on initial observations and results (see Section 4.4.2) which showed that the normalized radiance values of the selected light analysis areas (light area radiance values or LRVs) from Step 4 decreased (*i.e.*, got darker with more/"thicker" smoke present) around the time that the calculated smoke density increased. In both cases, the smoke layer height was estimated to be at the height of a contrasting pair when there was a large change in smoke density or light area radiance value at one point in time (or, most likely, across a narrow range of time) as shown in Figure 3.23.

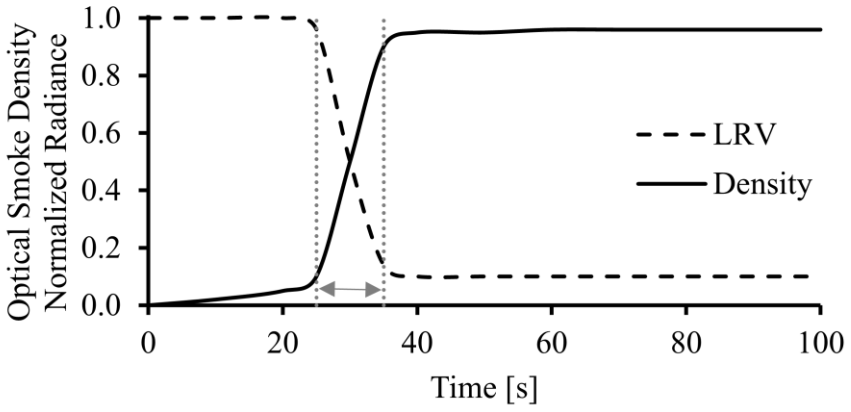

Figure 3.23: Conceptual plot showing how time varying optical smoke density (density) and light area radiance values (LRV) can indicate when (⁞↔⁞) the smoke layer reaches the height of a contrast pair

Analysis of the smoke density values to determine the smoke layer height, Z_{ij}, requires definition of a threshold value for D_{ij} that relates to the presence/non-presence of smoke at a given location in an image with time. To select the threshold value, first recall that 1) the height of each contrast pair was aligned with the vertical centre of the selected light and dark areas (or $\left(z_{top,j} - z_{bottom,j}\right)/2 = 0.5\Delta z + z_{bottom,j}$) and 2) the optical smoke density will fall between 0 (no smoke) and 1 (very dense smoke). As shown in Figure 3.24, if the smoke layer transition zone is very narrow, such that optical density is 1 at $z_{top,j}$ and 0 at $z_{bottom,j}$, the smoke layer height must occur within the selected area and the average optical density value

is likely to be around 0.5. If the transition zone is larger than one selected area, the same concept holds in that the smoke layer height will fall somewhere between no smoke and very dense smoke. Hence, a D_{ij} threshold value of 0.5 was initially selected because, on average, this corresponds to the stratified smoke layer reaching approximately the centre of the area for a specified height. In this research, when the smoke density D_{ij} for a given image pair *j* increases to a value of 0.5 at time *i*, the smoke is considered to have reached that height in the compartment being analyzed.

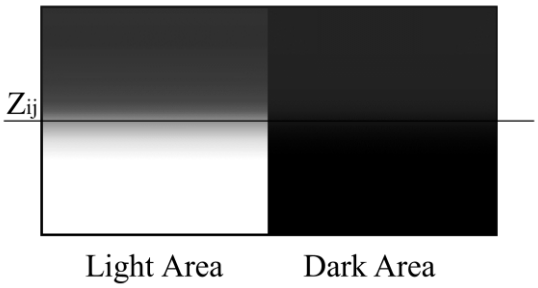

Figure 3.24: Diagram for selecting smoke layer height, Z_{ij}, threshold value

An alternative method to the use of the smoke density in determining the smoke layer height was also investigated. This method focused on determining the images in which decreases in the values of the light area radiance values were observed and using those to estimate the time at which the smoke layer passed through a particular height. This alternative method is premised on the anticipated relationship between a decrease in light area radiance values with increase in smoke density at a given height. Similar logic to that used for the smoke density determination above, and apparent in Figure 3.24, applies for selecting a threshold value because the mean (*i.e.*, arithmetic average) pixel value for each of the selected areas (light and dark separately) is calculated and normalized to a range of 0 to 1 with a mid-point of 0.5. However, as shown in Figure 3.23, the mean LRV will tend to get darker (*i.e.*, decrease in value) with smoke present. Thus, when the light area radiance, $N_{WS,ij}$, for pair *j* decreases to 0.5 in time *i* image, the smoke is considered to have reached that height in the compartment being analyzed. Results of both methods are presented and compared in Section 4.4.5.

During Step 7, the smoke density plots were examined to determine whether the magnitude of the smoke density had plateaued by the end of the analysis period. If so, the maximum smoke density had been reached and corresponded to that magnitude. If the same value was observed for (in increasing importance) multiple heights, multiple cameras, and/or multiple experiments with the same material, the confidence in the value greatly increased.

Step 8 is a repetition of Steps 1 through 7 for different video cameras which is a subset of the experiments assessed above. For this, images from the videos recorded by Cam2 in the Type A through C experiments, shown in Figure 3.25, were analyzed. The top of the window is not visible in the Cam2 recordings for the Type D and E experiments, so these were excluded

from the analysis. The window in the image from Cam2 was divided into three vertical areas similar to those used for Cam1 above, taking care to maintain the same 0.15 m spacing with some height overlap (1.70 m, 1.55 m and 1.40 m). This resulted in contrast areas of 20 pixels by 20 pixels. Once again, the horizontal positions were selected on the right side of the window at a distance from the fire and the areas chosen were close together while maximizing contrast and minimizing the impacts of shadow and glare. Analysis was completed for all images from the reference image through to the earlier of a) the video camera flipping to black and white or b) the fire blocking a contrast area.

Figure 3.25: Cam2 light (black outline) and dark (white outline) areas at a) 35 seconds (reference image) b) 240 seconds and c) 320 seconds [85]

As the final step, Step 9, uncertainties in the results from the Type A through E experiments were assessed. As part of this assessment, the smoke layer height and density results for these experiments, presented in Section 4.4.6, were compared to the smoke evolution characterizations detailed in Sections 3.2 and 3.3, respectively. Some of the uncertainties could be addressed with modification to the experimental instrumentation and procedures specific to the radiance method, hence, the results from the penultimate method guided additions and changes to the instrumentation discussed in Section 3.1.2. These instrumentation changes were made and new data was collected during the two Type F experiments, driving some additional modification of the radiance method, which are detailed in the next section.

3.6 Final Radiance Method

Unlike the previous method iterations, the final radiance method detailed in this section was applied to two Type F experiments in which some of the instrumentation was specifically designed to facilitate application and assessment the new radiance method developed during this research. The instrumentation, detailed in Section 3.1.2, allowed this final iteration of the method to address some of the uncertainties that could not be addressed using analysis of the existing video recordings alone. Recall that recordings of the historical fire experiments (Types A-E) were made with cameras Cam1-4 whereas the new fire experiments (Type F) were recorded with cameras V1-16. Additionally, in an effort to broaden the possible applications for the new method, the final radiance method was applied to both individual colour stream, and black and white images from the video recordings taken during the Type F experiments.

The final radiance method developed over the course of this research is largely similar to the penultimate method that was outlined in the previous section, with a few changes to refine the method and address identified uncertainties. There are ten steps to application of the final radiance method as listed in Table 3.10.

Table 3.10: Ten steps to the application of the radiance method

Step	Brief Description
1	Conduct an image frequency analysis and parse the fire video into individual frames.
2	Select a frame of reference from the beginning of the fire.
3	Determine minimum selection area and select contrasting light and dark areas in the reference image.
4	Extract mean pixel values for each area on each image, convert to radiance values, and plot with time.
5	Calculate the smoke density for all images and each contrast pair, and plot with time.
6	Determine possible impact of soot deposit on smoke density results.
7	Determine when the smoke layer reaches the height of each contrast pair.
8	If density converges, determine maximum smoke density.
9	If available, compare results to other cameras in the same area.
10	Assess uncertainty.

Since this final radiance method is a key and culminating contribution of the present research, each step is addressed in an associated sub-section below. Therefore, some sub-sections are essentially re-statement of the method as detailed in the previous developmental iterations. Of import, however, considerable investigation of the applicability of the final method was conducted during application of other steps. Therefore, as each step is presented, key aspects of the additional assessments and evaluations related to those steps are detailed as well. All results are contained in Section 4.5.

3.6.1 Step 1: Image Frequency Analysis and Image Extraction

As in the previous iterations, VLC Media Player [115] or other similar software was used to convert the fire video into individual frames. In Section 3.5.2, a frequency analysis was conducted with six options, outlined in Table 3.9, for the fire scenario and available resources. These options were applied to four selected areas in each image from a 300-second segment of Cam1, Cam2, and Cam4 recordings of experiments A1, B1 and C1. A separate frequency analysis was not conducted for the new Type F experiments because i) they are from very similar fire scenarios as those previously analyzed, ii) the videos were recorded at the same speed, iii) the contrast area arrangement worked for the previous five sofa materials, and iv) the new camera angles were believed to be sufficiently close to the three camera angles used in previous frequency analysis. Thus, in line with the previous

section, one image was extracted each second for each video and experiment. The selected averaging scheme, a 10 second rolling average, was noted and applied to the experimental data later (in Section 3.6.4).

3.6.2 Step 2: Selecting a Reference Image

For each video analyzed with the radiance method, a reference image was selected from the beginning of the fire following the two considerations previously determined to be important. As a result, the images were selected before the smoke layer formed at the ceiling so that the presence of smoke did not skew the reference radiance values, and optimally at, or prior to, ignition of the fire allowing analysis to be completed for the entire experiment. Second, lighting conditions in the relevant area(s) of the reference image were chosen to be the same as for the remainder of the experiment (excluding the growing fire) so that the path and background radiance are as consistent as possible.

3.6.3 Step 3: Select Contrasting Pairs

Selection of contrast pairs led to significant additional development and improvement of the final method over the penultimate method. This is because the penultimate method was developed using only colour images from the videos for each fire test, and thus required truncation of the analysis at the time when the camera switched from colour recording mode to black and white mode. This was a significant drawback since, for example, the existing Cam4 recordings could not be used for analysis because there were not any usable light areas in those images from which to create appropriate contrast pairs. More broadly, it was recognized that security cameras are widely used in fire experiments. In low lighting conditions (*e.g.*, at night or when the lights are off), many security cameras change to infrared (IR) recording [122] mode in which the light emitting diodes (LEDs) in the camera turn on and the camera captures infrared light intensity that is reflected back by the surroundings [122]. This infrared light is not within the visible light spectrum, hence images are recorded only in black and white [122].

Therefore, in order to extend the method to work with older video or to later times in the present videos when the security cameras switch to low-light recording mode, the method was extended to analysis of not only colour images, but also black and white images. This was done using images from the video recorded by V11 in the two Type F experiments, shown in Figure 3.26, with pixel analysis areas selected from the right checkerboard (CB11A). This analysis was not conducted in the penultimate method analysis of the living room camera recordings because there was no smoke-free IR reference image for the smoke density calculation. The analysis could not continue with the colour reference image once the camera changed to IR recording because, among other things, the assumption of constant transmission and scattering would not hold. Results are presented in Section 4.5.3.

Figure 3.26: Camera V11 image

As in Section 3.5.2, contrasting pairs were selected using the following guidelines:

- Each contrasting pair was selected at the same height to be more physically meaningful in the stratified smoke environment.
- Each contrasting pair was selected with the same dimensions.
- Contrasting pairs were selected at known heights (or heights that could be deduced).
- Areas in each contrasting pair were as close, in colour, to black and white as possible to maximize contrast.
- Contrasting pairs were selected at positions as far away from the fire as possible to minimize the impact of radiance from the growing fire on the path radiance of interest.
- Light and dark areas in each contrasting pair were physically close together to minimize the impact of path radiance differences.
- Light areas were selected to include natural radiance from light coloured materials (not materials brightened by glare) to minimize the change in path radiance.
- Dark areas were selected to include natural radiance from dark materials (not materials darkened by shadows) to minimize the change in path radiance.
- Areas of the image with shadows or glare were avoided when possible to minimize the change in path radiance.

In addition to assessing the method for use on black and white recordings, a major change in instrumentation was made over that used in the penultimate method. This is the addition of the checkerboards that were detailed in the Type F experimental instrumentation in Section 3.1.2 and are clearly evident in Figure 3.26. To determine the effectiveness of using checkerboards with the radiance method, the contrast from several 10 pixel by 10 pixel light and dark area pairs in cameras V1, V2, V4, V7 and V11 reference images from experiments F1 and F2 were compared as shown in Table 3.11. The 11 (of 12) camera views with visible checkerboards were provided previously in Figure 3.8. Of these, 5 were used in this part of

the analysis. V1 was used to compare the contrast of white paint versus light grey drywall backing (light area) with black paint (dark area). V1 and V4 were used to compare contrast for backlit light areas with existing dark areas, and existing light and dark background areas. V2 and V7 were used to compare the contrast of a new to a previously used and flipped checkerboard. V11 was used to compare the contrast of a new to a cleaned (wiped down) checkerboard, and the impact of checkerboard distance from the camera.

Table 3.11: Reference light and dark areas for various cameras (Cam.), experiments (Exp.), checkerboard conditions (Cond.) and background selection area sources

Cam.	Exp.	Checkerboard		Light	Dark
		#	Cond.	Source	Source
V1	F1	B1	New	White Paint	Black Paint
	F2	B1	New	Light Grey	Black Paint
	F1	N/A	N/A	Window	Drywall (New)
	F2	N/A	N/A	Window	Drywall (Used)
	F1	N/A	N/A	Drywall (New)	Drywall Mud
	F2	N/A	N/A	Drywall Mud	Drywall (Used)
V2	F1	B2	New	Light Grey	Black Paint
	F2	B2	Flipped	Light Grey	Black Paint
V4	F1	B4	New	Light Grey	Black Paint
	F2	B4	New	Light Grey	Black Paint
	F1	N/A	N/A	Window	Drywall (New)
	F2	N/A	N/A	Window	Drywall (Used)
V7	F1	B7	New	White Paint	Black Paint
	F2	B7	Flipped	White Paint	Black Paint
V11	F1	B11A (near)	New	White Paint	Black Paint
	F2	B11A (near)	Wiped	White Paint	Black Paint
	F1	B11B (far)	New	Light Grey	Black Paint
	F2	B11B (far)	Wiped	Light Grey	Black Paint

As expected (given that the checkerboards were installed for this purpose), the results presented in Section 4.5.3 indicated that the checkerboards provided higher contrast than available light and dark areas in the background but backlit windows also provided high contrast. Thus, contrast pairs for the final radiance method analysis were selected from a combination of the checkerboards and backlit windows. Results were also used to draw conclusions about how best to prepare and situate checkerboards in future experiments.

Finally, there was evidence that selection areas with fewer than 100 pixels might work in the analysis [76]. Therefore, as one step in optimization of the method for longer term use, it was of interest to determine the minimum size of area that could be selected for analysis while retaining accuracy in estimation of smoke layer height and smoke density. Since the

minimum area was expected to be related to image resolution, Cam1 recordings from experiments A1 and B1 with video resolution of 480p (720x480 pixels) and V1 recordings from experiments F1 and F2 with video resolution of 1080p (1920x1080 pixels) were utilized. These were chosen because the camera view was consistent across both experiments as indicated previously in Table 3.4. For the analysis, contrasting areas were selected from three heights: 1.55 m, 1.40 m and 1.25 m. With two exceptions, to be detailed momentarily, eight sizes and two shapes of contrast area were examined at each height: a 14x14 pixel square (196 pixels), a 10x14 pixel rectangle (140 pixels), a 10x10 pixel square (100 pixels), a 6x9 pixel rectangle (54 pixels), a 6x6 pixel square (36 pixels), a 4x4 pixel square (16 pixels), a 2x4 pixel rectangle (8 pixels), and a 2x2 pixel square (4 pixels). Even numbers were selected vertically (14, 10, 6, 4, 2 pixels) so that results could be calculated in a symmetric fashion around the selected heights. Areas were selected from both the backlit window and checkerboard in the experiment F1 and F2 recordings. Since no checkerboards were present, areas were selected from only the backlit window in the experiment A1 and B1 recordings. Unfortunately, the low resolution in the historical recordings meant that the window had fewer than the 42 vertical pixels (14 pixels x 3 pairs) necessary to conduct the analysis on the largest area. Accordingly, only one 14x14 pixel area was selected at the height of 1.40 m so, as mentioned above, there are no 14x14 pixel selection areas at 1.55 m or 1.25 m from experiments A1 or B1. Area selection from Cam1 and V1 are shown in Figure 3.27.

Figure 3.27: Minimum area size analysis areas for Cam1 (left) and V1 (right)

Figure 3.28: Final radiance method pixel analysis areas from a) V1, b) V2 and c) V7

The results of this analysis, presented in Section 4.5.3, found that the size and shape of contrast area were best set at dimensions of at least 6x6 pixels and not less than 30 mm x 30 mm. In order to have results with the highest vertical resolution possible, the remainder of steps three through ten were then completed using a 6x6 pixel square or a 7x7 pixel square (if

6x6 pixels is less than 30 mm x 30 mm) unless otherwise noted. Contrast pairs were selected from V1, V2, and V7 recordings of experiments F1 and F2 and are shown in Figure 3.28.

3.6.4 Step 4: Determine Radiance Values

Step 4 involves first extracting pixel values and converting them to radiance values. In this final radiance method, an effort was made to refine both the extraction and conversion parameters.

In early estimates of extracted pixel intensity values, the mean weighted RGB pixel values were used. During development of the Digital Optical Method [45–47], however, it had been found that use of individual colour values, red, green or blue, led to different results than use of the weighted RGB values. Thus, during refinement of this stage in the final radiance method, video images taken using Cam1 in experiment A1 and V1 in experiment F1 were processed multiple ways to investigate the impact of using a particular colour (RGB, red, green or blue) in the analysis. Since colour values were potentially thought also to relate to lighting conditions, video traces from these cameras were specifically selected because of the varied lighting conditions observed during the tests. 10x10 pixel contrasting areas were selected from each recording at heights of 1.55 m and 1.25 m at both the checkerboard and window (the latter only in experiment A1). ImageJ [55] was used to separate each image into its red, green, and blue components as shown in Figure 3.29.

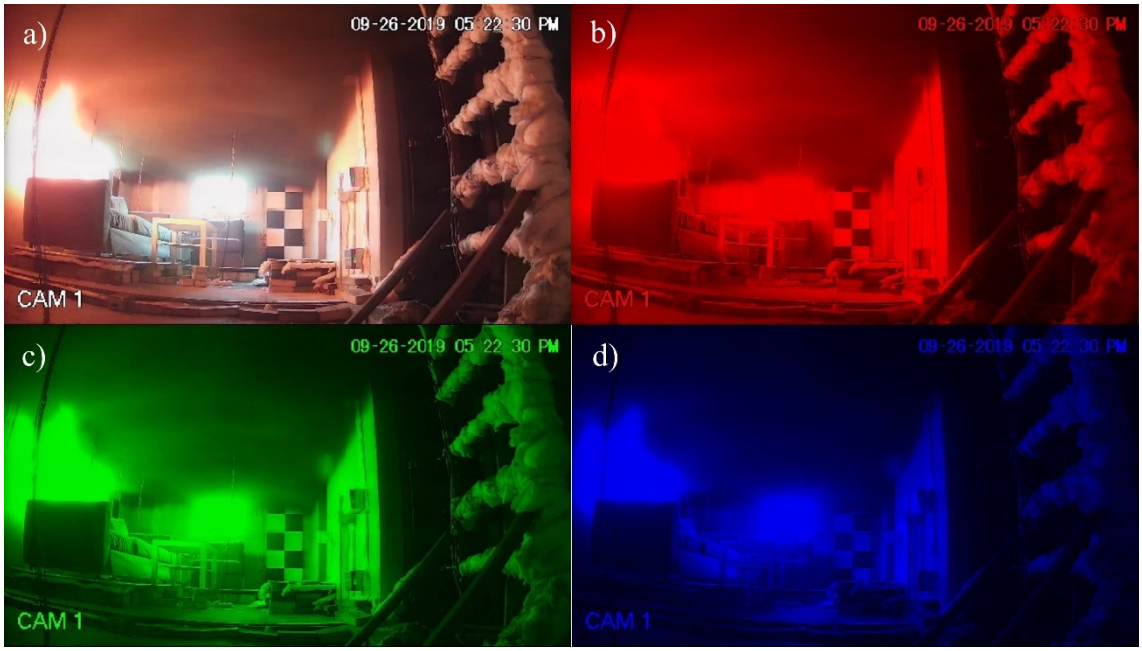

Figure 3.29: A sample V1 image in a) RGB, b) red, c) green and d) blue colour

Collectively, the light area radiance values (LRVs), dark area radiance values (DRVs), smoke layer height and smoke density results for the different colour streams, presented in

Section 4.5.4, indicated that the weighted RGB pixel values were preferred in these experiments; therefore, the remaining radiance method analysis was conducted accordingly.

The mean weighted RGB colour values for the contrast areas selected in Step 3 were extracted using the ImageJ software [117–119] for every colour image from the reference to the endpoint of the analysis sequence. The smoke evolution dictated the analysis endpoint and it corresponded to the time at which the camera flipped to black and white recording due to low lighting conditions, though it could have equally been taken when the image was completely obscured by smoke, when the experiment ended, or any other time as appropriate to a particular situation. Past the point that the camera flipped to black and white recording, the strategy discussed above for analysis of black and white images could have been adopted if a reasonable IR reference image had been available.

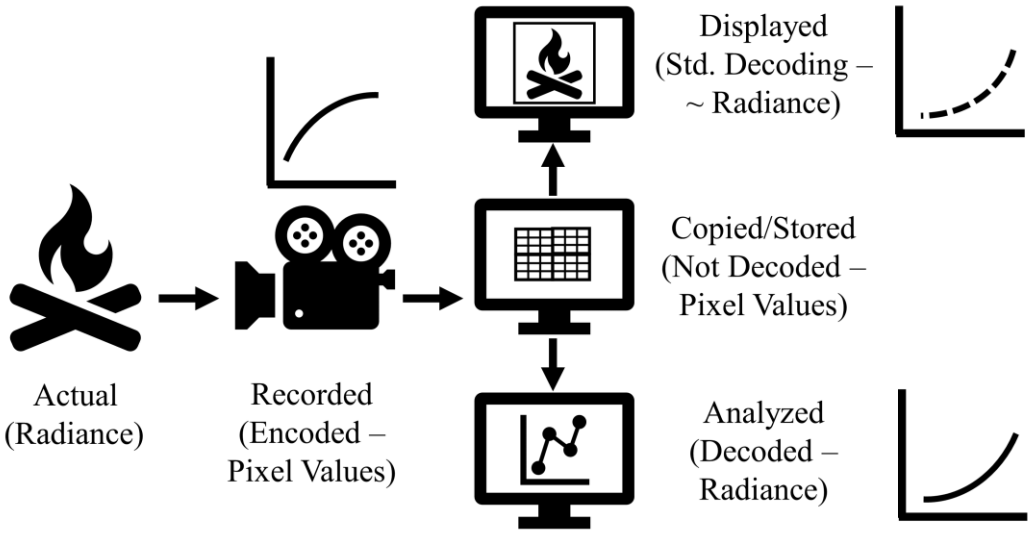

Figure 3.30: Diagram of camera encoding and decoding mechanisms

The extracted pixel values were then converted into radiance values using camera specific calibration curves. As shown in Figure 3.30, determining the camera calibration curve is a two-step process. It is necessary to 1) determine the encoding scheme used to convert radiance to pixel values and then 2) invert the function to determine the decoding scheme (camera calibration curve). There are three options for selecting a camera calibration curve (in decreasing order of accuracy): obtain the actual encoding scheme from the manufacturer, calibrate the camera after purchase to determine the encoding scheme, or assume an encoding scheme. In previous iterations, the camera decoding scheme was not known, the cameras were no longer available and, therefore, the decoding scheme was assumed. For development of the final method used in the Type F experiments, the curves could not be obtained from

the manufacturer. Therefore, the cameras were calibrated in order to develop an appropriate decoding scheme to be used in the analysis.

First, to determine the camera encoding scheme, a ColorChecker Video XL [123] was held up in front of each camera and checkerboard before each Type F experiment as shown in Figure 3.31. Each camera recorded a sequence of representative images that were then parsed using the VLC Media Player [115]. These images were then analyzed using ImageJ [118] to obtain the mean colour pixel value for each colour on the board. These measured pixel values were plotted relative to the listed manufacturer radiance values to determine the encoding scheme for the different cameras. This encoding scheme was then inverted to obtain the camera calibration curve (decoding scheme). The camera calibration curves were compared to establish the relative variations between various representative areas of each image, as well as between experiments and between cameras of the same model. Results are further discussed in Section 4.5.4.

Figure 3.31: Camera calibration board in front of a) camera and b) checkerboard

Next, four different calibration curves were selected and used in development of the final radiance method. Two curves were chosen based on the previous iterations ($N = PV$ and $N = (PV/255)^{2.2}$) and two were based on the lines of best fit from the ColorChecker results. All four calibration curves were applied to the pixel value results of V1 from experiment F1, and the LRV, DRV, smoke layer height and smoke density results were compared to determine the impact of different calibration curves on the final analysis. The results, presented in Section 4.5.4, indicate that the cameras used in the Type F experiments are best represented by an $N = PV$ calibration curve. However, since the eleven historical Type A-E experiments were analyzed using an $N = (PV/255)^{2.2}$ calibration curve [23,24,84,85] and the selected curve was found to impact the results (see Section 4.5.4), it was decided that the latter curve would be used going forward in this thesis so the Type F smoke evolution results could be compared to the Type A-E smoke evolution results.

Hence, as in the penultimate method, the extracted mean pixel values were converted into normalized radiance values ($N = (PV/255)^{2.2}$) to be used in determination of the smoke optical density. The averaging scheme from Step 1, a 10-second rolling average centered on

the fifth second was then applied to the radiance values. Once the LRVs and DRVs were determined for a particular video sequence, they were plotted with time to gain a better understanding of input values into the smoke density calculation outlined in the next step.

3.6.5 Step 5: Calculate Smoke Density

There was no change to Step 5 from the penultimate method. The smoke density, D_{ij}, is calculated for all contrasting pairs in all images using Equation 3.19 (repeated below for easy reference), recalling that $N_{W,j}$ and $N_{B,j}$ are light and dark area radiance values for pair j taken from the reference image, respectively. Similarly, $N_{WS,ij}$ and $N_{BS,ij}$ are the light and dark area radiance values, respectively, for pair j from image i which is being analyzed to determine whether or not a smoke layer is present. The resulting smoke density values are plotted against time to see how the smoke progresses at each height from image to image based on a given video sequence from each fire test.

$$D_{ij} = 1 - \frac{\left(N_{WS,ij} - N_{BS,ij}\right)}{\left(N_{W,j} - N_{B,j}\right)} \tag{3.19}$$

3.6.6 Step 6: Estimate Soot Deposit Impact

One of the assumptions made in the theoretical derivation, presented in Section 3.4, was that the radiance emitted by the background ($N_{W0,j}$ and $N_{B0,j}$) remains constant as the fire experiment progresses. However, this may not be true if soot deposits or burnt material impact the background as the experiment progresses. To address this concern, Step 6 involved determining the possible impact on smoke density results of soot deposition on the background surfaces in the Type F experiments.

Two different attempts to quantify the soot that was deposited on the drywall checkerboards were included in the Type F experiments. Both attempts involved short video recordings made with and without a white piece of paper, held in front of each camera and checkerboard, after the end of each experiment once the smoke had cleared. Images with and without the paper were extracted for each location using VLC Media Player [115].

First, the post-experiment images with the white paper, shown in Figure 3.32, were analyzed using ImageJ [117–119] to determine the mean pixel values (varied selection area size) of the white paper. These pixel values were then compared to the “Grey 2” ColorChecker squares (from the pre-experiment calibration images) to estimate how much the “white” had changed since the beginning of the experiment. “Grey 2” was selected because it was visually closest to the colour of the white paper as judged by an observer. Similar to the “clear beam” value and correction in the smoke density chamber test [56], the pre- and post-experiment white value difference was then related back to how much soot had been deposited on the checkerboards over the course of the experiment.

Figure 3.32: Figure one with white sheet held in front of a) camera V1 and b) checkerboard CB1

Second, the post-experiment images without the white paper were analyzed with ImageJ [117–119] to determine the mean pixel values in the white and black checkerboard squares. These pixel values were then compared to the reference image values to estimate how much the white, black, and contrast had changed since the beginning of the experiment. These value changes were then related back to the overall soot deposit in the experiment. Results for both analysis methods are presented in Section 4.5.6.

3.6.7 Step 7: Determine Smoke Layer Height

The two methods of data analysis used to determine the smoke layer height in the penultimate method were also used the final radiance method. The smoke layer height determination was attempted using both calculated smoke density and raw LRVs. In both cases, the smoke layer height was estimated to be at the height of a contrasting pair when there is a large change in smoke density or light area radiance value at one point in time (or, more likely, over a narrow range of time). The previous logic proved sound and effective so, as in the penultimate method, when the smoke density D_{ij} for a given image pair j increases to a value of 0.5 at time i, the smoke is considered to have reached that height in the compartment being analyzed. Conversely, when the light area radiance, $N_{WS,ij}$, for pair j decreases to 0.5 in time i image, the smoke is considered to have reached that height in the compartment being analyzed. Results of both methods are presented and compared in Section 4.5.7.

3.6.8 Step 8: Determine Maximum Smoke Density

There were no changes made to this portion of the process from the penultimate method. Thus, in Step 8 of the radiance method, the smoke density plots were examined to determine whether the magnitude of the smoke density had plateaued by the end of the analysis period. If so, the maximum smoke density had been reached and corresponded to that magnitude. If the same value was observed for (in increasing importance) multiple heights, multiple

cameras, and/or multiple experiments with the same material, the confidence in the value greatly increased.

3.6.9 Step 9: Compare to Other Results

As in the penultimate method, all of the previous steps (1 through 8) were repeated for different video cameras that captured the smoke evolution in the same space. The final radiance method was applied to the two cameras with a broad living room view, V1 and V2, as well as camera V7 that recorded in black and white and captured the corridor side of the living room. The selection areas for these camera views were shown in Figure 3.28. This process was completed for experiments F1 and F2 in order to compare results of repeat experiments. The results are presented in Sections 4.5.4 through 4.5.9.

3.6.10 Step 10: Assess Uncertainty

The final step of the radiance method is to assess the uncertainty of the results that are presented in Section 4.5.10. As with all experimental (and some theoretical) methods, uncertainty has many causes. Some of the uncertainties inherent in fire experiments and smoke evolution specifically were detailed in Chapter 2. Differences, and thus uncertainty, exist between various smoke layer height and density estimation methods including those discussed in Sections 3.2 and 3.3, respectively. Several inherent sources of uncertainty were discussed in the theoretical radiance method development of Section 3.4. Some of the uncertainties for the experiments detailed in Section 3 were addressed with the revised instrumentation in Section 3.1.2 and subsequent analysis conducted in Sections 3.5 and 3.6.

Key results and discussions from each of the stages are outlined in order in Chapter 4. The chapter culminates with results from each stage of application and evaluation of the final radiance method as well as any associated impact on uncertainty of those results. Finally, Chapter 5 draws conclusions and makes recommendations for future refinement of the methods used, experimental design, and application of the final radiance method in analysis of fire experiment recordings.

Chapter 4

Results and Discussion

The methods detailed in the previous chapter were applied to the burn house sofa fire experiments laid out in Section 3.1 to generate smoke layer height and density results. These results are presented and discussed in this Chapter, largely following the same sequence as used to present the steps in the methods outlined in Chapter 3. Section 4.1 details results of smoke layer height characterization during Type A-C sofa material experiments based on analysis of video recordings by multiple observers. These results are coupled with smoke layer height analyses based on existing heat release rate approximations and thermocouple temperature measurements via specific value, N-percent rule and integral ratio estimation methods. The smoke layer height estimates from these full-scale experimental data are used to set a baseline for comparison of various results obtained using the radiance method. In Section 4.2, complementary results for smoke density in the experiments are determined using a combination of small- and full-scale results. These results, from the smoke density chamber and video recordings of the burn house experiments, set the baseline for a comparison of smoke density values determined using the radiance method as well.

Next, results obtained during various iterations of development of the radiance method are presented. For this, video recordings are analyzed according to the methods outlined in Chapter 3 to estimate the smoke layer height and density. Specifically, Section 4.3 details the results and lessons learned during application of three early iterations of the radiance method to three of the historical burn house experiments (C1, C2 and B1). These lessons drove modifications to the original radiance method, resulting in the penultimate method which was then applied to data from the 11 historical burn house experiments (Types A-E). The penultimate radiance method results are detailed and compared to the baseline characterizations in Section 4.4. Finally, instrumentation specific to the radiance method was installed for two new (Type F) burn house experiments. This allowed further refinement of the method; the results of this final iteration of the radiance method are presented and discussed in Section 4.5. This culminating section of the chapter details the most refined results presented in this work. Conclusions and recommendations drawn from the discussion of these results are presented in the final chapter of the thesis.

4.1 Smoke Layer Height Characterization

The new radiance method for estimating smoke layer height and density forms the key contribution from this research. Therefore, as it was being developed and refined, results from the newly evolving method(s) had to be compared to results from existing and more accepted methods. In this section and the next, reference values of smoke layer height and then smoke density are reported. These values were obtained from a series of video recordings, heat release rate and thermocouple measurements taken during the Type A-C burn house experiments using the seven methods outlined in Sections 3.1 and 3.2. Through comparison of results across methods, baseline estimates are established against which to benchmark results of the new radiance method later in the chapter.

Seven existing methods were used to estimate the smoke layer height in the burn house. Section 4.1.1 presents the results from two observer-based methods using video recordings to estimate the smoke layer height. The t^2 heat release rate curves for the same representative experiments were then used to calculate the smoke layer height in the living room via two common fire compartment smoke fill analytical methods, the NFPA and T&Y methods, with results presented in Section 4.1.2. Finally, in each of the three representative experiments, results were obtained for the sensor-based methods using data from four thermocouple rakes to estimate the smoke layer height using the specific value (Section 4.1.3), N-percent rule (Section 4.1.4) and integral ratio (Section 4.1.5) methods. Collectively, the most accurate and robust existing method for smoke layer height estimation in these experiments was selected to characterize the smoke layer height development as a baseline to compare to results determined using the new radiance method.

4.1.1 Observer-Based Estimates

As the first stage in development of reference values, video recordings were analyzed via two observer-based methods for estimation of smoke layer height. For this, the evolution of smoke layer height with time during fires fueled by each of the Type A-C materials was assessed by three of five independent observers (O1-5) based on their observations of the time required for 1) a thin smoke layer to first form at the ceiling (Cam1, z=2.35 m), 2) the bulk of the smoke layer to reach the top and bottom of the window (Cam2, z=1.89 m and z=1.35 m), and 3) the smoke to obscure the view in Cam1 and Cam2 (z=0.41 m and z=0.60 m, respectively). The observers noted the camera time at the top right of the recordings for each event and these were subsequently converted to seconds after ignition by subtracting the ignition time for each experiment from the noted event time. Then, at 10-second intervals, two observers (O1 and O6) estimated the smoke layer height over the window visible in Cam2 recordings.

Results of the first analysis are summarized in Table 4.1. In the Table, * indicates that no usable entry exists and ‘U’ indicates that the event timeline was reported as unclear. In all instances, two independent usable data points are available. The average and range

(maximum time – minimum time) of the two or three recorded times are noted in the right-hand columns of Table 4.1 for reference as well.

Generally good agreement can be seen across observers in terms of their estimates of the time taken for the smoke layer to reach each of the five heights in the living room for experiment A2. The best agreement is for the time it takes for the layer to descend to 0.41 m above the floor (the point when Cam1 is obscured by smoke) with only 3 seconds difference between the three observer estimates. Conversely, the time when Cam2 is obscured has the least agreement for the Type A material with 15 seconds between the first and last recorded observation. In all cases though, the generally low variation in values across observers (≤15 s in a 15-30 minute experiment) indicates that the observers' interpretations of the presence of smoke were consistent and that the smoke layer in the Type A couch experiments was likely quite distinct with very little mixing zone between the upper and lower layer in the fire compartment.

Table 4.1: Observer-based living room smoke layer height estimation for experiments A2, B2 and C2 where three observers (O) estimate when (time in seconds after crib ignition) the smoke layer reaches five objects of known height in the living room except where the time is not available (*), unclear (U), or not attempted (—).

Exp.	Z [m]	Cam.	Observed Time [s]					Avg. Time [s]	Max.-Min. Range [s]
			O1	O2	O3	O4	O5		
A2	2.35	Cam1	143	—	—	*	148	145.5	5
	1.89	Cam2	287	284	283	—	—	284.7	4
	1.35	Cam2	*	296	301	—	—	298.5	5
	0.60	Cam2	374	—	—	389	374	379.0	15
	0.41	Cam1	361	—	—	362	359	360.7	3
B2	2.35	Cam1	69	—	—	*	73	71.0	4
	1.89	Cam2	285	237	178	—	—	233.3	107
	1.35	Cam2	*	299	269	—	—	284.0	30
	0.60	Cam2	477	—	—	474	475	475.3	3
	0.41	Cam1	453	—	—	452	453	452.7	2
C2	2.35	Cam1	269	—	—	*	317	293.0	48
	1.89	Cam2	586	587	605	—	—	592.7	19
	1.35	Cam2	*	632	631	—	—	631.5	1
	0.60	Cam2	U	—	—	1152	1179	1165.5	27
	0.41	Cam1	1232	—	—	1388	942	1187.3	446

From the Table as well, the observer-based estimates of smoke layer height during the Type A experiment show the expected descent of the smoke layer into the compartment over time. The average time taken to reach each height further indicates that the smoke layer height descended rapidly, with approximately 215 seconds between the first formation of smoke at

the ceiling and full obscuration of cameras. An exception to the pattern of smoke layer descent appears to be the time taken for the layer to descend to 0.6 m above the floor and obscure Cam2.This makes sense, however, when it is considered that Cam2 actually looks directly at the fire, which illuminates the view for a longer period of time and thereby lengthens the time it takes for that view to be obscured as shown in Figure 4.1.

Figure 4.1: Cam2 Image 360 s after crib ignition in experiment A2 (time of Cam1 obscuration)

As with the results in Table 4.1 for experiment A2, results of the observer-based smoke layer heights with time in experiment B2 show the anticipated descent of smoke layer, again except in the case of obscuration of Cam2. There are distinct differences in the results for experiments A2 and B2 in terms of the range of observed times reported by different observers. While the observers agree on the time at which the smoke layer was first visible and the times taken for the camera views to be obscured, a much wider range of values was reported for when the bulk of the smoke layer reached the top and bottom of the window. Given the relative consistency of their observations from experiment A2, this may indicate that the descending interface demarking the “bulk” of the smoke layer from the cleaner air below was more difficult to distinguish in experiment B2. One possible cause might be that the mixing zone was larger than in experiment A2. Based on the average observed times reported in Table 4.1, the smoke layer in experiment B2 most likely formed before that in experiment A2 but then took approximately 380 seconds to descend though the fire compartment to the height of the cameras.

The experiment C2 results in Table 4.1 show the expected descending smoke layer height but, unlike results for experiments A2 and B2, the time taken for Cam2 obscuration is not out of order. As can be seen in Figure 4.2, the smoke is dense, and the fire is simultaneously decreasing in size such that extraneous light from the fire does not delay obscuration of the Cam2 view in experiment C2. When looking at the observed time for each indicator, the ranges of value in this experiment is the reverse of that seen in experiment B2, with the values of time estimated for the bulk of the smoke layer to reach the window having comparatively low ranges relative to the other estimates of time in the experiment. This may indicate that there was a comparatively small mixing zone below the smoke layer.

Additionally, the Cam1 and Cam2 obscuration values have long durations, large ranges and include the only observer note that the event was unclear. Collectively, these observations may indicate that the smoke layer did not descend down past the camera height in experiment C2 but rather the fire compartment eventually was filled with enough smoke (not necessarily with a well demarcated “bulk” smoke layer interface) to obscure the camera views in the low lighting conditions. Finally, in addition to possibly not descending to camera hieght in the living room, the average observed times for smoke layer filling show that the smoke layer takes at least twice as long to form and descend to any height in experiment C2 compared to experiments A2 and B2. It is clear from this first observer-based analysis that distinct smoke layer height evolution patterns were recorded for each of the Type A through C fires.

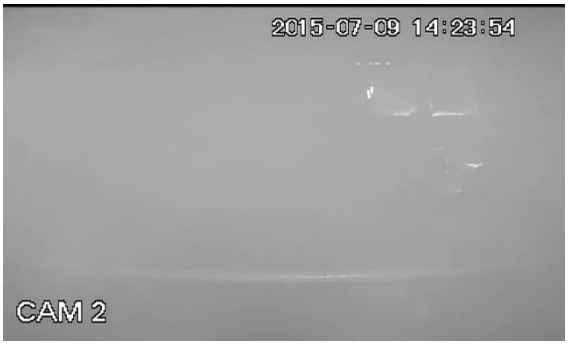

Figure 4.2: Cam2 Image 1140 s after crib ignition in experiment C2 (shortly before obscuration)

The second set of observer-based estimates of smoke layer descent in the living room were determined using a different method than the first. At 10-second intervals in Cam2 recordings, two observers (O1 from Table 4.1 and a new O6) worked together to decide where the “bulk” of the smoke layer began as it passed in front of the window. The observers counted the number of pixels to smoke layer height location relative to the top and/or bottom of the window. The known dimensions of the window, both physically and in pixels, were then used to convert the pixel values into smoke layer height at each time. In Figure 4.3, these results are presented in a plot of smoke layer height with time, along with results from Table 4.1. Further, throughout the characterization sections of this chapter (Sections 4.1 and 4.2), results from Type A, B and C materials are represented by the colours red, dark blue and light grey (moderate grey, dark grey and light grey in greyscale), respectively. Therefore, the results from the first three observers (Table 4.1) are represented in the plot by hollow symbols in the colour for the material type (A, B, or C). Only one of the C2 camera obscuration times (Cam1, 942 s) is marked to avoid stretching the time axis and compressing the results of interest. In addition, solid symbols in the colour indicating material type were overlaid to mark the second set of results in which two observers worked together to count pixels and relate that to smoke depth.

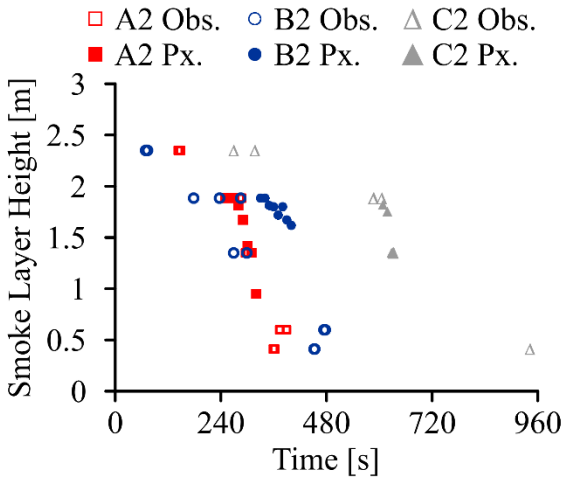

Figure 4.3: Living room observer-based smoke layer height estimates from objects (Obj., hollow) and counted pixels over window (Px., solid) for experiments A2, B2 and C2 (●, ■ and ▲, respectively)

It was found to take much longer to estimate smoke layer height using the second, counted pixel, method than the first observer method because of the precision required. Figure 4.3 shows that the counted pixel method results in more data points but is limited to the time during which the smoke layer is within the window height (and proximity) so does not cover the same range of physical heights or lengths of time as the first observer method. The two observer-based methods are in good agreement for estimates of both smoke layer heights and rates of smoke layer descent (slope) in experiments A2 and C2. This lends credibility to the method and its results. On the other hand, the large difference between the object and pixel count observer-based smoke layer height and descent estimates for experiment B2 at times after 240 s post ignition is notable and requires further investigation.

Figure 4.4 shows images from Cam2 at times of 270 s and 390 s in experiment B2, around the times when the discrepancies in observed smoke layer height occur. Figure 4.4 shows a “thin” smoke layer visible around the top of the window at 270 s while the “bulk” of the smoke layer does not descend to the top of the window until closer to 390 s after crib ignition. Smoke layer heights estimated using the pixel count method are considered more correct in this case and differences from those determined by observers using objects to estimate smoke layer height is attributed to observer error. Accordingly, the range of times for the smoke layer height to reach the heights of the five objects was recalculated to take into consideration both observer-based methods, for experiments A2, B2 and C2, as shown in Table 4.2. Nevertheless, that three observers making the same error on the same experiment must also be considered unlikely. As such, this instance serves to highlight the difficulty that observers can face when attempting to establish the smoke layer height using video image analysis [20–26]. Reducing observer subjectivity by establishing a range of possible values

for the given parameter, is precisely why multiple observers were used to complete the analysis.

a) B2, Cam2, 270 s

b) B2, Cam2, 390 s

Figure 4.4: Experiment B2 Cam2 images with a) a "thin" smoke layer visible 270 s and b) the "bulk" of the smoke layer visible at 390 s after crib ignition

Table 4.2: Observer-based living room smoke layer height minimum (Min.) and maximum (Max.) estimated times at five heights (Z) for experiments A2, B2 and C2

Z [m]	Observed Time [s]					
	A2 Min.	A2 Max.	B2 Min.	B2 Max.	C2 Min.	C2 Max.
2.35	143	148	69	73	269	317
1.89	250*	287	178	340*	586	605
1.35	296	301	269	>400*	628*	632
0.60	374	389	474	477	1152	1179
0.41	359	362	452	453	942	1388

*Based on a value from the pixel counting observer-based method

There were no upstairs windows in the Type A-C experiments and Cam4 was viewing only the second-floor landing and SW room. In order to precisely identify the smoke layer height using the present types of video analysis, the area must be backlit. Thus, only the object-based observer smoke layer height estimation method could be used to estimate the smoke layer height on the second floor of the burn house. The results in Table 4.3 indicate the times at which three individuals (O1, O4 and O5) independently identified 1) a thin smoke layer first forming at the ceiling (z=2.64 m), 2) the bulk of the smoke layer reaching the door soffit, door hinge/handle and a mid-height steel beam (z=2.13 m, 1.12 m and 1.05 m, respectively), and 3) the smoke obscuring the view in Cam4 (z=0.30 m). The observers noted the camera time at the top right of the recordings for each event which were subsequently converted to seconds after ignition by subtracting the ignition time for each experiment from the noted event time. In Table 4.3, 'U' indicates that the event timeline was reported as unclear. In both instances, however, two independent usable data points were available. The

average, minimum, maximum, and range (maximum time – minimum time) of the two or three recorded times are noted on the right side of Table 4.3 for reference.

Table 4.3: Observer-based second floor SW room smoke layer height estimation for Cam4 in experiments A2, B2 and C2 where three observers (O) estimate when (time in seconds after crib ignition) the smoke layer reaches five objects of known height except where the time was unclear (U). The average, minimum, maximum, and range of times are also provided.

Exp.	Z [m]	Observed Time [s]			Avg. Time [s]	Min. Time [s]	Max. Time [s]	Max.-Min. Range [s]
		O1	O4	O5				
A2	2.64	228	206	191	208.3	191	228	37
	2.13	271	233	201	235.0	201	271	70
	1.12	286	249	222	252.3	222	286	64
	1.05	305	272	282	286.3	272	305	33
	0.30	342	334	331	335.7	331	342	11
B2	2.64	223	218	218	219.7	218	223	5
	2.13	272	224	233	243.0	224	272	48
	1.12	371	258	243	290.7	243	371	128
	1.05	358	274	246	292.7	246	358	112
	0.30	395	394	395	394.7	394	395	1
C2	2.64	256	274	248	259.3	248	274	26
	2.13	513	U	286	399.5	286	513	227
	1.12	571	U	396	483.5	396	571	175
	1.05	491	457	436	461.3	436	491	55
	0.30	753	750	736	746.3	736	753	17

In contrast to measurements of smoke layer height in the fire room on the main floor, only moderate agreement can be seen across observer estimates of the time taken for the smoke layer to reach the five heights on the second floor in experiment A2. As in the living room, the best agreement between observed times is the time to camera, Cam4, obscuration. While the overall behaviour is as anticipated, it takes longer for the smoke to descend and obscure the camera in the second floor (11 seconds) than the main floor (3 seconds). The range of times estimated for camera obscuration on the second floor is also the only measurement range that falls below the highest range (15 seconds) of independently observed values in the living room for the same experiment. A larger range in value is likely related to a larger mixing zone, consistent with the notion that mixing increases as smoke spreads further from the fire compartment. In these experiments, the second floor SW room was several compartments and a staircase removed from the fire compartment.

Comparing experiment A2 results between Table 4.1 and Table 4.3, the smoke layer forms on the second floor (208 s) after the smoke layer is visible in the fire compartment (146 s). This sequence is logical because the smoke spreads from the living room, up the stairs,

through the upstairs landing, and into the SW room of the second floor. The expected collection of smoke at the ceiling and descent into the room is again evident but the smoke layer appears to descend more rapidly on the second floor, approximately 130 seconds between first formation and camera obscuration, in contrast to the living room where the smoke took about 215 seconds to cover the shorter distance between the ceiling and camera height. This is likely a result of differences in the buoyancy of the heated smoke relative to the cooler smoke-free air, as well as to flows due to the fire that might cause fresh air (oxygen) to be pulled from other areas of the house to sustain the fire once the readily available oxygen in the living room is depleted [89,90].

As in the results for smoke layer descent in the fire room for experiment B2, values of the time taken for smoke layer formation and camera obscuration on the second floor fell within a smaller range than times observed for the other three smoke layer height indicators. Once again, this may indicate that a specific demarcation between the “bulk” of the smoke layer and lower fresh air was difficult to distinguish. Again, consistent with expectation, the smoke layer formed in the fire compartment (71 s) before reaching the second floor (220 s). In general, results show the anticipated behaviour of the smoke layer descending into the compartment, except for one instance where the times observed for the smoke to reach the door hinge/handle and mid-height steel beam were inverted from the expected pattern. Given the close proximity of these two markers, 70 mm apart, the different pattern could have been caused by visibility issues and/or local characteristics of the smoke layer at each location. Based on the average observed times, the smoke layer on the second floor descended more quickly, within about 175 seconds, compared to the smoke layer in the fire room for the same experiment (approx. 380 seconds). The descent on the second floor again took longer than for experiment A2 (approx. 130 seconds) indicating that smoke evolution remains different for fires generated by different materials.

Unlike results for smoke layer height in the fire room for experiment C2 which had its own pattern, estimates of smoke layer height on the second-floor follow the same pattern as seen in experiment B2. Times to smoke layer formation and to camera obscuration were characterized by a smaller range of values than times observed for the other three smoke layer height indicators which suggests that the smoke layer interface was difficult to distinguish as a result of a large mixing zone. Unlike experiments A2 and B2, the average time noted by observers for the smoke layer to form on the second floor (259 s) occurs before the observed formation of a smoke layer in the fire compartment for experiment C2 (293 s). Looking at the individual responses for observers O1 (256 s vs. 269 s) and O5 (248 s vs. 317 s), which estimate times for smoke layer formation at both locations, they agree with this unexpected assessment indicating that the discrepancy is less likely to be observer error. Review of the recorded images, such as those in Figure 4.5, indicates that the large mixing zone and differing lighting conditions likely contributed to the observers perceiving that a smoke layer was forming on the second floor before the living room.

Figure 4.5: Cam1 (left) and Cam2 (right) images 260 seconds after crib ignition in experiment C2 (approximately when the observers noted smoke layer formation on the second floor)

The smoke layer behaviour on the second floor in experiment C2 is again consistent with expectations except for the apparently inverted times taken for the smoke to reach the door hinge/handle versus the mid-height steel beam as explained in experiment B2 above. Based on the average observed times, the smoke layer on the second floor descended more quickly, within about 490 seconds, compared to almost 900 seconds taken for the living room smoke layer to descend to the lowest point in the same experiment. The likely causes remain the same as those in experiments A2 and B2. In line with the results in the living room, smoke layer descent on the second floor was still the slowest of the three experiments confirming that the evolution and descent of the smoke layer is distinct in fires of different material.

Collectively, the observer-based smoke layer height estimates appear to largely follow the expected pattern of descent and smoke progression from the fire compartment to the second floor. In both observer-based methods used in the living room, there is a clear difference between the smoke layer progression for each material type. The difference in smoke layer behaviour between experiments A2 and B2 on the second floor is not as discernable, but in experiment C2 the smoke layer clearly descends later than in the other two tests. Observers counting pixels at 10-second intervals resulted in the same or a greater number of data points across the window, but the range was limited by the physical heights of the window and it required a significant analysis time on the part of the observers. Conversely, observers tracking the time taken for smoke to reach different objects in the compartment were not limited by window heights but were limited by visibility of objects with known heights that could be used to estimate the smoke layer evolution in the three experiments.

4.1.2 Analytical Methods

Two common smoke layer analytical methods, the NFPA and Tanaka & Yamana methods, were selected for characterizing the smoke layer height in the fire compartment for experiments A2, B2 and C2, as discussed in Chapter 3, Section 3.2. Both analyses require inputs including details of compartment geometry as well as definition of an appropriate t^2

heat release rate (HRR) fire growth curve per Equations 3.3 and 3.4. The specific inputs used in the present analyses are provided in Table 4.4 with reference in the rightmost columns as to which calculation(s) use each variable. Compartment geometry, including the clear ceiling height, ceiling height above surface of fuel and cross-sectional area of the compartment were taken directly from the dimensions of the burn room in the UW burn house (Figure 3.3). The t^2 HRR parameters, including incubation times (t_0), fire growth constants (α) and growth times (t_g), for each of the fires were previously determined [10] or can be calculated based on the determined values using Equation 3.2. Parameter k was selected assuming standard temperature and pressure in the ambient environment [23]. The values are used directly here for the t^2 fire growth curve (A2 = 350 s, B2 = 400 s and C2 = 700 s) as established in Section 3.2.2.

Table 4.4: Inputs for the NFPA and Tanaka & Yamana (T&Y) smoke layer height analytical methods

Variable		Value	Ref.	NFPA	T&Y
H	ceiling height	2.35 m		Y	Y
h	ceiling height above fire base	1.73 m		Y	Y
A	cross-sectional area of fire compartment	4.32 m x 3.2 m = 13.8 m^2		Y	Y
t_0	incubation time	A2=200 s B2=290 s C2=375 s	[10]	Y	Y
α	fire growth constant	A2=0.1778 kW/s^2 B2=0.1235 kW/s^2 C2=0.0178 kW/s^2	[10]	N	Y
t_g	growth time to reach 1055 kW	A2=277 s B2=382 s C2=618 s	Eq'n 3.2	Y	N
k	constant	0.0764	[6]	N	Y

Figure 4.6 includes plots of the smoke layer height with time determined using both analytical methods with the inputs in Table 4.4. Results of the two analyses are overlaid with results of observer estimated values of smoke layer height with time in the living room. As expected, the incubation time delays the smoke layer descent for both methods because minimal smoke is produced before the fire "gets going." Once the smoke begins to fill the compartment, however, the rate of filling with time is only slightly different, with the NFPA analytical method suggesting that the smoke initially fills the compartment somewhat faster, if moderately delayed, compared to the T&Y estimates. This similarity is expected since the methods are both based on the same HRR curves. The slight differences are likely related to the NFPA method's use of the α component of the t^2 fire growth curve contrasted with the T&Y method's use of t_g to capture a similar aspect of fire behaviour. As a consequence of

both methods using the same HRR curve, they agree that smoke descends first for material Type A, followed by Type B and finally Type C. The rate of smoke layer descent (line slope) does not appear to differ significantly by material type or analytical method. Results of the two analyses are overlaid with results of observer estimated values of smoke layer height with time in the living room in Figure 4.6.

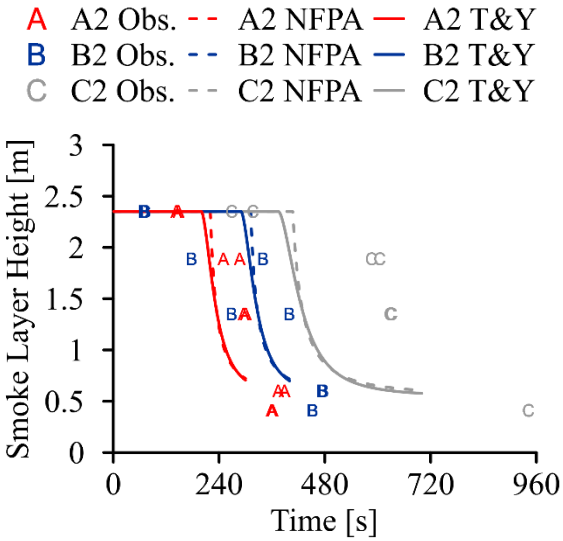

Figure 4.6: Living room range of observer smoke layer height estimates (A, B, C) for experiments A2, B2 and C2, respectively, with Tanaka & Yamana (T&Y) and NFPA calculated heights

Comparing the results of the four methods clearly shows that the calculated values for smoke layer height in the living room fall within the range of observed values only for experiment B2. The calculation results precede the observed smoke layer descent by 25-69 seconds and 155-202 seconds for experiments A2 and C2, respectively. However, it is notable that the range of values for experiment B2 is quite wide (162 and 131 seconds at z=1.89 m and z=1.35 m, respectively) compared to the ranges for A2 and C2 (≤ 37 seconds). In Section 4.1.1, the pixel analysis values were determined to be more correct than the object-based observer smoke layer height estimates. Then, more appropriately, the experiment B2 analysis results precede the observed pixel analysis values, the later (right-most) 'B' markers in Figure 4.6, by 25-72 seconds which is on par with the experiment A2 results.

The earlier times for smoke layer descent compared to observed values is likely because smoke layer height analytical methods are intended to estimate conservative times for egress purposes. Thus, the analytical methods do appear to serve that purpose in these three experiments. However, while conservative estimates are good for evacuation planning, they do not do a very good job of representing the range of observer-based values seen in the experiment and would potentially lead to underestimation of time to trigger smoke detectors

in real fire events. Accordingly, the observer-based smoke layer height profiles are used to assess the accuracy of the specific value, N-percent and integral ratio smoke layer height estimation methods discussed in the coming sub-sections.

4.1.3 Specific Value Estimates

As outlined in Section 3.2.3, the specific value method estimates that the smoke layer height in a room would be located at the height where the temperature reaches or passes 373 K (100 °C). Based on this model, the smoke layer height over time is estimated as the experiments progress using measured temperatures from thermocouple rakes T2, T3 and T4 in the living room, and T7 in the second floor SW room (shown in Figure 3.3). Linear interpolation of temperature between measurement locations (heights in Table 3.5) is used to estimate intermediate positions of the smoke layer height. In the living room, where there were three rakes rather than one, the estimated smoke layer height was calculated at each rake location and then averaged across the room. Estimates of smoke layer height in the living room versus time, estimated using the specific value method, are presented in Figure 4.7. Dashed lines indicate the height of the top and bottom thermocouples on the measurement rakes. The specific value-based smoke layer height can be interpolated in the regions between these bounds. The minimum and maximum observer-based smoke layer height estimates for each experiment have been overlaid on the plot using the symbol and colour representing the sofa material of the experiment (A, B or C).

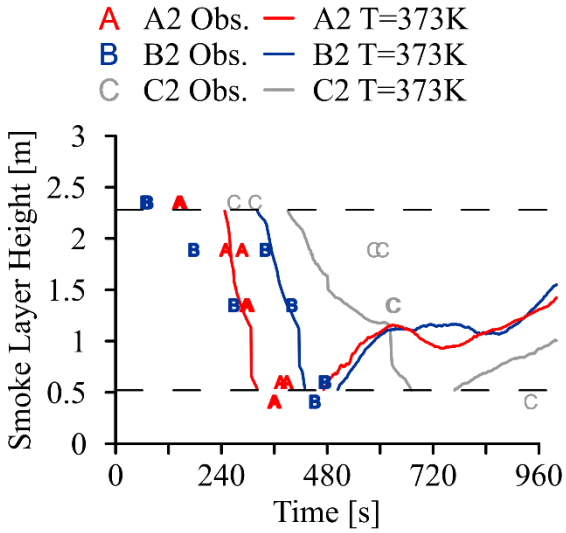

Figure 4.7: Living room average specific value (T=373 K) smoke layer height estimates between the highest and lowest thermocouples (— —) with reference observer (Obs.) ranges for experiments A2, B2 and C2

The average specific value (T=373 K) estimated smoke layer heights for the living room indicate that the smoke layer begins to descend earliest in experiment A2 followed by

experiments B2 and finally C2. The rate of smoke layer descent (line slope) appears to be similar for experiments A2 and B2 but much slower for experiment C2 These general trends agree with the observer-based results and the values align well, when the full range of observer-based times and observed pixel analysis values are considered for experiments A2 and B2, respectively. However, for experiment C2, the estimated time of smoke layer formation and initial descent is much earlier using the specific value estimation than the observer-based estimations. The observer-based estimates of smoke layer height fell within 19 seconds at z=1.89 m and z=1.35 m indicating good observer agreement on smoke layer descent time and, potentially, a small mixing zone. This supposition is supported by Figure 4.8 which shows a distinct transition between no smoke (lower half of window) and smoke (upper half of window). Thus, there is confidence in the observer results for experiment C2 and, therefore, a specific value of T=373 K does not do a good job of estimating the smoke layer height in this case. It is possible that a different, though necessarily subjective, temperature value might be more effective in estimating the smoke layer height in the living room for experiment C2.

Figure 4.8: Close up of window in Cam2 image of experiment C2 (625 s after ignition) showing a distinct transition between no smoke and smoke layer

Smoke layer heights on the second floor could not be determined using the specific value method because the thermocouples on the rake T7 in the second floor SW room never measured temperatures of 373 K. Thus, according to the specific value method, there was not a smoke layer in the second floor SW room. Given that all observers in the observer-based method identified a smoke layer in the room, using a temperature indicator of T=373 K in the specific value method is clearly not correct in this instance as was the case for the C2 living room analysis. While selecting a different indicator temperature was an option, it makes the results more subjective without adding any pertinent information to this work. Accordingly, the specific value method will not be used to characterize the smoke layer height and obtain values against which the radiance method accuracy can be assessed.

4.1.4 N-percent Rule Estimates

The N-percent method estimates that the smoke layer height is located at a position corresponding to where the measured temperature equals N-percent of the maximum temperature registered in a thermal profile (*i.e.*, thermocouple rake). Values of N = 10, 20, 50

and 90 were used in this analysis; thermocouple rakes T2, T3 and T4 in the living room and T7 in the second floor SW room were used to represent thermal distributions in those two rooms in experiments A2, B2 and C2. The entirety of results from the N-percent smoke layer height analysis includes a considerable number of smoke layer height estimates with time for each experiment. Accordingly, only a representative sub-set of the living room results from only one thermocouple rake are presented and discussed here. This is appropriate because smoke layer height estimates from the different thermocouple rakes lead to similar results, as illustrated in Figure 4.9 for the N-percent smoke layer height estimates with N = 50 at all three thermocouples in the living room for experiment A2. Thermocouple rake T3 (– – in Figure 4.9) was selected to represent the N-percent smoke layer height estimates for the living room in the remainder of this section. Plots of the remaining N-percent smoke layer height estimates with time for all three thermocouple rakes T2, T3 and T4 can be found in the Appendix. The N-percent method estimates that the smoke layer height would return to the ceiling, after ~480 s in Figure 4.9, due to temperature uniformity in the compartment. For this reason, estimates found using the N-percent method are only valid during the initial smoke layer descent [9].

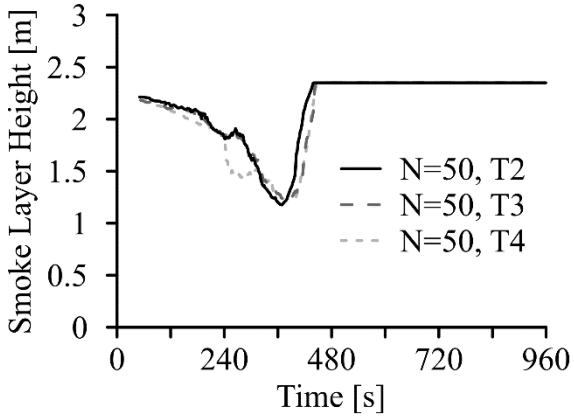

Figure 4.9: N-percent method smoke layer height estimation over time with N = 50 for thermocouple rakes T2, T3 and T4 in the living room of experiment A2

The results of smoke layer height with time using the N-percent method with values of N=10 (——), 20 (– – –), 50 (- - - -), and 90 (·····) are presented in Figure 4.10. For clarity, the results are split into six plots with the living room results on the left and second floor SW room on the right. Results from experiments A2, B2 and C2 are shown from top to bottom. The legend for all plots is located above each plot and heights of the top and bottom thermocouples (— —), between which the smoke layer height estimate can be interpolated, are included in each plot. Finally, the minimum and maximum observer-based smoke layer height estimates for each experiment have been overlaid on the appropriate plots with the symbol and colour representing the sofa material of the experiment (A, B or C).

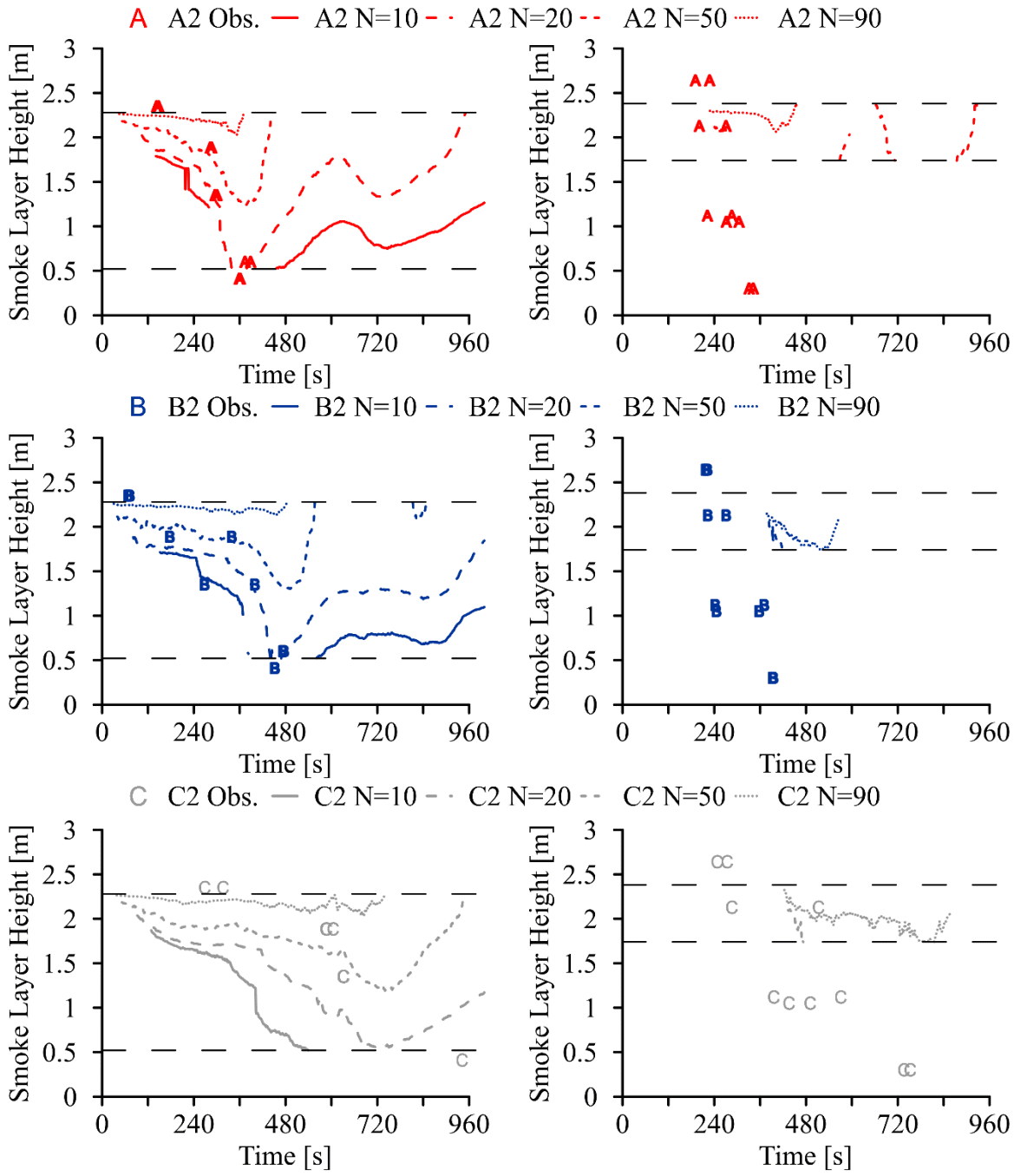

Figure 4.10: Living room (left) and second floor SW room (right) N-percent (N=10, 20, 50, 90) smoke layer height estimates between the highest and lowest thermocouples (— —) on rake TC3 with reference observer (Obs.) ranges for experiments A2 (top), B2 (middle) and C2 (bottom)

As illustrated in the three plots on the right-hand side of Figure 4.10, use of the N-percent method for estimation of smoke layer formation in the second floor SW room is not useful and in this compartment, remote from the fire compartment, another approach would need to be employed.

The living room results on the left side of Figure 4.10 follow a general, and anticipated, pattern. Results for N = 10 indicate that the smoke layer descends into the room earlier, faster and lower than estimates based on N = 20 that estimate earlier and faster growth than those using N = 50. Finally, results for N = 90 suggest that the smoke layers begin to descend at the latest time, progresses the slowest, and do not descend very far into the compartment. This is consistent with expectation because a lower N value requires a smaller temperature rise in order to signal the presence of the smoke layer.

When the N-percent results for experiment A2 are compared to the observer-based results in the top left plot, it is interesting to note that no single value of N from the N-percent analysis coincides entirely with the observed smoke layer. Rather, the observed values of time for smoke layer descent consecutively fall in the N = 10, to 20 and finally 50 range of traces. A similar trend appears to occur for the living room results from experiment B2 in the left, middle plot of Figure 4.10. In contrast, the observed values for smoke layer height with time in experiment C2 do not follow as consistent a trend, but instead are distributed across the range from N = 20 to N = 90 (bottom left plot). Based on analysis of data from these three experiments therefore, values of N could fall anywhere between N = 10 and N = 90; there is no single value of N that can be used in the N-percent method to reproduce smoke layer height estimates that follow the observed values. Thus, use of the N-percent rule for estimation of smoke layer height here is not particularly useful, and in the worst case can lead to very misleading characterizations of smoke development in a compartment. It is, on the other hand, in one sense conservative in terms of initial smoke layer development time, since the smoke layer is noted as having formed and begun descending before the observers noted that a smoke layer had even formed (*i.e.*, the highest A, B or C symbol(s) were right of where the N-percent results started).

As illustrated in the three plots on the right-hand side of Figure 4.10, use of the N-percent method for estimation of smoke layer formation in the second floor SW room is not useful and in this compartment, remote from the fire compartment, another approach would need to be employed.

As with the specific value method, it might be possible to guess and find a value of N that could be used in the N-percent analysis to estimate smoke layer formation and descent for each experiment and location. This approach would again add significant subjectivity to the results without adding any pertinent information to this work. Thus, the N-percent method will not be used to characterize the smoke layer height and obtain values against which the radiance method accuracy can be assessed.

4.1.5 Integral Ratio Estimates

The integral ratio method can be applied to estimate smoke layer height by calculating the uniformity of the upper- and, independently, the lower-layer temperatures in a compartment. That information is then used to determine the height that simultaneously results in the most uniform upper- and lower-layer temperatures. This height is taken to be the smoke layer height for that point in time. Calculations are then repeated at every time step for the duration of the period of interest. This method was used to estimate the evolution of smoke layer height over time in experiments A2, B2 and C2 for the three thermocouple rakes (T2, T3 and T4) in the living room and rake T7 in the second floor SW room.

Smoke layer height estimates determined using the integral method are plotted in Figure 4.11 with results of analyses from thermocouple rakes T2, T3, T4 and T7 shown in plots a), b), c) and d), respectively. The legend for all plots is located at the top of the figure. The top and bottom thermocouple heights (— —), that serve as the interpolation limits, do differ by thermocouple rake and are marked on each plot. The minimum and maximum observer-based smoke layer height estimates for each experiment have been overlaid on the plots with the symbols and colour representing the sofa material of the experiment (A, B or C).

Initial examination of Figure 4.11 indicates that results of smoke layer formation and descent as determined using the integral method with temperature data from thermocouple rakes T4 and T7 are generally unclear, unsteady and do not further the smoke layer height characterization process. Results of the integral ratio method using temperature data from rakes T2 and T3 in the living room, however, indicate that the smoke layer descends first in experiment A2, then B2, and finally C2 in line with the observed smoke layer descent. Further, both seem to do a reasonable job in approximating the observed results early in experiments A2 and B2. T3 also does a reasonable job of approximating the observed results in experiment C2. The rates of descent determined through analysis of data from T3 are quite encouraging as they follow the observed patterns of smoke layer development and descent for experiments A2 and B2, and indicate a slightly slower rate of descent for experiment C2. In contrast, detailed results from analysis of temperature data from rake T2 are more inconsistent in demonstrating the observed trends, except at early times in experiment A2 and to a lesser degree B2. Despite this early agreement, none of the usable integral ratio method results indicate that the smoke layer descends to the height of either Cam1 or Cam2 (<0.6 m). This contradicts the clear indications from the observers that the smoke layer did descend to these heights in at least experiments A2 and B2. Therefore, since the integral ratio method does not pick up the smoke layer descent to camera heights in the fire compartment (living room) and cannot predict the smoke layer height in the second floor SW room it is also removed from contention for characterizing smoke layer height.

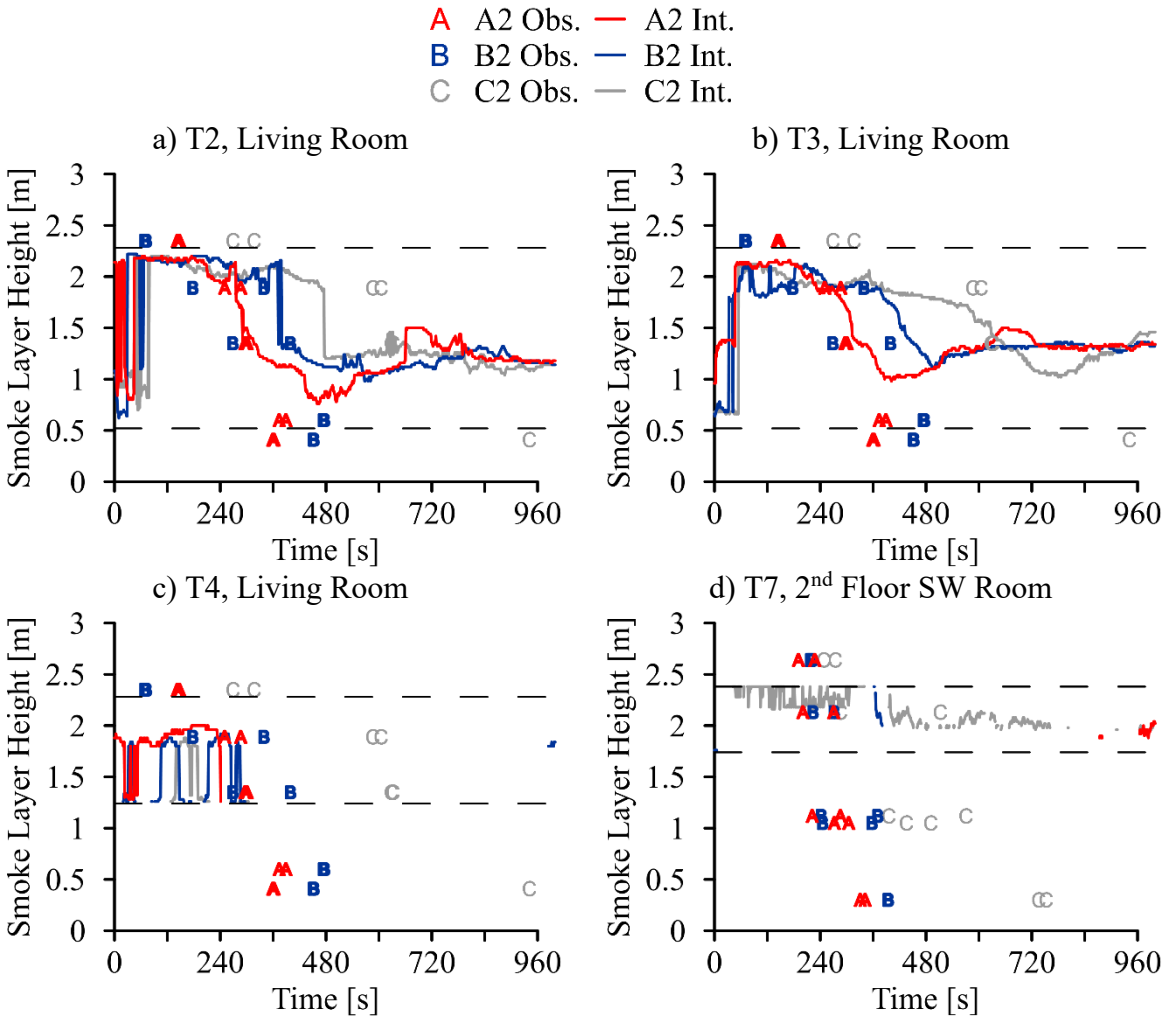

Figure 4.11: Living room thermocouple rakes a) T2 b) T3 and c) T4, and d) second floor SW room rake T7 integral ratio (Int.) smoke layer height estimates between the highest and lowest thermocouples (— —) with reference observer (Obs.) ranges for experiments A2, B2 and C2

Based on preliminary analysis of video traces, fire growth characteristics and temperature data collected during the A2, B2 and C2 fire experiments, the observer-based smoke layer height estimation has been established as the best method for characterizing smoke layer height in fire experiments. While there is some controversy [22], observer methods are also the most common "baseline" methods used for estimating smoke layer height in fires [23–25,30]. Conceptually, it may also be more intuitive to estimate the smoke layer height visually, rather than indirectly through temperature or the heat release rate of a fire, since it is ultimately intended for use in capturing the impact of the smoke layer (and the toxic gases within) on occupant visibility and ability to evacuate. Accordingly, the smoke layer heights,

as perceived by multiple observers of video recordings, are used to establish the "baseline" or "reference" smoke layer height against which results from the penultimate and final radiance methods are judged in Sections 4.4 and 4.5, respectively. Before discussion of those results, however, a similar analysis is outlined in the next section to determine which of a set of existing methods best characterizes, and thus can be used as a reference for determination of, the smoke density in this research.

4.2 Smoke Density Characterization

As the new radiance method for estimating smoke layer height and density was being developed and refined, it was necessary to compare the results of smoke layer height to other methods and to compare the results of smoke density estimations from the newly evolving method(s) to other methods as well. In this Section, the reference rankings for smoke density used for that purpose are reported and discussed. The smoke density rankings were obtained using the small- and full-scale methods outlined in Section 3.3. Small-scale values and rankings from saved Type A-C materials obtained using smoke density chamber tests are detailed in Section 4.2.1 where values are also compared to published values for similar materials. In Section 4.2.2, full-scale rankings are presented. These were obtained by independent observers who visually ranked the opacity and thus estimated the density of the smoke as the smoke layer passed over a window in the burn house experiments. These observer rankings are then compared to the smoke density chamber ranking by material type. Collectively, the results are used to characterize the smoke density of the Type A-C materials as a baseline reference for comparison to results obtained using the new radiance method later in this chapter.

4.2.1 Small-Scale Data Estimates

A total of 29 smoke density chamber ISO 5659-2 [56] tests were conducted on 75 mm x 75 mm samples of the foam and foam/fabric combinations used in Type A-C experiments. Each sample was cut to size and then exposed to an incident heat flux of 50 kW/m^2 in the chamber. These tests, completed in three distinct series, were used to determine maximum specific optical density, as discussed in Section 3.3.1. The last of the three series was conducted to determine the accuracy of the first two series after it was discovered that that the smoke density chamber had not been functioning correctly for the first two sets of tests.

Mean values and standard deviations of measured maximum specific optical density for each material and material combination were obtained across individual tests within each series. The number of samples included in each value, as well as resulting values are summarized in Table 4.5. In each test series, the mean maximum specific optical density ($D_{s,max}$) is used to rank the materials where higher values indicate smoke that is more dense and, thus, receive a higher rank (lower numerical value) on the scale of highest (1) to lowest (3) potential smoke density. The standard deviation (Std. Dev.) of the N samples included in the mean calculation indicate how varied the results were for each material within each series as well.

Table 4.5: Smoke density chamber maximum specific optical density results for Type A, B, and C foam and foam/fabric material combinations tested used to rank from most dense smoke (1) to least dense smoke (3) in three series

Type	N	Mean	Std. Dev.	**Rank**
Series 1 – Foam Only				
A	3	114.0	0.3	**2**
B	3	116.3	0.1	**1**
C	3	110.5	8.2	**3**
Series 2 – Foam/Fabric				
A	3	119.9	0.9	**1**
B	3	119.3	0.5	**2**
C	3	94.3	24.9	**3**
Series 3 – Foam Only				
A	4	236.6	19.1	**2**
B	4	570.1	144.8	**1**
C	3	163.1	13.5	**3**

In Series 1, the mean $D_{s,max}$ values for all three foams fall in the small range of 110.5 to 116.3. The Type A and B materials exhibit very small standard deviations in value (0.3 and 0.1, respectively) indicating good agreement of the measured value of $D_{s,max}$ between tests. The standard deviation in the Type C material tests was larger (8.2) indicating less agreement. The overall material rankings for Series 1 were that Type B foam samples resulted in the most dense smoke followed closely by Type A foam and finally Type C foam.

Results for mean $D_{s,max}$ of Type A and B foam/fabric combinations in the second series of tests, Series 2, were extremely close (119.9 and 119.3, respectively) and the standard deviation in values was again small, though larger than in Series 1 (0.9 and 0.5, respectively). The measured value of $D_{s,max}$ for the Type C combination is much lower (94.3) and the standard deviation much higher (24.9) than that of Types A and B. The significantly higher standard deviation in values of average maximum specific optical density for Type C materials from Series 1 and 2 testing is due to the large variation in ignition time; both the longest and shortest ignition times of all nine Series 2 foam/fabric tests were during Type C tests. The same may be true for the Series 1 foam only tests but this could not be verified since the time to ignition was not recorded for one of the tests. Based on the mean $D_{s,max}$ values, Type A foam/fabric combinations led to slightly more dense smoke than Type B with Type C a distant last. Thus, the rankings for smoke production from Type A and B materials flipped between Series 1 and 2 tests, but the standard deviations in Series 2 indicate that this was based on a very small margin of difference. As a result these materials could be considered to be very close in terms density of smoke produced under the test conditions. Overall, the values were consistent enough that mean values of $D_{s,max}$, were individually used

to rank the materials from 1 (highest smoke density) through 3 (lowest smoke density) in terms of their potential to produce smoke during a fire though the ranking was somewhat contradictory to visual evidence derived from the videos of the fires, prompting additional investigation.

On further testing through Series 3, where the smoke density chamber was known to have been fixed and was thus working reliably, a much larger range of values of mean $D_{s,max}$ and, consequently, larger standard deviation were measured for foam samples of each type. Despite the larger values of standard deviation (13.5-144.8) in this test series the mean values provide a clear ranking of smoke production across the three materials. Type B foam produced the most dense smoke (570.1), Type A produced less than Type B (236.6) and Type C produced the least dense smoke (163.1) under specified ISO test conditions.

Despite the large variations in value within a given series, the average maximum specific optical density value is consistently lowest for Type C foam and foam/fabric combinations. The maximum values of specific optical density for Type A and B materials indicate that they produce more dense smoke than Type C materials but their ranking in terms of smoke density appears difficult to ascertain since it was different in the tests with foam only samples (Series 1 and 3) versus those for the foam/fabric combination (Series 2) when the rank flipped by a small margin. It is felt that overall, the most reliable smoke density rankings are from Series 3 smoke density chamber tests on foam samples wherein, compared with Type A foams, Type C materials produced less dense smoke and Type B more dense.

With respect to uncertainty in the results presented in Table 4.5 and discussed above, it has been noted that in the earlier tests (Series 1 and 2) the smoke density chamber was most probably not working correctly, particularly in the lower transmission ranges, *i.e.*, as the specific optical density reached its maximum value. Unfortunately, it is also possible that some of the variations in the Series 3 results are because the foam aged over the time elapsed between Series 1/2 and Series 3 tests [90]. Specifically, changes in fire retardant concentration with time may be the cause of the larger standard deviation in measured values for the fire-retardant Type B materials in the Series 3 tests [124] in contrast to the Type A and C materials which were non fire-retardant and lightly fire-retardant, respectively. Further tests will be conducted in future work unrelated to this thesis to better ascertain the potential impact of material aging on results of smoke density testing of the materials used as well.

Despite uncertainty in the early test results and potential effects of ageing in the most recent tests, applicable measured values of maximum specific optical density reported in Table 4.5 for the three materials/material combinations compare reasonably to applicable results from the literature. Since results detailed in Chapter 2 Table 2.2 are for non fire-retardant flexible polyurethane foams, only Type A materials tested as foam only (Series 1 and 3) are comparable. Values of maximum specific optical density from Series 1 (flexible polyurethane) foam only tests (114.0) are below and those from Series 3 foam only tests

(236.6) are above the most applicable published value (127 [56]) for flexible polyurethane foam. Though the magnitudes are not equal, it should be noted that all values of maximum specific optical density measured in these tests for the Type A foam are reasonable, since they fall within the full range of published values for flexible polyurethane foam, 75 to 284 [53,56,57,63,65].

For comparison with these small-scale results, it was of interest to evaluate the video recordings of the Type A-C experiments in more detail as well and to determine whether the full-scale tests for comparable material types exhibited similar smoke progression characteristics and rankings as seen above. Specifically, the next section of the analysis addressed whether Type C sofa fires appeared, from visual video evidence, to produce less dense smoke than Type A or B sofa fires. Therefore, in the next phase of the preliminary analysis, the smoke density chamber results were compared to observer-based estimates of smoke density determined by three observers via visual inspection of images, coupled to global ranking of their perception of smoke density, seen in the video recordings from Type A-C experiments. These results form the subject of the next section.

4.2.2 Full-Scale Data Estimates

A crude observer-based smoke density estimation method was detailed in Section 3.3.2. An image was selected for each of the nine Type A-C experiments when the smoke layer was over the window visible in the Cam2 view. Three observers (O1-3 from Section 4.1.1) independently estimated the smoke 'thickness' in each of the nine images from highest smoke density (1) to lowest smoke density (9) with results shown in Table 4.6. The average rank for each material across all estimates (N=8 or 9) is also displayed. This value was used to provide an overall ranking of smoke density from each material as shown in the far-right column of the table. In the Table, * indicates that no usable entry exists.

Table 4.6: Three observers (O1-3) independently ranked the smoke density of the nine Type A-C experiments except where the rank is not available (*)

Material	O1	O2	O3	Average	Density Rank
Type A	7	5	5	6.1 (N=8)	2
	6	6	7		
	5	8	*		
Type B	2	2	1	2.0 (N=9)	1
	1	1	2		
	3	3	3		
Type C	4	4	4	6.6 (N=9)	3
	9	7	6		
	8	9	8		

Observer estimates of the smoke density in images from the Type A fire, as shown in Table 4.6, are a mix of mid- to low-density ranks (5-8) resulting in an average estimate of 6.1. There are only 8 estimates for this material but, regardless of what rank is used for the data point that is unavailable, the overall ranking of smoke density in the Type A fires relative to Types B or C would not change. Observers estimates uniformly rank the smoke density in the Type B fires as the highest (1-3) of the three materials with an average estimate of 2.0. Finally, smoke density based on images from the Type C experiments were consistently categorized by observers as being in the low-density range (6-9), though interestingly for one fire tests, the density was consistently ranked as being 4. This discrepancy perhaps indicated that actual accumulation and density of smoke varied quite widely between experiments or the observers were provided with a poorly selected image for ranking in this particular experiment. Averaging across all estimated values resulted in an overall smoke density ranking with an average of 6.6. From observer based analysis then, Type B material fires appear to produce the most dense smoke (rank 1), while Type A and Type C materials appear to generate the second and third most dense smoke during the large-scale fire experiments (ranks 2 and 3, respectively).

A comparative summary of the smoke density rankings for each material based on observer results from full-scale fire images and measurements obtained from the smoke density chamber is shown in Table 4.7. There is agreement between both small- and full-scale estimation methods that sofa fires fuelled by material Type B produce the most dense smoke with Type A materials next and Type C materials producing smoke that is the least dense. Accordingly, these ranks are used as a baseline for comparison of derived smoke density estimates as the radiance method is developed in the coming sections.

Table 4.7: Comparison of smoke density results between the small-scale smoke density chamber and full-scale burn house experiments

Rank	Smoke Density Chamber	Burn House Experiments
1	B	B
2	A	A
3	C	C

Results obtained for smoke layer height and smoke density during the iterative development of the radiance method are presented in the remaining sections of this chapter. Results from the earliest prototype of the radiance method are presented in the next section, and interpreted with focus on lessons learned and the potential impacts of those as they relate to how to improve the method. Those were applied in development of the penultimate method detailed in Section 3.5.2 with results presented in Section 4.4. Further refinements to the method were made as outlined in Section 3.6 and results for smoke layer height and density obtained using the final radiance method are presented and discussed in Section 4.5.

4.3 Lessons Learned in Early Radiance Method Iterations

Iterations of the early radiance method that were presented in Section 3.5.1 represent the first attempts to develop a method similar to the Digital Optical Method for smoke analysis in large-scale fire scenarios. Three early iterations were used successively to characterize smoke evolution based on video recordings from historical experiments C1, C2 and B1. Collectively, the results pointed to gaps and pitfalls in application of the method, prompting significant changes that were then incorporated into development of the penultimate method. Results of initial iterations and the consequent modifications from early to penultimate radiance method form the subject of this section.

4.3.1 Iteration 1

The first of the early radiance method iterations was used to analyze images from recordings captured by Cam1 and Cam2 in the living room and Cam4 in the second floor SW room during experiment C1. As detailed in Section 3.5.1, the video recordings from each camera were converted into sequences of images through time, a reference image was selected from the beginning of the fire and contrasting light and dark areas had to be selected from that reference. Next, pixel values had to be extracted from each of the contrast areas on each image. At first, however, it was unclear whether the mean, median, mode or even the standard deviation of the pixel values in each area would be the best indicator of a representative value for that area. Examination of the standard deviation was included to determine whether the data became "more uniform" in the selected areas as the analysis progressed and might precipitate a radiance method variation similar to the DOM transmission method but this did not work.

In this iteration, therefore, analysis was conducted to determine which statistical quantity would best represent pixel value, and changes in pixel value, for a given image during the radiance analysis. For this, the mean, median, mode and standard deviation of pixel values in sequential Cam1 (colour) and Cam4 (greyscale) images were extracted. These results are displayed as plots of each statistical measure of pixel value (0 = pure black, 255 = pure white) against time in Figure 4.12.

Looking at the results from colour images taken from Cam1 recordings and plotted in the left plot of Figure 4.12, a general pattern emerges, with relatively stable values for all statistical quantities for the first 360 seconds into the experiment. At this point the values of all statistical measures increase, by differing amounts, and the stability of the results varies depending on the measure chosen (mean, median, mode, standard deviation). Mean and median values follow similar trends to one another but with differing magnitude. Values of the mode broadly follow the same pattern as the mean and median but become much more unstable as they are influenced by short term changes in individual pixel values because of variations in lighting conditions in the compartment due to fire flickering, for example. The standard deviation of pixel values in images extracted from Cam1 show that the light from

the fire influences the standard deviation, which increases as the growing fire makes lighter (brighter) and darker (shadowed) areas more prevalent, thereby increasing the full range of individual pixel values in the images. The trends seen in the results for standard deviation of pixel values are contrary to expectation that the standard deviation of the individual values would decrease as the smoke descended and made the images a more uniform colour.

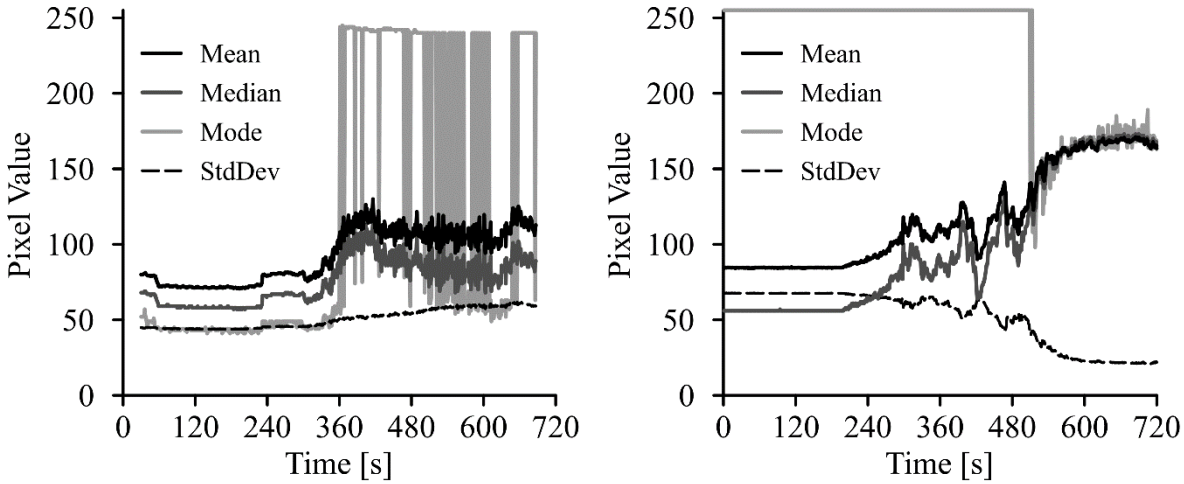

Figure 4.12: Mean, median, mode and standard deviation (StdDev) of all pixels in Cam1 (left) and Cam4 (right) images in experiment C1

Statistical measures calculated using pixel values extracted from the greyscale images captured by Cam4 upstairs in the structure are also plotted in Figure 4.12 on the right-hand side. In contrast to results from Cam1, these show the expected decrease in value of standard deviation as the smoke makes the image a more uniform shade of grey. In this case, while the mean and median start at different pixel values, difference between them gradually narrows and they approach the same values as the experiment progresses. The mode indicates an initially a fairly uniform shade of grey in the image, near pure white, before it drops in value at about 480 seconds into the experiment and subsequently follows approximately the same pattern and values as the mean and median.

Overall, the pixel value corresponding to the mode of individual pixel values in the image was easily discounted for the analysis because, in images from both cameras, it was too easily influenced by the presence of the fire or the descent of the smoke layer. The standard deviation showed susceptibility to lighting conditions based on the Cam1 results and so it was also discounted. Thus, the decision ultimately came down a choice between use of the mean or the median of the individual pixel values in each contrast area since these two statistical measures generally follow the same pattern. For the purposes of application with the radiance method, one did not appear to be strictly better than the other, as long as whichever quantity is chosen is used consistently throughout all steps in the analysis. Thus, the mean of the individual pixel values within each area was selected in this thesis, largely

because this was also the value used for the analysis in the original version of the Digital Optical Method although no reason was given for this choice [75,76].

After the above determination, the mean pixel values were extracted from each selected contrast area in each image. These pixel values (*PV*) were transformed into radiance values (*N*), by assuming $N = PV$, and then used in the framework of the radiance method to calculate the smoke density for each contrast pair in each image. Results from Cam1 in experiment C1 are presented first. Smoke density results from this first iteration are plotted against time in Figure 4.13 for selection areas taken from the top (T), bottom (B), left (L) and/or right (R) of the window (W) and chair (C) as well as at the smoke detector (Det) visible in the camera view shown in Figure 3.21. In order to better interpret the results, selection areas from the left-side of each object have been separated out and are displayed in the left plot (L) in Figure 4.13 while the remainder of the smoke density traces are displayed in the right plot (R, Det). Each trace in the plot is designated as W:T (window top), W:B (window bottom), C:T (chair top), C:B (chair bottom) or Det (detector).

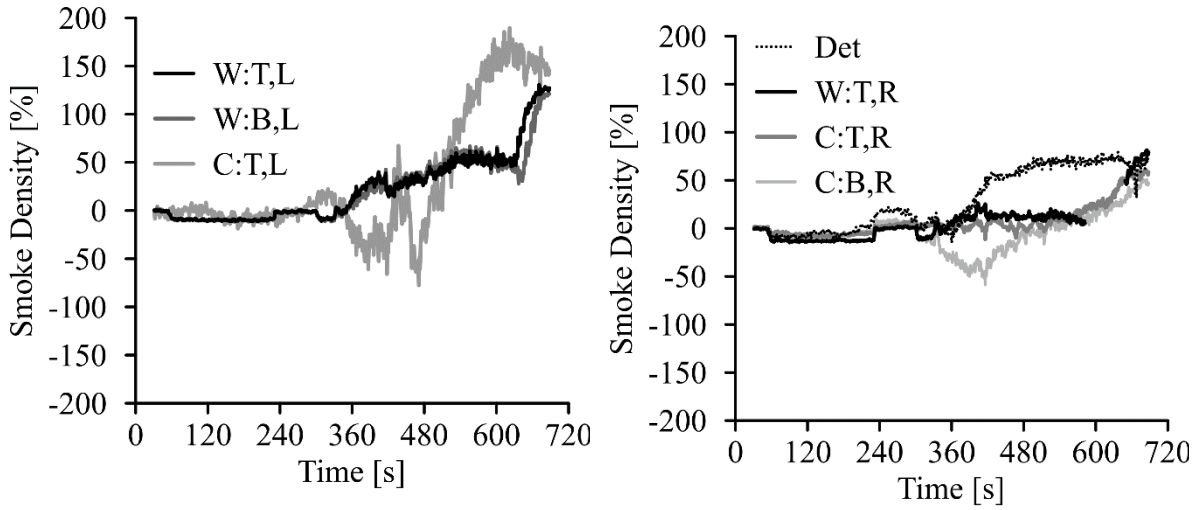

Figure 4.13: First iteration smoke density results for Cam1 in experiment C1 with selections at the top (T) and bottom (B) of a window (W) and chair (C). Left-side areas selections (L) are in the left plot while the right plot has right-side selections (R) and selections from a smoke detector (Det.)

As seen from the figure, this initial analysis resulted in an extremely wide range of "smoke density" values, with several laying outside of the expected range of 0-100%, making it difficult to interpret the calculated values. On the other hand, some clear trends were evident in that the smoke density traces from Cam1 which showed marked increases at certain times after ignition. This observation indicated that there was potential for the radiance method to be used to estimate the position of smoke layer height combined with an increase in smoke

density. Comparison of the left and righthand plots in Figure 4.13 show that the values of smoke density determined from pixel analysis of areas chosen from the left side to the right side of the window or chair are distinctly different. Values of smoke density derived from pixel analysis areas chosen on the left side of either object appeared much less stable than values determined using areas to the right side and also led to estimates of smoke density of well below 0% and above 100%. The discrepancies were likely related to susceptibility of the analysis to brief time when the pixel areas to the left of the objects were brightened or darkened by flickering of the fire.

In contrast, estimates of smoke density based on analysis of contrast areas chosen to the right side of the window and chair were generally smoother and remained below 100% smoke density. Focusing on the right plot in Figure 4.13, therefore, the smoke density values increase first based on pixel areas taken closest to the smoke detector, followed by those to the top right of the chair, and finally the bottom right of the chair. This sequence of selection areas actually corresponds to pixel areas in the image from highest to lowest physical locations in the compartment. Figure 4.14 supports this supposition because the smoke detector (circled) is almost entirely obscured while the smoke layer remains above the window (underlined) 480 s after ignition in line with Figure 4.13. Thus, it was ascertained that the method, with appropriate refinement, could most probably perceive descent of the smoke layer within a fire compartment. Smoke density estimates derived from the pixel areas to the top right of the window may also have matched the above pattern, but unfortunately an observer outside the burn house looked through the window in the time period of interest, greatly influencing the pixel values within in the measurement areas and thus estimated values of smoke density as well.

Figure 4.14: Cam1 image from 480 s after ignition in experiment C1 showing the smoke detector (circled) almost entirely obscured and the smoke layer above the window (underlined)

Smoke density estimates from initial radiance analysis of pixel areas chosen from images recorded by Cam2 in experiment C1 are plotted against time shown in Figure 4.15. Selection areas include those taken from the top (T), bottom (B), left (L) and right (R) of a window (W) visible in the camera view, with legends on the plot as outlined above. In order to better interpret the results, the selection area from the left-side of objects have again been separated out and are displayed in the left plot with the remainder of the smoke density traces displayed in the right plot.

Estimates of smoke density derived from Cam2 pixel areas are difficult to interpret because they are almost entirely large negative values (for reasons discussed shortly). As for Cam1, however, it can be seen from the plot that the smoke density estimates from the right side of the window (right plot) are smoother, can be calculated over a longer time period, are less negative, and increase at longer times, possibly indicating the presence of the smoke layer, though delayed relative to times seen in the analysis of images from Cam1. The spikey data determined based on analysis of pixel areas located on the left side of the window (left plot) is again likely related to susceptibility of the analysis to alternating times when the pixel areas to the left of the objects were brightened or darkened by flickering of the fire visible in the video recordings. Values of smoke density can be calculated for longer times using pixel areas chosen to the right side of the window since the fire grows from left to right in the image and therefore passes in front of the left pixel analysis areas before the right areas. Both observations indicate that pixel analysis areas should be chosen farther from the fire if possible, in line with the same requirement outlined in the derivation for consistency in determination of the radiance in Section 3.4.

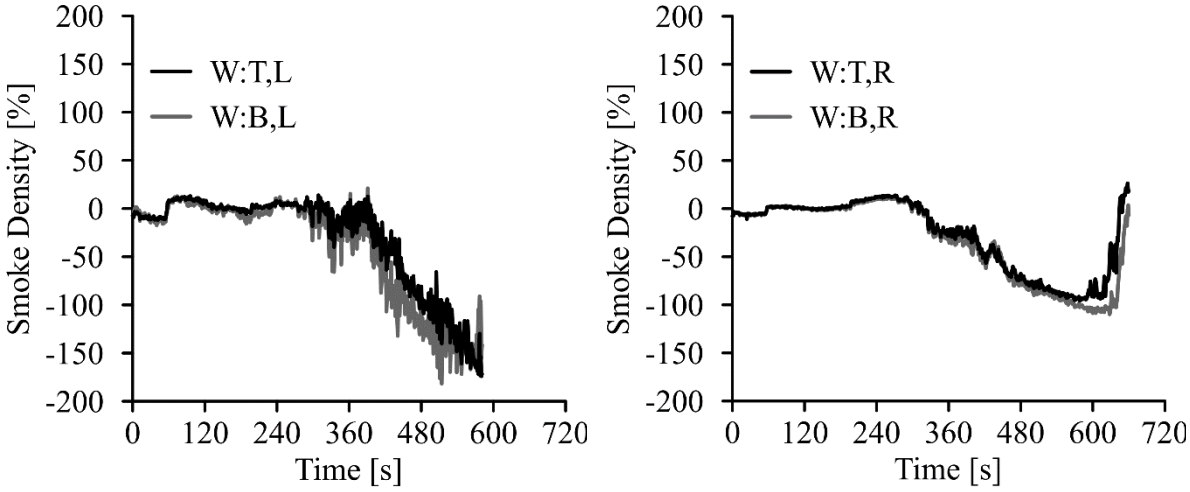

Figure 4.15: First iteration smoke density results for Cam2 in experiment C1 with selections at the top (T) and bottom (B) of a window (W). Left-side areas selections (L) are in the left plot while the right plot has right-side selections (R)

Examination of the times at which smoke density values do increase quickly in the right side plot, indicates that values start to rise first based on analysis from pixel areas situated at the top of the window followed by a rise from areas at the bottom of the window. This is again consistent with the anticipated pattern of smoke layer descent in the compartment. Finally, comparing between the Cam1 and Cam2 results in Figure 4.13 and Figure 4.15, respectively, many of the smoke density traces increase in value at between 600 to 660 seconds into the experiment, indicating that cross-verification may be possible and would certainly play an important role in both development and refinement toward any final method.

Upon further examination of the negative values of smoke density determined based on chosen pixel areas in images taken by Cam2, it was found that these are, in part, due to the camera angles used in the experiment. In this first application of the radiance method, selection of the dark areas in these images proved to be challenging (but crucial) since options were limited to not very dark drywall that was further brightened by glare in early recorded images. Additionally, as the experiment progressed, the glare on the drywall was reduced (possibly by a passing cloud or, more likely, because of accumulation of a very fine layer of smoke) while backlighting of the window maintained reasonably consistent values in the chosen light pixel areas. Since the range of pixel values increased, the resulting values of smoke density became negative since the calculation proceeds as

$$1 - \left[\frac{> Initial\ Range}{Initial\ Range}\right] = 1 - [> 1] = < 0$$

This observation spoke to the importance of choice of camera position for success in future radiance analysis and also prompted a brief investigation into the contrast achieved for each of the selection pairs in the Cam1 and Cam2 analyses.

Table 4.8 details the contrast (1-N_W/N_B [76]) and initial pixel range (N_W-N_B) for each of the selected contrast pairs chosen in images extracted from Cam1 and Cam2 recordings in experiment C1. The table shows that the contrast and initial pixel ranges are uniformly higher in pixel areas chosen from the right-side of the objects (window and chair) in the images compared to those chosen on the left-side of the objects for both Cam1 and Cam2. Given the noticeably improved results established through analysis of pixel values determined using the radiance method with data from areas to the right-side of the objects, and the initial contrast differences between right and left side summarized in Table 4.8, it was confirmed that the difference in initial light and dark area values is critical to success of radiance analysis of smoke evolution from fires.

Collectively, this first iteration radiance analysis based on mean pixel values from areas chosen within images from three camera views Cam1, Cam2 and Cam4 in experiment C1 provided results with sufficient promise to merit further investigation of the technique.

Table 4.8: Contrast and initial pixel range (N_W-N_B) from experiment C1 Cam1 and Cam2

	Window				Chair			Detector
	Top		Bottom		Top		Bottom	
	Left	Right	Left	Right	Left	Right	Right	
Cam1								
Contrast	48%	61%	44%	N/A	9%	48%	48%	28%
N_W-N_B	121.1	154.9	111.0	N/A	19.8	96.7	70.4	33.8
Cam2								
Contrast	22%	42%	15%	39%	N/A	N/A	N/A	N/A
N_W-N_B	55.5	105.5	38.9	99.8	N/A	N/A	N/A	N/A

4.3.2 Iteration 2

The second iteration conducted using the radiance method follows the same stages (A-G) as outlined in Section 3.5.1 but was applied to images extracted from the videos of experiment C2. Different images from those used in Iteration 1 were chosen to further assess applicability and challenges that might be associated with utilizing the method to track smoke evolution in images recorded during full-scale fire tests. In the first iteration, the smoke density trace from the pixel analysis areas at the bottom right of the window recorded by Cam1 was discounted (and therefore not shown in Table 4.8) because there were observers who disrupted the lighting levels at that position by looking through that window at various times during the experiment. In this iteration, it was decided that the estimate of smoke density obtained using pixel analysis areas from the bottom right portion of the window should be included because it could provide useful information about using pixel analysis areas located in the window when there were no observers present. The second iteration of application also included more and varied contrast pairs to see which pixel analysis areas produced the best results. Use of the varied pixel analysis areas resulted in two primary takeaways for future iterations as outlined here.

The first important result is illustrated with the two smoke density traces versus time shown in Figure 4.16. These two traces are from pixel analysis areas chosen at locations near the bottom of the velocity probe (P:B) and to the top left of the window (W:T,L). Comparison of the trends in smoke density, as calculated at these two positions, with time are notable because the traces appear to be very similar but with magnitudes somewhat symmetric relative to one another, about zero initially and then steadily increase reference value for times longer than 360 seconds into the fire. The observed symmetry was interesting because it linked these two selection areas that were physically opposite from each other in the compartment (at diagonally opposed corners in a rectangular room with a fire near the middle and slightly off to one side) in an unexpected way. With the fire located between the two positions, it was considered that the data symmetry was likely due to undesirable dependence

of the results on the changing light levels from the flickering and growing fire. The radiance values obtained from the velocity probe rack, wrapped in white insulation, proved to be influenced by reflected light from the fire. The bottom of the velocity probe rack and was, therefore, not used as a location from which to take pixel analysis areas again. However, the observation prompted the idea of using pixel values from reflecting surfaces to estimate the window and fire "brightness" and thus better understand influences of these elements on the smoke density values over time. Use of a reflection was ideal because it allowed measurement from discrete areas rather than attempting to measure the light change from the (physically) growing fire and shrinking window area (as the smoke covered it).

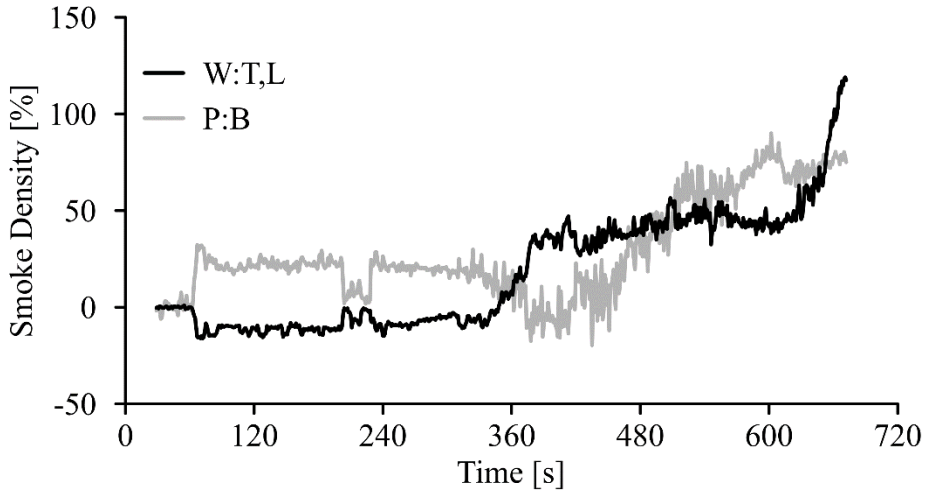

Figure 4.16: Iteration 2 smoke density results for experiment C2 Cam1 at the top left corner of the window (W:T,L) and bottom of the velocity probe (P:B)

The second key result was that the choice of pixel analysis and thus, contrast areas, matter. Pixel analysis areas were initially chosen to be located at the ceiling and also at top of the velocity probe, however, results from all of those areas were ultimately unusable because of the low contrast between light and dark areas. In fact, upon analysis of the radiance values, light and dark areas at the top of the velocity probe proved to present an 'optical illusion' whereby (what appeared to be) the "light" analysis area was actually the darker of the two contrasting areas selected. The reference contrast at this location, actually -1% rather than the positive value necessary for analysis, resulted in very unusual smoke density patterns that should have prompted investigation if the issue had not already been identified as a point of concern in the first iteration.

The lessons learned above were the primary differences between the first and second iterations. Generally, the smoke density results from after the first adjustment of the pixel areas were similar to those in the first iteration indicating further refinement was necessary. Thus, the lessons learned from Iteration 2 of the radiance analysis, conducted on video images taken in a fire experiment different than that used in Iteration 1, guided further

modification of the method, which was then tested through subsequent iterations of application to video taken during experiment B1.

4.3.3 Iteration 3

Building on the results of Iteration 2, the third iteration of the radiance method was completed using the Cam1 video recorded during experiment B1 with the method detailed in Section 3.5.1. Based on the lessons learned in the previous iteration, several additional pixel analysis areas were selected from each image and their pixel values measured, although in this iteration, the pixel values were not directly used in the smoke density calculations. Rather, the pixel values from the chosen areas or "markers" were aligned with locations of reflective surfaces in the images and were used as indicators of the fire and window brightness with aim to better understand the trends and overall behaviour of the smoke density-time traces relative to the occurrence of other events in the fire compartment (fire growth in particular).

Figure 4.17 shows plots of smoke density (left axis) with time for pixel analysis areas located at the top (T), bottom (B), left (L) and right (R) of the window (W) in the images extracted from the video recording for Experiment B1. Overlaid on the plot are the traces of pixel value obtained from the marker pixel analysis areas (right axis) to aid in synchronizing the time dependent variations in the window (WM) and fire (FM) brightness with the smoke density results. Figure 4.17 shows that the smoke density traces (left axis), from the second revision of pixel analysis areas, are in-line with expectations of smoke development during a fire. There are no large negative values or values significantly over 100%, both physically impossible if the method is applied correctly. Values of smoke density determined using the pixel analysis areas on the left of the window lead to slightly less consistent results than those from the right of the window. The evolution of smoke is credible though since the smoke density traces estimated from pixel analysis areas at the top of the window, both left and right, increase before the corresponding areas at the bottom of the window, indicating smoke is descending from the ceiling down across the window.

The smoke density trace from the pixel analysis areas at the bottom right of the window has been included in Figure 4.17; however, a data gap is visible between 240 and 360 seconds into the test. Data from this period were removed because, as noted in Iteration 1, there were observers looking through the window in that location at that time during the experiment. However, it was thought that the data (in this case missing) might provide some insight into the smoke evolution, even with the effect of those observers, and might aid in analysis when similar issues occurred. The data was not replaced here because it would distract from the other important observations from this iteration. Going forward all data is retained and unexpected patterns, such as outside observer influence, are accompanied by explanation.

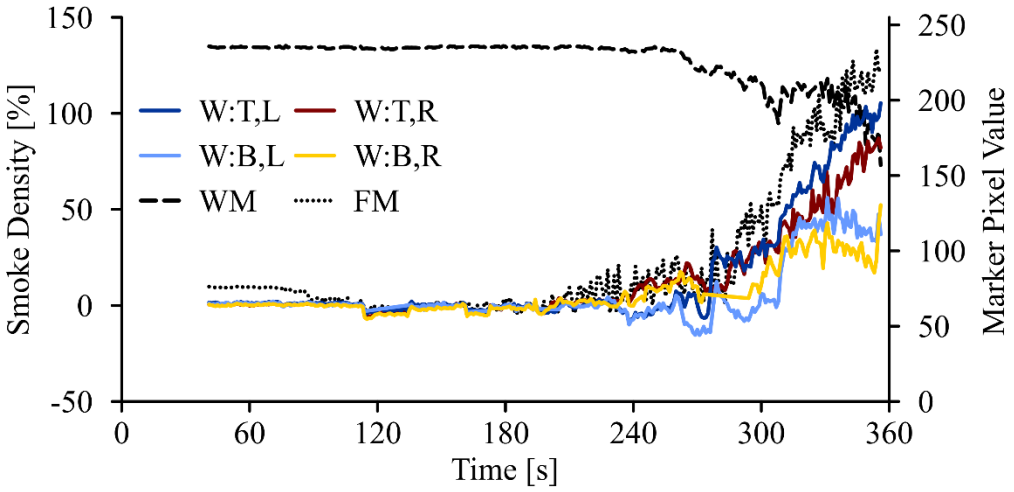

Figure 4.17: Iteration 3 smoke density results for experiment B1 from Cam1 at the window (W) with areas selected at the top (T), bottom (B), left (L) and right (R) and reflective markers of fire (FM) and window (WM) brightness

Comparison of the marker pixel values and smoke density traces Figure 4.17 indicate that the trends for all of the smoke density traces track with the fire brightness marker until light from the window begins to influence smoke density estimated using the pixel analysis area at bottom window at about 300 seconds into the experiment. The explanation is not that simple because the fire gets brighter around the time that the window provides less light, which would also be expected to occur with the presence of smoke (the sought-after variable in this analysis). Thus, from Iteration 3 it was determined that the window and fire markers were not the best indicators for better understanding the patterns in the smoke density traces. Instead, the smoke density input values (the light area and dark area values) are reviewed further and linked with time dependent smoke density patterns.

It was clear from the smoke density plots obtained during all early iterations that there was short-term variation in the smoke density results with time obtained using this early version of the radiance method though longer term trends appeared consistent with expectation. At this point, then the method was refined sufficiently to follow very general patterns of smoke development during these fires, so some of the results from this iteration of the new radiance method were included as part of a presentation at a University of Waterloo research symposium [116]. Further, the observed short-term instabilities in estimated values superimposed on top of the overall trends indicated that an appropriate averaging scheme could potentially be developed to smooth the data and aid in interpretation of the results. Accordingly, various averaging schemes were considered and investigated during development of the penultimate method. The lessons learned from these early iterations of video analysis with the radiance method iterations are incorporated in the penultimate method with results presented in the next section.

4.4 Penultimate Radiance Method Iteration: Results and Discussion

Once the lessons learned in the early iterations were incorporated, the penultimate radiance method evolved to include the nine analysis steps that were detailed in Section 3.5.2. This new penultimate method was then applied to video traces from the two living (fire) room cameras (Cam1 and Cam2) in each of the 11 historical (Type A-E) fire experiments conducted in the UW burn house. Results and further improvements are detailed sequentially in this section. Each fire experiment video recording was parsed into individual frames, and light and dark pixel analysis areas were selected from a reference frame chosen near the beginning of each video. Pixel values, extracted from each area and image, were normalized and converted into radiance values. The light and dark area radiance values were then plotted against time for areas from each experiment. These radiance values provide insight into the smoke density results, which are subsequently calculated and plotted. Finally, the time at which the smoke layer reaches the height of each contrast pair of pixel analysis areas is documented along with estimates of the maximum smoke density (if calculated values of the density converge). Results were collected for the video images taken by Cam1 then Cam2 for each experiment, as noted in Step 9, but are presented together here for discussion purposes. Various results from this penultimate iteration, with these 11 non fire-retardant (Type A,E&F), fire-retardant (Type B) and lightly fire-retardant (Type C) sofa fire experiments, have been presented at both national (Canadian) and international conferences [23,84,85,125].

4.4.1 Selecting Image Frequency

One of the lessons learned in the early iterations was that the smoke density traces tend to display short-term instabilities over time. To minimize this, six averaging schemes were considered as detailed in Section 3.5.2. The analysis was completed for images extracted from the recordings of each of Cam1, Cam2 and Cam4 in experiments A1, B1 and C1. The analysis included determination of the time variation in mean pixel values of the entire frame, of the general area of interest, and of a small light and dark area for each camera and experiment. Only demonstrative examples are provided here to support the discussion.

The first three data analysis schemes were based on comparing the raw mean pixel values determined from pixel analysis areas taken from images captured at various rates. First the mean pixel values in each pixel analysis area were determined by analyzing every frame (30Hz) of a video recording, while the second and third schemes were based on assessment of mean pixel value data from those same analysis areas, but based on values determined from a sequence of images extracted at one frame per second (fps) and at one frame per 10 seconds (1Hz and 1/10Hz, respectively) throughout the recording. The first option uses the maximum possible data for each pixel selection area. For the second option, the full data set was sampled at the rate used in the early iterations of Section 4.3 where observed instabilities in the results brought about this investigation. It was thought that the third option might

provide appropriate but smoother results than the other two analysis methods. Results of the time varying mean pixel values determined from a small dark pixel analysis area in every frame (grey dots), in images taken at 1 fps (black line) and in images taken at one frame every ten seconds (red line) from the video recording of experiment B1 Cam2 are shown in Figure 4.18. Two things are evident: 1) the results derived using any of the three analysis options follow the same broad pattern, and 2) the short-term instabilities in the results decrease with reduction in the frequency of data capture.

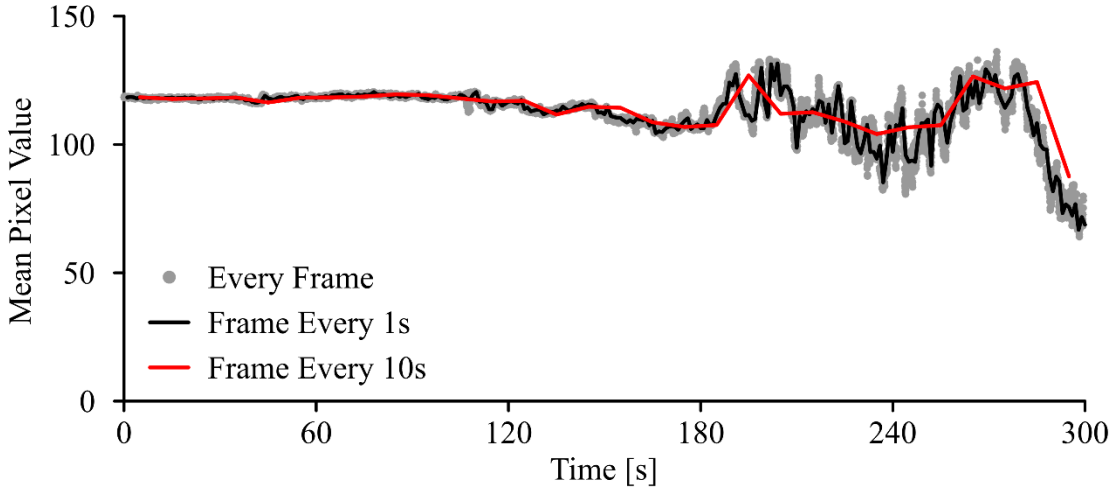

Figure 4.18: Mean pixel values from the small dark area of experiment B1 Cam2 for a frame every 0.017 s (grey dots), 1 s (black line) and 10 s (red line)

The relatively wide range of scatter in the data extracted from every frame and plotted in Figure 4.18 shows that the radiance analysis method is sensitive to “short-term” fluctuations in lighting and fire intensity. However, the overall trends followed by the grey scattered points on the plot indicate that “longer-term” time dependencies in the smoke evolution do appear to be captured. Using pixel values extracted from pixel analysis areas taken at one frame every second similarly follow the longer-term trends. However, the short-term fluctuations do not consistently follow a 1-second cycle so, by evaluating images at 1-second intervals, this analysis effectively selects a random point in the short-term fluctuations capturing parts of the short-term fluctuations as seen in the black line on Figure 4.18. While the pixel values obtained from pixel analysis areas taken from one frame every 10 seconds are not subject to the same amount of short-term fluctuations, the values still correspond to random values as a result of the short-term fluctuations; thus, this extraction rate may not always capture the true nature of the longer-term fluctuations in smoke within the fire compartment. In consequence, different averaging schemes were employed to see if it was possible to capture the longer-term fluctuations in pixel values without the same levels of short-term fluctuation in results.

Two simple average options were considered. In the first averaging option, the mean pixel values from the same selection areas in every frame were averaged over a one-second time period (*i.e.*, 30 data points per average value) and the resulting average values assigned to the 0.5 second point. In the second averaging option, pixel values determined from pixel analysis areas in images taken at one frame per second from the recording were averaged over a 10-second period (*i.e.*, 10 data points per average value) and results assigned to the 5 second point. When these two averaging schemes were applied to the same small dark area in images from experiment B1 Cam2 as used above, results in Figure 4.19 were obtained for the 1 s average of the raw data from every frame (black line) and the 10 s average of the raw data captured at 1 fps (red line). For reference, the raw data from every frame (grey dots) is included in the plot as well. Results from both of these averaging schemes follow the broad pattern visible in the raw data from every image, and fluctuations in values decrease with decreased number of data points in each estimate.

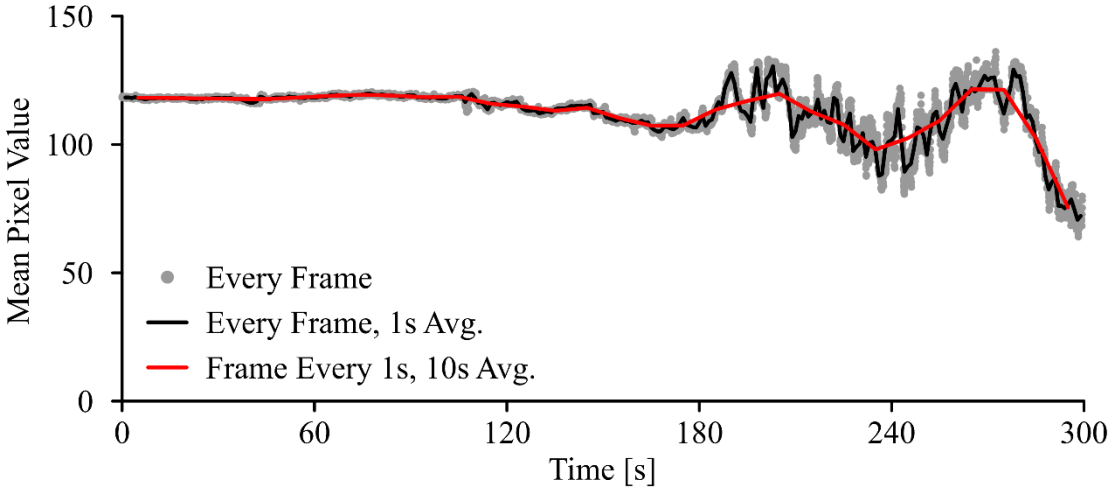

Figure 4.19: Mean pixel values from the small dark area of experiment B1 Cam2 for a frame every 0.017 s (grey dots), a 1 s average from a frame every 0.017 s (black line) and a 10 s average from a frame every 1 s (red line)

As seen in Figure 4.19 averaging the data from every frame increased processing time and effort, while still capturing both short- and longer-term fluctuations in the mean pixel values. In contrast, the 10 s (10 point) average of data from images extracted at 1 fps from the original video trace results captures most of the longer-term fluctuations while smoothing out short-term fluctuations in value. Conducting smoke evolution analysis based on only one data point every 10 seconds is not sufficient, given that the smoke layer can descend through the area of interest at a rate of 0.04 m/s or faster (as demonstrated by experiment A2 in Section 4.1.1). Thus, an image frequency and averaging scheme combination that contained more data points but was not as influenced by short-term fluctuations in value was still needed.

A happy medium was found by using a 10 s rolling average of the mean pixel values determined from images extracted at 1 fps from the original video trace with average value centred on the fifth data point. Results of this averaging method applied to mean pixel values obtained from the same experiment and selection areas used above are shown in Figure 4.20 as a blue line. Again, for reference, the averaged line is superimposed on the data determined for every frame (grey dots). It is immediately evident that this averaging scheme captures the longer-term fluctuations, without being overly influenced by short-term fluctuations, while still providing a data point every second.

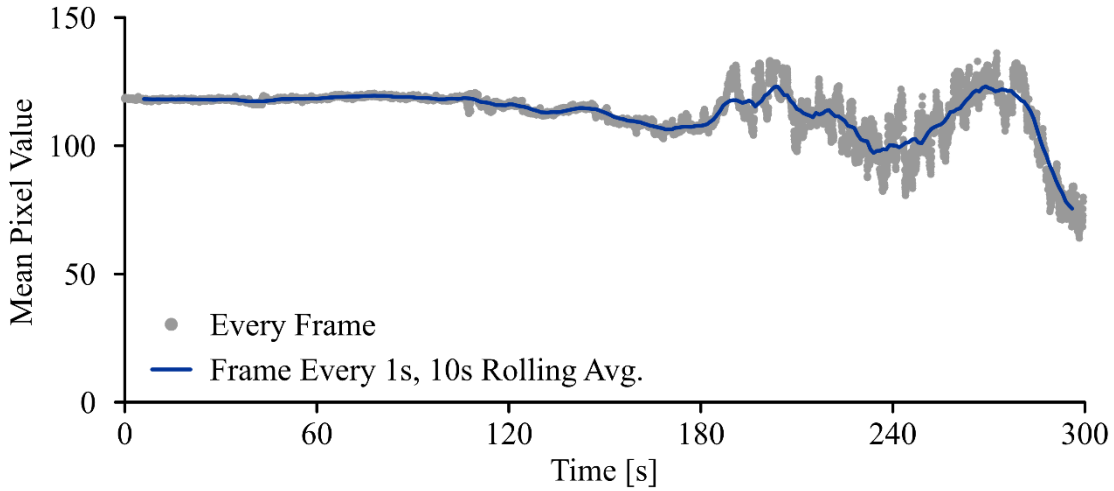

Figure 4.20: Mean pixel values from the small dark pixel analysis area of experiment B1 Cam2 for a frame every 0.017 s (grey dots) and a rolling 10 s average from a frame every 1 s (blue line)

Figure 4.21 shows results obtained using the same averaging scheme, the 10 s rolling average of 1 fps data from small light (left plots) and dark (right plots) pixel analysis areas from images extracted from the Cam1 (top plots) and Cam4 (bottom plots) video recordings for Experiment B1. Compared to the background grey scatter points of the mean pixel value data determined using the pixel analysis areas in every frame, this averaging scheme also worked well for all cameras and selected areas in that experiment. The same was true for each of the pixel analysis areas analyzed in images from video recordings of the other two experiments. Images were extracted at 1 fps from each of the recordings and a 10 s rolling average of the mean pixel value data from each chosen pixel analysis area was used to obtain results in the penultimate method iteration.

In the next step, per the method outlined in Section 3.5.2, video recordings from all 11 Type A-E sofa fire experiments were parsed at a rate of one frame per second. A reference image was selected from the beginning of each recording. From the reference image, several contrast pairs of light and dark pixel analysis areas were identified and selected based on requirements identified and lessons learned during derivation and early iterations of the

method. Mean pixel values were extracted from the contrasting light and dark areas and were converted to radiance values. Then, the light and dark area radiance values were plotted and analyzed to gain a better understanding of their relationship to the smoke density results obtained from the method as well. The light area radiance results are discussed in detail next.

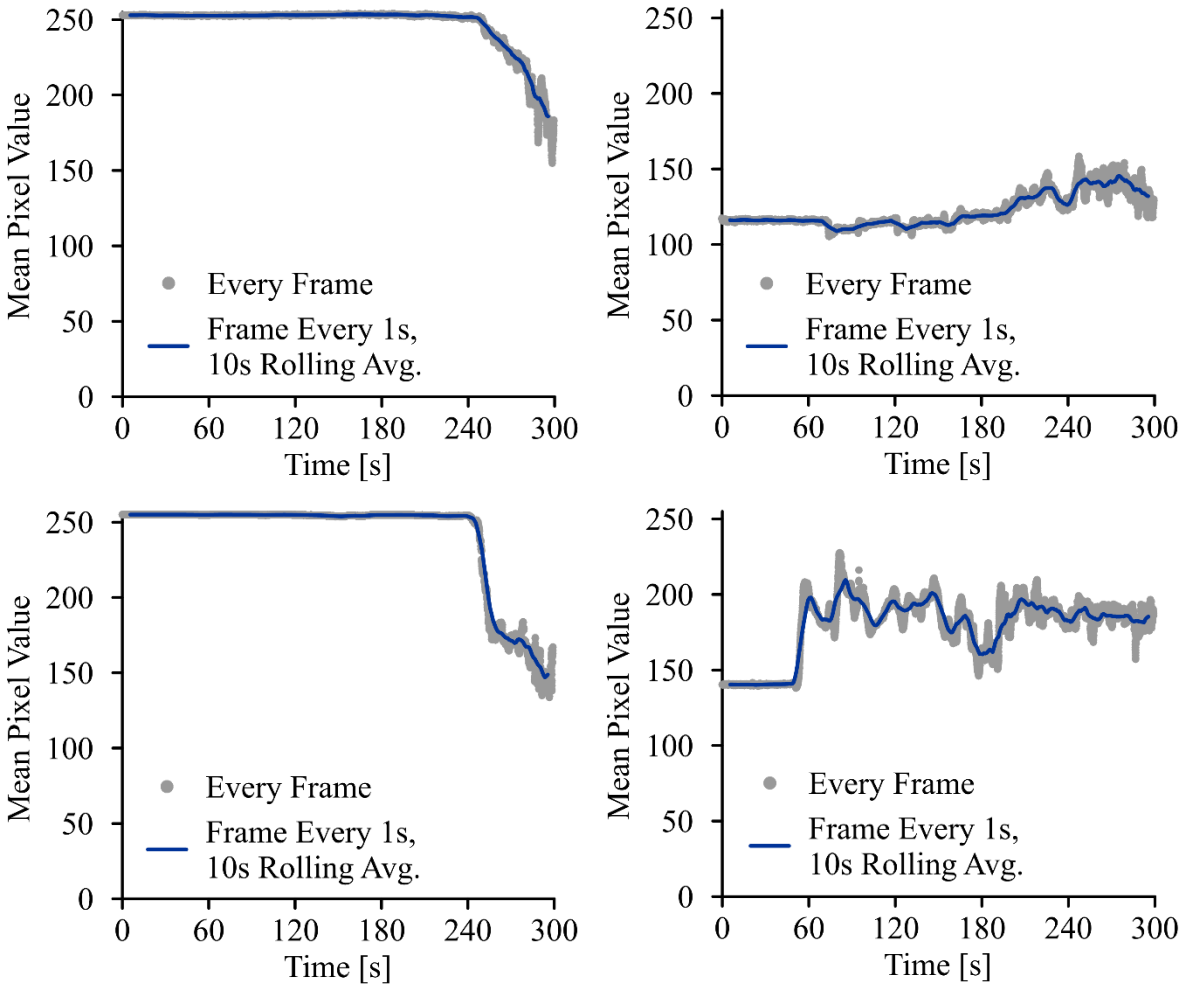

Figure 4.21: Mean pixel values from the experiment B1 Cam1 (top) and Cam4 (bottom) small light area (left) and small dark area (right) for a frame every 0.017 s (grey dots) and a rolling 10 s average from a frame every 1 s (blue line)

4.4.2 Light Area Radiance

While light area radiance analysis was completed for all pixel analysis areas in 11 fire experiments fueled by five material combinations, as was every step of the penultimate radiance method, only a selection of plots that highlight the relevant outcomes guiding the refinement of the radiance method are presented here. Two plots of normalized light area radiance values (LRV) against time are shown below. The first, Figure 4.22, shows

normalized LRVs with time for pixel analysis areas located at three heights in the fire compartment for images extracted from each of the video recordings from Cam1 (z=1.55 m, 1.40 m and 1.25 m) and Cam2 (z=1.70 m, 1.55 m and 1.40 m) in experiment B1. Figure 4.23 contains plots of the normalized LRVs with time at a height of z=1.55 m from videos recorded by each of Cam1 and Cam2 during all three Type A sofa fire experiments (A1, A2 and A3). In both plots, the normalized LRVs begin near 1 (pure white) as expected and, at some time into the experiment, each LRV drops in magnitude indicating that the pixel analysis area is becoming darker. This behaviour follows the expected pattern for a light area being filled with smoke and thus bodes well for success of the radiance method for smoke density analysis in fires.

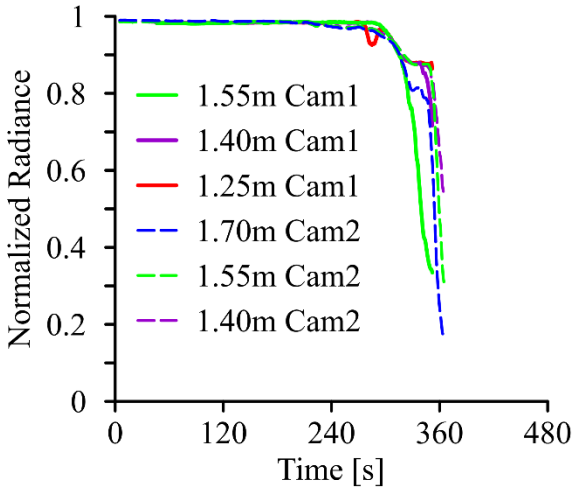

Figure 4.22: Experiment B1 normalized light area radiance values with time at four heights (z=1.70 m, 1.55 m, 1.40 m, 1.25 m) from Cam1 and Cam2 [85]

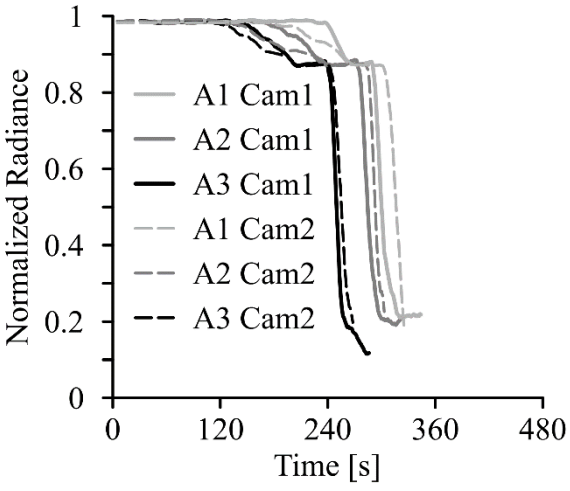

Figure 4.23: Normalized light area radiance with time at z=1.55 m in Cam1 and Cam2 from the three Type A repeat experiments (A1, A2 and A3) [85]

Figure 4.22 shows a slight lag between trends in the normalized LRVs obtained from pixel analysis areas located at z=1.55 m and z=1.40 m above the floor from images recorded by Cam1 versus those from Cam2. The same delay appears in normalized LRVs obtained from pixel analysis areas located at z=1.55 m in images from each experiment as plotted in Figure 4.23. This delay might be explained by proximity of the fire to the pixel analysis areas chosen in the images from Cam2 recordings. The fire may have delayed the apparent 'visible' presence of the smoke layer because additional light from the growing fire would increase the amount of light that is reflected into the visible light path (discussed in Section 3.4). It is not clear that this is the only effect, however, since the image in Figure 4.24 also indicates that the delay could be a result of delayed progress of the smoke layer in proximity to the fire due to the presence of the burning fire itself.

Figure 4.24: Fire proximity impact on smoke layer visible in angle of smoke layer over window

Further examination of Figure 4.22 and Figure 4.23, indicates a small drop of about 0.1 followed by a plateau in LRV visible in both plots at around 300 s and 120-240 s into the fire, respectively. This drop is related to the individual colour streams within the image and are discussed in detail in Section 4.5.4. For now, the most important component of these plots are the large, rapid drops following the plateau which appear to be related to the smoke layer passing though the height of the selected light pixel analysis areas in sequence. This is supported by the timing of these normalized LRV drops which, in Figure 4.22, appear at the highest location first and the lower locations subsequently in descending order for both Cam1 and Cam2.

The normalized LRV traces plotted in Figure 4.22 and Figure 4.23 also point to two other important aspects of the radiance method: repeatability of results and ability of the method to differentiate smoke development in fires of different fuel types. Previous works have established that the Type A-C experiments were repeatable within each material type and that each different (A-C) sofa material combination produced different results [86]. The same patterns were observed in smoke layer height and density characterizations in Sections 4.1 and 4.2, respectively. In Figure 4.23, which shows results from the repeated Type A experiments determined using pixel analysis areas located at the same height in each image, the patterns of normalized LRV variation with time are close together, as would be expected for repeatable results. These repeated Type A results show that the smoke layer likely passes z=1.55 m around 240-330 seconds into the fire while Figure 4.22 shows that the smoke layer likely passed z=1.55 m between 330-390 seconds in experiment B1. This difference in timing between Type A and B experiments does not appear too large but such differences become much clearer when all five material combinations (Type A-E) are considered together. Thus, normalized LRV traces with time determined from comparable pixel analysis areas analyzed in images extracted from video recordings of the fire experiments for each of the material types are shown in Figure 4.25.

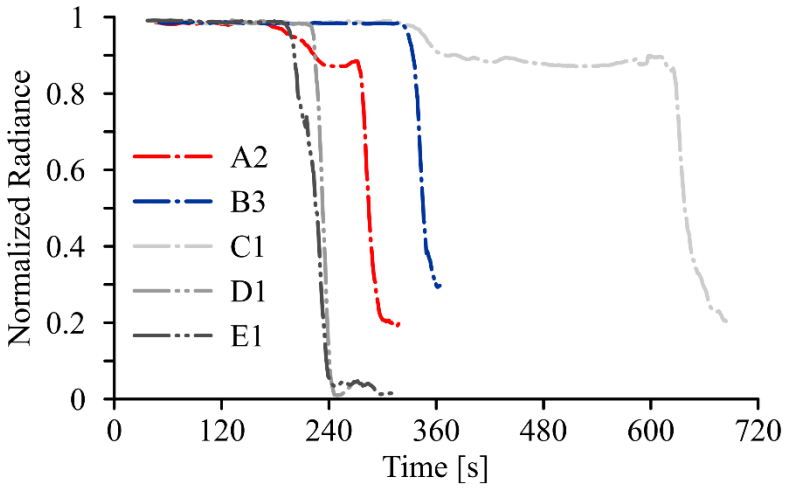

Figure 4.25: Light area radiance with time at z=1.55 m from Cam1 in experiments A2, B3, C1, D1 and E1 [85]

As expected, Figure 4.25 shows clear differences between the variation of normalized LRV with time determined from video traces of fires fueled by different materials. Based on the LRV results from experiments A2, B3 and C1, it appears that the smoke layer descends to z=1.55 m, from fastest to slowest, for Type A, Type B and Type C sofa fires. This observation agrees with the smoke layer height characterization of Section 4.1. The Type A, B, and C results can be directly compared since they had the same ventilation conditions, so the fuel material is likely the largest factor driving differences between the experiments. Differing ventilation conditions and fuel materials in the Type D and E experiments mean that, while the normalized LRV results from experiments D1 and E1 clearly indicate different and apparently much faster decay in LRV for this pixel analysis area, the trend in values is not solely related to the fuel type and so should not be compared to the other results in that context.

Collectively, analysis of normalized LRVs from light pixel analysis areas selected in images taken from all experiments show significant promise for the penultimate radiance method for analysis of smoke evolution from videos recorded in a wide range of fire experiments. As intended, they also appear to provide more information that helps in understanding details of the smoke density calculations to come. The next phase of development and proof of a full radiance method is to examine the dark area radiance values.

4.4.3 Dark Area Radiance

Normalized dark area radiance values (DRVs) determined using pixel analysis areas selected from images extracted from video recordings of the 11 Type A-E experiments were examined next. Several observations could be made, and conclusions drawn. Select plots are included here to facilitate discussion. It was found that the most important take away of this

part of the analysis was that it was difficult to interpret normalized DRVs in isolation. However, DRVs are a necessary element in development of a robust radiance method for analysis of smoke evolution in fires.

Normalized DRVs are plotted against time in Figure 4.26 and Figure 4.27 for images extracted from Cam1 and Cam2, respectively, videos in Experiment B1. Figure 4.26 shows normalized DRVs determined from pixel analysis areas located at five heights (z=2.30 m, 2.00 m, 1.55 m, 1.40 m and 1.25 m) within the fire compartment while Figure 4.27 displays values from areas at three heights (z=1.70 m, 1.55 m and 1.40 m). In both plots, normalized DRVs begin at a low value, between 0.1 and 0.3 (0 is pure black), which is expected and also promising in terms of contrast to the LRVs discussed above. At some point during the experiment, DRVs obtained from pixel analysis areas in images from each camera stray from the initial value but examination of the different plots suggests that they may change either up (as in most traces in Figure 4.26) or down (as in Cam2 traces in Figure 4.27).

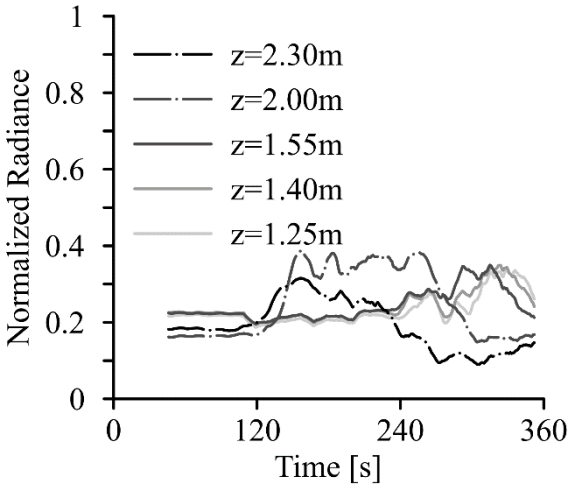

Figure 4.26: Experiment B1 normalized dark area radiance values at five heights (z=2.30 m, 2.00 m, 1.55 m, 1.40 m, 1.25 m) from Cam1 [84]

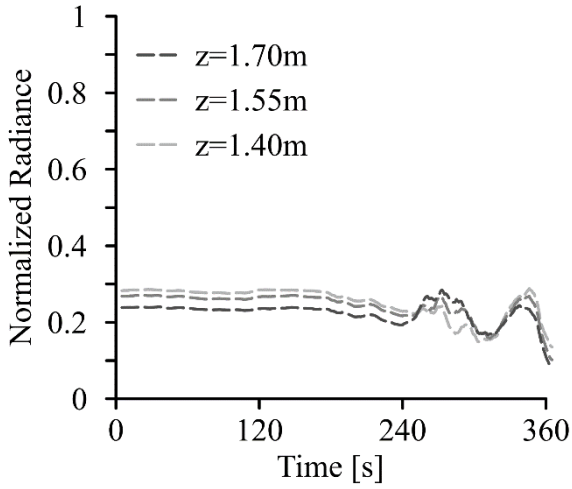

Figure 4.27: Experiment B1 normalized dark area radiance values at three heights (z=1.70 m, 1.55 m, 1.40 m) from Cam2 [85]

Unlike light area radiance that spans a wide range of values, normalized DRVs are typically confined to a small range of less than 0.3 points between the highest and lowest points. While this makes sense because the smoke produced by the sofas is typically a dark colour so the initial (no smoke) normalized DRVs are closer to the final (with smoke) values than would be expected for the normalized LRVs. The small range of values also makes interpretation of any patterns in the normalized DRVs difficult. Furthermore, it was found that the DRVs are susceptible to small external or environmental factors. For example, a person looking through the window to photograph and observe the experiment progress caused spikes and dips of up

to 0.1 points several times in one of the experiments not shown here[3]. In Figure 4.26, however, there is a dip of 0.03 points in normalized DRV for locations of z = 1.25 m and z = 1.4 m at around 115 seconds that can be attributed to external observer influence. While changes of 0.03 to 0.1 points does not seem large it does become significant when it is noted that the full range of values in a given experiment is 0.3 points or even less. Consequently, the influence of observers was common in the early method iteration results as, at the time, there were no plans to apply radiance methods for examination of smoke development (see Section 4.3).

Closer examination of the plots of normalized DRV with time indicated the DRV pattern itself is not consistent, sometimes for different pixel analysis areas even within images from the same experiment. For example, in Figure 4.26, normalized DRVs determined for different pixel analysis areas located at the highest locations on images extracted from Cam1 video recordings appear to increase when a "thin" smoke layer forms (likely attributable to a higher rate of path reflection from the broadly spaced particulate matter) while later the values appear to decrease as the smoke layer "thickens". At lower positions, DRVs appear to increase steadily and more in line with expectation. The DRVs determined based on images extracted from Cam2 videos in the same experiment (Figure 4.27) follow a different pattern with a decrease indicating smoke layer but also an increase later in the experiment and no clear marker of the onset or presence of a "thick" smoke layer.

Figure 4.28 shows normalized DRVs from experiment B3. Normalized DVRs determined from pixel analysis areas for positions related to eight heights (z=2.30 m, 2.15 m, 2.00 m, 1.85 m, 1.70 m, 1.55 m, 1.40 m and 1.25 m) in the video images from the experiment are plotted with time. In this case, the dark pixel analysis areas were extended to the ceiling in order to determine whether this might aid analysis. The results did not support this supposition.

Normalized DRVs plotted in Figure 4.28 are different than those discussed above with values that span large ranges and patterns in time that are quite difficult to interpret. This case clearly demonstrates one of the difficulties that arises in radiance analysis of historical video recordings. In this case, there was no choice but to select non-ideal pixel analysis areas to determine the dark radiance values. For example, key dark areas on the actual video images may be areas in shadow and/or impacted by glare, or have objects that are not particularly dark in the background. For this reason, the penultimate radiance method Step 4 includes plotting both the normalized LRVs and DRVs. This step is critical to interpretation of any inconsistent or unusual patterns in the smoke density results.

[3] External observers can also influence the light area results but this is much less common because it typically only happens if the observer moves precisely as the smoke layer passes through a particular location [84].

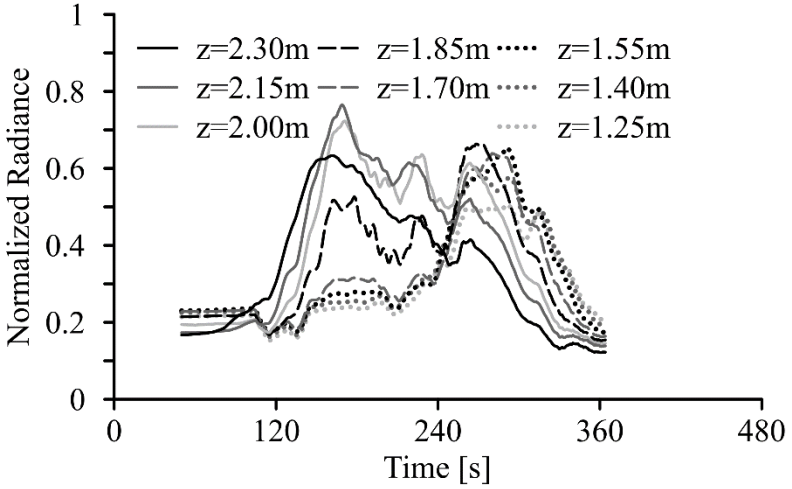

Figure 4.28: Experiment B3 normalized dark area radiance values at eight heights (z=2.30 m, 2.15 m, 2.00 m, 1.85 m, 1.70 m, 1.55 m, 1.40 m, 1.25 m) from Cam1

This DRV analysis makes it abundantly clear that interpreting smoke layer height from normalized DRVs alone, if possible, would require significant investigation that is beyond the scope of this work. However, as shown in the derivation outlined in Section 3.4, analysis of the time variations of radiance values obtained from pixel analysis dark areas is necessary to eliminate at least some unknowns from the experiment video images in order to better calculate smoke density. Thus, analysis of the present videos using the penultimate radiance method proceeds with the aid of the measured LRVs and DRVs discussed in this section. The next step involves inputting these values into the derived smoke density equation and determining the resulting smoke density progressions from each experiment. Results are presented and discussed next.

4.4.4 Smoke Density Progression

Per the method in Section 3.5.2, the smoke density was calculated from each image and contrast pair in the 11 Type A-E burn house experiments and the values were plotted against time to show variations in the smoke density over the course of each experiment. Illustrative examples of the results are included here.

Two smoke density plots are shown below. Figure 4.29 shows the smoke density values with time for three heights from each of Cam1 (z=1.55 m, 1.40 m and 1.25 m) and Cam2 (z=1.70 m, 1.55 m and 1.40 m) in experiment B1. Input normalized LRVs for these smoke density values are plotted in Figure 4.22 with normalized DRVs in Figure 4.26 and Figure 4.27. The second plot below, Figure 4.30, shows the smoke density values with time at a height of z=1.55 m from each of Cam1 and Cam2, for all three Type A sofa fire experiments (A1, A2 and A3). Input LRVs for these smoke density values are in Figure 4.23. In both Figure 4.29 and Figure 4.30, the smoke density values begin near zero (no smoke) as

expected. At some point early in the analysis (60-120 seconds), the changes in the relative magnitude of normalized radiance in the light versus dark pixel analysis areas leads to fluctuations in smoke density values at every analysis location. At a later point in the test, ideally linked with the smoke layer passing through the height corresponding to analysis areas, the value of normalized smoke density rises sharply. Since this behaviour is the expected pattern of behaviour for smoke density with time, the trends in these plots bode well for the feasibility and potential utility of a radiance-based method for tracking smoke evolution from various fire videos.

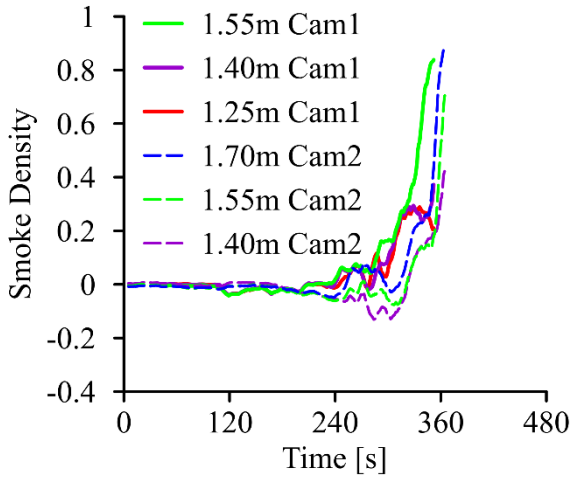

Figure 4.29: Experiment B1 smoke density values with time at four heights (z=1.70 m, 1.55 m, 1.40 m, 1.25 m) from Cam1 and Cam2 [85]

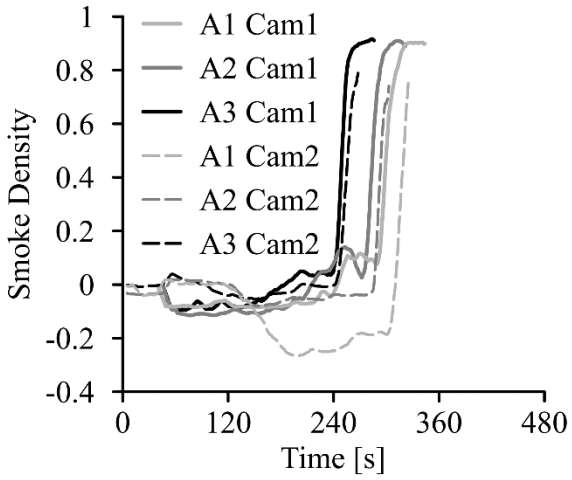

Figure 4.30: Smoke density with time at z=1.55 m in Cam1 and Cam2 from the three Type A repeat experiments (A1, A2 and A3) [85]

Due to the difficulties discussed above with interpretation of normalized DRVs, no attempt was made to interpret the comparatively small changes in smoke density that occur early in the experiment. Instead, assessment of results from this early method focused on the progression of smoke accumulation in the fire compartment indicated by the large changes in the smoke density. In over half the traces of smoke progression for experiment B1, shown in Figure 4.29, the values of smoke density do not pass the 0.5 mark (smoke layer presence indicator) before either the fire passed in front of the selected contrast areas or the camera changed to IR recording mode. In both cases, the analysis had to be truncated at this point. Conversely, all traces in Figure 4.30 exceed the threshold value of 0.5 and the presence of the smoke layer as it passes the chosen analysis position, z = 1.55 m above the floor, is clear-cut.

Figure 4.31 shows smoke density values obtained from Cam1 recordings plotted with time for experiment B3 at three heights (z=1.55 m, 1.40 m and 1.25 m). All three traces exhibit an unusually large rise and fall in smoke density value for times between 210 and 330 seconds into the experiment, just before the normalized smoke density values sharply increase,

presumably marking the smoke layer reaching each height between 330 and 360 seconds. The unexpected rise and fall of the smoke density values early in the trace is thought to be linked to the unusually large range of normalized DRVs that were shown for these traces in Figure 4.28. Therefore, this case demonstrates the importance of understanding the nature of both the normalized LRV and DRV inputs used in the smoke density equation – it is necessary to understand unusual patterns in LRVs and DRVs to truly assess the smoke density results as well.

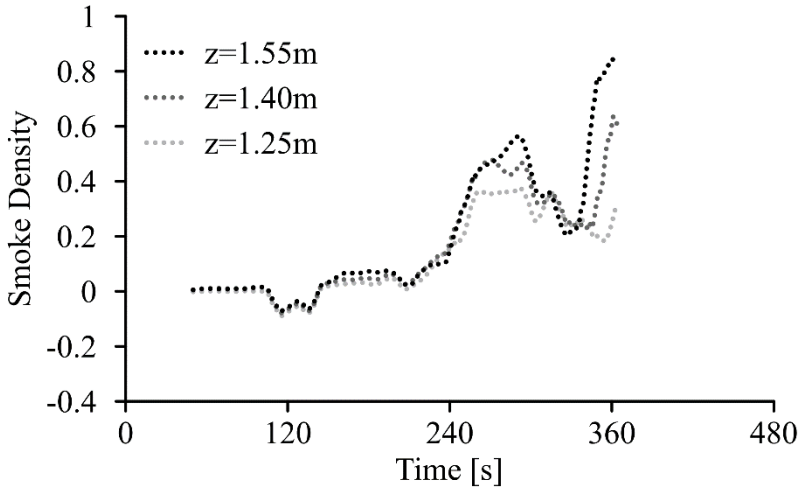

Figure 4.31: Experiment B3 smoke density values with time at three heights (z=1.55 m, 1.40 m, 1.25 m) from Cam1

The smoke density trace for analysis areas corresponding to a height of z = 1.55 m is a particularly interesting case because it involves the rare case of a premature “false positive” indicator of the presence of smoke at that location. The value of smoke density at z=1.55 m actually exceeds the threshold value of 0.5 at two distinct times, suggesting the presence of smoke at that height, followed by disappearance and subsequent reappearance of smoke – an unlikely occurrence in these fires and one that is not supported by visual observation of smoke accumulation in the videos. Thus, in general application of the a radiance method for tracking of smoke evolution, it is important to use the normalized LRVs and DRVs in combination with values of smoke density to ensure that correct values of time are correlated with smoke density surpassing the threshold value of 0.5 (in this case around 330 seconds), particularly when the radiance analysis is being used to estimate formation and height of smoke layers in the fire. Regardless of the unusual patterns in smoke density with time early in the experiment, the expected time sequence of spikes in smoke density still occurs clearly marking the descent of the smoke layer during the experiment. Thus, actual estimation of the smoke layer height within the fire compartment is the next step in analysis using the radiance method and is, accordingly, the next topic of discussion.

4.4.5 Smoke Layer Height

Two options for estimating smoke layer height using the radiance method were detailed in Section 3.5.2. The first option was to estimate the smoke layer to be present at the height of a contrast pair at a time corresponding to the time at which the value of smoke density increased above the chosen threshold of 0.5. The second option was to estimate that the smoke layer was present at a given height and time based on when the normalized LRV dropped below a chosen threshold value of 0.5. Estimates of the times at which the smoke layer descended to the heights corresponding to each pixel analysis area for these two analysis options are compared to the observer-based results of smoke layer height detailed in Section 3.2.1 and selected in Section 4.1. In the observer-based method, three independent observers estimated the time at which the smoke layer reached the top and bottom of the window resulting in the range of values contained in Table 4.9. While the analysis was completed for all 11 Type A through E experiments, results from both radiance method smoke layer height estimation options are presented here for only the six Type A and Type B experiments. These experiments were selected because they cover examples of both wide and narrow ranges of time determined during observer-based estimations of smoke layer height in the fire compartment. The results are presented and discussed for each material type before collective observations are made and discussed.

Table 4.9: Comparison of smoke layer descent times using the smoke density (SD), LRV and observer-based (Obs.) methods at four heights (z=1.70 m, 1.55 m, 1.40 m and 1.25 m), as possible with Cam1 and Cam2, in the living (fire) room of the Type A experiments. * indicates that the smoke density was close to, but did not quite reach, a threshold value of 0.5.

Exp.	Height [m]	Smoke Layer Descent Time [s]				
		Cam1		Cam2		
		SD	LRV	SD	LRV	Obs.
A1	1.70	N/A	N/A	312	309	307-331
	1.55	301	301	321	317	
	1.40	315	315	>325*	325	
	1.25	321	322	N/A	N/A	N/A
A2	1.70	N/A	N/A	289	288	250-301
	1.55	285	285	295	293	
	1.40	296	296	301	298	
	1.25	302	302	N/A	N/A	N/A
A3	1.70	N/A	N/A	251	250	244-272
	1.55	250	250	257	256	
	1.40	256	256	263	260	
	1.25	262	262	N/A	N/A	N/A

The time for the smoke layer to descend to four heights (z=1.70 m, 1.55 m, 1.40 m and 1.25 m), was estimated using smoke density increase, normalized LRV decrease and observer-based methods using video records from Cam1 and Cam2, in the living (fire) room in the Type A experiments. Results are shown in Table 4.9. The table is split into Cam1 and Cam2 results with each method, smoke density (SD), normalized LRV and observer-based (Obs.), having its own column. The range of observer times encompass the earliest time any observer marked smoke at the top of the window to the latest time any observer marked the smoke layer at the bottom of the window based on analysis of images from Cam2. In the table, * indicates that the smoke density was close to, but did not quite reach, a value of 0.5.

As anticipated, the estimated times for the smoke layer to pass all four measurement positions, determined using either the smoke density values or the LRVs, were sequenced to indicate that the smoke layer was accumulating at the ceiling and descending downward into the compartment with time. There is also excellent agreement, at most 4 s difference, between times estimated for the smoke layer to reach each height based a 0.5 threshold values for either smoke density or LRV in images from each of Cam1 and Cam2. In the one instance (Experiment A1, z = 1.25 m) where the values estimated by the two methods differed for Cam1, the time predicted based on smoke density (SD) preceded that estimated using LRV by 1 second. Conversely, for images taken from recordings captured by Cam2, the smoke descent times estimated using LRVs consistently slightly precede those estimated using the smoke density method. Particularly positive in terms of feasibility of the radiance method for this type of analysis, all of the times estimated using SD and LRV methods fall within the time range determined by observers, despite the rapid smoke layer descent in these experiments. Comparing times estimated using the video records from Cam1 and Cam2, it can be seen that estimates from Cam2 images lag slightly (≤20 s) behind those from Cam1 images, but otherwise are in good agreement for these three Type A sofa experiments. The slight lag is likely related to time lags observed and discussed previously with respect to the LRV results from Cam1 versus Cam2 as well.

A similar analysis was done on images from the two cameras for the Type B experiments, with results summarized in Table 4.10. Smoke layer descent times at the same four heights (z=1.70 m, 1.55 m, 1.40 m and 1.25 m) were estimated using the smoke density increase (SD), LRV decrease (LRV) and observer-based (Obs.) methods. The table is again split into results obtained from analysis of Cam1 and Cam2 recordings with each method, smoke density (SD), LRV and observer-based (Obs.), having its own column. As before, the observer time encompasses the earliest time any observer marked the smoke layer reaching the top of the window to the latest time any observer marked the smoke layer at the bottom of the window through visual analysis of Cam2 images. In the table, * indicates that the smoke density or LRV trace was close to, but did not quite reach, a value of 0.5 and - indicates that the smoke density or LRV trace did not even approach a value of 0.5.

Table 4.10: Comparison of smoke layer descent time using the smoke density (SD), LRV and observer-based (Obs.) methods at four heights (z=1.70 m, 1.55 m, 1.40 m and 1.25 m), as possible with Cam1 and Cam2, in the living (fire) room of the Type B experiments. * indicates that the SD or LRV was close to, but did not quite reach, a value of 0.5, - indicates that the SD or LRV did not approach a value of 0.5.

Exp.	Height [m]	Smoke Layer Descent Time [s]				
		Cam1		Cam2		
		SD	LRV	SD	LRV	Obs.
B1	1.70	N/A	N/A	354	356	231-373
	1.55	334	340	360	360	
	1.40	-	-	>365*	>365*	
	1.25	-	-	N/A	N/A	N/A
B2	1.70	N/A	N/A	385	386	178->400
	1.55	>355*	-	394	393	
	1.40	-	-	>394*	>394*	
	1.25	-	-	N/A	N/A	N/A
B3	1.70	N/A	N/A	352	368	227-397
	1.55	343	346	372	373	
	1.40	356	360	386	385	
	1.25	-	-	N/A	N/A	N/A

Time estimates based on analysis of Cam1 video images are somewhat limited, with 11 contrast pairs not approaching the value of 0.5 within the analysis time period. In addition, the Type B experiments had five contrast pairs where the smoke density (SD) values or LRVs approached, but did not quite reach, a value of 0.5. This was much higher than seen in the Type A experiments. Nonetheless, where available, the time sequences for descent of the smoke layer estimated using smoke density (SD) and LRV methods were consistent with expectation. There was also reasonable agreement, at most 16 s difference, between times estimated for the smoke layer to reach each height based on 0.5 threshold values for either smoke density or normalized LRV in images from each of Cam1 and Cam2. As in the Type A experiments, times estimated using SD values from Cam1 images tended to precede those using the LRV method. Where descent times differed between the two methods for images from Cam2, the value that lagged was not consistent, even within the same experiment (see B2 & B3 Cam2 in Table 4.10). Despite this, all times estimated using the SD and LRV methods on Cam2 images fall within the time range determined through observer-based analysis. Further, the time estimates for either method using Cam2 images also consistently lag (<40 s) behind those from Cam1 images as they did in the Type A experiments.

Collectively, both the smoke density and normalized LRV smoke layer estimation options from the radiance method performed very well in analyzing the time resolved smoke layer

descent for both the Type A and Type B experiments. Where multiple estimates of smoke descent times were available, they always indicated that the smoke layer was progressing from the ceiling down into the fire compartment. In all cases, estimates of time using the two radiance methods with Cam2 images fell within the range identified by independent observers. This implies that the threshold value of 0.5 to mark presence of the smoke layer worked well for analyses based on both smoke density values and normalized LRV estimates of smoke layer presence. A threshold value sensitivity study is beyond the scope of this thesis though a review of the smoke density plots in Section 4.4.4, Figure 4.30 for example, shows that the smoke density values rise sharply indicating that the smoke layer descent times would probably would not be sensitive to threshold value. However, values larger than 0.5, or smaller than 0.5 for LRVs, would likely result in fewer smoke layer descent values due to the analysis timeline (see values marked with an asterix in Table 4.9 and Table 4.10). The threshold value of 0.5 served to minimize "false positive" indicators of smoke layer presence, like the smoke density hump at z=1.55 m in experiment B3 discussed above, while still being low enough that the smoke density at most heights reached this value before the end of the analysis period.

Finally, smoke layer descent times estimated using Cam2 video recordings lagged (<40 s) behind those estimated based on the recordings captured by Cam1 though neither set of times was found to be definitively better than the other, in part because the observers did not review and estimate smoke layer descent from the Cam1 footage, leaving no visual basis for comparison. What was clear from the plots however, was that there were notable differences in the smoke density traces between fires fueled by different materials. This prompted evaluation of the possibility of determining a relative measure of maximum smoke density for each experiment using the radiance method as well.

4.4.6 Maximum Smoke Density

Smoke density values determined using the current pixel analysis areas clearly rise significantly as the smoke layer passes through a given analysis area, apparently depicting the arrival of smoke at the location corresponding to the area, followed by progression of the mixing zone through that area. To determine relative values of maximum smoke density, however, the smoke density trace with time must reflect the full passage of the mixing zone through the analysis areas and subsequently settle at/around a high value of smoke density value. In the radiance method therefore, the maximum smoke density can only be estimated if estimated values of smoke density reach this plateau during the analysis time period. Three examples where this was the case can be seen in Figure 4.30 for values of smoke density derived from recordings of the Type A experiments (Cam1, z=1.55 m). Of the 11 Type A-E experiments analyzed, the smoke density trace plateaued within the analysis period in only six experiments. All of these instances occurred during analysis of Cam1 recordings because

the time lag seen in smoke layer development as analyzed using recordings from Cam2 meant that the analysis period did not extend long enough for these traces to reach a plateau.

In each instance where the plot did reach a plateau, the value of maximum smoke density was calculated by averaging the estimated values of smoke density across the approximate duration of time at which they plateaued during the analysis period. These values of maximum smoke density from six experiments at each of three heights (z=1.25 m, 1.40 m and 1.55 m) are summarized in Table 4.11. The average, minimum and maximum values were then calculated and are listed in the right-hand columns of the table.

Table 4.11: Maximum smoke density at three heights (z=1.25 m, 1.40 m, 1.55 m) from six Type A-E experiments

Experiment	z=1.25 m	z=1.40 m	z=1.55 m	Average	Minimum	Maximum
A1	0.896	0.897	0.898	0.899	0.890	0.911
A2	0.897	0.890	0.891			
A3	0.903	0.904	0.911			
C1	0.849	0.866	0.872	0.862	0.849	0.872
D1	0.951	0.960	0.961	0.957	0.951	0.961
E1	0.986	0.988	0.990	0.988	0.986	0.990

Within each experiment, there is good agreement in estimated values of maximum smoke density at the three measurement heights. For Type A materials, there is good agreement between the values across the three repeat fire experiments as well, indicating that the derived results for maximum smoke density may be repeatable. In all cases presented here, the full range of estimated values (minimum to maximum) falls within ±0.01 of the average value for a given fire fuel material and each fuel results in a different average value for maximum smoke density as anticipated. The former observation shows consistency of the method and the latter consistency with results obtained previously using different methods as well.

The maximum smoke density results obtained from this portion of the radiance method indicate that fires established on Type A materials produce smoke that is more dense than that issued from fires fueled by Type C materials. This ranking is in agreement with data from the smoke density chamber tests and results determined using observer-based video analysis as discussed in Section 4.2. They show further promise for using the radiance method to estimate both the progression and macroscopic characteristics of smoke layers, in this instance the maximum smoke density. Results of maximum smoke density from videos of the Type D and E fires indicate that both of these experiments produced smoke that is more dense than either Type A or C experiments, with Type E having the most dense smoke. Relationships should of course not be drawn between these results and fuel types in the experiments, however, since there were different ventilation conditions present in each of the

Type D and E experiments and also the preceding experiments as well. Unfortunately, no material was saved from the sofas in the Type D and E experiments either, so comparative smoke density chamber tests could not be obtained. Finally, no observer-based smoke density ranks were estimated for either of these fires because of the location and orientation of the window in the Cam2 recordings for these experiments. Overall, then it is thought that further, more in-depth investigation is required to gain additional data with which to verify the validity of the radiance method for calculation of maximum smoke density across fire experiments.

Results of smoke analyses using the penultimate radiance method, as discussed in this section, proved that this novel method can yield valid and helpful data about accumulation and progression of smoke layers during fire testing. Additionally, the method developed for estimation of smoke density using radiance analysis shows promise, though it requires further validation though application to a wider subset of fire situations. From the combined results, several improvements to the methodology and instrumentation were also conceived leading to the final radiance method, with results presented in the next section. At the stage in the research, experiments were conducted with new instrumentation specifically designed to optimize collection of information needed for radiance analysis, in order to point to additional improvements that might lead to further refinement of the radiance method, as well as highlight potential modifications to experiments and instrumentation for future fire research.

4.5 Final Radiance Method: Results and Discussion

The final radiance method, following steps detailed in Section 3.6, was applied to two new Type F experiments using the modified instrumentation that was specifically designed and incorporated into the experiments with the radiance method in mind. The changes incorporated into this final stage in the research are described in more detail in Section 3.1.2. Video recordings captured by a variety of cameras are used in the analyses presented in this section. These include new cameras V1, V2, V4, V7 and V11 (layout in Figure 3.5, views in Figure 3.8) installed specifically for the Type F experiments, as well as Cam1 that was used in the historical Type A-E experiments (layout in Figure 3.3, view in Figure 3.4). The results obtained by applying the final radiance method to various pixel analysis areas in images extracted from these recordings are presented and discussed in this section and are, collectively, the culminating contribution of this thesis. Accordingly, results from each of the ten steps involved in application of the final radiance method to the images from the Type F experiments are detailed in the associated sub-sections below. Since parts of these results and discussions are directly related to results that have been discussed in earlier sections of the thesis with respect to previous iterations of the method, some sub-sections are essentially a brief re-statement of the corresponding results and discussions. Other sub-sections include considerable additional investigation into various topics in order to refine earlier iterations of

analysis and develop the final radiance method. None of the work in this section has been presented or published to date.

Step 1 in application of the final radiance method to the Type F experiment images required both an image frequency analysis and parsing of the recorded video into individual frames as outlined in Section 4.5.1. A reference image was selected from the beginning of the fire in Step 2 (Section 4.5.2). Results from Step 3, in Section 4.5.3, include outcomes of an analysis that was designed to determine whether black and white video recordings (as opposed to colour records) could be analyzed with the radiance method, as well as determinations of the preferred pixel analysis areas and the minimum size of those areas appropriate to this stage of the investigation. Section 4.5.4 details results from Step 4 including analysis of colour versus colour stream results and camera calibration results needed to convert extracted mean pixel values into radiance values. These radiance values are then converted to smoke density values and plotted for analysis in Step 5 (Section 4.5.5), while results from Step 6, presented in Section 4.5.6, include an analysis of the potential impacts of soot deposits on smoke density results. Step 7 (Sections 4.5.7) and Step 8 (Section 4.5.8) include time-traces of the individual smoke layer heights and values of maximum smoke density, respectively. Comparisons are drawn in Step 9 between results from the different cameras and across experiments (Section 4.5.9). Uncertainty embodied in the method and results is assessed in Step 10, presented in Section 4.5.10, concluding development and presentation of initial results from the new radiance method at the center of this research. To complete the thesis, conclusions and recommendations based on the results and discussions from all stages in development of the new method are collected and detailed in Chapter 5.

4.5.1 Step 1: Image Frequency Analysis and Image Extraction

An image frequency analysis from the penultimate method, in Section 3.5.2, was conducted for all three indoor camera angles in the historical burn house experiments with results presented in Section 4.4.1. The Type F experiments were very similar to the Type A-E experiments with a sofa as the fuel source in the same living room and with the same general burn house layout (historical and new layouts in Figure 3.3 and Figure 3.5 respectively). The Type F sofa material was different again than any of the materials burned in the Type A-E experiments. Cam1 and Cam2 in the living (fire) room, and Cam4 in the second floor SW room (views in Figure 3.4) were used in the historical fire experiments to record the smoke progression in those two rooms while new experiment cameras V1, V2, V4 and V7 monitored smoke progression in the living room and V11 in the second floor SW room (views in Figure 3.8). Both previous and new cameras were installed to record smoke progression in the same rooms, at the same recording rate, and with almost identical camera placements for three of the five cameras (V1, V4 and V11). The other two cameras, V2 and V7, were both positioned to observe the living room where the flickering light from the fire had caused the observed instability in radiance values determined using historical data from

Cam1 and Cam2 (see Section 4.4). Since it was deemed likely that the same issue would influence images captured using V2 and V7, the results of the frequency analysis done during application of the penultimate method was applied to determine image extraction rates from video recordings of the Type F experiments. Thus, one image was extracted from each camera recording every second for the duration of the analysis period in Step 1, and a 10 second (10 data point) rolling average centred on the fifth second was applied to the mean pixel data from each pixel analysis area in Step 4 (Section 4.5.4). This consistency allows data to be compared between Type A-E and Type F experiments without requiring additional consideration of time sequencing of the results.

4.5.2 Step 2: Selecting a Reference Image

Step 2 required selection of a suitable reference image from the beginning of the fire from which to obtain baseline ranges of pixel values for the various pixel analysis areas to be used as a scaling factor in the smoke density calculation. Requirements for reference image selection were dictated by the theoretical derivation of smoke density calculation via the radiance method (see Section 3.4) and have, therefore, not changed since they were first outlined in Stage B of the early radiance method iterations in Section 3.5.1. A reference image was selected from each video recording according to the requirements for use in the following analyses.

4.5.3 Step 3: Select Contrasting Pairs

In order to extend and refine the radiance method, several analyses were conducted using the methods detailed in Section 3.6.3. First, an analysis was conducted to determine whether the radiance method can be applied to black and white (non-colour) video recordings. The potential of this could not be verified using the video recordings for the Type A-E fires because i) only one camera, Cam4, recorded in black and white and ii) no pixel analysis areas could be found with sufficient contrast for analysis while still conforming to the area selection requirements (such as close proximity and same physical height). Following this initial investigation, preferred pixel analysis areas were determined for images extracted from videos of the Type F experiments, which now included checkerboards with designated light and dark areas. Finally, a minimum pixel analysis area size was determined across Type A-F experiments which, in turn, allowed the largest number of reliable pixel analysis areas to be selected and analyzed with the radiance method. The results of these analyses, detailed below, guided the selection of pixel analysis areas for the two Type F experiments that were then used to extract data for the results presented in Section 4.5.4 and beyond.

Non-Colour Application

As a trial, the final radiance method was applied to the non-colour, infrared images recorded by camera V11 in experiment F1. This analysis was possible because of the contrast areas created by checkerboard 11A (CB11A). Normalized light area radiance values (LRVs) and

dark area radiance values (DRVs) as well as the calculated smoke density with time at four heights (z=2.28 m, 1.98 m, 1.68 m and 1.38 m) are plotted in Figure 4.32 at the top left, top right and bottom, respectively. Time dependent trends in normalized LRVs and DRVs in these plots both resemble the DRV patterns that were difficult to interpret in Section 4.4.3; once again, this means that these values cannot be interpreted in isolation. Hence, both LRVs and DRVs must be used together, in the form of smoke density, to interpret the location of the smoke layer height at any time into the experiment. Despite both the normalized LRVs and DRVs having low values, the radiance method is able to calculate smoke density at each height with time (bottom plot) and the expected rise in value can be observed as the smoke layer is passing through a particular height.

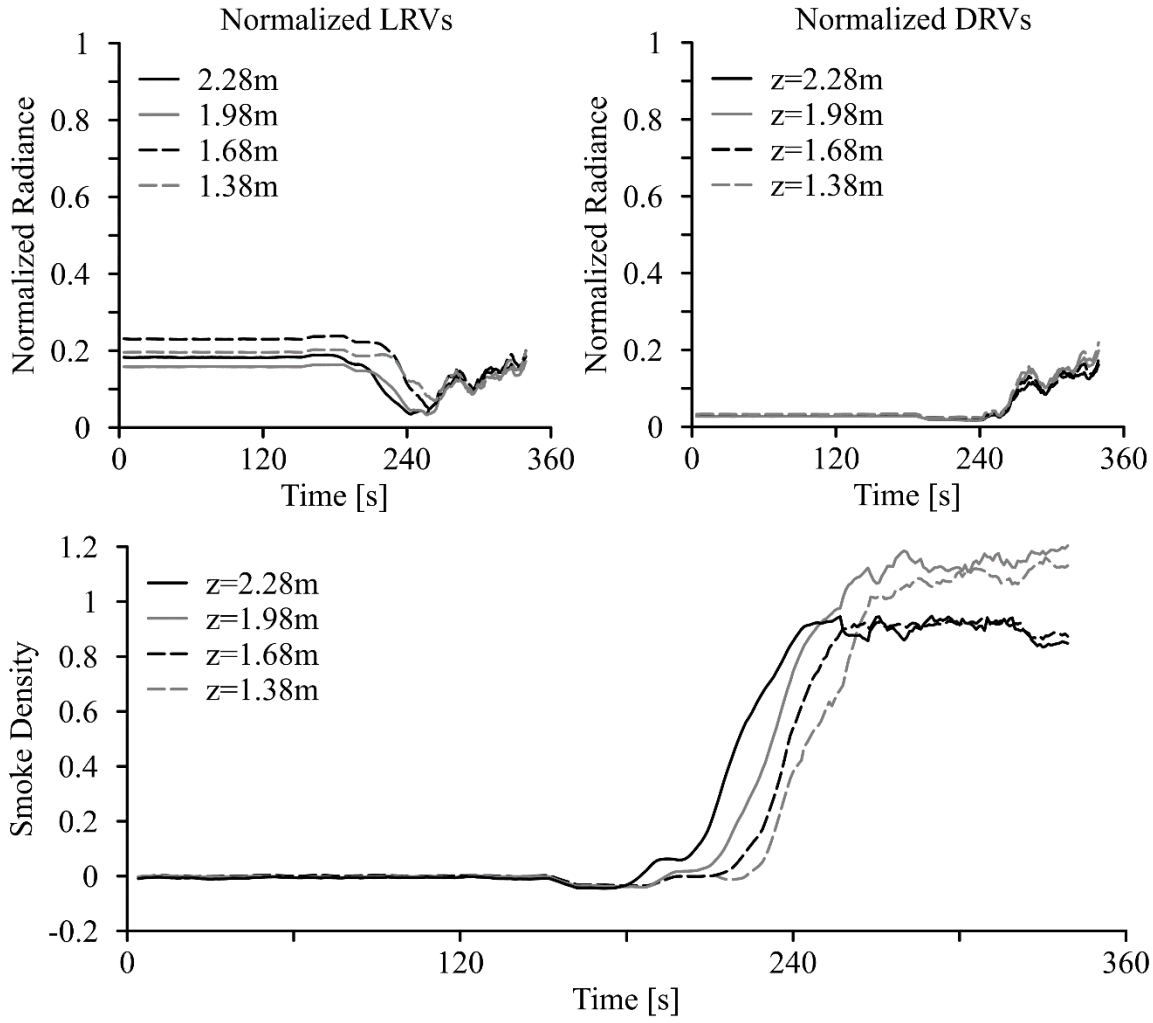

Figure 4.32: LRVs (top left), DRVs (top right), and smoke density (bottom) with time at four heights (z=2.28 m, 1.98 m, 1.68 m, 1.38 m) in non-colour images from camera V11 and checkerboard CB11A for experiment F1

Two patterns in the smoke density plot with time (bottom of Figure 4.32) are different from the results obtained previously with the penultimate method. This plot is characterized by a comparatively slow rise in smoke density values, and different plateau values. Both patterns are investigated further. The slow rise in smoke density was investigated by comparing the time for the smoke layer to descend to the four heights using three methods. The first method estimated smoke layer descent using the standard threshold value of 0.5 for smoke density as detailed in Section 4.4.5. The second followed a similar procedure but the smoke layer height threshold was a smoke density value of 0.9 instead of 0.5. Finally, the observer-based method, detailed in Section 3.2.1, was used. Three independent observers determined the times at which the smoke layer descended to the top of the relevant checkerboard square, and the range of these values, encompassing the earliest to latest times any observer noted the smoke layer had descended to the top of the square, was used in the comparison. Results from all three methods are displayed in separate columns in Table 4.12. All follow the expected pattern of smoke layer descent from the ceiling down into the compartment.

Table 4.12: Smoke layer descent time to four heights for experiment F1, camera V11 and checkerboard CB11A where observer-based values encompass the earliest to latest times any observer noted the smoke layer had descended to the top of the relevant checkerboard square

Height [m]	Smoke Layer Descent Time [s]		
	Radiance Method (Smoke Density = 0.5)	Smoke Density = 0.9	Observer-Based
2.28	221	244	237-260
1.98	233	249	258-266
1.68	239	258	266-268
1.38	246	264	268-274

The results in Table 4.12 show that the times estimated using a threshold smoke density of 0.5 in the radiance method are uniformly earlier than the observer-based estimates of times (by up to 27 seconds). If a smoke density threshold value of 0.9 is used with the radiance method, the estimated times of smoke layer descent fall either within, or closer to, the observer-based time ranges. This indicates that the observers perceived that the “bulk” of the smoke layer passed through a particular location at a smoke density value much closer to 100% (as determined by the radiance method) than the threshold of 50% used in this analysis. In this case, while a marker closer to 0.9 might be more in line with observer-based estimates of descent time, use of a threshold value of 0.5 is still recommended for the radiance method given that the original reasons for selecting this value (see Section 3.5.2) still hold true and the value of 0.5 value worked well in the penultimate method (see Section 4.4.5). Noteworthy here as well is that the results of the radiance method may differ from those visually ascertained by observers if there is a slow rise in smoke density value rather than the very rapid rise in value common in the previous results.

Another feature of the present results is the markedly different values of smoke density at the plateaus in the plots for each height as is apparent in the bottom plot of Figure 4.32 which is not at all similar to the results from the Type A-C experiments (shown in Section 4.4.6). The differences in maximum values of smoke density seen here are caused by variations in the local radiance value at different locations within the compartment. The impact of location is demonstrated in Table 4.13 which compares normalized LRVs and DRVs from the beginning to the end of the analysis times by location and designated according to the above, below, left and right designations shown on the analysis checkerboard in Figure 4.33.

Figure 4.33: Position influence of lighting on radiance values for experiment F1 camera V11 and checkerboard CB11A

Table 4.13: Position influence of lighting on radiance values at the beginning and end of the analysis period for four heights (z = 2.28 m, 1.98 m, 1.68 m, 1.38 m) in experiment F1 using camera V11 and checkerboard CB11A

Radiance Value		LRV		DRV	
		Left	Right	Left	Right
Initial	Above	0.181	0.158	0.028	0.028
	Below	0.230	0.195	0.033	0.032
Final	Above	0.185	0.172	0.198	0.161
	Below	0.200	0.198	0.219	0.175

It is clear from the results contained in Table 4.13 that both normalized LRVs and DRVs are higher (brighter) on the left hand side and lower down on the checkerboard, although the brightness varies to differing extents at specific locations. Initially, the differences in LRV (0.072) between right and left sides are much larger than those seen in the DRVs (0.005), but all radiance values finish near the same common radiance value (mean = 0.189) which, in this case, appears closer to white, though the lower left values are still brighter than the right. When the smoke density value is calculated, these input values lead to similar final values which are then scaled by disparate initial values, such that the value of the maximum smoke density at the plateau is not the same for all heights. However, going back to the derivation for the smoke density estimations (Section 3.4), it was clear that light and dark areas needed to be selected at the same height and close together. The following demonstrates of the impact of small distances between height-aligned pixel analysis areas. In this (rare) case, it was also possible to compensate for the distance impact.

Four light and dark pixel analysis pairs were selected immediately above and below the z=0.30 m black and white division line (z= 0.315 m and 0.285 m, respectively). They were near the checkerboard centerline (near) and the centerline of each square (far) as shown by the red, orange and blue boxes in Figure 4.33. These locations were selected to minimize the fisheye effect on the checkerboard and increase confidence that the pixel analysis areas were at the same height and distance from the checkerboard centreline. Figure 4.34 (left) shows the unaltered smoke density results for each pixel analysis area highlighting position dependent differences in value. The right plot shows the same smoke density results with all light area pixel values at the centerline of the square (far, dark and light blue in Figure 4.33) are shifted such that their initial pixel value is the same as the pixel value determined at the centerline of the checkerboard the same height (near, red and orange in Figure 4.33).

Several observations can be made about the results in Figure 4.34. The expected rise in smoke density is present at all positions indicating that the smoke layer passed through this analysis height. No clear pattern of descent can be observed but, given the close proximity of the pixel analysis areas, this is not unusual. Both plots also show that use of a threshold value of 0.5 to mark smoke layer height might work well in avoiding “false positives” (*e.g.*, see the short-term spike after 240 s in the ‘0.285, far’ trace of Figure 4.34) whereas a higher value (*e.g.*, 0.9 used in Table 4.12) might lead to unclear results. Since none of the smoke density traces plateau during this analysis period, maximum smoke density values obtained from each pixel analysis area cannot be compared although the traces are in much better agreement after the correction is made. Again, then the results in Figure 4.34 emphasize that it is crucial to understand the nature of the images used in the analysis as well as to select light and dark areas that are as physically close as possible.

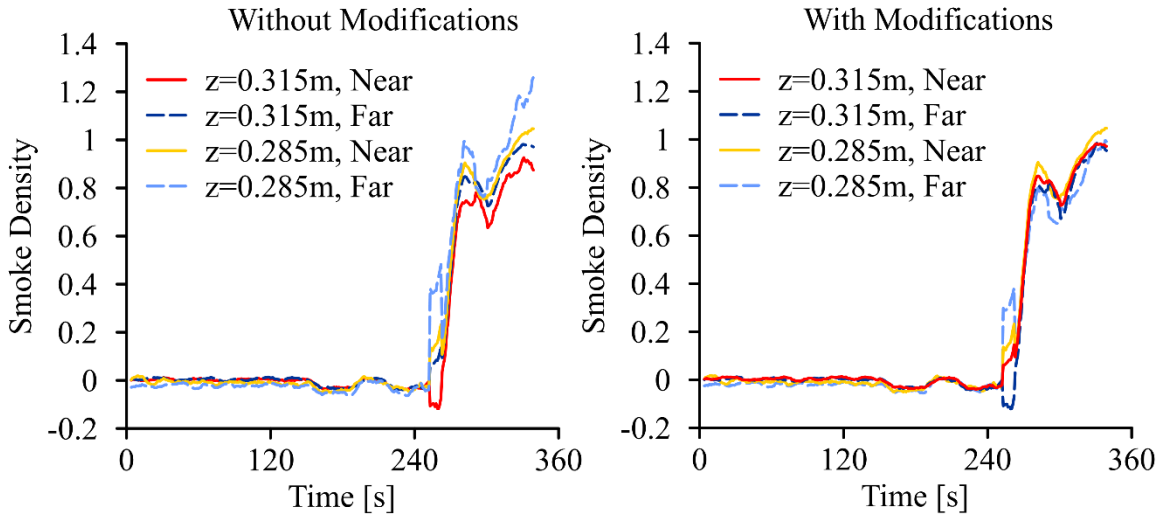

Figure 4.34: Position influence of lighting on smoke density from 4 symmetric positions around z = 0.30 m and the checkerboard centreline for experiment F1 camera V11 checkerboard CB11A without (left) and with (right) modifications

The analysis outlined above showed that the radiance method was able to produce good smoke layer height and density results using non-colour infrared recordings as well as RGB (colour) images discussed previously. This is consistent since the RGB values are the greyscale combination of the red, green, and blue colour streams of a recording so are effectively already treated as non-colour images[4]. Thus, while the radiance method has not been tested for smoke analysis on older black and white (non-colour) video recordings, it is a reasonable extension of the method which could lead to other possible applications in future.

Preferred Analysis Areas

Radiance method analysis of video recordings taken during the Type A-E burn house experiments (Sections 4.4.2 and 4.4.3) was conducted using existing background light and dark area options by necessity. The best selection areas in these experiments were essentially determined by trial and error with subsequent iteration and refinement. The introduction of checkerboards in the Type F experiments, detailed in Section 3.1.2, created additional options for selecting light and dark areas for analysis. It was interest to investigate whether results from application of the radiance method with the checkerboard installed compared favourably to results possible using only existing light and dark pixel analysis areas. As such, it was necessary to confirm that these new pixel analysis areas produced results that would justify their inclusion in future experiments and/or to establish any limitations that may exist with the use of checkerboards in the experiments or in the analysis itself. It was also

[4] The impacts of using individual colour streams to analyze smoke evolution with the radiance method is discussed further in Section 4.5.4.

important to know whether there was a significant difference in results when new and used (either cleaned or flipped as described in Section 3.1.2) checkerboards were utilized because this would influence the required resources for future experiments.

As detailed in Section 3.1.2, some checkerboards were painted with black and white squares while others were painted with black squares which contrasted with the light grey of the drywall. Prior to experiment F1, five black and white checkerboards and five black only checkerboards were installed in the 10 locations shown in Figure 3.5 and detailed in Table 3.4. As expected, during the experiment soot was deposited on all checkerboards in differing amounts and some sustained damage from heat and/or fire on their upper portions. To assess the variation in results between the black only and black and white checkboards, as well as the potential for cleaning and reusing the boards for multiple experiments, checkerboards (CB) CB1 and CB4 were replaced with black only checkerboards prior to experiment F2, CB2 and CB7 were flipped (top-to-bottom) and wiped down, and the white/light grey areas of the remaining checkerboards were simply wiped down. Analysis of corresponding video records provided a good opportunity to gain valuable information about how the values of radiance differ for pixel analysis areas captured across these circumstances. From the results, preliminary conclusions were then drawn about which contrast areas are preferable and when to replace a checkerboard in future experiments.

The first step in the analysis was to compare the radiance values obtained from each pixel analysis area at comparable locations in images extracted from the videos captured during experiments F1 and F2. Results are summarized in Table 4.14. Results were obtained from reference images for cameras (Cam.) V1, V2, V4, V7 and V11 in experiments F1 and F2 are detailed in the left-most columns. The first three cameras recorded in colour (RGB) while V7 and V11 recorded in black and white (B&W). If pixel analysis areas were selected from a visible checkerboard (CB#), the condition (Cond.) was noted as either new, flipped or wiped as applicable. V11 has two visible checkerboards CB11A and CB11B which were located different distances from the camera and are designated near and far, respectively. For both the normalized LRVs and DRVs, a brief description of the source area (Source) was provided as well as the normalized radiance value (N_W or N_B, respectively). Source area descriptions from the checkerboards are either white paint, light grey, or black paint with the remaining descriptions detailing parts of the existing living (fire) room background. The difference (Diff.) between the normalized LRVs and DRVs (N_W-N_B) is tabulated in the right-hand column of Table 4.14. Collectively, these results can be used to gain some understanding of the available contrast areas in images captured during these experiments and consequently, per Section 4.3, the likely viability of radiance method to analyze smoke evolution from these recordings.

Table 4.14: Reference normalized light and dark pixel analysis area values, and the difference (Diff.) between them (N_W-N_B) for various cameras (Cam.), Type F experiments (Exp.), checkerboard (CB#) conditions (Cond.), and areas sources

Cam.	Exp.	Checkerboard		Normalized LRV		Normalized DRV		Diff.
		CB#	Cond.	Source	N_W	Source	N_B	
V1	F1	1	New	White Paint	0.666	Black Paint	0.189	0.477
	F2	1	New	Light Grey	0.529	Black Paint	0.285	0.244
	F1	N/A	N/A	Window (New)	0.898	Concrete-board (New)	0.586	0.312
	F2	N/A	N/A	Window (New)	0.900	Concrete-board (Used)	0.424	0.476
	F1	N/A	N/A	Concrete-board (New)	0.484	Drywall Mud	0.413	0.071
	F2	N/A	N/A	Drywall Mud	0.147	Concrete-board (Used)	0.071	0.076
V2	F1	2	New	Light Grey	0.096	Black Paint	0.015	0.081
	F2	2	Flipped	Light Grey	0.056	Black Paint	0.010	0.047
V4	F1	4	New	Light Grey	0.314	Black Paint	0.124	0.190
	F2	4	New	Light Grey	0.218	Black Paint	0.079	0.139
	F1	N/A	N/A	Window (New)	0.875	Concrete-board (New)	0.373	0.502
	F2	N/A	N/A	Window (New)	0.830	Concrete-board (Used)	0.136	0.694
V7	F1	7	New	White Paint	0.078	Black Paint	0.011	0.066
	F2	7	Flipped	White Paint	0.078	Black Paint	0.015	0.063
V11	F1	11A (near)	New	White Paint	0.191	Black Paint	0.030	0.161
	F2	11A (near)	Wiped	White Paint	0.124	Black Paint	0.017	0.107
	F1	11B (far)	New	Light Grey	0.346	Black Paint	0.064	0.282
	F2	11B (far)	Wiped	Light Grey	0.208	Black Paint	0.035	0.173

It can be seen from the Table that a surprisingly wide range of normalized LRVs (0.056-0.900) were recorded while normalized values for the dark area had a smaller range (0.010-0.586). As desired, the values determined for all light areas were higher (closer to pure white = 1) than those for their corresponding dark areas with differences between values ranging from 0.047 to 0.476 depending on location. As expected, since they had with the same conditions initially, normalized LRVs determined for the V1 window, V4 light grey and V4 window, respectively, have similar values between experiments F1 and F2 (less than 0.1

points difference) as do the estimated dark radiance values determined based on black painted areas in images extracted from V1 and V4 in those experiments. Such small differences in LRVs and DRVs may be due to different outdoor lighting conditions given the location of the camera views relative to windows, visible in Figure 3.5, and the different times during the day that the experiments were conducted.

Upon further review of instances where conditions change between experiment F1 and F2 in Table 4.14, several different relationships can be gleaned from the results:

- The contrast between white paint and black paint is higher than between unpainted light grey drywall paper and black paint (V1)
- Pixel analysis areas located in backlit windows result in higher radiance differences than those situated on the checkerboards (V1, V4)
- Pixel analysis areas chosen on the checkerboards in turn result in significantly higher difference in radiance values than those aligned with existing light and dark areas in an image (V1)
- Analysis from checkerboards on used (soot covered) concrete board results in higher radiance differences than from those on new drywall (V1[x2], V4)
- Analysis of results from pixel areas on new checkerboards results in higher radiance differences than for areas on flipped checkerboards (V2, V7)
- Analysis of results from pixel areas on new checkerboards results in higher radiance differences than from areas on wiped checkerboards (V11[x2])
- Pixel analysis areas located on checkerboards farther from the camera results in higher radiance differences than areas chosen on checkerboards nearer to the camera (V11[x2])

All except the last are intuitive relationships. The last observation is particularly counterintuitive because, in the images recorded by camera V11 with the same lighting levels, the closer checkerboard has white and black paint rather than the light grey and black paint on the farther checkerboard. This also contradicts the first observation, though arguably the situations of the V1 and V11 checkerboards are not perfectly analogous. Unfortunately, there were no other images that contained two visible checkerboards aligned in a comparable orientation to the V11 checkerboards and at different distances away from the camera that could be used to verify results. Thus, the cause of this apparent discrepancy cannot be discerned with such a small sample size, though it could be related to the issues encountered during analysis of black and white recordings discussed earlier in this section. For this, and all other relationships noted above, more experiments are required to determine if the preliminary results will hold true across a wider range of fire and lighting situations.

There were two checkerboards visible in two other camera views; however, these checkerboards were angled relative to the camera which points to different important challenges that must be considered in application of the radiance method. B4 is visible in

camera V1 images and B2 is visible in V8 images. However, using these checkerboards for determination and comparison of pixel analysis areas was discounted for two main reasons. First, there would be more uncertainty in any estimated radiance values because the user would have to select either a rectangular analysis area (not preferred, discussed next in this section) or attempt to select light and dark areas that were the same size and at the same height (see derivation in Section 3.4), which is very difficult (if not impossible) to accomplish given the difficulties of correcting for perspective in the images. Thus, using an angled checkerboard is not recommended unless there is no other option. Further, in some images, the checkerboards were fully or partially blocked by objects between the camera and checkerboard such as instrumentation or furniture. In these cases, analysis was necessarily limited to only those pixel analysis areas that were entirely visible in the extracted images. Therefore, in instances where there are no other options for checkerboard location in future experiments, the checkerboard should be as square as possible to the camera and it should be verified that there is a direct line of sight between the checkerboard and camera without interference from other objects.

Based on the more promising contrast pairs in Table 4.14, the radiance method was used to obtain smoke density traces for heights of z=1.55 m in the living (fire) room. The smoke density traces from these contrast pairs, shown in Figure 4.35, were estimated based on radiance values determined using images from the four cameras in the living room (V1, V2, V4 and V7), and both checkerboard (CB) and window (W) pairs where available. Pixel analysis pairs located on the concrete board and drywall mud from images recorded by V1 were not included because they were located on the ceiling and produced poor contrast. Further, images from Experiment F2 were selected for this part of the analysis because the concrete board was used (soot covered) which increased the window radiance range thereby providing better results. For reference, observer-based minimum (- - -) and maximum (– –) smoke layer descent times (method in Section 3.2.1) have been included as vertical dashed lines in the plot. Generally speaking, the traces for smoke density versus time in Figure 4.35 follow the expected pattern, with smoke density values starting around 0, and rising as the smoke layer passes through the area, then levelling off at values of around 1. The smoke density results derived from V2 and V7 video images are slightly unstable but this is expected given the relatively low radiance ranges at this position in the reference image (as shown in Table 4.14) per Section 4.5.4.

Of the six pixel analysis areas selected and plotted, smoke density values for half of these reached the threshold value of 0.5 indicating smoke layer presence within the range of observer-based smoke layer descent times. Estimate of the presence of the smoke layer derived from pixel analysis areas on the window (V1 and V4) reached the threshold value later than the estimates derived using pixel analysis areas on the checkerboard or by visual observation. This is expected because the backlighting of the window shown in Figure 4.36 means that the smoke layer actually has to be more dense to reach the same value of ‘smoke

density' relative to the background than for pixel analysis areas that are not backlit and, thus, the presence of the smoke layer is noted later in the experiment. On the other hand, due to the increased backlighting, the presence of smoke is more marked so that values of smoke density rise more quickly than at the adjacent checkerboards as seen in Figure 4.35).

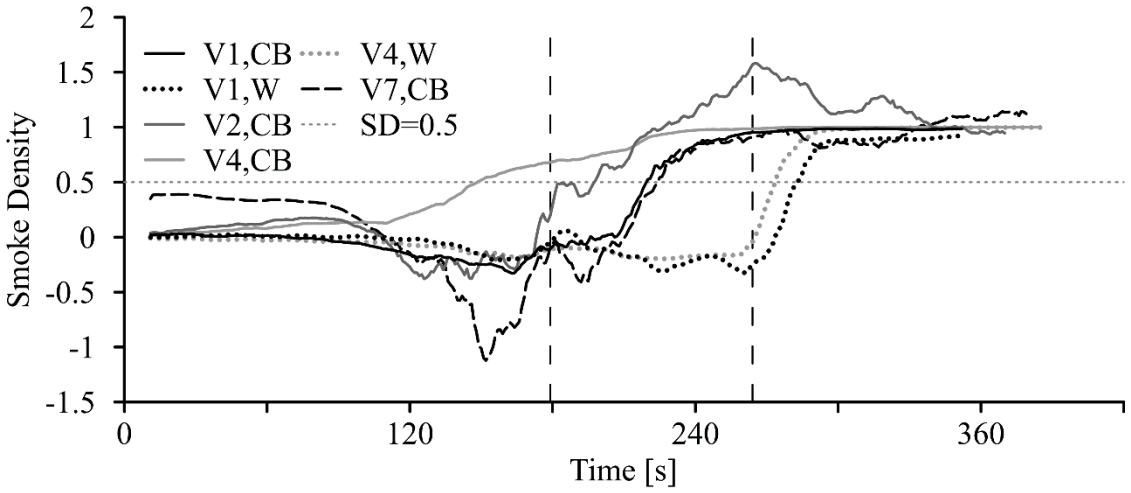

Figure 4.35: Experiment F2 smoke density at z=1.55 m from four cameras (V1, V2, V4, V7) using checkerboard (CB) or window (W) contrast areas relative to the minimum (- - -) and maximum (– –) observer-based smoke layer descent time

Figure 4.36: Experiment F2 at 270 s showing the smoke layer appearing lower on the checkerboard than the window

Conversely, application of the radiance method to pixel analysis areas on the V4 checkerboard CB4 indicates a much more gradual increase in smoke density with indication of the presence of a smoke layer earlier than determined visually from the same images by the observers. This may be caused by reduced glare from the window because of early accumulation of a fine smoke layer in this area of the compartment (seen previously in Section 4.3). It is difficult identify the full reason for the difference, however, since the slow

rise of smoke density and early estimate for the presence of smoke was also an issue during application of the method to the black and white video recordings discussed earlier in this sub-section. The issue of apparently slow rates of rise in values of smoke density may indicate that a threshold value higher than 0.5 would be the best option as a marker of smoke layer presence. For now, however, the use of the threshold value of 0.5 is recommended because the initial reasoning (see Section 3.5.2) for selecting this value still holds. On the other hand, future work may include further investigation into threshold values to mark smoke layer presence through analysis of images recorded with more camera angles, experiments, and different experimental set-ups to determine the best, non-subjective value.

Thus, while further investigation is required to determine the exact relationships between results obtained using different pixel analysis areas, some preliminary guidance for better selection of these areas to reduce uncertainty can be gleaned from the current data set. The checkerboards that are located physically further away from the fire, and possibly camera, appear to result in improved estimates of smoke density and smoke layer height. Further investigation, with other experimental set-ups, however, is required to confirm whether a threshold value of 0.5 is ideal for indicating smoke layer presence.

It is clear from the results presented above that the radiance method can be applied for determination of smoke layer accumulation and progression from images extracted from both existing and future video recordings. When using existing data from experiments, or potentially even video evidence collected for fire investigations, such as the Type A-F experiments detailed in Section 3.1.1, there are likely to be limitations related to available camera view(s) and information available about the fire situation. Conversely, to optimize application of the method for use in future experiments, it may be possible to select cameras and design camera, checkboard or other pixel analysis area placement to improve and optimize radiance method results as was done in the Type F experiments detailed in Section 3.1.2.

Minimum Pixel Analysis Area Size

The radiance method has two primary components in the analysis, the normalized LRV and the normalizes DRV, resulting in two critical output values: smoke layer height and maximum smoke density. To obtain appropriate results for these values, determination of the minimum pixel analysis area for the radiance method is critical, thus forming the basis for the investigation outlined in this section. For both output values, the difference between the radiance values and smoke density values, respectively, is the quantity of interest so the intent here is to determine how much that value changes as the size of the pixel analysis areas change. In this section of the analysis, the selected “baseline” value is 10x10 pixels (100 pixels) because this size has been used with the radiance method to obtain the successful results reported in previous sections (see Section 4.4). This size is also the largest square selection area that can be used at all three window heights (z=1.55 m, 1.40 m and 1.25 m) to

apply the radiance method to images extracted from video recorded during experiments A1 and B1 by Cam1 (see method in Section 3.6.3 for details) for comparison with values obtained through analysis of images from Experiment F1 and F2.

Time for smoke layer descent to three heights (z=1.55 m, 1.40 m and 1.25 m) in the four experiments (A1, B1, F1 and F2) were analyzed first. Eight sizes of pixel analysis area were considered and are shown in Table 4.15: 196 pixels (14 pixels in height x 14 pixels in width), 140 (10x14), 100 (10x10), 54 (6x9), 36 (6x6), 16 (4x4), 8 (2x4) and 4 (2x2). These sizes include five square (Sq., rows in Table highlighted white) areas and three rectangular (Rec., rows in Table highlighted grey) areas. The different camera resolutions used in experiments A1 and B1 versus F1 and F2 (see Sections 3.1.1 and 3.1.2, respectively) mean that each set of pixel dimensions encompassed a different physical size (mm x mm) so those are also listed in the Table. The light pixel analysis areas were all chosen at the appropriate height within the window for images captured in all four experiments while the dark pixel analysis areas were located on the adjacent concrete board as before. Pixel analysis areas from checkerboard CB1 were also used in radiance method analysis of images from the Type F experiments. The values in the columns for each experiment and pixel analysis area location and size in Table 4.15 indicate the difference in time between the time taken for the smoke density within a given size of pixel analysis area reached the threshold value of 0.5 and the time taken for the smoke density in the corresponding "baseline" 100 (10x10) pixel area to reach that value. A positive number therefore indicates that it took more time for the smoke density to increase to a value of 0.5 in the different sized pixel analysis areas than in the baseline area; likewise, a negative value indicates less time taken.

In general, agreement between the estimated times taken for the smoke layer to descend to each height were in very good agreement, with all except two values (to be discussed shortly) separated by less than five seconds. This means that, regardless of size and shape of the chosen pixel analysis areas, the estimate of time taken for the smoke layer to reach a given height within the compartment never shifted by more than five seconds, though unfortunately this does not speak to the reality of potentially larger differences occurring in some situations. Given mixing along the smoke layer-fresh air interface, and the general uncertainty of smoke layer location in fires, a larger pixel analysis area, encompassing more information, was assumed to lead to more accurate representations of smoke layer presence. Noting the differences seen here in estimated times for smoke layer descent between the largest area (14x14 pixels) and the previously used/accepted 10x10 pixel area, then suggested that a difference in estimated times of ±1 s (relative to the baseline) could be considered acceptable during optimization of pixel analysis areas.

In terms of situations that lead to larger differences in estimated times to smoke layer presence, it is immediately evident that the use of rectangular shaped pixel analysis areas (grey in Table 4.15) results in larger differences in estimated times of smoke layer presence

Table 4.15: Difference in smoke layer descent time (in seconds versus Baseline) in camera V1 from four experiments (A1, B1, F1 and F2) and three heights (z = 1.55 m, 1.40 m, 1.25 m) with square (Sq., white) and rectangular (Rec., grey) selection areas of various sizes (# of pixels and physical size [mm x mm]) taken from the window and checkerboard (CB1)

# of Pixels	Shape	Size [mmxmm]	A1	B1	Size [mmxmm]	F1	F2	F1	F2
			Window			Window		CB1	
z = 1.55 m									
196 (14x14)	Sq.	210x210	N/A	N/A	72x72	-1	-1	0	0
140 (10x14)	Rec.	150x210	1	4	52x72	0	2	1	2
100 (10x10)	Sq.	150x150	Baseline		52x52	----- Baseline -----			
54 (6x9)	Rec.	90x135	1	4	31x47	0	2	1	2
36 (6x6)	Sq.	90x90	0	1	31x31	-1	0	0	0
16 (4x4)	Sq.	60x60	1	1	21x21	-1	0	0	0
8 (2x4)	Rec.	30x60	1	4	10x21	-4	2	1	2
4 (2x2)	Sq.	30x30	1	1	10x10	-4	1	0	0
z = 1.40 m									
196 (14x14)	Sq.	210x210	-1	-	72x72	-1	0	-1	0
140 (10x14)	Rec.	150x210	1	-	52x72	2	1	2	1
100 (10x10)	Sq.	150x150	Baseline		52x52	----- Baseline -----			
54 (6x9)	Rec.	90x135	1	-	31x47	2	1	3	1
36 (6x6)	Sq.	90x90	0	-	31x31	0	0	1	0
16 (4x4)	Sq.	60x60	0	-	21x21	0	0	2	0
8 (2x4)	Rec.	30x60	1	-	10x21	0	1	3	0
4 (2x2)	Sq.	30x30	0	-	10x10	0	0	2	0
z = 1.25 m									
196 (14x14)	Sq.	210x210	N/A	N/A	72x72	-1	0	0	-1
140 (10x14)	Rec.	150x210	0	-	52x72	1	1	0	0
100 (10x10)	Sq.	150x150	Baseline		52x52	----- Baseline -----			
54 (6x9)	Rec.	90x135	1	-	31x47	0	1	1	0
36 (6x6)	Sq.	90x90	0	-	31x31	-1	0	1	0
16 (4x4)	Sq.	60x60	0	-	21x21	-2	0	1	0
8 (2x4)	Rec.	30x60	0	-	10x21	-7	0	1	1
4 (2x2)	Sq.	30x30	0	-	10x10	-11	0	1	0

than for the baseline square analysis areas. The reason for this difference was not ascertained, although it may well be a result of bias introduced into the values on account of the inherent local spatial variations in smoke layer density and height. Choice of rectangular pixel analysis areas is therefore not recommended for the radiance method. The remaining time differences of more than ±1 s relative to the baseline time estimates occur in the Type F experiments, with square selection areas of less than 6x6 pixels. Since none of the smaller square pixel analysis areas in experiments A1 and B1 resulted in similar time differences, it is clear that differences in estimates based on different size pixel analysis areas is driven by the physical size of the area chosen relative to experimental geometry rather than the number of pixels in an analysis area. With this in mind, it appears that selecting an area of less than 30x30 mm in physical size may lead to larger differences in the estimation of times to arrival of smoke layer height at different vertical positions for the kinds of fire experiments included here. Thus, a combination of rectangular pixel analysis area shape and physical size of the area relative to experimental dimensions account for the two large differences in values seen in Table 4.15 at z=1.25 m for experiment F1.

A similar analysis was conducted to analyze the impact of pixel analysis area on estimation of values for maximum smoke density at the same three heights (z=1.55 m, 1.40 m and 1.25 m) in the same four experiments (A1, B1, F1 and F2). The same eight sizes of pixel analysis area were considered and are shown in Table 4.16: 196 pixels (14 pixels in height x 14 pixels in width), 140 (10x14), 100 (10x10), 54 (6x9), 36 (6x6), 16 (4x4), 8 (2x4) and 4 (2x2). Once again, these sizes include five square (Sq., rows in Table highlighted white) areas and three rectangular (Rec., rows in Table highlighted grey) areas, with each set of pixel dimensions encompassing a different physical size (mmxmm). Again pixel analysis areas in the window were chosen as the light regions and areas on the concrete board for dark areas. Pixel analysis areas from checkerboard CB1 were used for the Type F experiments as well. The values in Table 4.16 indicate differences between values of maximum smoke density obtained through analysis of each different area size and those estimated using information for the “baseline” 100 (10x10) pixel area. All results from experiment B1 and estimates based on a pixel analysis areas in the window for images from experiment F1 have been excluded from the table because values of smoke density did not plateau at any of the three heights, so maximum values of smoke density could not be calculated. The excluded results are notable, however, because they are consistent with expectations that the choice of pixel analysis area size does not impact whether estimated values of smoke density will plateau. Instead, whether or not these value plateau in a given experiment is much more closely related to the exact nature and timing of smoke progression in each recorded fire situation.

Table 4.16: Difference in maximum smoke density in camera V1 from three experiments (A1, F1 and F2) and three heights (z=1.55 m, 1.40 m, 1.25 m) with square (Sq., white) and rectangular (Rec., grey) selection areas of various sizes (# of pixels and physical size [mmxmm]) taken from the window and checkerboard (CB1)

# of Pixels	Shape	Size [mmxmm]	A1	Size [mmxmm]	F2	F1	F2
			Window		Window	CB1	
z = 1.55 m							
196 (14x14)	Sq.	210x210	N/A	72x72	0.003	-0.001	0.001
140 (10x14)	Rec.	150x210	-0.001	52x72	0.000	0.000	0.000
100 (10x10)	Sq.	150x150	Baseline	52x52	----- Baseline -----		
54 (6x9)	Rec.	90x135	-0.002	31x47	-0.002	0.001	-0.001
36 (6x6)	Sq.	90x90	-0.001	31x31	-0.002	0.001	-0.002
16 (4x4)	Sq.	60x60	-0.003	21x21	-0.003	0.003	-0.002
8 (2x4)	Rec.	30x60	-0.004	10x21	-0.003	0.003	-0.002
4 (2x2)	Sq.	30x30	-0.004	10x10	-0.003	0.004	-0.002
z = 1.40 m							
196 (14x14)	Sq.	210x210	0.003	72x72	0.003	0.001	-0.002
140 (10x14)	Rec.	150x210	0.000	52x72	0.000	0.000	-0.001
100 (10x10)	Sq.	150x150	Baseline	52x52	----- Baseline -----		
54 (6x9)	Rec.	90x135	-0.003	31x47	-0.002	0.000	0.001
36 (6x6)	Sq.	90x90	-0.003	31x31	-0.003	0.000	0.002
16 (4x4)	Sq.	60x60	-0.004	21x21	-0.003	0.000	0.002
8 (2x4)	Rec.	30x60	-0.006	10x21	-0.004	0.000	0.002
4 (2x2)	Sq.	30x30	-0.006	10x10	-0.004	0.000	0.002
z = 1.25 m							
196 (14x14)	Sq.	210x210	N/A	72x72	0.003	0.001	-0.001
140 (10x14)	Rec.	150x210	0.000	52x72	0.001	0.000	0.000
100 (10x10)	Sq.	150x150	Baseline	52x52	----- Baseline -----		
54 (6x9)	Rec.	90x135	-0.003	31x47	-0.001	0.000	0.001
36 (6x6)	Sq.	90x90	-0.003	31x31	-0.001	0.000	0.001
16 (4x4)	Sq.	60x60	-0.005	21x21	-0.002	0.000	0.001
8 (2x4)	Rec.	30x60	-0.007	10x21	-0.001	0.000	0.001
4 (2x2)	Sq.	30x30	-0.006	10x10	-0.003	-0.002	0.002

Once again, agreement in estimated values of maximum smoke density for all pixel analysis area sizes were very good, with the maximum values of smoke density varying by no more than ±0.007 (effectively ±0.7%) between any area and the reference analysis area. Using the same concept as for smoke layer height, acceptable differences between maximum smoke density values were defined as being no larger than the differences seen in value between the 14x14 pixel analysis area and the accepted 10x10 pixel analysis area, meaning for this case differences of value within ±0.003 were considered acceptable. Unlike results seen for estimation of the smoke layer height with time, in the analysis of maximum value of smoke density, the rectangular pixel analysis areas did not appear to give results that were distinctly better or worse than from the square pixel analysis areas. This difference likely occurs because the maximum smoke density analysis is completed where the smoke is most dense (hence, maximum) rather than at the leading edge of the smoke layer where local variations are much more evident.

Differences of more than ±0.003 occur exclusively for pixel analysis areas that are chosen to be less than 6x6 pixels. In this case, however, this pattern was observed for all three experiments, and thus both camera resolutions, so that the cause does not appear to be physical size of the area as it was with the smoke layer height. In fact, in this case maximum smoke density estimates obtained using smaller pixel analysis areas in images extracted from video records of experiment A1 appear to be most susceptible to variation. This is consistent with early results from the Digital Optical Method, where it was found that using 25 or more pixels in the analysis reduced uncertainty [76][5], a number which falls between what appears to provide acceptable, 36 (6x6) pixel analysis areas, and unacceptable, 16 (4x4) pixel analysis areas, results in the experiments examined here. As mentioned in Section 3.6.3, only even numbers of vertical pixels were selected in this work, so no 25 (5x5) pixel area was tested.

Results from this section regarding application of the radiance method to both existing and new video recordings of the fire experiments collectively indicate the following for selection of pixel analysis areas in fire experiments. First, the pixel analysis areas used in application of the radiance method should be chosen as square areas of at least 6x6 pixels and represent a physical area of not less than 30 mm x 30 mm in size. Application to other experiments is required to determine whether this is a general rule or specific to these experiments. In the interim, an analysis of the impact of pixel analysis area or output from the radiance method should be conducted for each application to limit uncertainty in the results from this source.

The results of these three analyses were next used to guide further analysis of radiance values obtained from the normalized light and dark pixel analysis areas for the Type F experiments.

---

[5] The paper indicates that “rectangular areas of interest” were selected but the associated figure shows that the smaller selection areas were 9 pixels, 25 pixels and 100 pixels [76], indicating that the rectangular areas were likely 3x3, 5x5, and 10x10 squares.

In addition to images from cameras V1 and V2 that recorded in colour, images from the black and white recording from camera V7 were used in this more in-depth radiance method analysis. Pixel analysis areas were selected from the windows and checkerboards in locations where the above analyses showed that results would be favourable. Finally, based on the minimum area analysis, the finest mesh (*i.e.*, highest level of detail) used was 6x6 square pixel analysis areas, or alternatively 7x7 square pixel analysis areas in recordings where an area of 6x6 pixels on the image was less than 30 mm x 30 mm in the physical experiment. The selected pixel analysis areas were used to obtain the fine area radiance value results presented at the end of the next sub-section.

4.5.4 Step 4: Determine Radiance Values

Similar to Step 3, two new methodologies, detailed in Section 3.6.4, were conducted in Step 4 of the analysis in order to refine the radiance method prior to applying the refined method to a set of Type F sofa burn house experiment video recordings. The first analysis examines the radiance values determined using the different colour streams within the video recordings to determine whether a) the radiance method can be applied to individual colour streams from existing videos and b) whether use of an individual colour stream, rather than the full colour content of the images, may be the preferred method for determining radiance values in the analysis.

The second analysis involves calibration of the cameras. This was done during the Type F experiments to provide insight into the importance of obtaining an accurate calibration curve for converting pixel values to radiance during application of the method. The results of these analyses guided the final selection of colour components and camera calibration curve used to convert pixel values, extracted from the pixel analysis areas selected in the previous step, to radiance values for use in determination of smoke evolution during the two Type F experiments.

Colour Stream Analysis

Given that individual colour streams, red, green or blue, were found to provide different results than use of the combined RGB values during development of the Digital Optical Method [45–47], this same possibility was investigated for the analysis of video recordings of the fire experiments analyzed in this research. Thus far, the combined RGB pixel values have been used in all steps of development of the radiance method.

Every pixel in a full colour image includes three bytes of information; one for each of the red (R), green (G) and blue (B) colour streams. Each of the streams include 8 bits, with 256 possible values, which is why pixel values range from 0 to 255. All three colour streams are needed to form a full colour image. Therefore, if only one colour stream is analyzed it is effectively a greyscale image. However, rather than the more than 16 million possible colours, RGB have been used in the radiance method. RGB values are an average of the red,

green and blue values from 0 to 255 (*i.e.*, RGB = (R+G+B)/3). Thus, RGB values are also effectively a greyscale image that incorporates each of the three colour streams.

The radiance method has been applied to the weighted colour (RGB), red, green, and blue streams of the same image sequences in this section to determine the impact of the colour streams on smoke layer height and density results. This analysis was completed using data obtained from images recorded during experiments A1 and F1. Colour stream results from historical experiment A1 are presented first because it is the best place to begin explaining the method used to understand the impact of changing light conditions on the colour stream radiance method results. Colour stream results from new experiment F1 are subsequently detailed to further outline the impacts of lighting variations on radiance method results.

Time resolved values of normalized LRV, DRV and smoke density were obtained using the radiance method to analyze RGB values, as well as individual colour streams, on images taken from videos recorded by Cam1 during experiment A1. Results are shown in the top left, top right and bottom of Figure 4.37, respectively. The analysis was completed at two heights z=1.55 m (solid line) and z=1.25 m (dotted line). Results are broken down into their colour source with black representing the RGB value and red (R), green (G) and blue (B) representing the associated colour stream. In all cases, the LRV, DRV and smoke density traces generally behave as expected and clearly illustrate that the radiance method can be applied to either the RGB value or the individual colour streams. However, it is equally clear that trends and values obtained through application of the method of each of the individual colour streams, red in particular, are different.

To better understand the impact of these differences in values across colour streams, smoke layer descent times and maximum smoke density were determined for each of the traces in Figure 4.37. Table 4.17 summarizes the results by colour stream (rows) with a column for each height (z=1.55 m and 1.25 m) and each of smoke layer descent time (left) and maximum smoke density (right).

As a starting point, if RGB values (bolded) are taken as the reference, since they contain the most information about the mix of colours in an image and are used everywhere else in this work, use of the blue and green streams in the analysis appears to provide the best results. Application of the radiance method analysis using the blue stream appears slightly better for estimation of the smoke layer descent time and using green appears to be slightly better for determination of maximum smoke density. The different trends in radiance values, and thus estimates of smoke progression, determined using each of the colour streams was expected because the colour content of the image will vary with changing lighting conditions in the fire compartment, and associated changes in scattering and absorption of the smoke, throughout the experiment. Most notably, LRVs estimated through analysis of only the red stream, shown in Figure 4.37 (top left), drop by about 0.3 points around 240 s into the fire. This was when the fire started growing rapidly (more light) and the smoke layer began to fill

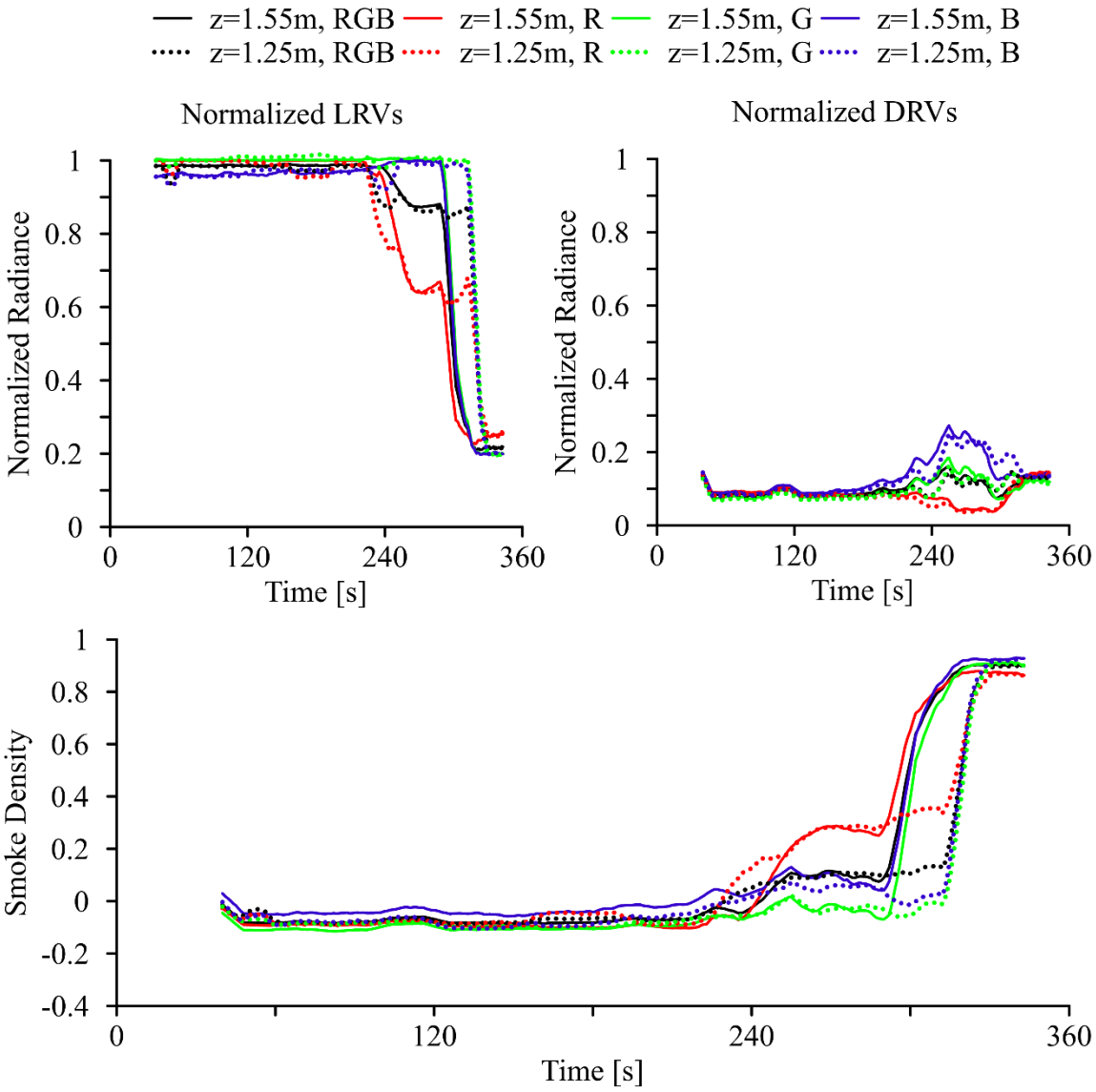

Figure 4.37: Normalized LRVs (top left) and DRVs (top right), and smoke density (bottom) with time at two heights (z = 1.55 m, 1.25 m) for experiment A1 Cam1

Table 4.17: Smoke layer descent time (in seconds) and maximum smoke density by colour stream at two heights (z = 1.55 m, 1.25 m) for experiment A1 Cam1

Colour	Smoke Layer Descent Time [s]		Maximum Smoke Density	
	1.55 m	1.25 m	1.55 m	1.25 m
RGB	**300**	**320**	**0.901**	**0.897**
Red	297	318	0.870	0.867
Green	302	321	0.909	0.906
Blue	300	320	0.926	0.921

the fire compartment (more scattering and absorption) so further investigation was required to determine how the competing aspects interact. However, regardless of cause, inclusion of the red colour content in the overall RGB value, radiance values estimated using those values decreased by around 0.1 points at this same time, as noted in Section 4.4.2. The fact that such decreases can potentially be related back to the colour content of the image by extending the analysis to use the individual colour streams suggests that it may be helpful to undertake such an analysis if unusual patterns are observed with the weighted RGB values.

To gain further insight into the differences that might occur when the radiance method was applied to the individual colour streams, the video recording of smoke descending over checkerboard CB1 taken by camera V1 in experiment F1 was analyzed next. The smoke produced in the Type F experiments may be slightly (0.03) more dense than that produced in the Type A experiments (see Section 4.5.8) but only patterns were analyzed here so this difference was not taken into consideration. Normalized LRV, DRV and smoke density results with time are shown in the top left, top right and bottom of Figure 4.38, respectively. The analysis was again completed at two heights z=1.55 m (solid line) and z=1.25 m (dotted line) with black representing RGB and red (R), green (G) and blue (B) representing the associated colour stream. In a general sense, the traces in these plots follow expected patterns though they do exhibit differences in values and trends between colour streams.

Smoke layer descent times and maximum smoke density derived using the above values in subsequent analysis are summarized in Table 4.18 for RGB value and each individual colour stream (rows) with a column for each height (z=1.55 m and 1.25 m) and each of smoke layer descent time (left) and maximum smoke density (right). Use of radiance values obtained through analysis of the red, green, and blue streams leads to slightly different results relative to the RGB results but, unlike results determined for images from experiment A1, the colour stream results that most closely match the RGB values vary by height and value of interest (smoke layer descent time or maximum smoke density).

The LRVs, and to a lesser extent the DRVs, obtained through application of the radiance method to the red colour streams and plotted in Figure 4.38 are characterized by a notable increase in magnitude for times between 120 s and 240 s into the fire. Observation of the video recording indicates that the increase in red colour content correlates to a period of growth for the fire. Initially, the smoke layer was above the windows such that light with a fairly balanced visible spectrum (approximately equal red, green and blue parts) came through the windows. As the fire established, the steadily growing flames in the fire plume generate more light in the red and yellow portions of the spectrum which then reflects off the white (and to a lesser extent black) squares of the checkerboard as shown in Figure 4.39 (left). As the smoke layer began to cover the windows and descend into the room, it scattered and absorbed red light and obscured a part of the fire. The blue light (and to a lesser extent green) began to dominate again, visibly apparent in Figure 4.39 (right) around 240 s, leading

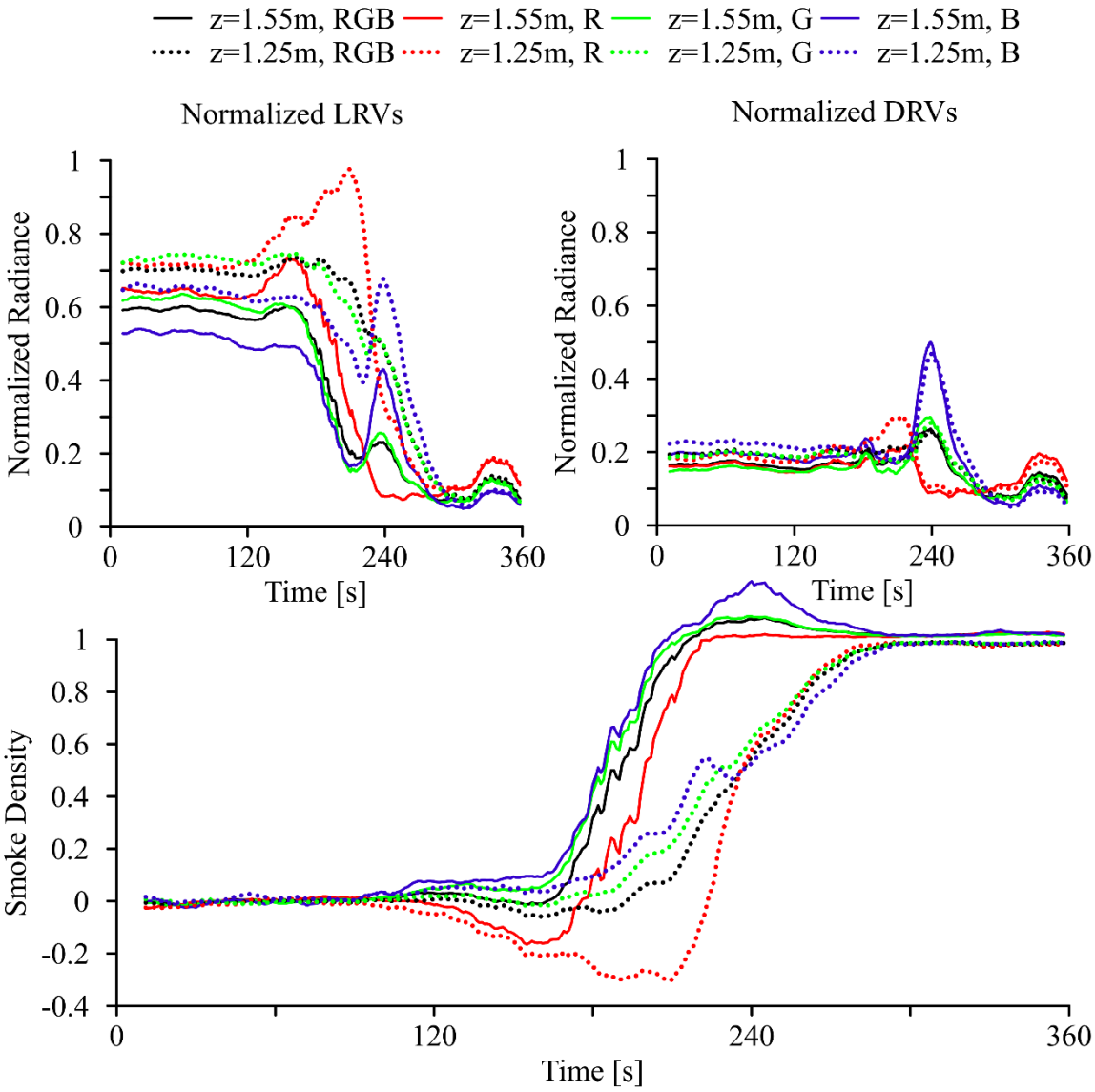

Figure 4.38: Normalized LRVs (top left) and DRVs (top right), and smoke density (bottom) with time at z = 1.55 m and 1.25 m for experiment F1 camera V1 and CB1

Table 4.18: Smoke layer descent time [s] and max. smoke density by colour stream at z = 1.55 m and 1.25 m for experiment F1 camera V1 at checkerboard CB1

Colour	Smoke Layer Descent Time [s]		Maximum Smoke Density	
	1.55 m	1.25 m	1.55 m	1.25 m
RGB	**191**	**236**	**1.020**	**0.984**
Red	200	236	1.024	0.981
Green	185	228	1.017	0.988
Blue	182	237	1.022	0.989

to a spike in the LRVs and DRVs of these colour streams as shown in Figure 4.38 (top left and right, respectively). This sequence of lighting events is consistent with results seen in experiment A1 and shown in Figure 4.37, except that in A1 the pixel analysis areas used to determine normalized LRVs are selected in the window behind the chair. With those analysis areas, the backlighting from the window dominates relative to any scattered and reflected light from the growing fire. Accordingly, only the smoke layer passing over the windows and top of the flames registered (*i.e.*, the red colour stream radiance values dropped as the smoke layer began to descend into the room).

a) F1, V1, 210 s

b) F1, V1, 240 s

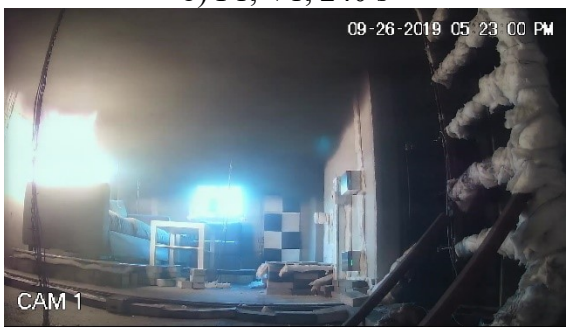

Figure 4.39: Experiment F1 camera V1 at a) 210 s and b) 240 s

This sequence of events can be verified by looking at results obtained from images recorded by the same camera V1 in the same experiment F1, with pixel analysis areas selected at the window rather than on the checkerboard. The normalized LRV and DRV results are shown in Figure 4.40 (left and right, respectively). The analysis was completed at the same two heights, z=1.55 m (solid line) and z=1.25 m (dotted line) as above, with black representing RGB and red (R), green (G) and blue (B) representing the associated colour stream as before. The plots illustrate an interesting mix of results, where the normalized LRVs resemble those for pixel analysis areas selected at the window in experiment A1 and plotted in Figure 4.37 and the normalized DRVs more closely resemble those based on assessment of pixel analysis area on the checkerboard in experiment F1 and shown in Figure 4.38.

This mix of normalized radiance plot similarities provides support for the hypothesis formed about the lighting changes in the living (fire) room during these experiments. The red stream DRVs in Figure 4.40, with selected areas on the wall beside the window, register the increasing size of the flaming fire with a spike at the same time (120-240 s) as those in Figure 4.38; however, the same spike is not seen in the LRVs, determined using pixel analysis areas selected from the window. In fact, normalized LRVs determined through analysis of the red colour stream instead exhibit a drop in magnitude around 240 s, also noted in experiment A1, and thought to be linked to formation of the thin smoke layer, which passes over the window and preferentially obscures and scatters red light from the flaming fire plume. The interactions between the descending smoke layer and light from the fire

plume is further supported by the spike in both LRV and DRV for RGB, blue and green streams at around 240 s that was consistent with that observed around the same time in values obtained using pixel analysis areas on the checkerboard in experiment F1 and (at a different time) in experiment A1.

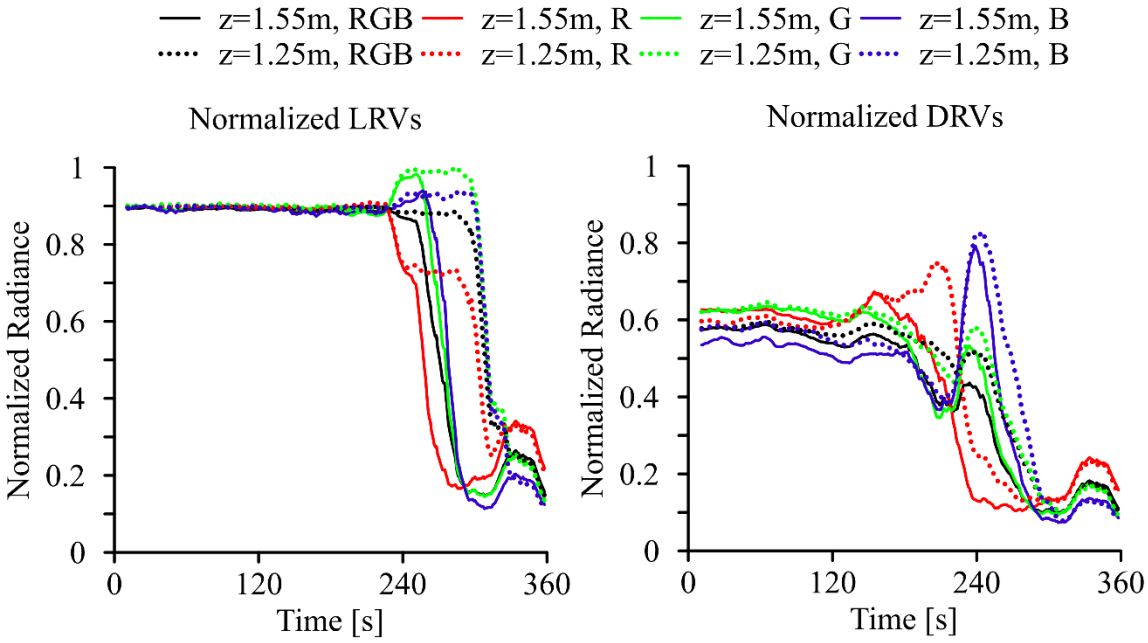

Figure 4.40: Normalized LRVs (left) and DRVs (right) with time at two heights (z = 1.55 m, 1.25 m) for experiment F1 camera V1 at the window

Clearly, different colour streams dominate at different locations and times in fire experiment as the flaming fire plume and smoke evolve within the room. Consequently, radiance analysis applied to pixel analysis areas for the different colour streams at locations adjacent to, and below a window, will likely exhibit different behaviour and potentially suggest different progression of the smoke layer under different lighting situations. Thus, to promote consistency between estimations of smoke layer height and density, it is recommended that the RGB values for each pixel analysis area in a given set of images be used in the radiance analysis. Unless the lighting patterns are well understood and there is a distinct reason for selecting a particular colour stream for analysis with the radiance method, there does not appear to be benefit in basing the analysis on any one of the colour streams. Instead, analysis of radiance values obtained using the individual colour streams has proven useful for interpreting unusual patterns in estimates of LRV and DRV and linking those to changing lighting conditions or other physical phenomena occurring in a compartment during the fire experiment of interest. Nonetheless, both corrections for lighting patterns and the use of colour streams in the analysis may well merit further investigation in any future extensions of the method.

Camera Calibration

The second part of the analysis around Step 4 in the radiance method involved a study of camera calibration that was done during the Type F experiments to determine the necessity and impact of using calibration curves for converting pixel values to radiance. Two aspects of selecting a camera calibration curve are important to the analysis: 1) the camera calibration curve itself, and 2) how the calibration curve affects estimations of the radiance values and thus smoke layer height and density results. The process used to determine the calibration curve is outlined in Figure 3.29. For this, it is necessary to first determine the encoding scheme that the camera used during recording of the video images in order to invert that scheme and generate a decoding scheme, or camera calibration curve that can be used to best restore the original information. No calibration data was available for any of the video cameras used in the Type A-E experiments, so the proof of concept upon which the radiance method was developed was completed using a direct 1:1 ratio of original to encoded information as described in discussions of the early iterations (see Section 3.5.1). This was then extended to use of a more generic gamma (γ=2.2) decoding scheme during the analysis undertaken using the penultimate method (see Section 3.5.2). As mentioned in Section 3.1.2, in development and refinement of the final radiance method, a ColorChecker Video XL unit (calibration tool) was used to calibrate the cameras in the Type F experiments in order to better determine an appropriate strategy for calibration of the cameras. Before the experiments, the calibration tool was held near each camera and at the checkerboard(s) far from the camera and images were recorded and later analyzed to determine the camera encoding scheme. Once the camera encoding scheme was determined, pixel values in images recorded during the Type F experiments could be decoded to better define radiance values, and thus examine the effect of using these calibrated values for estimation of smoke layer height and density.

Determining the Camera Encoding Scheme

The measured red, green and blue pixel values from each of 32 different colours in the calibration image were compared to the actual red, green and blue colour (radiance) values as provided by the manufacturer of the colour calibration tool. The values were plotted as measured pixel value against actual radiance value. Radiance is on the x-axis with pixel values on the y-axis because the cameras encode actual radiance values into the pixel values extracted from any given image. The lines of best fit between these values was then determined (RGB Best Fit in Figure 4.41) for all cameras in the two Type F experiments. Individual red (R), green (G) and blue (B) values were converted to RGB values by finding the averages ([R+G+B]/3) for both reference and recorded points on the calibration image with minimal impact on the line of best fit. A representative example is shown in Figure 4.41 for calibration images captured by camera V1 in experiment F2 when the calibration tool was held close to the camera (near). The scatter in this data is likely not representative of results

for calibration under the very well controlled conditions in a photography laboratory but is expected here given the atypical use of the tool for full-scale field fire experiments. The scatter plots in all cases showed that recorded pixel values increase as the actual radiance values increase and further that a line is the best function to represent the relationship. While the line of best fit in this example does happen to cross the axes near the origin, this was not the case for all cameras in the experiments.

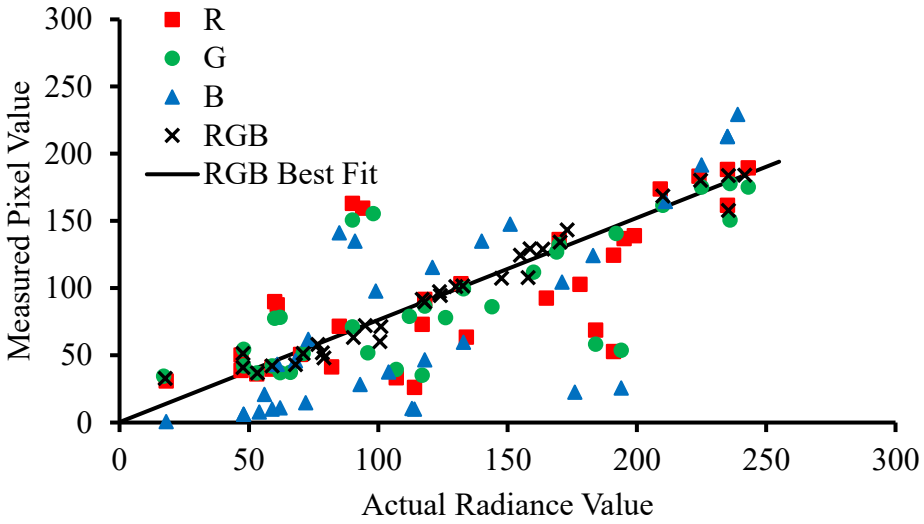

Figure 4.41: Measured red (R), green (G) and blue (B) pixel values versus actual radiance values used to determine the line of best fit for a representative RGB calibration curve (F2 V1 near)

This technique for determining the camera encoding scheme worked very well for colour images, such as the one in Figure 4.41. However, for infrared (IR) images recorded by the video cameras the RGB pixel values for the 12 non-grey colours on the right side of the calibration tool (Figure 4.42) nearly all result in very high RGB radiance values (close to pure white), which skews the line of best fit. Since this pattern was evident for all IR calibration images, these values were uniformly excluded during determination of the lines of best fit. A representative example, with red (R), green (G) and blue (B) pixel values plotted versus actual radiance values, is shown in Figure 4.42 from images recorded by camera V5 in experiment F2 with the calibration tool close to the camera (near). For simplicity, pixel and corresponding radiance values for all colours on the right side of the calibration tool (hollow symbols) were excluded from the analysis, including the dark and light grey squares (circled with a dotted line in Figure 4.42 and Figure 4.43) despite their fit with the curve. Since there were already sufficient points for determination of the line of best fit, and the same colours also exist in the lower left corner of the calibration tool (Grey 1 and 10, as shown in Figure 4.43), the exclusions were deemed acceptable here. Once again in the IR images, the

expected positive relationship between measured pixel values and actual radiance values is best represented by a line function.

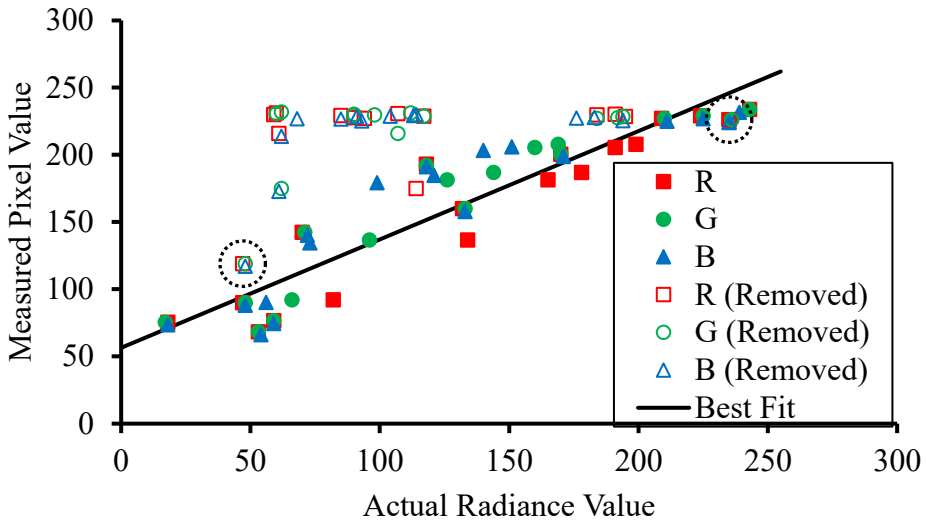

Figure 4.42: Measured red (R), green (G) and blue (B) values that are included (solid) and excluded (hollow) from the line of best fit for a representative IR calibration curve (F2 V5 near)

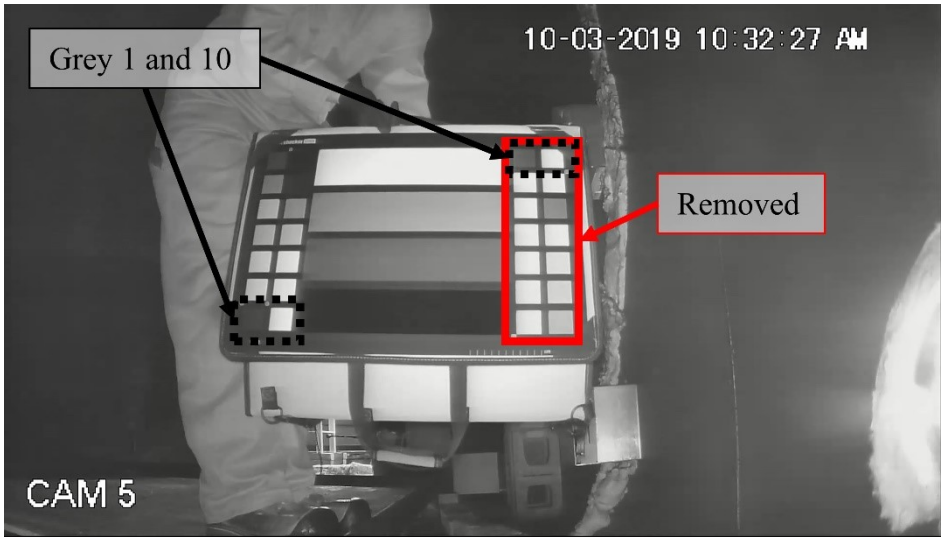

Figure 4.43: Camera calibration image used to determine the line of best fit for a representative IR calibration curve (F2 V5 near)

Finally, lines of best fit obtained using only the individual red, green or blue components of RGB value were found to have inconsistent agreement with the line of best fit based on the overall RGB value. Good agreement for lines of best fit between colour components is

indistinguishable on a plot. Thus, only an example of poor agreement is provided in Figure 4.44 for calibration images recorded by camera V5 from experiment F1. It is clear that the lines of best fit for measured pixel value versus actual radiance value based on only red, green or blue values are all different when the calibration tool was both close to the camera (near) and held at the checkerboard CB5 (far). Thus, while RGB values are used going forward per the previous analysis, if a single colour stream is used in application of the radiance method, the associated encoding scheme and calibration curve should be selected and used in the analysis.

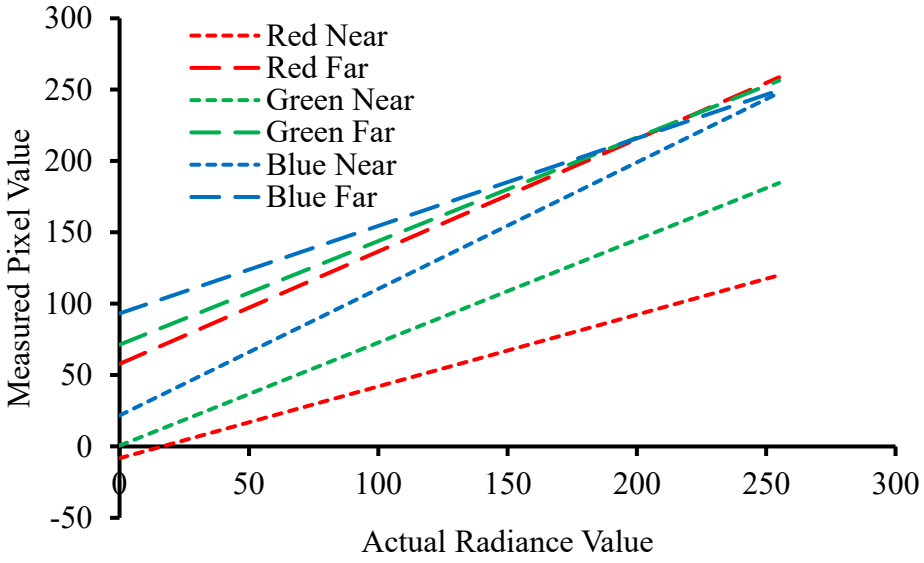

Figure 4.44: Six lines of best fit close to the camera (near) and checkerboard CB5 (far), all three RGB (red, green, blue) colour streams, for camera V5 in experiment F1

Differences Between Calibration Curves

Once the encoding schemes for each camera were determined, it was important to assess whether the curves were the same from position to position and situation to situation and, if not, whether any were similar. Conveniently, during the calibration of camera V5 for experiment F1, the camera changed from recording colour (RBG) images to recording IR images as calibration images were compiled at both at the camera (near) and at the checkerboard (far). This provided a great set of comparative data. Figure 4.45 shows the lines of best fit used in encoding measured pixel value to actual radiance value for six available greyscale equivalents, as obtained from calibration images from camera V5 in experiments F1 and F2.

Evidently, none of these encoding curves are the same, including the four F1 curves that were captured within 10 seconds of each other, indicating that it is unlikely that any two curves from the Type F experiments will be the same. However, the encoding schemes from

the IR near camera calibration images in both experiments are almost the same and, when the F1 RGB scheme is included, the slopes of all of the lines appear to be similar for calibration images recorded with the calibration tool near to the camera. A similar pattern is visible in the encoding schemes determined using images captured at the location far from the camera, except in the case of F1 RGB Far which, in this case, has a slope closer to that of F1 RGB Near. For the two Type F experiments, it was further found that the best fit calibration curves for cameras of similar type had similar slopes and, when analyzed as a group, the intercept of these best fit lines could be determined. Thus, the camera encoding schemes were separated into eight groups: IR near, IR far, RGB near (excluding V2-4), RGB far (excluding V2-4), V2 near, V2 far, V3&V4 near, and V4 far. The V2 camera was grouped separately from the others because that camera looked through the window which changed the relationship between pixel and radiance values whereas V3 and V4 cameras were separated because they were different (metal) cameras than the others.

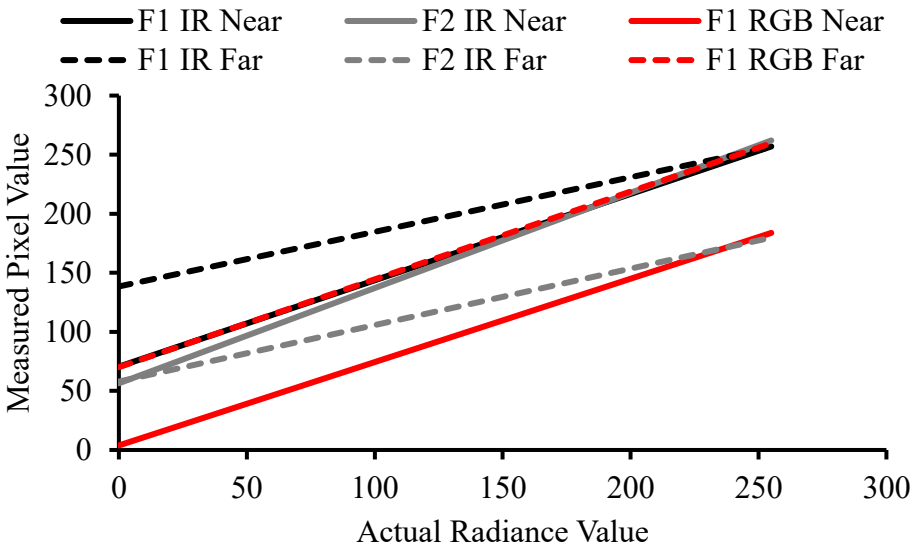

Figure 4.45: Six lines of best fit close to camera V5 (near) and checkerboard CB5 (far) in experiments F1 and F2 recorded in IR (both experiments) and RGB (F1 only)

Representative samples of the three camera encoding options considered in this work are overlaid on a plot of actual radiance value versus measured red, green and blue pixel values recorded with the calibration tool positioned at a location far from the camera and shown in Figure 4.46. All of the existing encoding schemes were included, regardless of apparent utility, to help understand the impact of different calibration curve assumptions on the results of the radiance method presented previously. For the 1:1 line (– –), it is assumed that measured pixel value (PV) is equal to actual radiance value (N), as was used in Section 4.3. The gamma encoding scheme (- - -) uses a power function (Power (0.45)) relation between

the values with γ=0.45 (*i.e.*, $PV=N^{\gamma=0.45}$) since it is the inverse of the decoding scheme ($N=PV^{\gamma=2.2}$) that was used in Section 4.4. As discussed above, the relationship between measured and actual values is best represented by the line of best fit from the measured calibration data (Linear (Measured), ——). It is also clear from this plot that each possible encoding scheme is quite different, making it important to understand how use of each curve might affect the estimations of smoke layer height and density made using the radiance method.

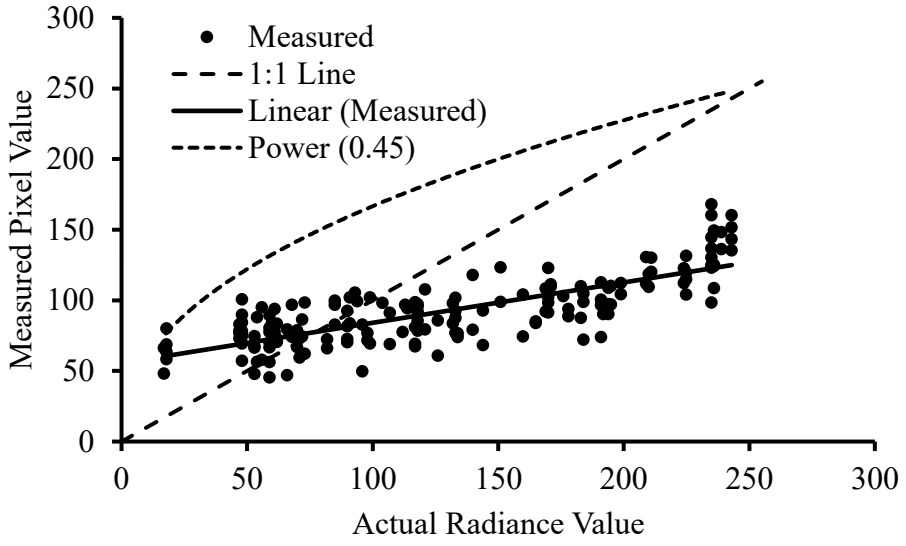

Figure 4.46: Three possible encoding schemes (linear best fit of measured data, 1:1 ratio, γ=0.45) from the RGB far category

The decoding schemes, or the camera calibration curves, are the inverse of the encoding schemes plotted in Figure 4.46 and are needed to convert from recorded (measured) pixel values to radiance values which is why the axes are flipped in Figure 4.47. The 1:1 line (– –), by definition, does not change upon inversion but the other two schemes, gamma (Power (2.2), - - -) and line of best fit from measured data, do change when inverted. The linear best fit of the measured data in Figure 4.46 does not cover the full range of possible measured pixel values, 0 to 255, but instead covers only the range of values between 50 and 150. To extend the range to cover the full extent of values found in the recorded images, two options were considered. The first was to extend the line based on extrapolated radiance values (Measured (Extend), • • •) and the second was to cap the radiance values at the limits of the measured pixel values (Measured (Capped), ——). Accordingly, four calibration curves (shown in Figure 4.47) were tried in determining the impacts of different calibration curves on radiance method results.

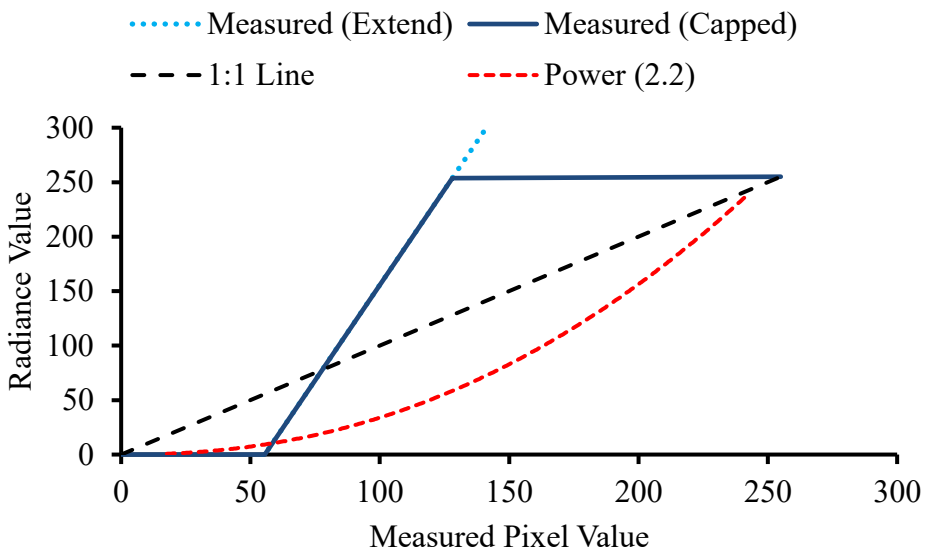

Figure 4.47: Four possible calibration curves (two options for linear best fit of measured data, 1:1 ratio, γ=2.2) in the RGB far category

Selecting a Calibration Curve

The impact of camera calibration curve selection was investigated by applying the various curves to the same set of data. The analysis was conducted using measured pixel values from pixel analysis areas positioned at z=1.55 m from camera V1 images in experiment F1. The measured pixel values were normalized by the range of possible pixel values (255) before the four calibration curves in Figure 4.47 were used to calculate normalized LRVs and DRVs with time. It was necessary to normalize the pixel values before applying the calibration curves (decoding schemes) because the input values for the gamma=2.2 decoding scheme (2.2 Power curve) must be between 0 and 1. Normalized LRVs and DRVs, and smoke density results with time are plotted in Figure 4.48 for the 1:1 line (black), 2.2 Power curve (red), best fit capped (dark blue) and best fit extended (light blue dash). Unsurprisingly, it is immediately clear from the plot that both normalized LRVs and DRVs are quite different depending on the selected camera calibration curve. Given that the normalized LRVs and DRVs thus far in this research were calculated using the gamma = 2.2 decoding scheme, the results obtained by calibrating the data with the 2.2 power curve (red) most closely resembles the radiance-time patterns seen previously.

In all cases, the normalized radiance values found using information from this pixel analysis area with the 1:1 calibration curve (black line) are higher than those values using the calibration strategy associated with the power (γ=2.2) based calibration curve (red line) which is consistent with the fact that the power (γ=2.2) calibration relationship is always below that for the 1:1 relationship (Figure 4.47). As expected, the radiance values of the two

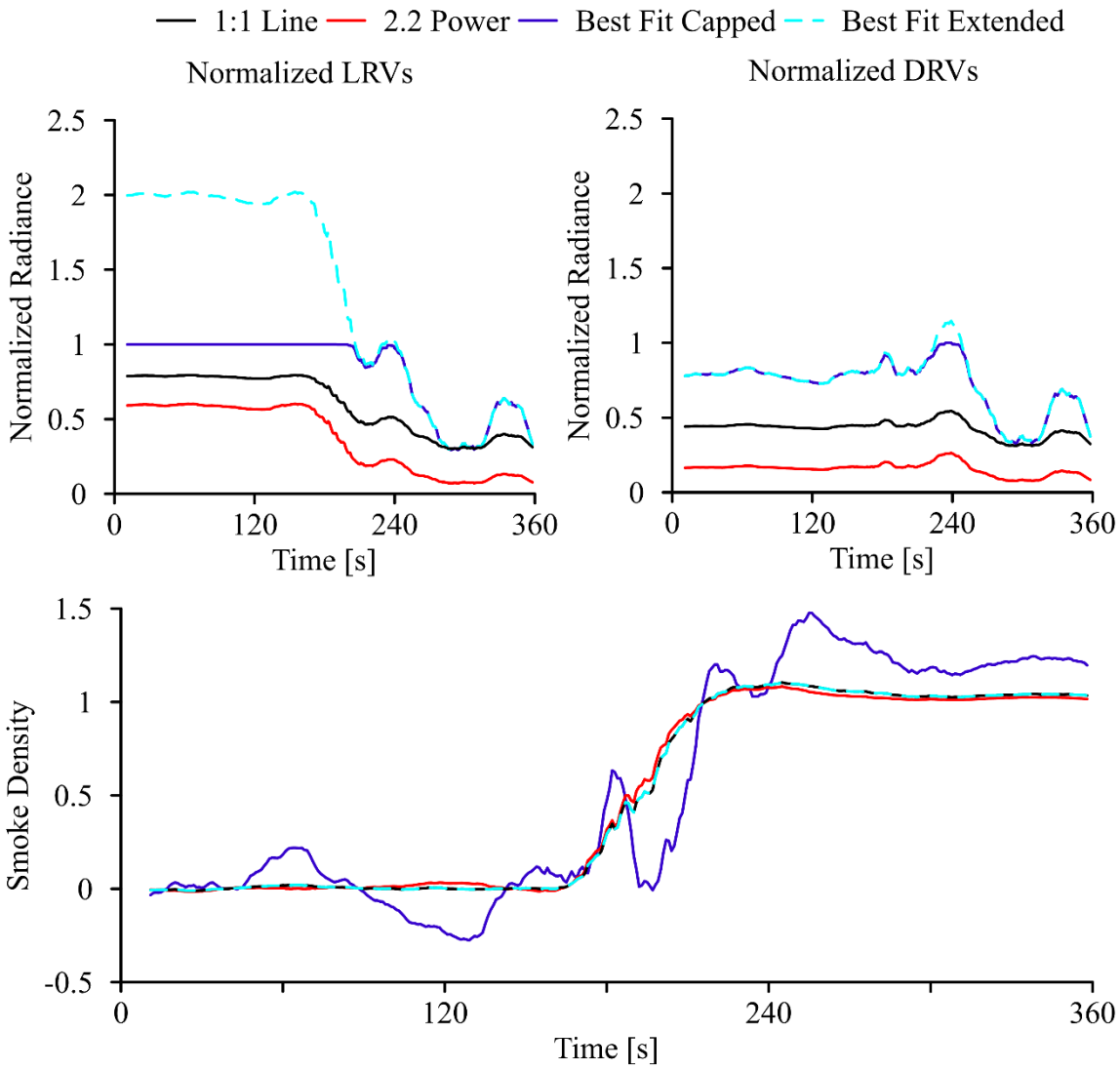

Figure 4.48: Normalized LRVs (top left) and DRVs (top right), and smoke density (bottom) with time at z = 1.55 m using four possible calibration curves (1:1 ratio, power with γ=2.2, linear best fit of measured data [x2]) for experiment F1 camera V1 (RGB far category)

Table 4.19: Smoke layer height and maximum smoke density estimates at z=1.55 m for four camera calibration curves for experiment F1 camera V1 (RGB far category)

	Smoke Layer Height [s]	Maximum Smoke Density
1:1 Line	194	1.039
Power γ=2.2	191	1.020
Best Fit Capped	210	1.220
Best Fit Extended	194	1.039

best fit options are the same when the radiance is between 0 and 1. Further, the normalized LRVs, and to a lesser extent the normalized DRVs, determined using the extended best fit calibration strategy (light blue dash line) did rise well above the radiance limit of 1. This difference can largely be attributed to differences in lighting conditions between the calibration images and the images from the recordings of the experiments. It was clear from these results that the procedure for obtaining calibration images should be altered in future (discussed in the sub-topic Experimental Application later in this section); however, the analysis was continued with the present curves in order to gain additional insight into the use of these various calibration strategies as well.

For the smoke density results, it is immediately evident that putting an upper cap on values from the line of best fit is not a good solution. In retrospect, the addition of the cap means that past a certain point the magnitudes of the normalized LRVs, and sometimes DRVs, are constrained such that the difference between the two values that are used to estimate the smoke density is effectively arbitrary, leading to inconsistent results. This could be anticipated by the overly large magnitude difference between the normalized LRVs from the best fit extended curve and the best fit capped curve (shown in Figure 4.48) which serve to emphasize the impact of capping the radiance values in the calibration curve.

A very notable result is that smoke density traces with time determined based on analysis of pixel analysis areas using the 1:1 calibration relationship and the extended line of best fit produce identical curves. Evidently, the differential radiance values obtained using any either of these lines for this particular set of pixel analysis areas are scaled versions of another. The conclusion is corroborated when looking at the time taken for the smoke layer height to reach $z = 1.55$ m and the maximum smoke density results for this experiment based on application of the radiance method using each of the four calibration curves presented in Table 4.19. There is no difference in either value between those determined using the 1:1 calibration strategy and those based on calibration using the extended line of best fit. The consistency between the 1:1 and extended line of best fit relationships was the same for every scenario checked for this analysis, including different heights and locations within an image as well as using IR images. Investigation of a potential theoretical basis for such an observation should be revisited in future by closer examination of the original smoke density equation. In contrast, the 2.2 power results, which appear similar to results obtained with the 1:1 line and extended line of best fit in Figure 4.48 and Table 4.19, the similarity between the linear and 2.2 power relationships was not consistent across tests and locations as discussed further below. It appears from these results that if the measured pixel value versus actual radiance value data is best represented by a straight line, then the easiest solution is to use a 1:1 relationship as the camera calibration curve, as this will also conveniently avoid having to extrapolate radiance values past the known limit of 255 for a given image set. It should still be noted, however, that given the range of possible camera calibration curves known to exist [112], it cannot be assumed that the optimal calibration curve will always be linear, so it is

recommended that the impact of using other curves on the results of smoke analysis using the radiance method should be considered further.

In Figure 4.48 and Table 4.19, the power (γ=2.2) calibration curve shows that results are close to those of the 1:1 and extended line of best fit, but do differ a small amount for this experiment due to the calibration curve selected. For this set of images in experiment F1, the difference in time taken for the smoke layer height to descend to 1.55 m into the room is only 3 seconds. In other locations and for other experiments, however, the difference may be much larger. For example, for these same images and pixel analysis areas located at a height 1.55 m but at the window, rather than at the checkerboard, the difference in estimated time for the smoke layer to descend to this height (z = 1.55 m) is 11 seconds relative to that for the 1:1 line in Table 4.19. Similarly, differences in maximum smoke density are about 2% on the high end across heights, locations, and camera angles for this particular test; but these differences could be larger for other situations and experiments as well.

Based on the analysis above, it appears that the best camera calibration curve to use with the radiance method for estimation of the smoke layer progression and smoke density would be the 1:1 line fit between pixel and radiance values, at least for the Type F experiments. The selected curve will be carefully considered for any future analysis. At present, however, consistency in calibration curve and approach was deemed extremely important to ensure that results could be compared between experiments. Therefore, since the results of the radiance analysis conducted on the eleven Type A-E experiments (some of which have been published elsewhere [23,84,94,116,125]) had been derived using the power (γ=2.2) curve to relate image pixel and radiance values, use of the power (γ=2.2) calibration curve was continued for the remainder of development of the radiance method and application to images extracted from video recordings of the two Type F experiments in this thesis.

Experimental Application

In summary, several important takeaways were determined through the analysis of camera calibration strategies with the radiance method. First, when radiance analysis is to be conducted on the video records of an experiment, it is recommended to use some method of camera calibration prior to or during the experiments, unless the camera calibration curve is already known with certainty. Based on the significant impact of lighting noted in the analysis above, it is clearly important to try to match the lighting conditions between the calibration images and the experiment as well. This was particularly true for scenes that were brighter (recorded in RGB) and darker (recorded in IR) as was shown for camera V5 in Figure 4.45 and subsequent discussion. The differing red, green, and blue calibration lines for camera V5 in Figure 4.44 also demonstrate the importance of lighting because the impact of lighting can differ by colour stream and, ultimately, impact the RGB calibration curve due to the interdependence. In addition, the above analysis showed that the calibration curves differ depending on distance between the calibration tool and the camera. The same two plots from

camera V5 also demonstrate the impact of distance because of the apparent change in calibration curve based on whether the calibration tool was near or far from the camera. In some cases, such as that of camera V5, changes in lighting and distance are interdependent and both influence the calibration curve simultaneously. Thus, it is also important to capture and analyze calibration images and obtain curves for each distance and location where an accurate relationship between pixel and radiance values is key to the results.

From an equipment point of view, the ColorChecker Video XL (calibration tool) used here worked quite well. The extra-large (XL) size of the squares in this calibration tool was critical for completing the calibrations of the pixel analysis areas chosen at some distance from the camera because the colour squares in smaller calibration tools would have been too small to analyze. A ColorChecker Classic XL has subsequently been released by the manufacturer and may be a good alternative to the tool used here since it comes with a free program that might automatically generate the camera calibration curve, removing the necessity of manually analyzing and estimating the colour content of each square and resulting in significant time savings during this step in application of the radiance method. Unfortunately, the ColorChecker Classic consists of squares of similar colour to those which did not register well during calibration of pixel values and radiance for the IR images however so it may not be very effective when radiance analysis of images from IR recordings of experiments are of interest. Based on the results found here, another solution to address camera calibration required for the radiance method might be to purchase a smaller, less expensive, calibration tool with colour/gray squares appropriate for use close to the camera in order to determine whether each camera calibration curve appears to be linear. In the case that it is, the camera calibration curve could potentially be extrapolated to points farther from the camera by assuming that the relation between pixel and radiance values are linear at those positions as well. However accomplished, it is clear that some form of camera calibration tool is recommended for use in future experiments where application of the radiance method is intended. If this is not possible, a sensitivity analysis of the results related to any assumed camera calibration curve should be completed.

Based on the above analysis, RGB pixel values are used for subsequent analysis in this thesis. A gamma=2.2 decoding scheme is also used going forward in this work. Thus, RGB pixel values from the selected pixel analysis areas in the experiment F1 and F2 video recordings from Section 4.5.3 were converted to radiance values with a 2.2 power camera calibration curve.

Resulting Normalized LRVs and DRVs

The final radiance method was applied to data extracted from a set of pixel analysis areas located on the checkerboards CB1, CB2 and CB7 associated with cameras V1, V2 and V7, respectively, for images extracted from each camera recording of experiments F1 and F2. Analysis was also completed using pixel analysis areas on the window and concrete board

beside CB1 in images captured by camera V1 for experiment F2. The latter pixel analysis areas were selected because there was soot deposited on the concrete board from the previous experiment, increasing the available contrast between the light and dark analysis areas. Of this full set of results created with the final radiance method, three sub-sets of the data were selected to be analyzed in detail on a step-by-step basis. The normalized LRVs and DRVs of these three sub-sets are analyzed in this section followed by the smoke density (in Section 4.5.5), smoke layer height (in Section 4.5.7) and maximum smoke density (in Section 4.5.8). The sub-sets were selected to assess specific issues and highlight the range of possible outcomes from analyses undertaken using the final radiance method. Comparison of the full set of final radiance method results has been saved until Section 4.5.9 because Step 9 is where comparison takes place in the radiance method. The comparison step was placed towards the end of the method to emphasize the importance of completing and analyzing each step for an individual data set to avoid missing crucial information.

The first sub-set of data from the final radiance method is from pixel analysis areas selected at the window and adjacent concrete board visible in images captured by camera V1 during experiment F2. This is presented first because it most closely resembles the data presented previously so works well as a transition. A maximum of 14 pixel analysis areas, up from three previously, could be selected in the window area and were analyzed with the radiance method. Figure 4.49 presents the normalized LRV (left plot) and DRV (right plot) results with time for half the collected data (every other trace): seven heights (z=1.76 m, 1.70 m, 1.63 m, 1.57 m, 1.50 m, 1.44 m and 1.38 m).

The normalized LRVs (left plot) follow the now familiar pattern of more or less constant values prior to a large drop. The initial normalized LRV is noticably below 1, but is well above the normalized DRVs suggesting that there is sufficient contrast for the analysis. The normalized LRV traces obtained at sequentially lower heights cascade downward in order over time, indicating the expected smoke layer descent down from the ceiling into the fire room. The normalized DRVs (right plot) start at slightly higher values than was common in the earlier results but otherwise are fairly typical.

The second sub-set of data from analysis using the final radiance method is from pixel analysis areas selected from checkerboard CB1 in images obtained by camera V1 during experiment F1. For this, 58 pixel analysis areas were selected. For comparison, the data shown for normalized LRV (left plot) and DRV (right plot) in Figure 4.50 are for seven heights (z=1.77 m, 1.72 m, 1.65 m, 1.58 m, 1.48 m, 1.41 m and 1.34 m) intentionally aligned with the heights used above during analysis of pixel areas at the window.

Once again, the normalized LRVs (left plot) exhibit the characteristic trend - starting at more or less constant values followed by large decreases in value that occur at sequentially later times with descending height of the pixel analysis areas. As was typical in previous results, the DRVs (right plot) patterns cannot be easily interpretted. The initial normalized LRVs are

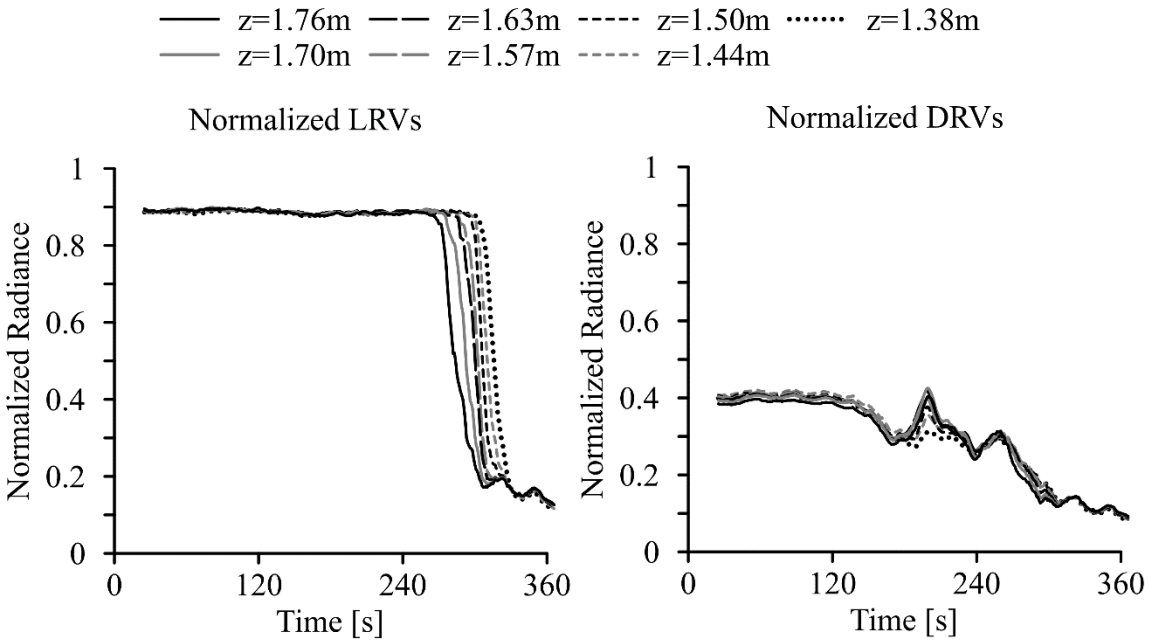

Figure 4.49: Final radiance method normalized LRVs (left) and DRVs (right) for experiment F2 camera V1 at seven heights (z=1.76 m, 1.70 m, 1.63 m, 1.57 m, 1.50 m, 1.44 m, 1.38 m) across the window

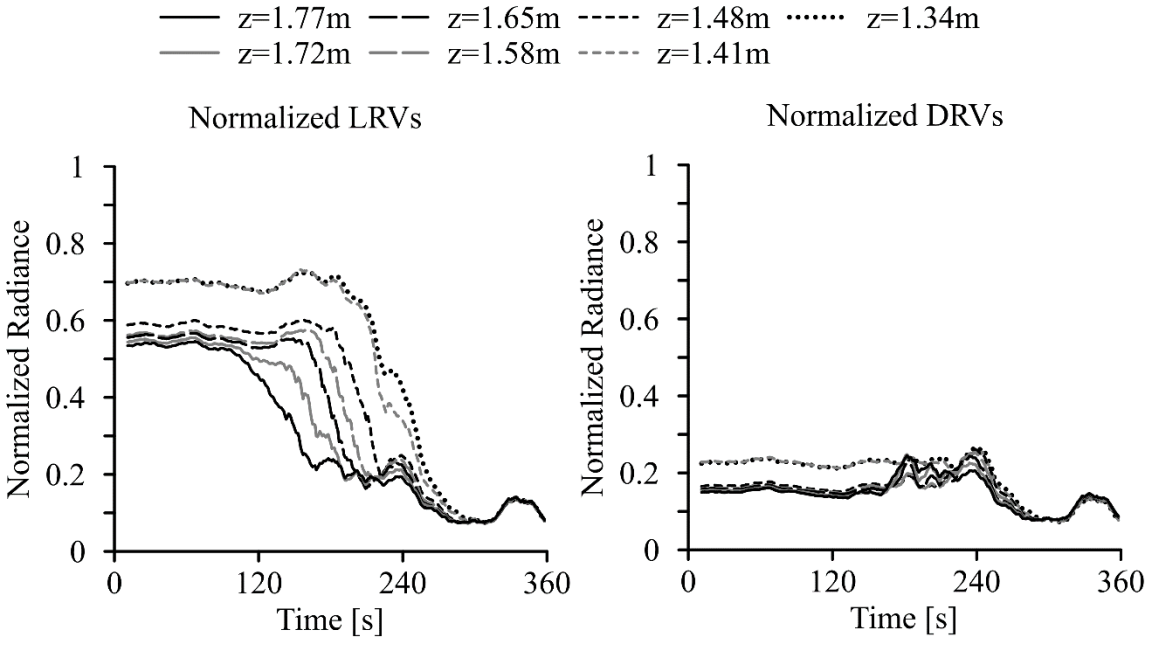

Figure 4.50: Final radiance method normalized LRVs (left) and DRVs (right) for experiment F1 camera V1 at seven heights (z=1.77 m, 1.72 m, 1.65 m, 1.58 m, 1.48 m, 1.41 m, 1.34 m) on checkerboard CB1

closer to 0.5 than 1 for the pixel analysis areas chosen, but they remain well above the normalized DRVs (right plot), suggesting that there is sufficient contrast to apply the radiance method for smoke density analysis. Nonetheless, due to the inherently lower LRVs that are observed for pixel analysis areas chosen on the checkerboards, it is necessary to assess the relative difference in the LRV and DRV values for each analysis. Therefore, this data set was selected precisely to demonstrate the "best" contrast seen across six sets of normalized radiance data obtained through application of the final radiance method to pixel analysis areas on the checkerboards for experiments F1 and F2. Of all analysis done on pixel analysis areas on checkerboards, the areas analyzed from CB1 in images recorded by camera V1 in experiment F1 had the highest ratio of LRV values starting over 0.5 (45/58 traces) of radaince method results analyzed on checkerboards.

Conversely, the set of detailed radiance data that represent the "worst" of the six sets of normalized radiance data were those obtained from pixel analysis areas on checkerboard C7 in images recorded in black and white by camera V7 in experiment F2. 48 pixel analysis area pairs were analyzed from images such as the ones shown in Figure 4.51. Figure 4.52 shows normalized LRV and DRV traces with time at six heights, spaced at approximately 300 mm intervals (z=2.20 m, 1.90 m, 1.60 m, 1.29 m, 1.00 m and 0.70 m), that were selected to represent the spread in results from this data set.

a) F2, V7, 20 s (reference) b) F2, V7, 240 s

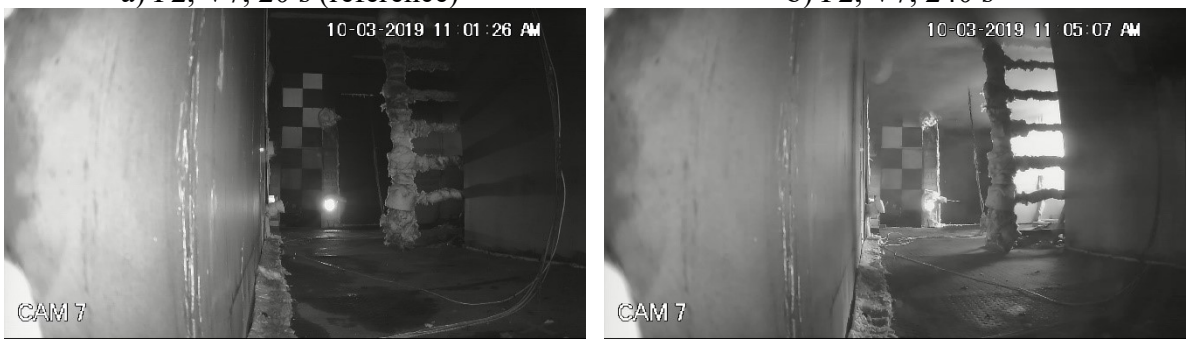

Figure 4.51: Experiment F2 camera V7 at a) 20 s (reference image) and b) 240 s

The normalized LRV traces (left plot in Figure 4.52) are very low and appear to be only marginally larger in magnitude than those in the normalized DRV traces (right plot). These low values are common of IR images (see Figure 4.32). As a result, the available contrast for calculation of smoke density using the radiance method was a major concern and the normalized radiance values were closely scrutinized.

Collectively then, the detailed data sets incorporate a window scenario, and the "best" and "worst" of the six checkerboard scenarios analyzed to provide an idea of the range of possible final radiance method outcomes. Results from the next step in the radiance method analysis, smoke density calculation, is presented in the next section.

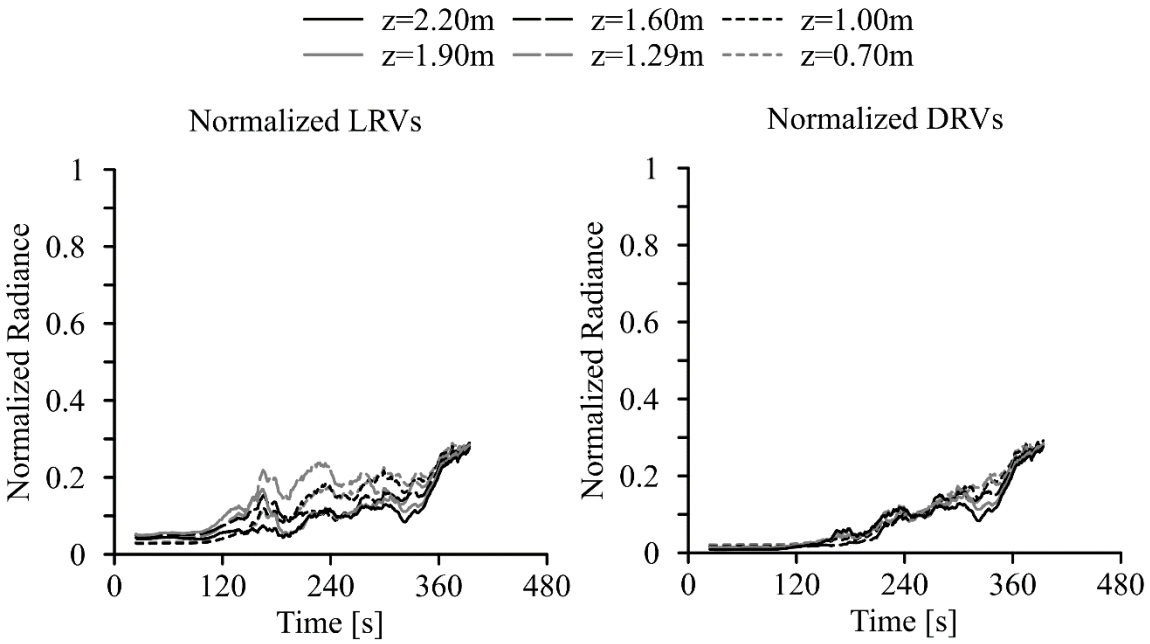

Figure 4.52: Final radiance method normalized LRVs (left) and DRVs (right) for experiment F2 camera V7 at six heights (z=2.20 m, 1.90 m, 1.60 m, 1.29 m, 1.00 m, 0.70 m) on checkerboard CB7 with the lowest height having the correct z=0.70 m

4.5.5 Step 5: Calculate Smoke Density

The smoke density values for the three tests with six or seven heights, as detailed in the previous section, were calculated using the normalized radiance values as detailed in Section 3.6.5. This was done as a preliminary check in Step 5 of the application of the final radiance method. As such, only the detailed smoke density data corresponding to the three sub-sets of normalized radiance values discussed above, *i.e.* window, best and worst, are presented in this section and used to gain an idea of the range of possible outcomes from the smoke density calculations with the final radiance method.

Figure 4.53 shows the smoke density results as a function of time from the window based pixel analysis areas at seven heights (z=1.76 m, 1.70 m, 1.63 m, 1.57 m, 1.50 m, 1.44 m and 1.38 m) identified in images recorded by camera V1 during experiment F2. As expected, given the typical radiance values shown in Figure 4.49, the smoke density traces in Figure 4.53 are very typical of what was seen for estimated smoke density previously. There is a dip into negative values of smoke density between about 150 and 310 s. While this artifact is not realistic, it is not in and of itself particularly concerning since it has been observed before in almost all previous smoke density traces without compromising estimates of smoke layer height or maximum smoke density. Although the radiance method smoke density results are presented in a form that implies a continuous function, the results are calculated at discrete

points in time. Consequently, each determination is independent of all prior and subsequent results. Thus, smoke density (SD) estimates that are within the bounds of the radiance method analysis (*i.e.*, $0 < SD < 1$) are valid even if the trace was outside the bounds at previous times. Of course, pixel analysis areas that produce smoke density results within the bounds of the radiance method analysis for the entire duration are preferred and should be preferably selected if multiple analysis areas are available.

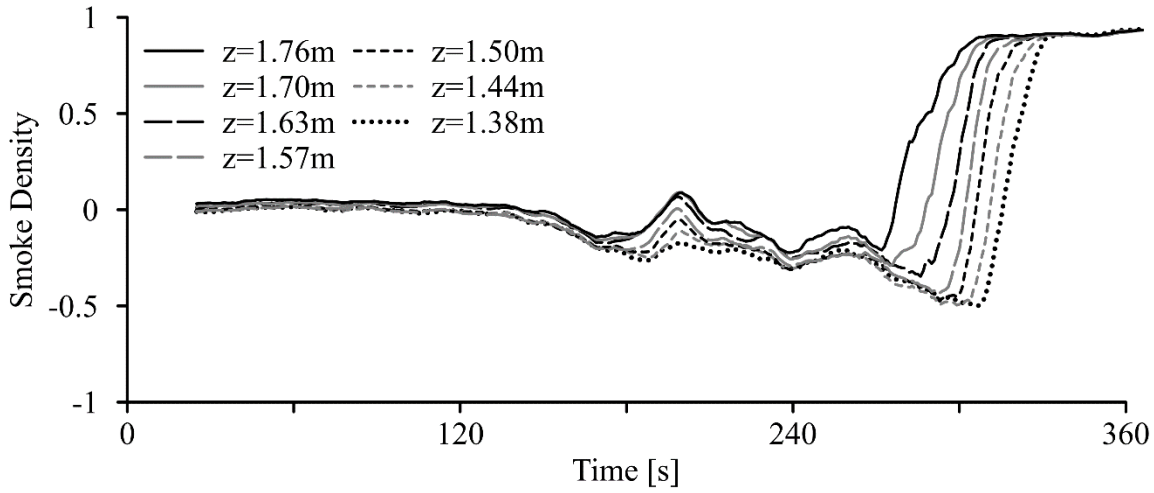

Figure 4.53: Final radiance method smoke density values for experiment F2 camera V1 at seven heights (z=1.76 m, 1.70 m, 1.63 m, 1.57 m, 1.50 m, 1.44 m, 1.38 m) across the window

The plot shows that the results for smoke density obtained using the final radiance method with information from these pixel areas are very promising. The expected marked increase in smoke density value occurs in all traces, ordered in increasing times or decreasing order of height, and all traces appear to plateau at a fairly constant, and equal, value. Since the method proceeds in several additional steps from here, more specific details and values obtained from these smoke density traces (and the two sets below) are discussed in the upcoming sections that focus on smoke layer height and maximum smoke density (Sections 4.5.7 and 4.5.8, respectively).

Figure 4.54 shows the smoke density results with time from pixel analysis areas at seven heights (z=1.77 m, 1.72 m, 1.65 m, 1.58 m, 1.48 m, 1.41 m and 1.34 m) on checkerboard CB1 in images captured by camera V1 during experiment F1and discussed in the previous section as the best case. This plot again displays very typical smoke density traces with time, with values beginning near zero and ultimately rising to a value around 1. The sharp increase in smoke density that indicates the presence of the smoke layer occurs with increasing time for descending order of height meaning that with these pixel analysis areas the radiance method was able to pick up the smoke layer passing down from the ceiling and into the room.

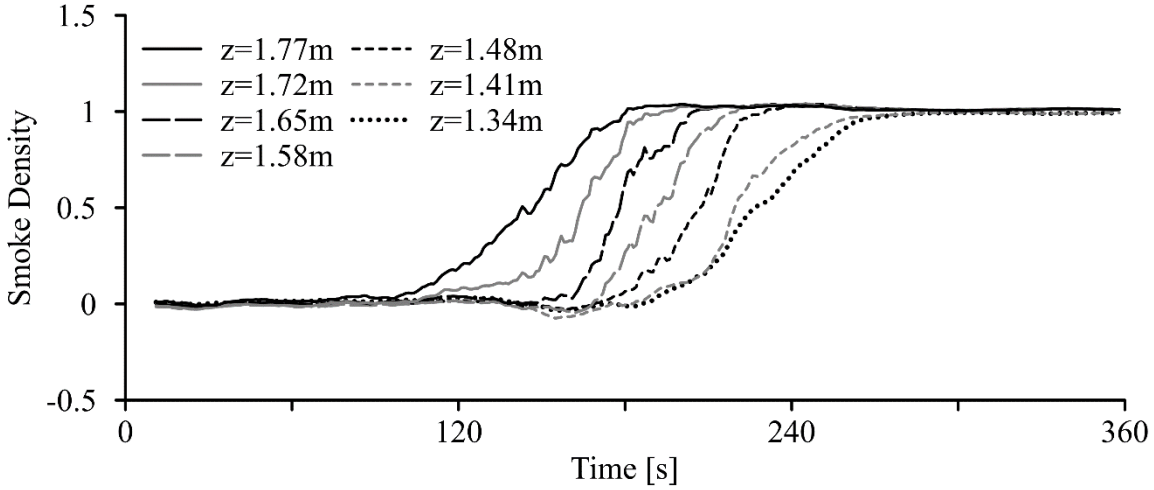

Figure 4.54: Final radiance method smoke density values for experiment F1 camera V1 at seven heights (z=1.77 m, 1.72 m, 1.65 m, 1.58 m, 1.48 m, 1.41 m, 1.34 m) on checkerboard CB1

Two changes are evident in the results from this checkerboard analysis that were not seen in penultimate radiance method results (*e.g.*, Figure 4.30). First, the slopes of the smoke density-time traces suggest that the smoke density increases more slowly than indicated with all penultimate radiance method results. Particularly, the penultimate estimates that used pixel analysis areas taken from the window display a very sharp rise in smoke density values. The lower slopes in smoke density-time plots seen here were actually first observed in analyses using the final radiance method on pixel analysis areas taken in images extracted from the black and white recordings (see Figure 4.32) and consistently appears when the final radiance analysis is conducted with pixel analysis areas chosen on the checkerboards. In contrast, a sharp rise in values of smoke density with time was apparent when the final radiance method was applied to pixel analysis areas taken in the window (Figure 4.53). As discussed in Section 4.5.3, this is likely because the smoke must be more dense to be visible in front of the backlit window so the radiance method resolves this as a sharper transition in smoke density (and potentially more clearly defined lower edge to the smoke layer interface) in time. Thus, it would appear that the sharp increases in smoke density seen in some analyses with both the penultimate and final versions of the radiance method are likely related to the fact that pixel analysis areas were selected from a backlit window and not connected to specific details of either version of the method. This conclusion is corroborated by the observed lag in increase of smoke density for pixel analysis areas in the window illustrated in Figure 4.35 wherein the backlighting appears to overcome any “thin” smoke that is accumulating in the room and is clearly visible against the checkerboard and in the corresponding radiance results as well. The analysis conducted using pixel analysis areas in the window only registered “thick” smoke later in the experiment as the smoke layer passed

the height in question and directly obscured light from the window, resulting in a rapid increase in measured values of smoke density.

The second interesting trend visible in these checkerboard results, that was not seen in previous analysis based on pixel analysis areas in the window or using the penultimate method, is a pattern where the smoke density increases slightly past a value of 1 before plateauing at a lower value which remains slightly above 1. For the five traces plotted in Figure 4.54 (z=1.77 m, 1.72 m, 1.65 m, 1.58 m, 1.48 m), the estimated smoke density passed the value of 1 and remained above 1 until the end of the analysis period. For smoke density values above one to occur, the DRVs must exceed the LRVs (as was verified in this data) because the calculation at time *i* proceeds as

$$1 - \left[\frac{LRV_i - DRV_i}{Initial\ Range}\right] = 1 - [< 0] = > 1$$

while the normalized LRVs and DRVs must fall in the range between 0 and 1 by definition. This pattern appears to be related to undertaking the analysis using pixel analysis areas on the checkerboard rather than any inherent limitation with the final radiance method because this was not an issue in Figure 4.53 (window analysis) but appears in both Figure 4.38 and Figure 4.48 (checkerboard analyses). This effect is likely a result of changing lighting conditions. However, as mentioned previously, radiance method smoke density results are independent and, therefore, smoke density (SD) estimates that are within the bounds of the radiance method analysis (*i.e.*, 0 < SD < 1) are valid even if the trace later exceeds the bounds. Unfortunately, if the radiance method results are outside the analysis bounds (*i.e.*, >1) towards the end of the analysis, values of maximum smoke density do come into question as is discussed in Section 4.5.8.

Results of this final representative analysis relating normalized radiance values to smoke density are shown in Figure 4.55 as smoke density versus time estimated from pixel analysis areas on checkerboard CB7 at all six heights (z=2.20 m, 1.90 m, 1.60 m, 1.29 m, 1.00 m and 0.70 m) from images recorded by camera V7 in experiment F2. This plot is clearly characterized by many very negative values of smoke density. This is not surprising given the very low contrast between normalized radiance values observed for these traces and shown in Figure 4.52. However, while these data traces are unusual, several promising results are still apparent.

The prevalence of large negative values in Figure 4.55 is similar to the plots determined based on pixel analysis areas taken from images in experiment C1 and analyzed using Iteration 1 of the method (see Figure 4.15 in Section 4.3.1) as those also exhibited some very negative values of smoke density. Unlike the previous results, however, the smoke density traces in Figure 4.55 eventually return to positive values and do pass the value of 0.5 that is the marker for the presence of the smoke layer. As in the results from Iteration 1 of the

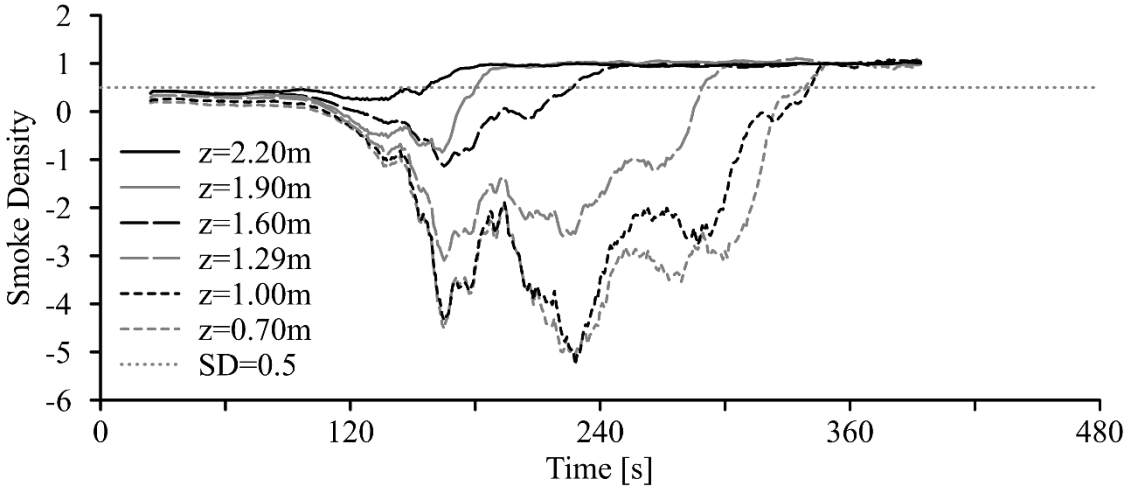

Figure 4.55: Final radiance method smoke density values for experiment F2 camera V7 at six heights (z=2.20 m, 1.90 m, 1.60 m, 1.29 m, 1.00 m, 0.70 m) on checkerboard CB7

method, the smoke density values here began as positive values, but became negative since the calculation proceeds as

$$1 - \left[\frac{> Initial\ Range}{Initial\ Range}\right] = 1 - [>1] = <0$$

In the present case, the cause is light pixel analysis area values that are actually lighter than the reference values, likely as a result of accumulation of a "thin" layer of smoke in the room near the window that reflects the light from the window and the fire, which results in a larger radiance range than the reference (initial) value. This influence can be seen in the slightly larger difference between normalized LRVs compared to DRVs in the plots on Figure 4.52 (left plot vs. right plot) between about 120-300 s, which coincides with the negative smoke density values in Figure 4.55. However, despite the very limited contrast and resulting large negative values early in the test, the smoke density values later pass the value of 0.5 that indicates the presence of the smoke layer at each height. This happens as time increases, or in descending order of height, excluding the lowest height of z=0.70 m which passes 0.5 approximately 3 seconds before z=1.00 m. Overall, because the sequential descent of smoke layer into the room is observed, this means that it might still be possible to obtain useful smoke layer height estimates using the final radiance method even for the case of very low contrast in the data.

Based on the results from the detailed analysis of these three tests all with quite different image characteristics, it was clear that the final radiance method continued to produce promising results. This prompted continuation of the analysis by digging deeper into the impact of soot deposits on surfaces, one of the key considerations related to use of certain pixel analysis areas in the images for determination of appropriate normalized radiance

values. Thus, at this point, an investigation was made into the impact of surface soot deposits on the smoke density results. With this established, smoke layer heights and maximum smoke density for the three initial data sets are examined in detail. Following this, a complete set of results from the application of the final radiance method to seven data sets are presented and compared. A discussion of potential sources of uncertainty are then assessed in the final section of this chapter.

4.5.6 Step 6: Estimate Soot Deposit Impact

This section details an experiment designed to estimate potential impacts on the smoke density results of soot deposit on the camera lenses during the Type F experiments. The method used was outlined in Section 3.6.6 with results presented and discussed here. Two critical aspects of soot deposits as related to their impacts on analysis with the final radiance method are discussed in this section: first, whether it is possible to quantify the soot deposit that has occurred during each experiment as observed in the clean up after the experiment; second, if the soot deposit can be quantified, what the value indicates in terms of estimation of smoke progression and maximum smoke density measurements using the final radiance method.

A white piece of paper was held up to each interior camera and near each checkerboard after experiments F1 and F2 and series of images were recorded. An independent observer determined that a piece of white paper was closest to the “Grey 2” colour on the calibration tool. Therefore, the RGB pixel values from the “Grey 2” square on the calibration tool during pre-experiment calibration were compared to the RGB values of the white paper as captured post-experiment. This was done both at the camera and the associated checkerboard for cameras V1, V4 and V11 in experiment F2 with results shown in Table 4.20. White paper was not used during pre-experiment calibration because instead the full range of calibration tool colours was needed for camera calibration and a second calibration with white paper, in an already complex experiment, did not appear justified. The calibration tool was not used post-experiment because airborne particulate in the post-fire environment would alter the colours and thus compromise additional calibration.

Unfortunately, there are no consistent patterns apparent in this data. The inconsistency can be attributed to different lighting conditions at the position of the target before (calibration tool) and after (white paper) each experiment, and also the distances between the camera and target in two circumstances measured. In the living room (V1 and V4), the door was open and several researchers were present as the calibration image was recorded. Post-experiment, the living room door was also open but there was only one researcher present, the furniture had been removed, and the windows were soot covered, severely limiting the natural light coming into the compartment. It would be expected that, under the condition of soot deposit on the camera lens, the RGB value would decrease (get darker) which was not the case for

Table 4.20: Pixel values before (calibration) and after (white paper) experiment F2 at the camera and checkerboard for three cameras (V1, V4, V11)

Camera	Location	RGB Pixel Value	
		Pre-Experiment Calibration (Grey 2)	Post-Experiment Soot Measure (White Paper)
V1	Camera	180	194
	Checkerboard (CB1)	121	102
V4	Camera	121	172
	Checkerboard (CB4)	69	75
V11	Camera	216	111
	Checkerboard (CB11A)	140	113

three of four sets of pixel values. In the fourth the value decreased which is what had been expected. At the final camera upstairs (V11), there was a vent open in the post-experiment image that had been used to clear the air of smoke in the house, but also significantly changed the lighting conditions. In this case, the area was brighter than during the calibration images and RGB values decreased as might be anticipated but unfortunately the increase lighting clearly also masked any impact of soot deposit on this camera lens as well. Finally, in retrospect, the differing locations of the calibration tool (pre-experiment) and paper (post-experiment) would have impacted the results; the calibration tool was held at waist height at both the camera (sufficiently far that the whole tool could be seen, about 0.5 m) and checkerboard pre-experiment whereas the paper was held close to the camera (about 0.05 m) and near the top on the checkerboard post-experiment. As discussed in Section 4.5.3, it was later found that both distance and height would impact the pixel value measurement suggesting that, as with the camera calibration (Section 4.5.4), the experimental protocol for measuring soot deposit should be revised in future experiments in order to minimize the effects discussed here.

Of the twenty-four possible soot deposit measurements (12 cameras x 2 experiments), one reasonable measurement was possible. The lighting conditions in images recorded by Camera V6 from experiment F2 were similar at the time of camera calibration, pre-experiment recording (approx. two minutes of "baseline" data), and soot deposit measurement. Here, the colours related to the "white" of the paper became darker as expected when deposited soot made objects darker than the original. The measured pixel values were converted to radiance using the γ=2.2 curve used throughout the present analysis and the white paper post-experiment was measured as 0.38 and 0.03 darker compared to the equivalent "Grey 2" from pre-experiment calibration when held at the camera and at the checkerboard, respectively. With only the one usable measurement, it is difficult to determine how best to convert the darkening of the white paper as recorded by the camera (soot deposit on the camera lens) and

as recorded at the checkerboard (camera and checkerboard soot deposit) into comparable and useful values to extend to the intended examination. Additionally, although the lighting issue was addressed at this position, the limitations with different distances and heights for the calibration tool, white paper and camera still exist and will impact the results. More experiments with a carefully revised soot deposit measurement procedure are required to determine how best to investigate the potential impacts of soot deposits on the camera and on the checkerboards when applying the final radiance method to estimate smoke progression and maximum smoke density values from videos recorded during fire experiments.

Of course, one critical question remains as to the extent to which the soot deposits that might form on the camera and checkerboard need to be quantified and whether they also need to be separated from one another. The experimental procedure for estimating soot deposit was conceived in an attempt to quantify something similar to the "clear beam" value and correction that is done in a smoke density chamber test. In the smoke density chamber "clear beam" determination, no differentiation is made between the soot deposited on the optical windows at the floor versus the ceiling of the chamber so in the present situation, differentiation between soot deposited on the camera lens versus on the checkerboards may not be required. It should be noted here though that, unlike the two glass lens in the smoke density chamber, the soot deposits considered here are on different surface types: glass and drywall. Second, unlike the smoke density chamber test that immediately evacuates the smoke after the last smoke density measurement is recorded, the smoke cannot be evacuated from the compartments during the full-scale experiments so they continue well after the smoke density estimates are completed. For example, in experiment F2 the smoke layer was first present around 150 seconds after ignition and the last smoke density estimate was about 360 seconds after ignition. The experiment continued for an additional 40 minutes after this last estimate of smoke density. In terms of soot accumulating on the camera or the checkerboard, then, a post experiment determination would be biased toward the fact that a large majority of the observed soot would have been deposited after the time that the last value of smoke density was determined. Further, the smoke density results calculated in this analysis would suggest the same. If there is a drop in value of smoke density as the plateau toward maximum smoke density is reached, the dip is quite small, indicating minimal impact of soot deposit on smoke density estimates during the analysis period (and consequently Steps 7 and 8 of the radiance method). In fact, the value of smoke density is more likely to increase slightly or remain constant as it reaches the plateau, further suggesting minimal impact of soot deposit during the analysis period. Thus, although soot deposit measurement in the full-scale experiments cannot be used in the same manner as the "clear beam" measurement in the smoke density chamber tests, it should be pursued further, as it may be quite useful to indicate the overall extent of soot deposit over the duration of the experiment.

Based on the above re-analysis of the method, an alternative technique for estimating soot deposit in the full-scale experiments was considered. For this, the calibration and soot deposit

"Grey 2" measurements were discounted entirely, and it was found possible to obtain normalized radiance values using pixel analysis areas from the checkerboard light and dark areas from an image at the beginning of the experiment and from a post-experiment image after the smoke had cleared from the burn structure. This technique revealed an average initial range of normalized radiance values (N_W-N_B) of 0.040 while the average final range of values was only 0.006. Specifically, the normalized radiance values from the light pixel analysis areas got about 0.030 darker and the black areas got about 0.004 lighter with the soot deposited. This solution did not allow for differentiation between soot deposits on the camera lens versus on the checkerboard surface but it did provide an indicator of general soot deposit, in this case on the drywall of the checkboard, that could potentially be determined from, and ranked, between experiments or material surfaces, *etc*. in future fire experiments. This soot deposit estimation technique has the advantage of being very flexible and requiring one less component in the experimental procedure, important advantages to broaden its potential use per the former and simplifying implementation when there are already a significant number of components. Another advantage is the reduced training required for implementation. Additionally, it would be quite simple to add a "soot deposit" image to the image processing scheme to get a soot deposit estimate.

The latter soot deposit technique still could not be used in the living room for the present tests because of the different window lighting from start to finish of the F1 and F2 experiments. However, this could be turned into an advantage and a similar technique might be employed to estimate the soot deposit on the window(s) and/or cameras in future versions of the technique. The difference would mean that the values are not directly comparable, but the associated ranking might be. Further investigation would be required to determine the validity of this approach.

Three techniques have been presented for applying the final radiance method in estimating soot deposit during fire experiments. One differentiates between soot deposit levels at the camera and checkerboard, while two do not. All three techniques show promise but additional experiments with revised experimental procedures and further, more detailed investigation are required to determine how useful this information might be in future.

4.5.7 Step 7: Determine Smoke Layer Height

Two methods of estimating smoke layer height with the final radiance method were considered. These involved determining the times at which the estimated values of either smoke density or normalized LRVs reached a threshold value of 0.5, as detailed in Section 3.6.7 with preliminary results discussed in Section 4.4.5. Results of the analyses using both methods, where possible, are detailed in this section. Both methods are compared to observer-based results (method in Section 3.2.1) which were obtained using pixel analysis areas chosen from images recorded by camera V1 during experiment F2 and V1 during experiment F1 respectively. These were located on the window at seven heights (z=1.76 m,

1.70 m, 1.63 m, 1.57 m, 1.50 m, 1.44 m and 1.38 m) and on checkerboard CB1 for the five heights (z=2.30 m, 2.07 m, 1.77 m, 1.46 m and 1.16 m) indicated with the red lines in Figure 4.56.

Figure 4.56: Observers estimated smoke layer descent time to each of the five heights (z=2.30 m, 2.07 m, 1.77 m, 1.46 m, 1.16 m) indicated with red lines on checkerboard CB1 from camera V1

Table 4.21 shows the times of smoke layer descent to each height obtained using the smoke density, normalized LRV and observer-based estimation methods from the window based pixel analysis areas. Whether based on values of smoke density or normalized LRV reaching the threshold value of 0.5, the methods indicate that the smoke layer descends in time with descending height (top to bottom in Table 4.21) as desired.

Table 4.21: Smoke layer descent time for experiment F2 camera V1 at seven heights (z=1.76 m, 1.70 m, 1.63 m, 1.57 m, 1.50 m, 1.44 m, 1.38 m) across the window as estimated using the smoke density, normalized LRV and observer-based methods

z [m]	Smoke Layer Descent Time [s]		
	Smoke Density	Normalized LRV	Observer-Based
1.76	289	284	179-270
1.70	296	293	
1.63	303	301	
1.57	307	305	
1.50	311	309	
1.44	317	314	257-308
1.38	323	319	

In this case, the estimated times at which the smoke reaches a certain height are universally a few (maximum 5) seconds faster using the smoke density value of 0.5 as the marker instead of the normalized LRV of 0.5. However, both strategies of analysis with the final radiance method result in smoke layer descent times that are notably slower than the observer-based time estimates. There are two potential causes for the difference in results. The first possible cause lies with an issue in the theory or calculations used to obtain the final smoke density values during the radiance method itself, or in some component within the method. This is less likely the cause because, particularly in this window scenario, no real changes were made to the relevant components of the method between the penultimate and final iterations of the radiance method and good agreement with observer based smoke height estimates were seen for the penultimate method.

The second, more likely, explanation is that the difference in results was caused by a change in the observer-based method after the original comparison (Section 4.1.1). In the previous analysis, smoke layer descent times were chosen based on the smoke reaching the top and bottom of the window whereas in the current method, the times are obtained using visual cues as to when an observer felt they could see smoke registered on checkerboard CB1 adjacent to the window. As discussed previously, the presence of the backlit window as the images are recorded can lead to a visual lag between seeing smoke across the window (radiance method in this instance) versus on the checkerboard (observer based estimate here), thereby making the change in observer-based analysis the likely explanation for the observed lag in smoke layer descent times when using the radiance method. Clearly then, it is important to consider factors such as this, that are directly related to choice of pixel analysis areas, in future applications of the final radiance for estimation of smoke layer descent times.

Table 4.22 shows the smoke layer descent time results obtained using the smoke density, normalized LRV and observer-based estimation methods from the same pixel analysis areas at seven heights (z=1.77 m, 1.72 m, 1.65 m, 1.58 m, 1.48 m, 1.41 m and 1.34 m) on checkerboard CB1 as recorded in images from experiment F1 camera V1. Both the smoke density and normalized LRV methods obtain smoke layer descent times in descending order (top to bottom in Table 4.22) as desired.

Smoke layer descent times in Table 4.22 with pixel analysis areas chosen on the checkerboard differ from the results in Table 4.21 (window-based pixel analysis areas) for the same experiment, camera and comparable heights. In Table 4.22, the time taken for the smoke density to exceed a value of 0.5 are universally slower, by up to 50 seconds, the times estimated based on the normalized LRV reaching the threshold of 0.5. This reversal, taken in conjunction to results presented previously in Section 4.4.5, shows that there is no universal pattern in the ordering of results (leading or lagging) between smoke descent times estimated using the 0.5 threshold with smoke density values or normalized LRVs obtained using the final radiance method.

Table 4.22: Smoke layer descent time for experiment F1 camera V1 at seven heights (z=1.77 m, 1.72 m, 1.65 m, 1.58 m, 1.48 m, 1.41 m, 1.34 m) on checkerboard CB1 as estimated using the smoke density, normalized LRV and observer-based methods

z [m]	Smoke Layer Descent Time [s]		
	Smoke Density	Normalized LRV	Observer-Based
1.77	148	107	159-231
1.72	165	115	
1.65	179	167	
1.58	192	179	
1.48	208	192	
1.41	220	217	217-293
1.34	227	221	

Unlike the previous results, in this test the smoke layer descent times determined using the final radiance method lie towards the beginning of the range of observer-based times and three values (z=1.77 m with smoke density, z=1.77 m, 1.72 m with normalized LRV) register the presence of smoke slightly ahead of the minimum observer-based estimates. The tendency for the radiance analysis times to be earlier than the observer-based estimates may be related to the use the value 0.5 in the radiance method, whereas observers might register the "bulk" of the smoke layer at a particular height at closer to 100% smoke density, rather than 50%, as was discussed previously in Section 4.5.3. Nevertheless, the general agreement with observer-based smoke layer descent time results show that the final radiance method can provide comparative, and thus relatively accurate determinations of the progression of the smoke layer down into the fire compartment.

Finally, Table 4.23 shows the smoke layer descent time results obtained using the smoke density and observer-based estimation methods from the same pixel analysis areas at all six heights (z=2.20 m, 1.90 m, 1.60 m, 1.29 m, 1.00 m and 0.70 m) on checkerboard CB7 from images recorded using camera V7 in experiment F2. The normalized LRV method of estimating smoke layer descent time could not be used for these images because the normalized LRVs did not reach the required threshold value of 0.5 over the duration of the analysis. Smoke layer descent times estimated using the threshold value of 0.5 for smoke density do increase in time with descending height into the room (top to bottom in Table 4.23), again excluding the outlier at z=0.70 m. It is also very positive that all smoke layer descent times estimated with the radiance method smoke density fall within the observer-based descent time ranges.

Table 4.23: Smoke layer descent time for experiment F2 camera V7 at six heights (z=2.20 m, 1.90 m, 1.60 m, 1.29 m, 1.00 m, 0.70 m) on checkerboard CB7 as estimated using the smoke density and observer-based methods

z [m]	Smoke Layer Descent Time [s]	
	Smoke Density	Observer-Based
2.20	157	121-167
1.90	181	165-193
1.60	227	179-270
1.29	289	257-308
1.00	342	>306
0.70	339	

Based on this step in the analysis, while it is evident that the use of threshold values of 0.5 for smoke density or normalized LRV as marking the presence of smoke during application of radiance method are not analogous, they do produce similar results when both can be calculated. Normalized LRVs cannot be used to estimate the smoke layer height in tests when the LRVs are low (*e.g.*, in IR images such as those in camera V7), whereas in these same situations, looking instead at the smoke density reaching a value of 0.5 can produce results. There are two scenarios in which estimations of smoke descent time using the LRVs may be more suitable. The first scenario is if it is not possible to estimate the smoke density due to a lack of dark pixel analysis areas in the vicinity and the same height as the light pixel analysis areas (*e.g.*, smoke descending over a white wall). The second scenario is when the LRVs are used to produce rough first estimates to save time in setting up and processing images for a more detailed radiance analysis, or for analysis during or between experiments. In general, however, for consistency and application to more scenarios, estimating the smoke layer height using the smoke density values is recommended unless smoke density cannot be calculated, or it is not feasible to process in the time allocated.

4.5.8 Step 8: Determine Maximum Smoke Density

In fulfilment of Step 8 of the final radiance method, the maximum smoke density was calculated, where possible, using the method outlined in Section 3.6.8. Table 4.24 shows the maximum smoke density results at all fourteen heights (z[m]) from pixel analysis areas taken across the window in images obtained from camera V1 in experiment F2. The minimum, maximum and average value for maximum smoke density were 0.925, 0.939 and 0.929, respectively, which is excellent agreement for 14 data points. As in Section 4.4.6, consistency is displayed across the determinations since the full range of values (minimum to maximum) fall within ±0.01 of the average value. The average value for maximum smoke density in experiment F2 is also distinct from the average maximum values of smoke density

obtained for fires fueled by the other sofa materials. Comparison of results indicates that the smoke in experiment F2 was more dense than that in the Type A experiments and experiment C1, and less dense than the smoke in experiments D1 and E1. Type F materials have yet to be tested in the smoke density chamber to determine whether ranking of results in the small-scale smoke density test agrees with the relative smoke density rank determined here.

Table 4.24: Final radiance method maximum smoke density values for experiment F2 camera V1 at fourteen heights (z[m]) across the window

z [m]	Maximum Smoke Density	z [m]	Maximum Smoke Density
1.759	0.929	1.535	0.928
1.727	0.925	1.503	0.928
1.695	0.926	1.471	0.930
1.663	0.927	1.439	0.931
1.631	0.927	1.407	0.932
1.599	0.929	1.375	0.934
1.567	0.927	1.343	0.939

The other two scenarios with detailed data sets discussed in the previous sections, where pixel analysis areas were selected from the checkerboards (CB1 and CB7), are not considered to be sufficiently reliable for determining the maximum smoke density because the smoke density values pass or approach a value of 1. As mentioned in Section 4.5.5, smoke density data that reach plateaus at values that are greater than 1 indicate that the smoke density calculation is no longer functioning as intended (*i.e.*, the DRVs are greater than the LRVs). Therefore, it would not make sense to use values of maximum smoke density in these instances, particularly since the maximum smoke density usually occurs towards the end of the analysis period. In general, smoke density values obtained using the radiance method with checkerboard pixel analysis areas appear to have the propensity to be greater than 1 later in the analysis time period. This propensity may mean that maximum smoke density cannot be reliably calculated using pixel analysis areas that are not backlit as is the case with windows. Alternatively, it may point to the need for a modification to the method in order to extend the analysis to determination of maximum smoke density. Either way, further investigation is required to better understand estimation of maximum smoke density using the final radiance method with pixel analysis of checkerboards.

4.5.9 Step 9: Compare to Other Results

The final radiance method (detailed in Section 3.6) developed through the various steps discussed above was finally applied to pixel analysis areas chosen from checkerboards CB1, CB2 and CB7 on images extracted from videos recorded by cameras V1, V2 and V7

respectively for experiments F1 and F2. Radiance analysis was also completed using pixel analysis areas on the window and concrete board beside CB1 as captured in images taken by camera V1 for experiment F2. The previous sections used a sub-set of this data to perform a detailed analysis and highlight the range of possible outcomes from the final radiance method. This section will include a comparison of the results obtained for the progression of smoke layer height with time for all heights analyzed from these camera images and experiments.

Progression of smoke layer height with time was determined using calculated values of smoke density, with a threshold value of 0.5, for a series of pixel analysis areas in images captured during experiment F1. Shown in Figure 4.57 are the results obtained from images taken by three cameras, V1 (●), V2 (▲) and V7 (■), with pixel analysis areas selected from the associated checkerboards (CB1, CB2 and CB7, respectively) at 58, 69 and 69 heights above the floor of the room, respectively. The height of the ceiling (——) is included as a reference, as are the minimum and maximum observer-based smoke layer descent times (F1 Range, +). The small mesh size of 6x6 or 7x7 pixels chosen for the pixel analysis areas allowed significantly more detailed assessment of smoke progression into the compartment to be derived using the final radiance method.

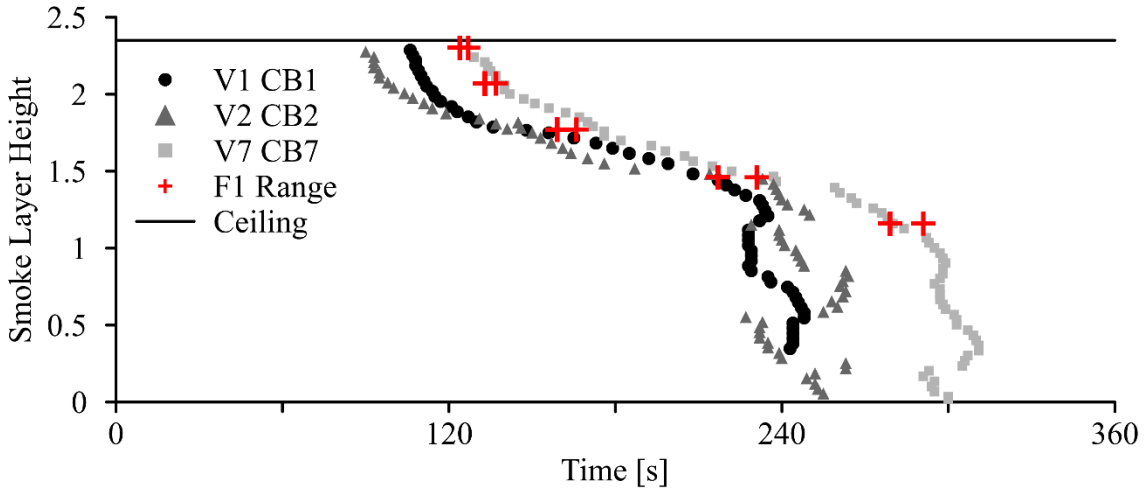

Figure 4.57: Final radiance method smoke layer height values from smoke density values with time for experiment F1 cameras V1, V2 and V7 at 58, 69 and 69 heights from checkerboards CB1, CB2 and CB7, respectively. Ceiling height and observer-based smoke layer heights (F1 Range) are included for reference.

The three traces for time resolved smoke layer descent as a function of height obtained using the final radiance method with the pixel analysis areas above in images extracted from experiment F1 follow the same general patterns. The smoke layer is determined to begin descending into the room at around 120 s into the test, then descends through a height of 1.5 m at around 180 s, and reaches the floor at around 275 s after the start of the fire. Some of

these results are slightly counterintuitive because they appear to indicate that the smoke layer height was in more than one location after around 230 s. However, as with the smoke density results, the radiance method smoke layer height results are calculated at discrete points in time, and are, consequently, independent of all prior and subsequent results. Thus, it is possible for a set of radiance method results to indicate that the smoke layer height is in more than one location at a time. Though this occurrence is not physically possible, it can indicate rapid smoke layer descent through the compartment since the radiance method identifies the time when the smoke density crosses the 0.5 threshold.

Of the three traces, those obtained through analysis of the IR recordings captured by camera V7 with pixel analysis areas chosen from checkerboard CB7 most closely match the observer-based smoke layer estimates of smoke layer heights with time. The estimates of time taken for the smoke layer to descend to z = 1.16 m based on analysis of images from camera V7 fell within the range of times estimated by the observers though for other heights more typically registered that the smoke layer, using a smoke density threshold = 0.5, arrived at a given height less than 10 seconds after the four times estimated by the observers for z=2.30 m, 2.07 m, 1.77 m and 1.46 m. Conversely, the comparable smoke density traces obtained from the radiance method using pixel analysis areas on checkerboards CB1 and CB2, from images captured in colour by cameras V1 and V2, signaled smoke layer height presence consistently before the earliest times identified in the observer-based method. The smoke density layer descent times based on analysis of images recorded by camera V2 were at most 35 seconds ahead of the observer time (at z=2.07 m) and for images from camera V1 were at most 64 seconds ahead of the observer time (at z=1.16 m).

The traces from all three cameras in Figure 4.57 suggest that the smoke layer height in the fire compartment begins to exhibit an apparent discontinuity in smoke layer descent times for heights below about z=1.00 m. In results from camera V2 images in particular, the value jumps when the pixel analysis areas change from one square down to the next on the checkerboard. A similar situation was encountered in analysis of the images from the black and white recordings from camera V11 in Section 4.5.3. However, unlike the previous instance, the change in radiance pattern between the two heights was not consistent enough to allow compensation for the change.

Progression of the smoke layer height with time was also determined using calculated smoke density values from experiment F2. Results are shown in Figure 4.58 for data obtained through radiance analysis of images from three cameras, V1, V2 and V7, with pixel analysis areas selected from the associated checkerboards CB1 (●), CB2(▲) and CB7(■) at 58, 42 and 38 heights, respectively, and from camera V1 at 14 heights across the window (○). Fewer heights were analyzed in calculations from checkerboards CB2 and CB7 for this experiment than in experiment F1 because at lower heights the contrast was decreasing and there was concern about the impact on results. This was previously flagged for CB7. The ceiling height

(——) is again included as a reference as are the minimum and maximum observer-based smoke layer descent times (F2 Range, +).

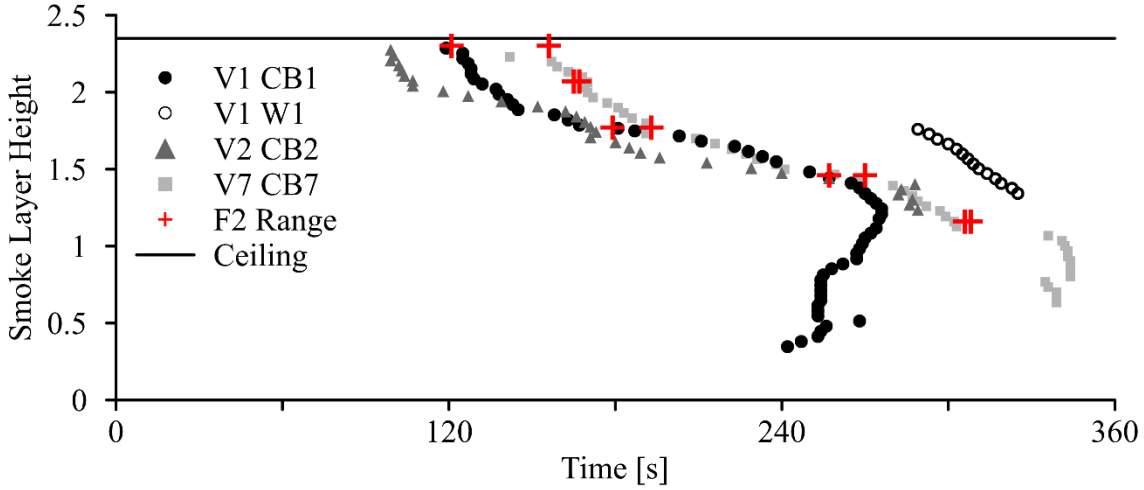

Figure 4.58: Final radiance method smoke layer height values from smoke density values with time for experiment F2 cameras V1, V2 and V7 at 58, 32 and 48 heights from checkerboards CB1, CB2 and CB7, respectively, as well as camera V1 at 14 heights across the window (W2). Ceiling height and observer-based smoke layer heights (F2 Range) are included for reference.

All three traces obtained using the final radiance method to analyze images from experiment F2 follow the same general pattern. They indicate that the smoke layer begins to descend around 120 s into the test, then descends through a height of 1.5 m at around 210 s, and they correspond closely to one another until around 275 s after ignition when reduced (or reversed) contrast begins to degrade the ability of the radiance method to follow the smoke layer progression. The overall pattern of the descent is quite similar to that seen through analysis of images from experiment F1 which is promising because those two tests would expected to have similar smoke development since they were based on the same fuel materials (Type F) with similar compartment ventilation.

As for experiment F1, the smoke layer descent profiles estimated through analysis of images from the IR recording by camera V7 with pixel analysis areas chosen on checkerboard CB7 in experiment F2 most closely matches the observer-based smoke layer descent times. Estimates from images extracted from the V7 videos fell within the observer range for three of the five observer heights (z=2.30 m, 1.77 m and 1.46 m) though estimated times were up to 4 seconds before or after the observer range for heights of z=1.16 m and 2.07 m, respectively. As in experiment F1, smoke density traces obtained using images from colour recordings by cameras V1 and V2 using the radiance method with pixel analysis areas on checkerboards CB1 and CB2, typically signaled the presence of the smoke layer before the earliest observer time estimates. Of the two, pixel analysis areas chosen on CB1 from camera

V1 tended to result in times closer to, or within (at z=1.77 m), the time range estimated by the observers, while smoke layer descent times based on analysis of images from V2 could precede the earliest observer times by up to 58 seconds (at z=2.07 m). Conversely, pixel analysis areas across the window in images from camera V1 indicated smoke layer height descent times that were furthest from the observer values, lagging 91 and 41 seconds behind the last observer time at z=1.77 m and 1.46 m, respectively.

In both Type F experiments, the pixel analysis areas selected from checkerboards in colour camera recordings (V1 and V2) tended to predict smoke layer descent times earlier than observer based values, while those from the IR recordings (V7) appeared to perform very well relative to the observer based range of smoke layer descent times. The pixel analysis areas selected from the backlit areas across the window in images extracted from camera V1 recordings from experiment F2 suggested distinctly later smoke layer descent times than the observer-based times. Further investigation would be required to determine whether this pattern, seen several times in this work, is consistent or a coincidence. If the former, an indicator of the presence of a smoke layer other than the current smoke density value of 0.5 might prove necessary to extract appropriate information for different situations.

In Figure 4.58, estimates of smoke layer descent times for heights below about 1.2 m do not follow the expected pattern for smoke layer desent. Estimated values of smoke layer presence obtained from images recorded by camera V7 jump forward to about 340 s due to the change in radiance estimated between one checkboard square and the next one down (transition at z=1.16 m)) and then again slightly back to about 330 s (transition at z=0.77 m) as discussed after Figure 4.57.

On the other hand, estimates of smoke layer height with time derived from pixel analysis areas on checkerboard CB1 in images from camera V1 appear to suggest that the smoke layer is present in several places at once for times after about 240 s. While a discretely distributed smoke layer might hypothetically be possible, is extremely unlikely for a descending smoke layer to occur at only a set of discrete locations at a given time and, as can be seen in Figure 4.59, there is no clear visible evidence that this did occur in these circumstances. Further investigation of the images for times between 240-270 s reveals an unfortunate combination of “thin” smoke, decreasing level of intensity of the window backlight (see impact on colour streams in Section 4.5.4), increases in light from the fire and frequent shadows from the reflection of the fire flickering on the lower portion of the checkerboard. In fact, once the issue was flagged here, it became apparent that similar lighting issues were a common problem in applying the radiance method for smoke layer height estimation from images recorded by cameras in the living (fire) room. In Figure 4.57, the traces suggest that the smoke layer rapidly descended to the floor between 240-300 s according to the radiance method analysis based on cameras V1, V2 and V7. However, Figure 4.60 displays the recorded image from camera V1 captured at 240 s, the approximate time when the smoke

layer is estimated to descend to the floor according to the radiance method. The image clearly shows that the bulk smoke layer height is still well above the floor.

Figure 4.59: Camera V1 image at 270 s into experiment F2

Figure 4.60: Camera V1 image at 240 s into experiment F1

This example clearly illustrates that, at this stage in development of the method, even results obtained using the final radiance method must be interpreted with care and caution. The radiance method itself could be applied to analyze the images captured by the various cameras during the experiments and, based on a threshold value of 0.5 to identify the time at which the smoke density passes a certain height, the progression of smoke layer descent was determined. The radiance method is based solely on normalized radiance values obtained from pixel analysis areas situated in particular locations in an image. As such, values of normalized radiance or values of smoke density of 0.5 resulting from shadows in an image cannot be distinguished from those arising from the presence of the smoke layer. Conversely, an observer watching a video is able to identify that the lighting in the image focus area has changed significantly and will adjust their visual parameters accordingly or, as necessary, look to adjacent spaces to observe the smoke layer if it is unclear in the original area. With

future refinement, it may be possible to improve the capabilities of the radiance method in this respect but, in the mean time, it is necessary for researchers to independently identify times at which significant changes in lighting (and therefore radiance) may have occured within a set of images and ensure that this is taken into account either in application or in interpretation of results from radiance method.

It is worth noting at this juncture that, though the smoke layer height values below 1.2 m in the living (fire) room are questionable and the accuracy of the maximum smoke density values are not yet proven, significant progress has been made toward development and application of a totally new radiance method for tracking smoke development and progression in experimental fires. Results in Section 4.1 determined that the most accurate method of estimating smoke layer height prior to the radiance method was to use observers who, from the early videos, could only estimate the smoke layer descent time at 13 points of known height (5 objects + up to 8 pixel-based observations over the window). With significant resources it might be possible to increase the number of smoke layer height estimates but it is unlikely the number of smoke density estimates could be increased. Through this thesis work, the radiance method has been advanced to the point where up to 35 smoke layer height markers (those above 1.2 m) can be utilized in one camera view. Up to 69 points, extending from floor to ceiling in the compartment, can be analyzed for estimation of smoke layer descent and smoke density using images extracted from a single camera angle. Comparing radiance method results between different camera angles allows extraction of more detail related to smoke progression in an experiment as well as leading to more confidence in the results.

Overall, the radiance method shows incredible promise for smoke analysis in large scale fire experiments. Results are useful in agregate, but are also particularly useful for comparison against detailed computational fire models, where data on a fine mesh is needed to validate smoke progression and associated impacts in fire and evacuation models. For instance, the radiance method also makes it possible to model smoke density with a contour plot. As a finale to the thesis, Figure 4.61 shows a contour plot of the progression of smoke, as marked by radiance method estimates of smoke density, at 58 heights spanning from 0.35 m above the floor to 2.29 m, very near the ceiling. Values are estimated at 30 second time intervals from ignition to 330 s into the fire, calculated using pixel analysis areas in images captured by the living (fire) room camera V1 in experiment F1. The smoke density contour colours get darker as the estimated value of smoke density increases from 0-0.2 (light grey) to 0.8-1 (black) while the orange areas indicate where the smoke density registered a physically inconsistent value (either below zero or above one). This plot shows how the smoke builds first at the ceiling (top) and becomes more dense (darker) before beginning to descend down through the compartment over time (moving down) until the entire compartment is filled with dense smoke.

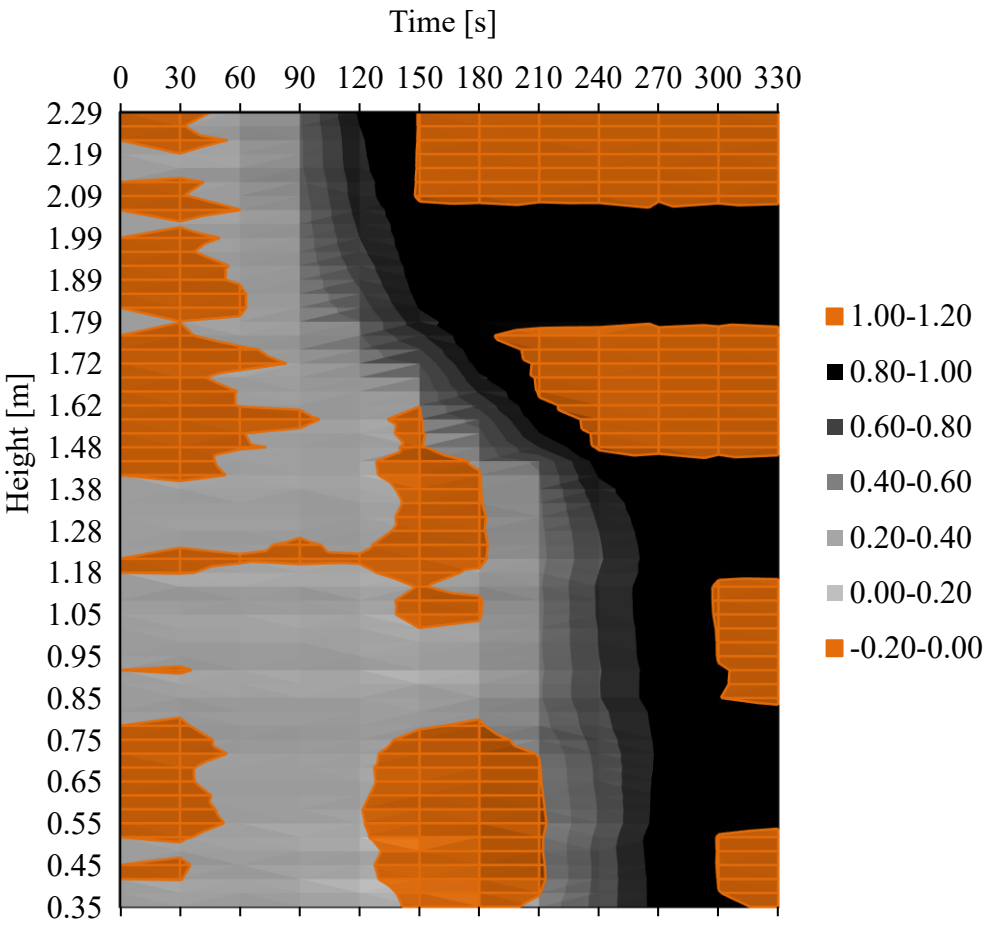

Figure 4.61: Contour plot of smoke density at 58 heights spanning 0.35 m to 2.29 m and 30 second time intervals from ignition to 330 s from camera V1 in experiment F1

4.5.10 Step 10: Assess Uncertainty

As with every measurement method, there are sources of uncertainty associated with application and implementation of the radiance method. Every effort was made to reduce the uncertainty at each stage in the development of the method—from theoretical development and early iterations, through to the final radiance method. Some of these considerations are discussed in this section.

Two major assumptions were made as part of the derivation in Section 3.4 that were incorporated in the radiance method and later corroborated with results. First, it was assumed that the background radiance should be as close to constant as possible. With the potential impact of this on the results verified in the early iterations of the method (Section 4.3), the reference image was always carefully selected to minimize the impact (and consequently uncertainty) of changes in background radiance. Soot deposit was found to have minimal

impact on the background radiance in these experiments (Section 4.5.6). On the other hand, while an effort was made to select pixel analysis areas farther from the fire and with care taken to avoid glare, shadows, and reflections (Sections 4.3 – 4.5), it was still necessary to discount some of the final radiance method data (below about 1.2 m in the living (fire) room for example) for this reason. In general, a concerted effort and outcome checks were employed to reduce the uncertainty relating to background radiance.

Second, necessity dictated that the path radiance and transmission losses were assumed to be constant, between contrasting areas and between images, in the theoretical derivation for the radiance method (Section 3.4). Individual colour stream results indicated that the path radiance and transmission do change over the course of the experiment (Section 4.5.4) and fire flickering was found to create short term patterns in the effects (Section 4.3). The impact of these changes was minimized through careful selection of image extraction frequency (Section 4.4.1), use of RGB or grey-scale radiance values (Section 4.5.4) rather than values based on analysis of individual colour streams, and selection of light and dark pixel analysis areas close together and at the same height (Section 4.5.3).

Over the course of development of the radiance method, several decisions were made that also impacted the uncertainty of the results. The averaging scheme used to smooth the raw pixel intensity data (Section 4.4.1) added some uncertainty relative to the original values. At the same time, the averaging scheme also removed some uncertainty during interpretation of results consequent to the smoothing effect of the process. In this case, the decision was made that the interpretation of results was more important than use of every individual value from the original raw data. The camera calibration curve was shown to have a moderate impact on the results with up to 11 seconds difference in smoke layer descent time and 2% difference in maximum smoke density (Section 4.5.4). While a camera calibration curve was determined in later experiments using a camera calibration tool, and the choice of calibration curve was definitely shown to have an impact on the results, it was determined that within the scope of the present research the ability to compare between experiments was critical so a single calibration curve was employed in all of the final stages of analysis. At the same time, the effect of this decision should certainly be investigated in the future. Pixel analysis area size and shape was found to have a significant effect on the results at all stages in the radiance method analysis, so the areas were carefully selected to minimize the uncertainty in this regard (Section 4.5.3). In addition, results were cross-verified between heights, camera angles, and repeat experiments where possible to optimize as many parameters as possible in the analysis and thus reduce the overall uncertainty of the results (Section 4.4 and 4.5.9).

Results from the early iterations (Section 4.3) made it clear that the radiance method had potential for application in smoke progression and smoke density analysis in indoor, fire scenarios with smoke as the particulate matter of interest and using pixel analysis areas chosen from sequential security camera images compared to reference images as the basis for

the analysis. The penultimate iteration results (Section 4.4) showed that a specific smoke density value or normalized light area radiance value, both using 0.5 as the threshold value for indicating the presence of smoke, could be used to accurately determine the height of the smoke layer in comparison to corresponding estimates made by independent observers. Results of the final radiance method indicate, however, that while it works well in many situations and was a good starting point (Sections 4.4.5 and 4.5.7), choice of a non-subjective value of 0.5 to indicate the presence of a smoke layer may not be the best indicator in all situations. Consequently, this choice introduces some uncertainty in the results. The range of situations analyzed in the present experiments include black and white images (Section 4.5.3), red, green and blue streams within images (Section 4.5.4), pixel analysis areas from checkerboards (Section 4.5.3), light pixel analysis areas only (Sections 4.5.4 and 4.5.7), pixel analysis areas from backlit windows (Section 4.5.7), and combinations thereof (Section 4.5.9). Each of these merits additional investigation using more camera angles and experiments in future. In this work, the uncertainty with respect to the smoke layer height was quantified by comparing with observer-based smoke layer heights as the reference. The largest comparative error in smoke layer descent time determined with the radiance method was 91 s (in Section 4.5.9) which is lower than the error reported for many of the existing methods that were utilized during the initial smoke layer height characterization (Section 4.1).

Finally, there is some uncertainty regarding values of maximum smoke density obtained from the radiance method. This is largely related to there being insufficient data to prove or disprove the merit of application of the radiance method in determining maximum values of smoke density in the different situations analyzed during this research (Sections 4.4.6 and 4.5.8). Preliminary results show that the maximum smoke density value obtained from different heights across a backlit window and between repeat experiments of the same fire scenario are very repeatable (±0.01 of the average value with up to 14 data points). Application of the radiance method to a range of images extracted from video recordings of experiments with fires fueled by different material types (Types A, C, D, E and F in this case) resulted in distinctly different values of maximum smoke density values. The results are very promising but could be compared in only two cases to independent characterization of smoke production from the materials leading to the conclusion, with some confidence, that values of maximum smoke density correctly indicate that Type A materials produce more dense smoke than Type C. Future investigation against independent testing and characterization of smoke production from more materials would reduce the uncertainty that remains in terms of the potential for ranking the quantity of smoke produced in different experiments based on comparison of values of the maximum smoke density obtained using the final radiance method.

The next, and final, chapter will detail the conclusions and recommendations that can now be made regarding both development and implementation of the novel radiance method for measuring smoke evolution presented in this thesis.

Chapter 5

Conclusions and Recommendations

The primary goal of this work was to develop a novel method for measuring smoke evolution that is based on analysis of video recordings of fire experiments, is suitable for a wide variety of applications, and requires minimal subjectivity. In charting smoke evolution, smoke layer height and smoke density were specifically considered of highest priority because of their importance to public safety. Video, temperature, and heat release rate data that was used to develop and refine the radiance method were obtained from 13 full-scale living room furniture fire experiments conducted in the University of Waterloo burn house. Existing methods were employed to characterize the smoke layer height in burn house living room during sofa fire experiments. The observer-based method was found to be the best existing option. Full-scale experiment video recordings and small-scale smoke density chamber experiment results were conducted in concert with the full-scale tests to characterize the smoke density of Type B, A and C materials as having the most to least dense smoke.

The concept for the new radiance method of measuring smoke evolution in full-scale fire experiments using video recordings was first derived theoretically to ensure that the approach was viable. The theory entailed comparing changes in contrasting light and dark pixel analysis areas in video images as the fire experiment progressed. Of interest was the change in values relative to the initial contrast value in analysis reference image chosen early in the experiment. Three iterations of radiance-based analysis of the images were used to identify several areas for improvement, and the penultimate radiance method was developed and used to estimate the smoke evolution in 11 historical burn house experiments. Changing and initial contrast values were used to calculate smoke density. Smoke density was found to rise significantly when the smoke layer was present at a location and further appeared to plateau at a maximum value of smoke density at some time after ignition. Normalized radiance values determined from light pixel analysis areas were also found to drop significantly when the smoke layer was present at a location. Thus, the final radiance method was advanced and was further refined using experimental results from two new experiments; these experiments included checkerboards in the background and careful selection of cameras and camera placement specifically tailored for development of the technique.

Comparison with characterization data indicated that the radiance method has significant potential to accurately determine smoke layer height on a much smaller mesh than was previously possible. Whether values of maximum smoke density can be used to rank smoke production from different fuel materials needs to be further verified but the results from this work are promising. For both of these smoke evolution components, there was agreement in values for repeat experiments and clear differentiation in results between experiments with different furniture materials as the fuel source.

5.1 The Radiance Method

The final radiance method consists of 10 steps as follows. First, the best rate of image extraction, and radiance value averaging scheme, is determined, and the fire video is parsed into individual frames for the analysis. A reference image is chosen from early in the fire (Step 2) and pixel analysis contrast areas are carefully identified (Step 3) for use in the analysis. Given that these selections were found to be critical for usable results, guidance is provided on which images and contrast areas are likely to produce the best results. A technique for identifying shape restrictions and minimum size for selected contrast areas is also provided because more contrast pairs means more precision in the smoke layer height and density results and more potential points of comparison for maximum smoke density. Next (Step 4), greyscale (RGB) mean pixel values are extracted from each contrast area and every image in the analysis. The camera calibration curve is determined, or assumed, in order to convert the extracted pixel values into radiance values. Once radiance values are obtained, smoke density is calculated in Step 5 for each contrast pair and every image. The contrast area radiance and smoke density values are plotted with time to observe visible patterns, including whether the smoke density plateaus. Step 6 involves estimating the impact of any soot deposits on surfaces used as pixel analysis areas. In this work, the smoke layer height was determined to be when the smoke density rose through a value of 0.5 (Step 7), though results indicate that a different value might be better in some scenarios. If the smoke density values with time plateaus, maximum smoke density was taken as the plateau value in Step 8. Thus far, the results indicate that the maximum smoke density may only be valid for contrast pairs when the light pixel analysis area is selected from a backlit window. If no dark areas are visible in the video image, the smoke layer height can be estimated using the light pixel analysis area radiance values, but no maximum smoke density estimate can be made. In either case, Step 9 involves repeating the process for each camera in an area wherein consistent values generate more confidence in the results. Finally, in Step 10, an uncertainty analysis is conducted for the radiance method results.

Analysis results indicated that, for the six furniture materials used in these 13 experiments (Types A-F) at least, the best rate of image extraction was one frame per second, with a data averaging scheme utilizing a centred 10-second rolling average, and square selection areas of at least 36 pixels in total or spatial extent of 30 mm x 30 mm. A gamma = 2.2 decoding scheme was used as the camera calibration curve for the 11 existing experiments. For

consistency, the same curve was applied to the two new Type F experiments, despite the camera calibration technique indicating that a 1:1 calibration curve would have been more appropriate.

Unusual smoke density patterns were better understood by reviewing the time-resolved plots of light and dark pixel analysis area radiance values, in RGB form or using the individual (red, green, and blue) colour streams, and watching the video recording for visible changes that indicated a cause for any patterns noted. Checkerboards were found to create better contrast selection areas relative to the existing background unless a backlit window was present in the image. New and used (flipped and wiped) checkerboards were all successfully used in the radiance method analysis, although new checkerboards provided higher contrast. Windows also provided better contrast and could be used to estimate values of maximum smoke density. Unfortunately, however, smoke layer height results from backlit windows were not as accurate as those obtained through radiance analysis of the checkerboards. Contrast areas selected from the existing background that was not a window, such as concrete board or drywall mud, tended to provide poor results due to low contrast in the selected areas.

Penultimate radiance method results showed distinct smoke density progressions for the 11 existing Type A-E experiments. For the Type A-C experiments, the smoke layer descent time to a particular height fell within the range of observer values in all cases. In the Type F experiments, the accuracy of the smoke layer descent times, relative to observer-based estimates, depended on the scenario in question. In the living (fire) room the Type F fires, results below a height of about 1.2 m were determined to be inaccurate as a result of interference in the images due to interactions amongst the growing fire, evolving smoke layer and presence of shadows.

In the Type A-E experiments, the smoke density of four of the materials plateaued at least once to a consistent value that was different for each material. The smoke density values for the Type F experiments also plateaued to a consistent value when the light pixel analysis area was selected from a backlit window. Within each material, the plateau value at each measured height (up to N=3 for experiments C1, D1 and E1) and across all heights (N=14 in experiment F2) were within ±0.01 of the average value for the corresponding test. The Type A experiment smoke density plateaued at all three heights in all three repeat experiments (N=9) and each plateau value remained within ±0.01 of the average value, showing good repeatability. Soot deposit during the experiments was found to have minimal, if any, impact on smoke density measurements.

Results show that the radiance method can be applied to existing or future video recordings that are designed for radiance method analysis or not, are colour or non-colour, are recorded at differing speeds and resolutions with a variety of cameras that may or may not be ideally situated for the application. The only caveat is that the image background must have at least

one sufficiently large white or light coloured area (minimum 100 pixels) that does not change in radiance value over the course of the analysis. Accordingly, the radiance method is now actively considered when designing experiments with smoke evolution factors at the University of Waterloo Live Fire Research Facility.

Over the longer term, the radiance method should be applicable to video recordings from historical fires and fire experiments through to future fire experiments and even recordings obtained in relation to fire investigations. With extension, the data generated by this method could be used to develop new theories, improve our understanding of fire dynamics, validate computer fire and fire evacuation models, and inform firefighters and the general public about the dangers of fire and smoke.

5.2 Recommendations for Future Work

Based on the analysis presented in this thesis, re-evaluation of checkerboard and video camera placement is recommended to enhance the accuracy of smoke evolution results in future full-scale living room furniture fires conducted in the University of Waterloo burn house apparatus. For example, Camera V11 may be better situated in a modified location such that checkerboard CB11A is as square as possible to the camera, and the cost of including checkerboard CB4 may not outweigh the questionable results likely to be obtained from a checkerboard at that location.

Use of another full-scale smoke density measurement method is recommended to be incorporated into several of the upcoming experiments in order that results from the radiance method can be directly compared to a second independent method. Small-scale smoke density chamber tests should also be conducted on the materials used as fuel in future experiments as well. Such comparison data would provide opportunity to further validate the accuracy of maximum smoke density rankings determined using the radiance method. Ascertaining and/or quantifying uncertainty at various steps would benefit the radiance method.

Calibration and soot deposit recordings should be made in lighting conditions that are as close to those in the experiment as possible. The data from these future experiments can be used to determine whether the soot deposit can be ranked for various experiments. Though not observed on the existing recordings, the checkerboard paint may off-gas the first time it is heated, therefore experiments should be conducted to investigate any influence that off-gassing of the checkerboard paint may have on toxicity measurements.

Some of the radiance method results presented in this work indicate that a different threshold value of smoke density may be better suited as an indicator of smoke layer height in certain situations. Given the well-reasoned logic and successful use of the threshold value of 0.5 in many locations and across this set of experiments, use of a smoke density value of 0.5 is still recommended to indicate smoke layer height. To determine an ideal threshold value with

minimal subjectivity, it is recommended that the radiance method be used to analyze smoke evolution in more fire experiments, including those conducted at different scales and/or under different set-ups and instrumentation. Application to other fire experiment scenarios would further validate the radiance method proposed in this work.

JOHN WILEY AND SONS LICENSE
TERMS AND CONDITIONS

Nov 09, 2020

This Agreement between Mrs. Jennifer Ellingham ("You") and John Wiley and Sons ("John Wiley and Sons") consists of your license details and the terms and conditions provided by John Wiley and Sons and Copyright Clearance Center.

License Number	4944980574268
License date	Nov 09, 2020
Licensed Content Publisher	John Wiley and Sons
Licensed Content Publication	Fire and Materials
Licensed Content Title	Smoke development and movement during ventilation-limited fires in a multi-storey house
Licensed Content Author	Noah Ryder, Peter Senez, Matt DiDomizio, et al
Licensed Content Date	May 28, 2020
Licensed Content Volume	0
Licensed Content Issue	0
Licensed Content Pages	12

Type of use	Dissertation/Thesis
Requestor type	University/Academic
Format	Print and electronic
Portion	Figure/table
Number of figures/tables	1
Will you be translating?	No
Title	MASc Student
Institution name	University of Waterloo
Expected presentation Date	Nov 2020
Portions	Figure 1
Requestor Location	Mrs. Jennifer Ellingham Attn: Mrs. Jennifer
Publisher Tax ID	EU826007151
Total	0.00 CAD

Terms and Conditions

TERMS AND CONDITIONS

This copyrighted material is owned by or exclusively licensed to John Wiley & Sons, Inc. or one of its group companies (each a "Wiley Company") or handled on behalf of a society with which a Wiley Company has exclusive publishing rights in relation to a particular work(collectively "WILEY"). By clicking "accept" in connection with completing this licensing transaction, you agree that the following terms and conditions apply to this transaction(along with the billing and payment terms and conditions established by the Copyright Clearance Center Inc., ("CCC's Billing and Payment terms and conditions"), at the time that you opened your RightsLink account (these are available at any time at http://myaccount.copyright.com/).

Terms and Conditions

- The materials you have requested permission to reproduce or reuse (the "Wiley Materials") are protected by copyright.
- You are hereby granted a personal, non-exclusive, non-sub licensable (on a stand-alone basis), non-transferable, worldwide, limited license to reproduce the Wiley Materials for the purpose specified in the licensing process. This license, **and any CONTENT (PDF or image file) purchased as part of your order,** is for a one-time use only and limited to any maximum distribution number specified in the license. The first instance of republication or reuse granted by this license must be completed within two years of the date of the grant of this license (although copies prepared before the end date may be distributed thereafter). The Wiley Materials shall not be used in any other manner or for any other purpose, beyond what is granted in the license. Permission is granted subject to an appropriate acknowledgement given to the author, title of the material/book/journal and the publisher. You shall also duplicate the copyright notice that appears in the Wiley publication in your use of the Wiley Material. Permission is also granted on the understanding that nowhere in the text is a previously published source acknowledged for all or part of this Wiley Material. Any third party content is expressly excluded from this permission.
- With respect to the Wiley Materials, all rights are reserved. Except as expressly granted by the terms of the license, no part of the Wiley Materials may be copied, modified, adapted (except for minor reformatting required by the new Publication),translated, reproduced, transferred or distributed, in any form or by any means, and no derivative works may be made based on the Wiley Materials without the prior permission of the respective copyright owner. **For STM Signatory Publishers clearing permission under the terms of the STM Permissions Guidelines only, the terms of the license are extended to include subsequent editions and for editions in other languages, provided such editions are for the work as a whole in situ and does not involve the separate exploitation of the permitted figures or extracts,** You may not alter, remove or suppress in any manner any copyright, trademark or other notices displayed by the Wiley Materials. You may not license, rent, sell, loan, lease, pledge, offer as security, transfer or assign the Wiley Materials on a stand-alone basis, or any of the rights granted to you hereunder to any other person.
- The Wiley Materials and all of the intellectual property rights therein shall at all times remain the exclusive property of John Wiley & Sons Inc, the Wiley Companies, or their respective licensors, and your interest therein is only that of having possession of and the right to reproduce the Wiley Materials pursuant to Section 2 herein during the continuance of this Agreement. You agree that you own no right, title or interest in or to the Wiley Materials or any of the intellectual property rights therein. You shall have no rights hereunder other than the license as provided for above in Section 2. No right,

license or interest to any trademark, trade name, service mark or other branding("Marks") of WILEY or its licensors is granted hereunder, and you agree that you shall not assert any such right, license or interest with respect thereto

- NEITHER WILEY NOR ITS LICENSORS MAKES ANY WARRANTY ORREPRESENTATION OF ANY KIND TO YOU OR ANY THIRD PARTY,EXPRESS, IMPLIED OR STATUTORY, WITH RESPECT TO THE MATERIALSOR THE ACCURACY OF ANY INFORMATION CONTAINED IN THEMATERIALS, INCLUDING, WITHOUT LIMITATION, ANY IMPLIEDWARRANTY OF MERCHANTABILITY, ACCURACY, SATISFACTORYQUALITY, FITNESS FOR A PARTICULAR PURPOSE, USABILITY,INTEGRATION OR NON-INFRINGEMENT AND ALL SUCH WARRANTIESARE HEREBY EXCLUDED BY WILEY AND ITS LICENSORS AND WAIVEDBY YOU.
- WILEY shall have the right to terminate this Agreement immediately upon breach of this Agreement by you.
- You shall indemnify, defend and hold harmless WILEY, its Licensors and their respective directors, officers, agents and employees, from and against any actual or threatened claims, demands, causes of action or proceedings arising from any breach of this Agreement by you.
- IN NO EVENT SHALL WILEY OR ITS LICENSORS BE LIABLE TO YOU ORANY OTHER PARTY OR ANY OTHER PERSON OR ENTITY FOR ANYSPECIAL, CONSEQUENTIAL, INCIDENTAL, INDIRECT, EXEMPLARY ORPUNITIVE DAMAGES, HOWEVER CAUSED, ARISING OUT OF OR INCONNECTION WITH THE DOWNLOADING, PROVISIONING, VIEWING ORUSE OF THE MATERIALS REGARDLESS OF THE FORM OF ACTION,WHETHER FOR BREACH OF CONTRACT, BREACH OF WARRANTY, TORT,NEGLIGENCE, INFRINGEMENT OR OTHERWISE (INCLUDING, WITHOUTLIMITATION, DAMAGES BASED ON LOSS OF PROFITS, DATA, FILES, USE,BUSINESS OPPORTUNITY OR CLAIMS OF THIRD PARTIES), AND WHETHEROR NOT THE PARTY HAS BEEN ADVISED OF THE POSSIBILITY OF SUCHDAMAGES. THIS LIMITATION SHALL APPLY NOTWITHSTANDING ANYFAILURE OF ESSENTIAL PURPOSE OF ANY LIMITED REMEDY PROVIDEDHEREIN.
- Should any provision of this Agreement be held by a court of competent jurisdiction to be illegal, invalid, or unenforceable, that provision shall be deemed amended to achieve as nearly as possible the same economic effect as the original provision, and the legality, validity and enforceability of the remaining provisions of this Agreement shall not be affected or impaired thereby.
- The failure of either party to enforce any term or condition of this Agreement shall not constitute a waiver of either party's right to enforce each and every term and condition of this Agreement. No breach under this agreement shall be deemed waived or excused by either party unless such waiver or consent is in writing signed by the party granting such waiver or consent. The waiver by or consent of a party to a breach of any provision of this Agreement shall not operate or be construed as a waiver of or consent to any other or subsequent breach by such other party.
- This Agreement may not be assigned (including by operation of law or otherwise) by you without WILEY's prior written consent.

- Any fee required for this permission shall be non-refundable after thirty (30) days from receipt by the CCC.
- These terms and conditions together with CCC's Billing and Payment terms and conditions (which are incorporated herein) form the entire agreement between you and WILEY concerning this licensing transaction and (in the absence of fraud) supersedes all prior agreements and representations of the parties, oral or written. This Agreement may not be amended except in writing signed by both parties. This Agreement shall be binding upon and inure to the benefit of the parties' successors, legal representatives, and authorized assigns.
- In the event of any conflict between your obligations established by these terms and conditions and those established by CCC's Billing and Payment terms and conditions, these terms and conditions shall prevail.
- WILEY expressly reserves all rights not specifically granted in the combination of (i)the license details provided by you and accepted in the course of this licensing transaction, (ii) these terms and conditions and (iii) CCC's Billing and Payment terms and conditions.
- This Agreement will be void if the Type of Use, Format, Circulation, or Requestor Type was misrepresented during the licensing process.
- This Agreement shall be governed by and construed in accordance with the laws of the State of New York, USA, without regards to such state's conflict of law rules. Any legal action, suit or proceeding arising out of or relating to these Terms and Conditions or the breach thereof shall be instituted in a court of competent jurisdiction in New York County in the State of New York in the United States of America and each party hereby consents and submits to the personal jurisdiction of such court, waives any objection to venue in such court and consents to service of process by registered or certified mail, return receipt requested, at the last known address of such party.

WILEY OPEN ACCESS TERMS AND CONDITIONS

Wiley Publishes Open Access Articles in fully Open Access Journals and in Subscription journals offering Online Open. Although most of the fully Open Access journals publish open access articles under the terms of the Creative Commons Attribution (CC BY) License only, the subscription journals and a few of the Open Access Journals offer a choice of Creative Commons Licenses. The license type is clearly identified on the article.

The Creative Commons Attribution License

The Creative Commons Attribution License (CC-BY) allows users to copy, distribute and transmit an article, adapt the article and make commercial use of the article. The CC-BY license permits commercial and non-

Creative Commons Attribution Non-Commercial License

The Creative Commons Attribution Non-Commercial (CC-BY-NC)License permits use, distribution and reproduction in any medium, provided the original work is properly cited and is not used for commercial purposes.(see below)

Creative Commons Attribution-Non-Commercial-NoDerivs License

The Creative Commons Attribution Non-Commercial-NoDerivs License (CC-BY-NC-ND)permits use, distribution and reproduction in any medium, provided the original work is properly cited, is not used for commercial purposes and no modifications or adaptations are made. (see below)

Use by commercial "for-profit" organizations

Use of Wiley Open Access articles for commercial, promotional, or marketing purposes requires further explicit permission from Wiley and will be subject to a fee.

Further details can be found on Wiley Online Library
http://olabout.wiley.com/WileyCDA/Section/id-410895.html

Other Terms and Conditions:

v1.10 Last updated September 2015

Questions? customercare@copyright.com or +1-855-239-3415 (toll free in the US) or+1-978-646-2777.

References

[1] Canadian Centre for Justice Statistics, Fire statistics in Canada, Selected Observations from the National Fire Information Database 2005 to 2014, 2017. www.cafc.ca (accessed August 9, 2019).

[2] Society of Fire Protection Engineers, Research Needs for the Fire Safety Engineering Profession: The SFPE Roadmap, 2018. https://cdn.ymaws.com/www.sfpe.org/resource/resmgr/roadmap/180703_SFPE_Research_Roadmap.pdf.

[3] D. Drysdale, An Introduction to Fire Dynamics, 3rd ed., John Wiley & Sons Ltd, 2011.

[4] G.E. Gorbett, J.L. Pharr, S.R. Rockwell, Fire Dynamics, 2nd ed., Pearson Education, Inc., Boston, 2016.

[5] National Fire Protection Association, NFPA 921: Guide for Fire and Explosion Investigations, (2017). https://www.nfpa.org/codes-and-standards/all-codes-and-standards/list-of-codes-and-standards/detail?code=921 (accessed July 14, 2020).

[6] National Fire Protection Association, NFPA 92: Standard for Smoke Control Systems, (2018). https://www.nfpa.org/codes-and-standards/all-codes-and-standards/list-of-codes-and-standards/detail?code=92 (accessed September 7, 2019).

[7] J.A. Milke, Smoke Control by Mechanical Exhaust or Natural Venting, in: M.J. Hurley, D. Gottuk, J.R. Hall Jr., K. Harada, E. Kuligowski, M. Puchovsky, J.L. Torero, J.M. Watts Jr., C. Wieczorek (Eds.), SFPE Handb. Fire Prot. Eng., 5th ed., Springer Science+Business Media, 2016: pp. 1824–1862. doi:10.1007/978-1-4939-2565-0.

[8] E.E. Zukoski, Development of a stratified ceiling layer in the early stages of a closed-room fire, Fire Mater. 2 (1978) 54–62. doi:10.1002/fam.810020203.

[9] L.Y. Cooper, M. Harkleroad, J. Quintiere, W. Rinkinen, An experimental study of upper hot layer stratification in full-scale multiroom fire scenarios, J. Heat Transfer. 104 (1982) 741–749. doi:10.1115/1.3245194.

[10] T. Tanaka, T. Yamana, Smoke Control in Large Scale Spaces. (Part 1: Analytic Theories for Simple Smoke Control Problems), Fire Sci. Technol. 5 (1985) 31–40. doi:10.3210/fst.5.31.

[11] M. Janssens, H.C. Tran, Data Reduction of Room Tests for Zone Model Validation, J. Fire Sci. 10 (1992) 528–555. doi:10.1177/073490419201000604.

[12] Y. He, On Experimental Data Reduction for Zone Model Validation, J. Fire Sci. 15 (1997) 144–161. doi:10.1177/073490419701500205.

[13] Y. He, A. Fernando, M. Luo, Determination of interface height from measured

parameter profile in enclosure fire experiment, Fire Saf. J. 31 (1998) 19–38. doi:10.1016/S0379-7112(97)00064-7.

[14] J.G. Quintiere, B.J. McCaffrey, W. Rinkinen, Visualization of room fire induced smoke movement and flow in a corridor, Fire Mater. 2 (1978) 18–24. doi:10.1002/fam.810020106.

[15] J.G. Quintiere, K. Steckler, D. Corley, An Assessment of Fire Induced Flows in Compartments, Fire Sci. Technol. 4 (1984) 1–14. doi:https://doi.org/10.3210/fst.4.1.

[16] R.H. Whiteley, Short communication: Some comments concerning the measurement of smoke, Fire Mater. 18 (1994) 57–59. doi:10.1002/fam.810180108.

[17] B. Karlsson, J.G. Quintiere, Enclosure Fire Dynamics, CRC Press LLC, Boca Raton, 2000. http://linkinghub.elsevier.com/retrieve/pii/S0379711201000315.

[18] Ontario Ministry of the Solicitor General, Ontario Smoke Alarm Status in Residential Fires 2012 to 2016, (2017). https://www.mcscs.jus.gov.on.ca/english/FireMarshal/MediaRelationsandResources/FireStatistics/OntarioFires/SmokeAlarmStatusinHomeFires/stats_sa_status.html (accessed August 10, 2019).

[19] M. Ahrens, Smoke Alarms in U.S. Home Fires, 2019. https://www.nfpa.org/News-and-Research/Data-research-and-tools/Detection-and-Signaling/Smoke-Alarms-in-US-Home-Fires (accessed February 27, 2020).

[20] Z. Xu, J. Zhao, Q. Liu, H. Chen, Y. Liu, Z. Geng, L. He, Experimental investigation on smoke spread characteristics and smoke layer height in tunnels, Fire Mater. 43 (2019) 303–309. doi:10.1002/fam.2701.

[21] Z.H. Gao, J. Ji, C.G. Fan, L.J. Li, J.H. Sun, Determination of smoke layer interface height of medium scale tunnel fire scenarios, Tunn. Undergr. Sp. Technol. 56 (2016) 118–124. doi:10.1016/j.tust.2016.02.009.

[22] C. Abecassis Empis, A. Cowlard, S. Welch, J.L. Torero, Chapter 3, Test One: The ‘Uncontrolled’ Fire, in: G. Rein, C. Abecassis Empis, R. Carvel (Eds.), Dalmarnock Fire Tests Exp. Model., School of Engineering and Electronics, University of Edinburgh, 2007: pp. 63–81. http://hdl.handle.net/1842/2411.

[23] J. Ellingham, H. Carton, E.J. Weckman, Comparing Smoke Density Chamber and Full-Scale Test Results, in: 3rd Int. Fire Saf. Symp. (IFireSS 2019), Ottawa, Canada, 2019: pp. 434–440.

[24] H. Carton, J. Ellingham, E.J. Weckman, Comparing Small-Scale and Full-Scale Smoke Density Test Results, in: 3rd Int. CNS Conf. Fire Saf. Emerg. Prep. Nucl. Ind., Ottawa, Canada. [In Press], 2019.

[25] S. Kerber, Study of the Effectiveness of Fire Service Vertical Ventilation and Suppression Tactics in Single Family Homes, 2013. https://ulfirefightersafety.org/docs/UL-FSRI-2010-DHS-Report_Comp.pdf (accessed

October 4, 2019).

[26] A.J.M. Heselden, P.L. Hinkley, Fire Research Note No. 832: Smoke Travel in Shopping Malls Experiments in Co-operation with Glasgow Fire Brigade - Part 1, 1970. https://www.iafss.org/publications/frn/832/-1/view/frn_832.pdf (accessed September 7, 2019).

[27] A. Rafinazari, G. Hadjisophocleous, A Study of the Effect of Make-Up Air Velocity on the Smoke Layer Height with Symmetric Openings in Atrium Fires, Fire Technol. 54 (2018) 229–253. doi:10.1007/s10694-017-0682-y.

[28] T. Rinne, J. Hietaniemi, S. Hostikka, Experimental validation of the FDS simulations of smoke and toxic gas concentrations, 2007. http://www.vtt.fi/inf/pdf/workingpapers/2007/W66.pdf.

[29] T. Yamana, T. Tanaka, Smoke Control in Large Scale Spaces (Part 2: Smoke Control Experiments In A Large Scale Space), Fire Sci. Technol. 5 (1985) 41–54. doi:https://doi.org/10.3210/fst.5.41.

[30] W.K. Chow, Determination of the smoke layer interface height for hot smoke tests in big halls, J. Fire Sci. 27 (2009) 125–142. doi:10.1177/0734904108096852.

[31] H.W. Yao, J. Bin Chen, Z. Zhao, F. Liu, D. Liang, Measurement of the smoke layer interface in fires, Autom. Constr. 37 (2014) 223–227. doi:10.1016/j.autcon.2013.09.005.

[32] C.M. Lai, C.J. Chen, M.J. Tsai, M.H. Tsai, T.H. Lin, Determinations of the fire smoke layer height in a naturally ventilated room, Fire Saf. J. 58 (2013) 1–14. doi:10.1016/j.firesaf.2013.01.015.

[33] S. Verstockt, Multi-modal Video Analysis for Early Fire Detection, Ghent University, 2011. http://hdl.handle.net/1854/LU-1969758.

[34] T. Beji, S. Verstockt, R. Van de Walle, B. Merci, On the Use of Real-Time Video to Forecast Fire Growth in Enclosures, Fire Technol. 50 (2014) 1021–1040. doi:10.1007/s10694-012-0262-0.

[35] S. Verstockt, T. Beji, P. De Potter, S. Van Hoecke, B. Sette, B. Merci, R. Van De Walle, Video driven fire spread forecasting (f) using multi-modal LWIR and visual flame and smoke data, Pattern Recognit. Lett. 34 (2013) 62–69. doi:10.1016/j.patrec.2012.07.018.

[36] T. Beji, S. Verstockt, R. Van De Walle, B. Merci, Global analysis of multi-compartment full-scale fire tests ('Rabot2012'), Fire Saf. J. 76 (2015) 9–18. doi:10.1016/j.firesaf.2015.05.005.

[37] National Fire Protection Association, NFPA 92B: Standard for Smoke Management Systems in Malls, Atria, and Large Spaces, (2009). https://www.nfpa.org/codes-and-standards/all-codes-and-standards/list-of-codes-and-standards/detail?code=92B (accessed August 24, 2019).

[38] J.G. Quintiere, B.J. McCaffrey, The Burning of Wood and Plastic Cribs in an Enclosure: Volume 1, 1980. https://tsapps.nist.gov/publication/get_pdf.cfm?pub_id=106992 (accessed August 24, 2019).

[39] G. Rein, J.L. Torero, W. Jahn, J. Stern-Gottfried, N.L. Ryder, S. Desanghere, M. Lázaro, F. Mowrer, A. Coles, D. Joyeux, D. Alvear, J. a Capote, A. Jowsey, P. Reszka, Chapter 10, A Priori Modelling of Fire Test One, in: G. Rein, C. Abecassis Empis, R. Carvel (Eds.), Dalmarnock Fire Tests Exp. Model., School of Engineering and Electronics, University of Edinburgh, 2007: pp. 173–192. http://hdl.handle.net/1842/2405.

[40] G. Heskestad, Letter to the Editor, Fire Technol. 27 (1991) 174–185.

[41] P. Reszka, C. Abecassis Empis, H. Biteau, A. Cowlard, T. Steinhaus, I. Fletcher, A. Fuentes, M. Gillie, S. Welch, Chapter 2, Experimental Layout and Description of the Building, in: G. Rein, C. Abecassis Empis, R. Carvel (Eds.), Dalmarnock Fire Tests Exp. Model., School of Engineering and Electronics, University of Edinburgh, 2007: pp. 31–61. http://www.era.lib.ed.ac.uk/handle/1842/1152.

[42] A. Cowlard, T. Steinhaus, C.A. Empis, J.L. Torero, Chapter 4, Test Two: The "Controlled Fire," in: G. Rein, C. Abecassis Empis, R. Carvel (Eds.), Dalmarnock Fire Tests Exp. Model., School of Engineering and Electronics, University of Edinburgh, 2007: pp. 83–96. http://hdl.handle.net/1842/2409.

[43] W. Jahn, G. Rein, J.L. Torero, Chapter 11, A Posteriori Modelling of Fire Test One, in: G. Rein, C. Abecassis Empis, R. Carvel (Eds.), Dalmarnock Fire Tests Exp. Model., School of Engineering and Electronics, University of Edinburgh, 2007: pp. 193–210. http://hdl.handle.net/1842/2404.

[44] G. Mulholland, T. Handa, O. Sugawa, H. Yamamoto, Smoke Filling in an Enclosure., Fire Sci. Technol. 1 (1981) 1–31. doi:10.3210/fst.1.1.

[45] G.D. Lougheed, G. V. Hadjisophocleous, C. McCartney, B.C. Taber, Large-scale physical model studies for an atrium smoke exhaust system, ASHRAE Trans. 105 (1999) 676–698. https://pdfs.semanticscholar.org/bcdf/bea876140a31e906dbbab3fe8f2a3d7bfac0.pdf.

[46] G. Hadjisophocleous, J. Zhou, Evaluation of Atrium Smoke Exhaust Make-Up Air Velocity, ASHRAE Trans. 114 (2008) 147–155. https://search.proquest.com/docview/192537108/fulltextPDF/857E695465B54321PQ/1?accountid=14906 (accessed September 6, 2019).

[47] G. V. Hadjisophocleous, G.D. Lougheed, S. Cao, Numerical study of the effectiveness of atrium smoke exhaust systems, ASHRAE Trans. 105 (1999) 699–715. https://nrc-publications.canada.ca/eng/view/accepted/?id=b607df17-de78-4e98-ad4d-e0dcbc1ff7c8.

[48] G. V. Hadjisophocleous, C.J. McCartney, Guidelines for the use of CFD simulations

for fire and smoke modeling, ASHRAE Trans. 111 (2005) 583–594. https://www.proquest.com/docview/192550408/27B8CBAD1FE343BDPQ/1.

[49] F. Tang, Q. He, Q. Shi, Experimental study on thermal smoke layer thickness with various upstream blockage–fire distances in a longitudinal ventilated tunnel, J. Wind Eng. Ind. Aerodyn. 170 (2017) 141–148. doi:10.1016/j.jweia.2017.08.003.

[50] U.S. Nuclear Regulatory Commission, Predicting Hot Gas Layer Temperature and Smoke Layer Height in a Room Fire with Natrual Ventilation, in: Fire Dyn. Tools Quant. Fire Hazard Anal. Methods U.S. Nucl. Regul. Comm. Fire Insp. Progr., 1805.0, U.S. Nuclear Regulatory Commission, 2004.

[51] S.P. Nowlen, Enclosure Environment Characterization Testing for the Baseline Validation of Computer Fire Simulation Codes, NUREG/CR-4681, SAND86-1296, 1987. https://www.nrc.gov/docs/ML0622/ML062260163.pdf (accessed July 22, 2020).

[52] Technical Committee on Smoke Management Systems, 1990 Fall Meeting Technical Committee Documentation, Quincy, 1990. https://www.nfpa.org/codes-and-standards/all-codes-and-standards/list-of-codes-and-standards/detail?code=92B&year=1991 (accessed August 1, 2020).

[53] D.J. Rasbash, R.P. Phillips, Quantification of Smoke Produced at Fires: Test Methods for Smoke and Methods of Expressing Smoke Evolution, Fire Mater. 2 (1978). doi:10.1002/fam.810020303.

[54] U. Flisi, Testing the Smoke and Fire Hazard, Polym. Degrad. Stab. 30 (1990) 153–168.

[55] B.A.L. Östman, Smoke and Soot, in: V. Babrauskas, S.J. Grayson (Eds.), Heat Release Fires, Elsevier Applied Science, London, 1992: pp. 233–250.

[56] ISO 5659-2, Plastics - Smoke generation - Part 2: Determination of optical density by a single-chamber test, 2nd ed., International Organization for Standardization, Geneva, 2006.

[57] ASTM E662-15: Standard Test Method for Specific Optical Density of Smoke Generated by Solid Materials, ASTM International, 2015. doi:10.1520/E0662-15.

[58] ASTM International, ASTM International Name Change Reflects Global Scope, News Release. (2001). https://www.astm.org/HISTORY/astm_changes_name.pdf (accessed July 19, 2020).

[59] BS 6401:1983 - Method for measurement, in the laboratory, of the specific optical density of smoke generated by materials, [Preview], British Standards Institution, 1983. https://shop.bsigroup.com/en/ProductDetail/?pid=000000000001040690 (accessed June 2, 2020).

[60] NFPA 258: Recommended Practice for Determining Smoke Generation of Solid Materials, National Fire Protection Association, Quincy, 2001. https://www.nfpa.org/codes-and-standards/all-codes-and-standards/list-of-codes-and-

standards/detail?code=258 (accessed June 2, 2020).

[61] NFPA 270: Standard Test Method for Measurement of Smoke Obscuration Using a Conical Radiant Source in a Single Closed Chamber, National Fire Protection Association, Quincy, 2018.

[62] Fire Testing Technology, Users' Guide for the Smoke Density Chamber: For Instruments with the FTT Enhanced PM Unit, 3.0, East Grinstead UK, 2008.

[63] M.M. Hirschler, An attachment for use with the NBS smoke density chamber for measurement of smoke obscuration at different orientations, Fire Mater. 17 (1993) 173–183. doi:10.1002/fam.810170405.

[64] T.G. Lee, NBS Technical Note 708: Interlaboratory Evaluation of Smoke Density Chamber, U.S. National Bureau of Standards, Washington, 1971. https://nvlpubs.nist.gov/nistpubs/Legacy/TN/nbstechnicalnote708.pdf (accessed July 27, 2018).

[65] ASTM International, Research Report E05-1002: Interlaboratory Study to Establish Precision Statements for ASTM E662 , Standard Test Method for Specific Optical Density of Smoke Generated by Solid Materials, West Conshohocken, 1977.

[66] L. Arnold, A. Belt, T. Schultze, L. Sichma, Spatiotemporal Measurement of Light Extinction Coefficients in Compartment Fires, in: 15th Int. Fire Sci. Eng. Conf. (Interflam 2019), London, UK, 2019: pp. 489–501.

[67] T. Yamada, Y. Akizuki, Visibility and Human Behaviour in Fire Smoke, in: SFPE Handb. Fire Prot. Eng., 5th ed., 2016: pp. 2181–2206.

[68] T. Jin, Visibility through Fire Smoke (I) [Google Translation], Bull. Fire Prev. Soc. Japan. 19 (1970). doi:10.11196/kasai.19.2.1.

[69] M.J. Rood, 2018 Kappe Lecture: Optical Remote Sensing of Particulate Matter to Quantify Plume Opacity and Mass Emission Factors, (2018).

[70] K. Du, M.J. Rood, B.J. Kim, M.R. Kemme, B. Franek, K. Mattison, Quantification of plume opacity by digital photography, Environ. Sci. Technol. 41 (2007) 928–935. doi:10.1021/es061277n.

[71] K. Du, M.J. Rood, B.J. Kim, M.R. Kemme, B. Franek, K. Mattison, J. Cook, Field Evaluation of Digital Optical Method to Quantify the Visual Opacity of Plumes, J. Air Waste Manage. Assoc. 57 (2007) 836–844. doi:10.3155/1047-3289.57.7.836.

[72] K. Du, M.J. Rood, B.J. Kim, M.R. Kemme, B. Franek, K. Mattison, Evaluation of digital optical method to determine plume opacity during nighttime, Environ. Sci. Technol. 43 (2009) 783–789. doi:10.1021/es800483x.

[73] K. Du, Optical Remote Sensing of Airborne Particulate Matter to Quantify Opacity and Mass Emissions, University of Illinois, 2007.

[74] K. Du, P. Shi, M.J. Rood, K. Wang, Y. Wang, R.M. Varma, Digital Optical Method to

quantify the visual opacity of fugitive plumes, Atmos. Environ. 77 (2013) 983–989. doi:10.1016/j.atmosenv.2013.06.017.

[75] W. Yuen, Y. Gu, Y. Mao, S. Koloutsou-Vakakis, M.J. Rood, H.K. Son, K. Mattison, B. Franek, K. Du, Performance and uncertainty in measuring atmospheric plume opacity using compact and smartphone digital still cameras, Aerosol Air Qual. Res. 17 (2017) 1281–1293. doi:10.4209/aaqr.2016.08.0369.

[76] W. Yuen, Y. Gu, Y. Mao, P.M. Kozak, S. Koloutsou-Vakakis, H.K. Son, K. Mattison, B. Franek, M.J. Rood, Daytime atmospheric plume opacity measurement using a camcorder, Environ. Technol. Innov. 12 (2018) 43–54. doi:10.1016/j.eti.2018.07.003.

[77] B.J. Kim, M.J. Rood, K. Du, Digital Optical Method (DOM) and System for Determining Opacity, US 7.495,767 B2, 2009.

[78] M.J. McFarland, S.H. Terry, D.A. Stone, S.L. Rasmussen, M.J. Calidonna, Evaluation of the Digital Opacity Compliance System in High Mountain Desert Environments, J. Air Waste Manage. Assoc. 53 (2003) 724–730. doi:10.1080/10473289.2003.10466210.

[79] M.J. McFarland, S.H. Terry, M.J. Calidonna, D.A. Stone, P.E. Kerch, S.L. Rasmussen, Measuring Visual Opacity Using Digital Imaging Technology, J. Air Waste Manage. Assoc. 54 (2004) 296–306. doi:10.1080/10473289.2004.10470908.

[80] M.J. McFarland, S.L. Rasmussen, D.A. Stone, G.R. Palmer, J.D. Wander, Validation of the Digital Opacity Compliance System under Regulatory Conditions, J. Air Waste Manage. Assoc. 56 (2006) 1260–1266. doi:10.1080/10473289.2006.10464588.

[81] M.J. McFarland, S.L. Rasmussen, D.A. Stone, G.R. Palmer, A.C. Olivas, J.D. Wander, M. Spencer, Field demonstration of visible opacity photographic systems, J. Air Waste Manage. Assoc. 57 (2007) 31–38. doi:10.1080/10473289.2007.10465297.

[82] M.J. McFarland, G.R. Palmer, A.C. Olivas, Life cycle cost evaluation of the digital opacity compliance system, J. Environ. Manage. 91 (2010) 927–931. doi:10.1016/j.jenvman.2009.11.010.

[83] Z. Tan, Air Pollution and Greenhouse Gases: From Basic COncepts to Engineering Applications for Air Emission Control, Springer Science+Business Media, 2014. doi:10.1007/978-981-287-212-8.

[84] J. Ellingham, E.J. Weckman, Video Analysis of Smoke Density in Full-Scale Fires, in: Combust. Inst. – Can. Sect. Spring Tech. Meet. 2019, Kelowna, Canada, 2019.

[85] J. Ellingham, B. Forrest, E.J. Weckman, Analyzing Smoke Evolution in Full-Scale Fire Experiments from Recorded Video, in: 15th Int. Fire Sci. Eng. Conf. (Interflam 2019), London, UK, 2019: pp. 1503–1514.

[86] P. Senez, P. Mulherin, E.J. Weckman, Repeatability of Underventilated Compartment Fire Testing with Complex Fuel Packages, in: 15th Int. Conf. Exhib. Fire Mater. 2017, Interscience Communications Ltd, San Francisco, USA, 2017: pp. 342–355.

[87] B. Forrest, E.J. Weckman, P. Senez, N.L. Ryder, M. DiDomizio, The Evolution of a Ventilation-Limited Fire in a Multistorey House, in: 15th Int. Fire Sci. Eng. Conf. (Interflam 2019), London, UK, 2019: pp. 1515–1526.

[88] B. Forrest, E.J. Weckman, N.L. Ryder, P. Senez, The Effects of a Ventilation-Limited Fire Environment on Furniture Burning Characteristics, in: 3rd Int. Fire Saf. Symp. (IFireSS 2019), Ottawa, Canada, 2019: pp. 455–463.

[89] B. Forrest, E. Weckman, M. DiDomizio, P. Senez, N. Ryder, Smoke development and movement during ventilation-limited fires in a multi-storey house, Fire Mater. (2020) 1–12. doi:10.1002/fam.2860.

[90] B. Forrest, Heat Release Rate in Ventilation-Limited Furniture Fires, University of Waterloo, 2020. http://hdl.handle.net/10012/16065.

[91] British Standards Institution, BS 5852: Methods of test for assessment of the ignitability of upholstered seating by smouldering and flaming ignition sources, (2006).

[92] B. Forrest, K. Amini, E.J. Weckman, CFAST Simulations of Large-Scale Furniture Burns, in: Combust. Inst. – Can. Sect. Spring Tech. Meet. 2018, Toronto, Canada, 2018: p. P32.

[93] B. Forrest, E.J. Weckman, A Comparison of Methods for the Calculation of Furniture Heat Release Rate, in: 3rd Int. Fire Saf. Symp. (IFireSS 2019), Ottawa, Canada, 2019: pp. 417–424.

[94] B. Forrest, E.J. Weckman, J. Ellingham, C. White, A Comparison of Methods for the Calculation of Heat Release Rate of Furniture, in: Combust. Inst. – Can. Sect. Spring Tech. Meet. 2018, Toronto, Canada, 2018: p. P73.

[95] M. DiDomizio, Experimental Study of Thermal Degradation of Fire Resisting Compartment Partitions in Fires, University of Waterloo, 2017. http://hdl.handle.net/10012/12228.

[96] Home Depot International, The Home Depot, (2019). https://www.homedepot.ca/en/home.html (accessed July 18, 2019).

[97] Home Hardware Stores Limited, Home Hardware, (2019). https://www.homehardware.ca/en/ (accessed July 18, 2019).

[98] Lowe's, Lowe's, (2019). https://www.lowes.ca/ (accessed July 18, 2019).

[99] Rona, Rona, (2019). https://www.rona.ca/en (accessed July 18, 2019).

[100] Rust-Oleum Corportaiton, Rust-Oleum Specialty High Heat Tough Protective Enamel, (2007).

[101] Lorex Technology Inc., IP Rating for Security Cameras, (2017). https://www.lorextechnology.com/self-serve/ip-rating-for-security-cameras/R-sc2700033 (accessed May 22, 2020).

[102] Lorex Corporation, LBV2531 Series High Definition 1080p Security Camera, (2017). https://www.lorextechnology.com/downloads/security-cameras/LBV2531/LBV2531_Series_Specs_R5.pdf (accessed July 19, 2019).

[103] Lorex Corporation, LBV2711 Series True High Definition Bullet Security Camera, (2017). https://www.lorextechnology.com/downloads/LBV2711B/LBV2711TB_Series_Spec_R6.pdf (accessed July 17, 2019).

[104] Lorex Technology Inc., DV900 Series DVRs: 4K Ultra High Definition Digital Video Surveillance Recorder, (2018). https://www.lorextechnology.com/downloads/security-dvr/DV900/DV900-Series-DVRs_Series_Specs_R2.pdf (accessed July 19, 2019).

[105] Classic Microsoft Paint, Microsoft Corporation, Redmond WA, 2018.

[106] Filmora Version 8.6.1, Wondershare Technology Company, Burnaby BC, 2018.

[107] Fire Testing Technology, Users' Guide for the SmokeBox Software Package Version 3.7: For Use With The FTT Smoke Density Chamber, East Grinstead UK, 2008.

[108] V. Babrauskas, D. Baroudi, J. Myllymakr, M. Kokkala, The cone calorimeter used for predictions of the full-scale burning behaviour of upholstered furniture, Fire Mater. 21 (1997) 95–105. doi:10.1002/(SICI)1099-1018(199703)21:2<95::AID-FAM601>3.0.CO;2-A.

[109] T.W. Fritz, P.L. Hunsberger, Testing of mattress composites in the cone calorimeter, Fire Mater. 21 (1997) 17–22. doi:10.1002/(SICI)1099-1018(199701)21:1<17::AID-FAM590>3.0.CO;2-G.

[110] M. Wendisch, P. Yang, Theory of Atmospheric Radiative Transfer: A Comprehensive Introduction, Wiley-VCH, Wienheim, Germany, 2012.

[111] H. David, R. Resnick, J. Walker, Fundamentals of Physics: Extended, 8th ed., John Wiley & Sons, Inc, 2008.

[112] M.D. Grossberg, S.K. Nayar, Modeling the space of camera response functions, IEEE Trans. Pattern Anal. Mach. Intell. 26 (2004) 1272–1282. doi:10.1109/TPAMI.2004.88.

[113] K.J. Hay, Email Subject: Digital Optical Method Software, (2018).

[114] M.J. Rood, Email Subject: Digital Optical Method Lecture at the University of Waterloo, (2018).

[115] VideoLAN, VLC Media Player, (n.d.). http://www.videolan.org/vlc/ (accessed May 13, 2020).

[116] J. Ellingham, Fire, Smoke and You, in: W3 Represent. A Res. Symp., University of Waterloo, 2019. https://uwaterloo.ca/w3-represents/.

[117] C.A. Schneider, W.S. Rasband, K.W. Eliceiri, NIH Image to ImageJ: 25 years of image analysis, Nat. Methods. 9 (2012) 671–675. doi:10.1038/nmeth.2089.

[118] W.S. Rasband, ImageJ, U.S. National Institutes of Mental Health, Bethesda, Maryland, USA, 2018. https://imagej.nih.gov/ij/ (accessed April 3, 2019).

[119] M.D. Abràmoff, P.J. Magalhães, S.J. Ram, Image processing with imageJ, Biophotonics Int. 11 (2004) 36–41. doi:10.1201/9781420005615.ax4.

[120] C. Poynton, Chapter 6: Gamma, in: A Tech. Introd. to Digit. Video, John Wiley & Sons Ltd, New York, 1996: pp. 100–103.

[121] Lorex Technology Inc., No, (2019). https://www.lorextechnology.com/ (accessed March 15, 2019).

[122] Lorex Technology Inc., Security Camera Night Vision, (n.d.). https://www.lorextechnology.com/site/self-serve/security-camera-night-vision/R-sccont21100003 (accessed May 28, 2020).

[123] X-Rite Incorporated, ColorChecker Video XL & MEGA, (2020). https://xritephoto.com/ph_product_overview.aspx?id=2524# (accessed May 23, 2020).

[124] V. Ibrahimli, J. Ellingham, Personal Communication, (2020).

[125] H. Carton, J. Ellingham, E.J. Weckman, Comparing Small-Scale and Full-Scale Smoke Density Test Results, in: 3rd Int. CNS Conf. Fire Saf. Emerg. Prep. Nucl. Ind., Ottawa, Canada, 2019.

Appendix

This appendix includes the N-percent method smoke layer height estimate results for all living room thermocouple rakes (T2, T3 and T4). As shown in Figure 3.3, thermocouple rakes T2, T3 and T4 were located in the centre, corridor side and SW corner of the living room, respectively. The smoke layer height estimates are included in each plot if the height falls between the top and bottom thermocouple in the rake (see Table 3.5).

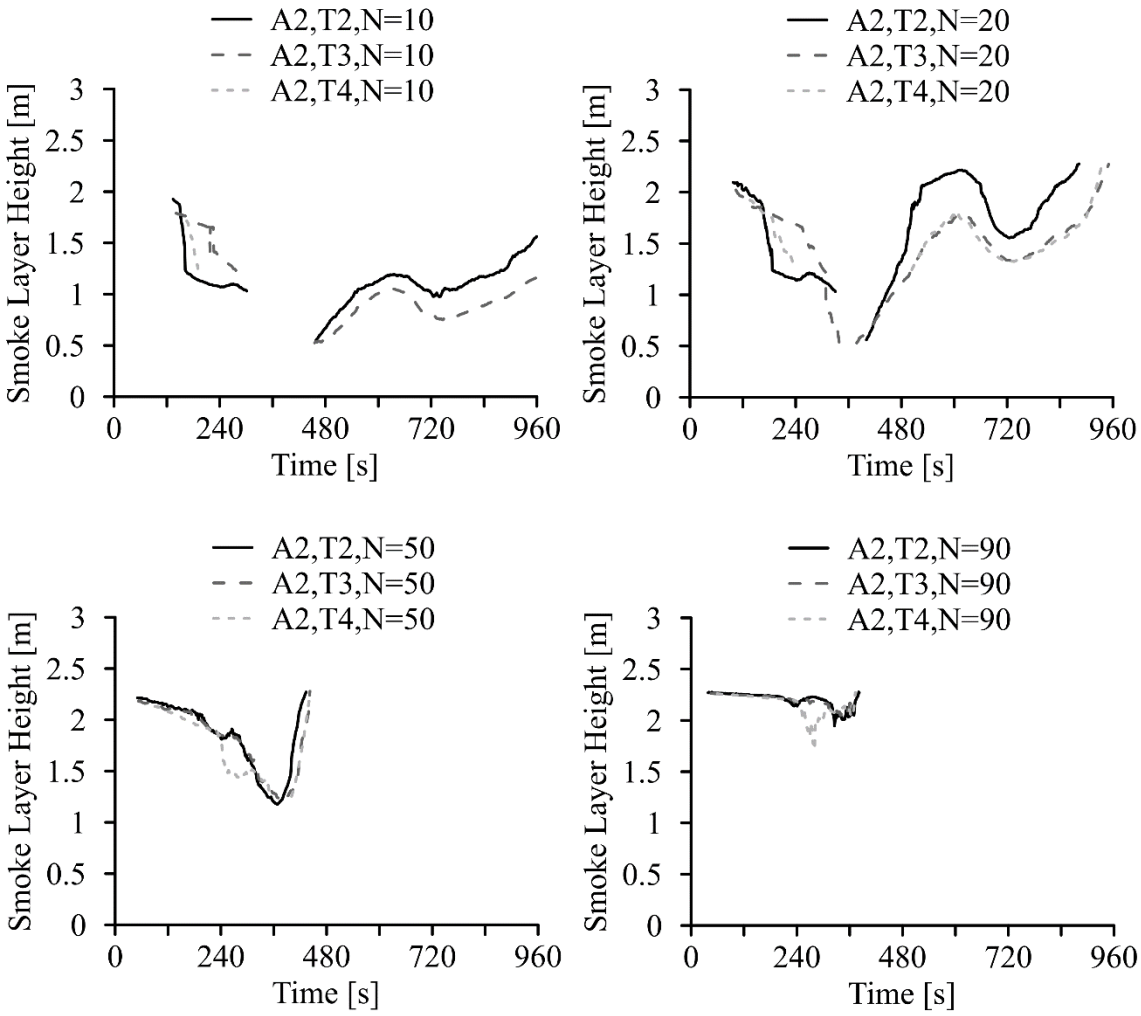

Figure A.1: N-percent method smoke layer height estimation over time with N = 10, 20, 50 and 90 for living room thermocouple rakes T2, T3 and T4 in experiment A2

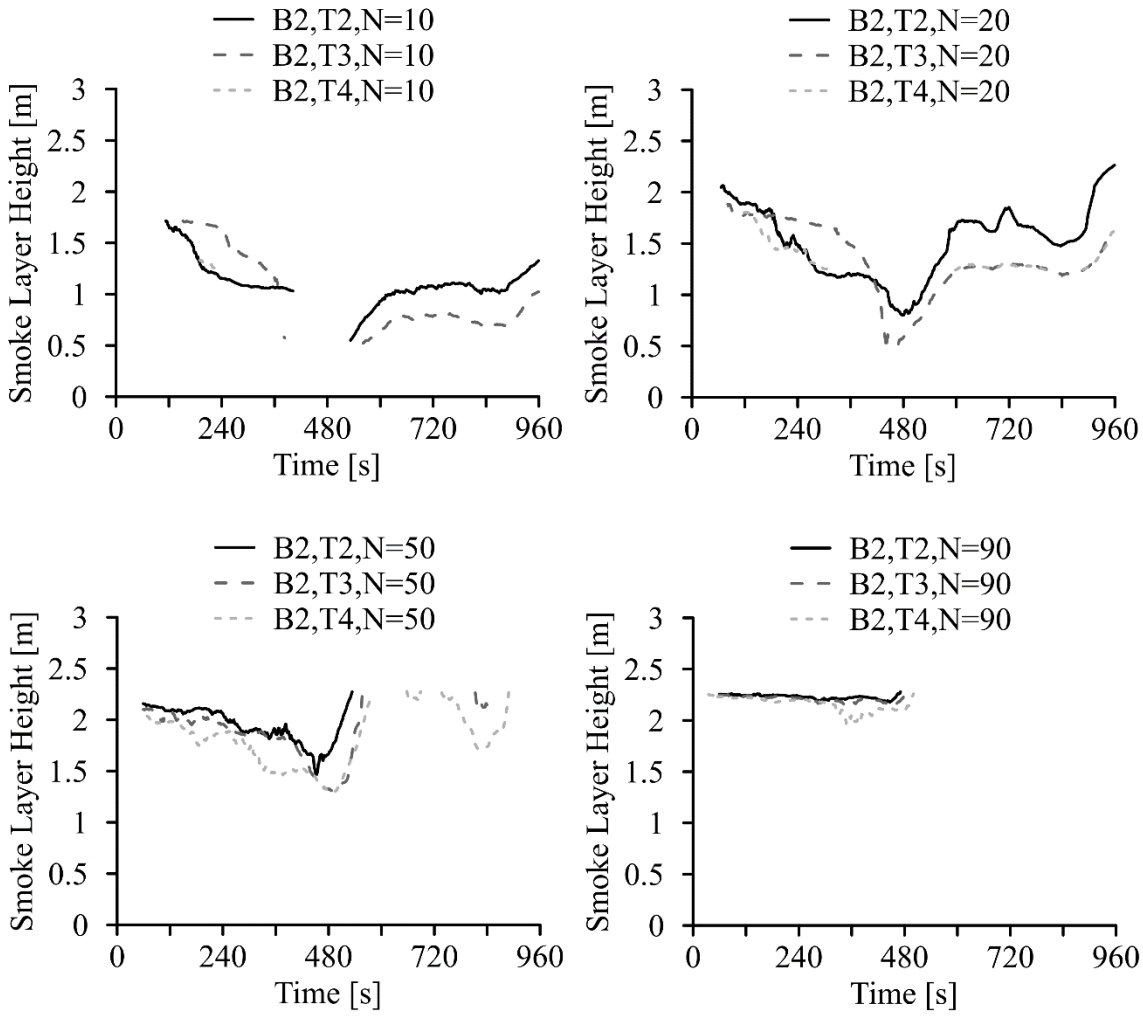

Figure A.2: N-percent method smoke layer height estimation over time with N = 10, 20, 50 and 90 for living room thermocouple rakes T2, T3 and T4 in experiment B2

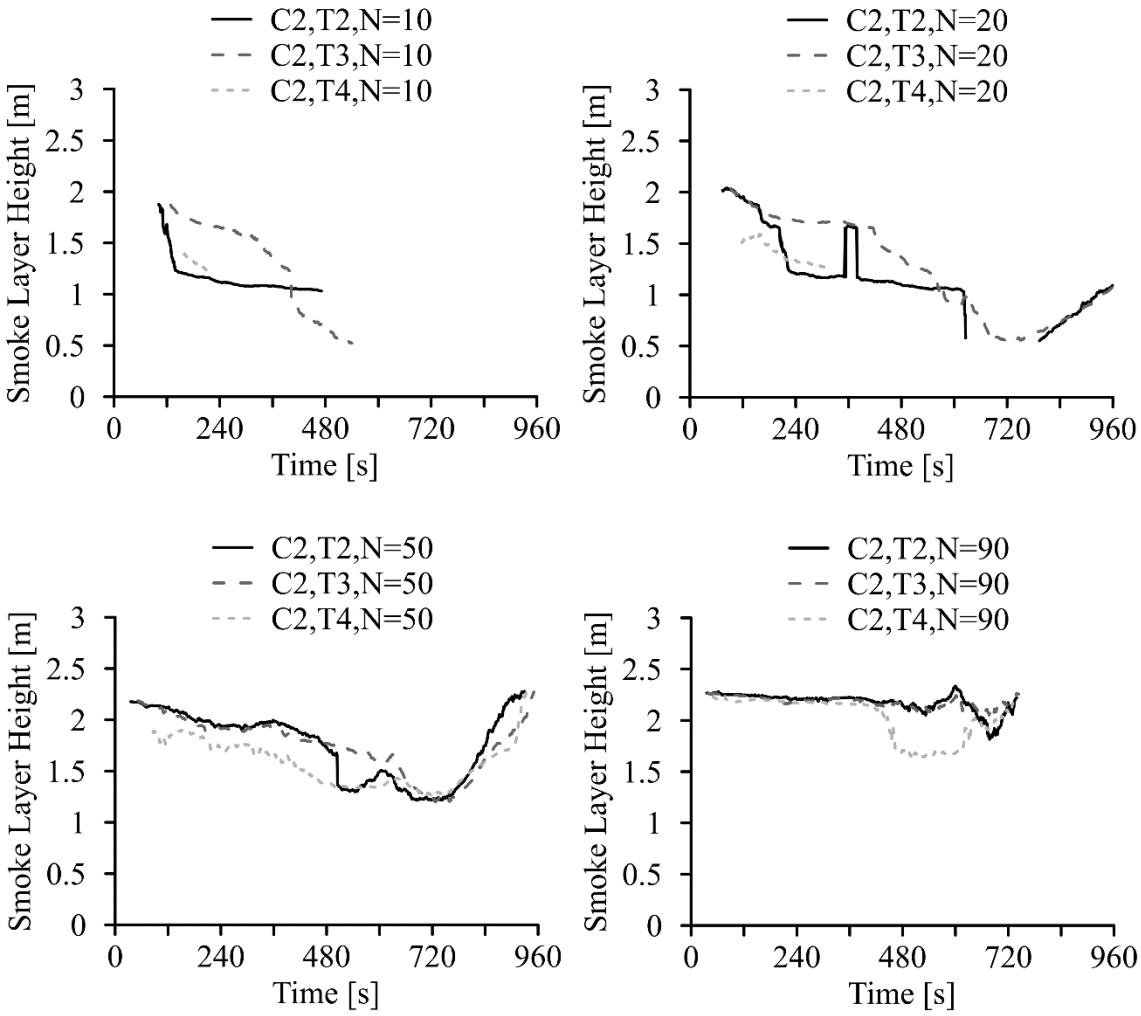

Figure A.3: N-percent method smoke layer height estimation over time with N = 10, 20, 50 and 90 for living room thermocouple rakes T2, T3 and T4 in experiment C2